

INVESTIGATION OF SPLIT INJECTION
IN A SINGLE CYLINDER OPTICAL DIESEL ENGINE

A thesis submitted for the degree of Doctor of Philosophy

By

Álvaro Díez Rodríguez

School of Engineering and Design
Brunel University
United Kingdom

April 2009

Abstract

Over the last decade, the diesel engine has made dramatic progress in its performance and market penetration. However, in order to meet future emissions legislations, Nitrogen Oxide (NO_x) and particulate matter (PM) emissions will need to be reduced simultaneously. Nowadays researchers are focused on different combustion modes like homogeneous charge compression ignition (HCCI) combustion and premixed charge compression ignition (PCCI) which have a great potential for both low soot and low NO_x. In order to achieve these combustion modes, different injection strategies have been investigated.

This study investigates the effects of split injection strategies with high levels of Exhaust Gas Recirculation (EGR) on combustion performance and emissions in a high speed direct injection optical diesel engine. The investigation is focused on the effects of split injections at different injection pressures, injection timings and dwell angles using base diesel and biodiesel fuels.

The effect of fuel properties has been also investigated as an attempt to reduce regulated exhaust emissions in diesel engines. Performance, emissions and combustion characteristics have been examined for two different biodiesel fuels, namely BTL 50 and BTL 46.

A Ricardo Hydra single cylinder optical engine was used in which conventional experimental methods like cylinder pressure data, heat release analysis and exhaust emissions analysis were applied. Optical techniques like direct spray and combustion visualization were applied by means of a high speed imaging system with a copper vapour laser illumination system.

A high-speed two-colour system has been developed and implemented to obtain in-cylinder diesel combustion temperature and soot measurements to gain better understanding of the mixture formation and combustion processes.

This investigation concludes that the split injection strategies show potential to achieve low emissions combustion.

Acknowledgements

I would like to express my deepest gratitude to Professor Hua Zhao, for giving me the opportunity to do this research, for his encouragement, support and advice over the last four years.

I would like to thank all the people at Brunel who have made my work possible. Firstly to Kiran Gill who has always been very helpful giving me advices and sharing his knowledge of the hydra engine. Technician Andy Selways for rebuilding the engine so many times and so quickly when needed and Clive Barrett for his help and assistance with all the electronic “bits” and patience while doing so. And my friends here, Tonio, for his contribution to this PhD and his help in the lab, Paul Wytch for his great help at the end of my PhD and Raul for sharing so many good things since we started together in our MSc.

I would further like to thank my parents, brother and sister because, regardless of the distance, I always feel them very close to me and I have always had their support for everything I have done.

Finally, to my family: Rakibe and Dolunay because I found in you my “sun” and my “moon”.

Abbreviations

| | |
|------|---|
| AFR | Air/Fuel Ratio |
| ATDC | After Top Dead Center |
| BTL | Biomass to liquid fuel |
| BTDC | Before Top Dead Center |
| CA | Crank Angle |
| CARB | Californian Air Resource Board |
| CCD | Charge-Couple Devices |
| CI | Compression Ignition |
| CN | Cetane Number |
| CO | Carbon Monoxide |
| CR | Common Rail |
| CR | Compression Ratio |
| CV | Calorific Value |
| CVL | Copper Vapour Laser |
| DC | Direct Current |
| DI | Direct Injection |
| ECU | Electronic Control Unit |
| EGR | Exhaust Gas Re-circulation |
| EPA | Environmental Protection Agency |
| EU | European Union |
| FID | Flame Ionisation Detector |
| FIE | Fuel Injection Equipment |
| FILE | Forward Illumination Light Extinction |
| HCCI | Homogeneous Charge Compression Ignition |
| HR | Heat Release |
| HSDI | High Speed Direct Injection |
| IC | Internal Combustion |
| ICCD | Intensified Charge-Couple Devices |
| ID | Ignition Delay |
| IMEP | Indicated Mean Effective Pressure |
| IVC | Intake Valve Closing |
| IVO | Intake Valve Opening |

| | |
|-----------------|---|
| LAS | Laser Absorption-scattering |
| LED | Light-emitting Diode |
| LII | Laser Induced Incandescence |
| LIEF | Laser-Induced Exciplex Fluorescence |
| LIF | Laser-Induced Fluorescence |
| LRS | Laser Rayleigh scattering |
| LTC | Low Temperature Combustion |
| NDIR | Non Dispersive Infrared |
| N ₂ | Nitrogen |
| NI | National Instruments |
| NICE | New Integrated Combustion System for future Passenger Cars Engines |
| NO | Nitric Oxide |
| NO _x | Nitrogen Oxides |
| OH | Hydroxyl radical |
| PC | Personal Computer |
| PCCI | Premixed Charge Compression Ignition |
| PIV | Particle Image Velocimetry |
| PM | Particulate Matter |
| ppm | Parts per Million |
| rpm | Revolutions per Minute |
| SI | Spark Ignition |
| SOC | Start of Combustion |
| SOI | Start of Injection |
| TDC | Top Dead Center |
| THC | Total Hydrocarbons |
| uHC | Unburned Hydrocarbons |
| VGS | Variable Geometry Spray |
| VVL | Variable Valve Lift |
| WHO | World Health Organisation |

Contents

| | |
|---|------------|
| Abstract | i |
| Acknowledgements | ii |
| Abbreviations | iii |
| Table of Figures | x |
| Chapter 1 Introduction | 1 |
| 1.1 Introduction | 1 |
| 1.2 Aims and Objectives | 3 |
| 1.3 Thesis Outline | 3 |
| Chapter 2 Literature Review | 5 |
| 2.1 Overview of Diesel Engines | 5 |
| 2.2 Diesel Engines Combustion and Emissions | 6 |
| 2.2.1 NO _x | 7 |
| 2.2.2 Particulate Matter | 7 |
| 2.2.3 Unburned Hydrocarbons | 9 |
| 2.2.4 Effects of Diesel Pollutants | 9 |
| 2.3 Diesel Combustion | 10 |
| 2.3.1 Homogeneous Charge Compression Ignition | 10 |
| 2.3.2 Premixed Charge Compression Ignition | 11 |
| 2.3.3 Low-Temperature Combustion (LTC) | 13 |
| 2.4 Injection Strategies | 13 |
| 2.5 Biodiesel Fuels | 16 |
| 2.5.1 Biomass to Liquid (BTL) fuels | 17 |
| 2.6 Optical Diagnostics | 17 |
| 2.6.1 Injection Visualization | 18 |
| 2.6.2 Combustion Imaging | 22 |
| 2.6.3 Laser Induced Incandescence (LII) | 23 |
| 2.6.4 Two-Colour Method | 23 |
| 2.7 Summary | 24 |
| Chapter 3 Experimental Setup | 25 |
| 3.1 Introduction | 25 |
| 3.2 Single Cylinder Research Engine with Optical Access | 25 |
| 3.2.1 General Description | 25 |
| 3.2.2 Cylinder Head | 27 |

| | |
|---|-----------|
| 3.2.3 Optical Arrangement | 27 |
| 3.2.4 Crankshaft Position System | 29 |
| 3.2.4 Fuel Systems | 30 |
| 3.2.5 Intake System | 31 |
| 3.3 Cylinder Pressure Data Acquisition Systems | 33 |
| 3.3.1 Cylinder Pressure Measurement | 33 |
| 3.3.2 Data Acquisition System | 33 |
| 3.3.3 Experimental Procedure | 34 |
| 3.4 Optical Set-Ups | 34 |
| 3.4.1 Combustion Imaging | 35 |
| 3.5 Exhaust Emissions Measurements | 36 |
| 3.5.1 Horiba MEXA-7170DEGR Emissions Analyser | 36 |
| 3.5.1.1 Horiba AIA-72X Series: CO and CO ₂ measurement | 36 |
| 3.5.1.2 Horiba MPA-720: O ₂ measurement | 37 |
| 3.5.1.3 Horiba FIA-720: Unburnt Hydrocarbon measurement | 37 |
| 3.5.1.4 Horiba CLA-720A: NO and NO _x measurement | 38 |
| 3.5.2 AVL 415 Soot Measurements | 39 |
| 3.6 Data Analysis | 39 |
| 3.6.1 Cylinder Volume Calculation | 39 |
| 3.6.2 Engine Combustion Heat Release Analysis | 40 |
| 3.7 Summary | 44 |
| Chapter 4 Two-Colour Method for High Speed Camera | 45 |
| 4.1 Introduction | 45 |
| 4.2 Theory of the Two-Colour Method | 45 |
| 4.2.1 Flame Temperature Estimation | 46 |
| 4.2.2 KL factor and Soot Concentration Estimation | 47 |
| 4.3 Implementation | 48 |
| 4.3.1 Selection of Parameter α | 48 |
| 4.3.2 Choice of Wavelengths | 49 |
| 4.3.3 Instrumentation, Use of High Speed Camera | 50 |
| 4.3.4 Calibration | 54 |
| 4.3.5 Data Analysis | 57 |
| 4.3.6 The LabVIEW and MATLAB Programs | 60 |
| 4.4 Summary | 62 |
| Chapter 5 Split Injection Studies for Diesel Fuel | 63 |

| | |
|--|-----|
| 5.1 Introduction | 63 |
| 5.2 Test Conditions | 63 |
| 5.3 Injection Strategies | 65 |
| 5.4 Strategies at Injection Pressure 1200 bar | 67 |
| 5.4.1 Strategy A | 67 |
| 5.4.1.1 Effects of Injection Timing on Performance and Emissions | 67 |
| 5.4.1.2 A1 Injection and Combustion Visualization | 72 |
| 5.4.1.3 A1 Flame Temperature and Soot Concentration (KL factor) | |
| Measurements | 74 |
| 5.4.1.4 A3 Injection and Combustion Visualization | 76 |
| 5.4.1.5 A3 Flame Temperature and Soot Concentration (KL factor) | |
| Measurements | 77 |
| 5.4.1.6 A5 Injection and Combustion Visualization | 79 |
| 5.4.1.7 A5 Flame Temperature and Soot Concentration (KL factor) | |
| Measurements | 80 |
| 5.4.2 Strategy B | 82 |
| 5.4.2.1 Effects of Injection Timing on Performance and Emissions | 82 |
| 5.4.2.2 B2 Injection and Combustion Visualization | 87 |
| 5.4.2.3 B2 Flame Temperature and Soot Concentration (KL factor) | |
| Measurements | 89 |
| 5.4.2.4 B5 Injection and Combustion Visualization | 91 |
| 5.4.2.5 B5 Flame Temperature and Soot Concentration (KL factor) | |
| Measurements | 92 |
| 5.4.3 Strategy C and Strategy D | 94 |
| 5.4.4 Strategy E | 96 |
| 5.4.4.1 Effect of Injection Timing on Performance and Emissions | 96 |
| 5.4.4.2 E3 Injection and Combustion Visualization | 101 |
| 5.4.4.3 E3 Flame Temperature and Soot Concentration (KL factor) | |
| Measurements | 102 |
| 5.4.5 Conclusions for Strategies at 1200 bar | 104 |
| 5.5 Strategies at Injection Pressure 800 bar | 105 |
| 5.5.1 Strategy A | 105 |
| 5.5.1.1 Effects of Injection Timing on Performance and Emissions | 105 |
| 5.5.1.2 A1 Injection and Combustion Visualization | 110 |

| | |
|--|------------|
| 5.5.1.3 A1 Flame Temperature and Soot Concentration (KL factor) | |
| Measurements | 111 |
| 2 Strategy B | 113 |
| 5.5.2.1 Effects of Injection Timing on Performance and Emissions | 113 |
| 5.5.2.2 B1 Injection and Combustion Visualization | 117 |
| 5.5.2.3 B1 Flame Temperature and Soot Concentration (KL factor) | |
| Measurements | 119 |
| 5.5.3 Strategy C | 120 |
| 5.5.3.1 Effects of Injection Timing on Performance and Emissions | 120 |
| 5.5.3.2 C3 Injection and Combustion Visualization | 123 |
| 5.5.3.3 C3 Flame Temperature and Soot Concentration (KL factor) | |
| Measurements | 125 |
| 5.5.4 Strategy D | 127 |
| 5.5.5 Strategy E | 128 |
| 5.5.5.1 Effects of Injection Timing on Performance and Emissions | 128 |
| 5.5.5.2 E5 Injection and Combustion Visualization | 131 |
| 5.5.5.3 E5 Flame Temperature and Soot Concentration (KL factor) | |
| Measurements | 132 |
| 5.5.6 Conclusions for Strategies at 800 bar | 134 |
| Chapter 6 Split Injection Studies for Bio-diesel Fuels | 135 |
| 6.1 Introduction | 135 |
| 6.2 Alternative Fuels | 135 |
| 6.3 Test Conditions | 136 |
| 6.4 Injection Rate Experiments | 137 |
| 6.4.1. Injection Rate Test Rig | 137 |
| 6.5 Injection Strategies Studied for BTL 50 | 138 |
| 6.5.1 Strategy A | 138 |
| 6.5.1.1 Effect of Injection Timing on Performance and Emissions | 138 |
| 6.5.1.2 A1 Injection and Combustion Visualization | 143 |
| 6.5.1.3 Injection rate measurements for strategy A | 144 |
| 6.5.2 Strategy B | 145 |
| 6.5.2.1 Effect of Injection Timing on Performance and Emissions | 145 |
| 6.5.2.2 B5 Injection and Combustion Visualization | 149 |
| 6.5.2.3 Injection rate measurements for strategy B | 151 |
| 6.5.3 Strategy E | 151 |

| | |
|--|------------|
| 6.5.3.1 Effect of Injection Timing on Performance and Emissions | 151 |
| 6.5.3.2 E3 Injection and Combustion Visualization | 155 |
| 6.5.3.3 Injection rate measurements for strategy E | 156 |
| 6.6 Injection Strategies Studied for BTL 46 | 157 |
| 6.6.1 Strategy A | 157 |
| 6.6.1.1 Effect of Injection Timing on Performance and Emissions | 157 |
| 6.6.2 Strategy B | 160 |
| 6.6.2.1 Effect of Injection Timing on Performance and Emissions | 160 |
| 6.6.3 Strategy E | 163 |
| 6.6.3.1 Performance and Emissions | 163 |
| 6.7 Conclusions of BTL 50 and BTL 46 split injection experiment | 167 |
| Chapter 7 Conclusions and Recommendations for Future Work | 169 |
| 7.1 Introduction | 169 |
| 7.2 The Two-Colour Method | 169 |
| 7.3 Split Injection Investigation | 169 |
| 7.4 Split Injection with Biodiesel | 171 |
| 7.5 Recommendation for future work | 171 |
| Appendix A | 174 |
| Appendix B | 175 |
| Appendix C | 176 |
| Appendix D | 177 |
| References | 178 |

Table of Figures

| | |
|--|----|
| Figure 2.1 Heat release rate of diesel combustion [4]..... | 6 |
| Figure 2.2 Schematic diagram of diesel engine exhaust particles [10]..... | 8 |
| Figure 2.3 Schematic of the soot formation model [15] | 8 |
| Figure 2.4 LTC concept on Φ - T [47]..... | 13 |
| Figure 2.5 Diagram of a Simple Schlieren Technique..... | 18 |
| Figure 2.6 Diagram of Direct Shadography Technique..... | 18 |
| Figure 2.7 Exciplex Fluorescence | 20 |
| Figure 2.8 Vapour and Liquid Fluorescence Spectra..... | 21 |
| | |
| Figure 3.1 Engine Test Facility Figure 3.2 Front View of Ricardo Hydra engine | 26 |
| Figure 3.3 Sectional Schematic View of the Optical Layout..... | 27 |
| Figure 3.4 3D schematic view of side windows | 28 |
| Figure 3.5 Sectional Schematic View of the Piston Window | 29 |
| Figure 3.6 LED position..... | 29 |
| Figure 3.7 Schematic of the Fuel System [116]..... | 30 |
| Figure 3.8 Intake System for the Hydra engine | 31 |
| Figure 3.9 Supercharging System | 32 |
| Figure 3.10 Intake Heating System..... | 33 |
| Figure 3.11 NDIR analyser (Horiba Instruments Ltd)..... | 36 |
| Figure 3.12 Configuration of magneto-pneumatic oxygen analyser (Horiba Instruments Ltd)..... | 37 |
| Figure 3.13 Schematic diagram of a (FID) Flame Ionisation Detector (Horiba Instruments Ltd)..... | 38 |
| Figure 3. 14 p-V diagram for an actual diesel engine [113] | 41 |
| | |
| Figure 4.1 The effect of the value of parameter α on the estimated temperature [93].... | 48 |

| | |
|--|----|
| Figure 4.2 The spectral radiance of a blackbody as a function of temperature (Zhao and Ladommatos [93])..... | 50 |
| Figure 4.3 Schematic of the Two-Colour Experimental Set-up..... | 51 |
| Figure 4.4 Spectral Response of the High Speed Camera | 52 |
| Figure 4.5 Spectral Response of the intensifier | 52 |
| Figure 4.6 Band pass filters and image doubler | 53 |
| Figure 4.7 The Two-Colour Setup | 54 |
| Figure 4.8 Schematic Setup of the Two-Colour Calibration with Tungsten Lamp | 55 |
| Figure 4.9 Calibration Curve for Tungsten Ribbon Lamp..... | 55 |
| Figure 4.10 Schematic of the Numerical Scheme for Solving Equation 4.8 (Zhao & Ladommatos, [82])..... | 58 |
| Figure 4.11 Front Panel of Align and Crop LabVIEW program | 60 |
| Figure 4.12 Front Panel Two-Colour.vi..... | 61 |
| Figure 4.13 Flame Temperature and KL factor Colour maps from MATLAB | 62 |
| | |
| Figure 5.1 Cylinder pressure traces for experiments in Strategy A at 1200 bar | 72 |
| Figure 5.2 Heat release rate curves for experiments in Strategy A at 1200 bar..... | 72 |
| Figure 5.3 Combustion Images Sequence for experiment A1 at 1200 bar | 73 |
| Figure 5.4 Flame Temperature and KL factor images sequence for A1 at 1200 bar | 75 |
| Figure 5.5 Combustion Images Sequence for experiment A3 at 1200 bar | 76 |
| Figure 5.6 Flame Temperature and KL factor images sequence for A3 at 1200 bar | 78 |
| Figure 5.7 Combustion Images Sequence for experiment A5 at 1200 bar | 79 |
| Figure 5.8 Flame Temperature and KL factor images sequence for A5 at 1200 bar | 81 |
| Figure 5.9 Cylinder pressure traces for experiments in Strategy B at 1200 bar | 87 |
| Figure 5.10 Heat release rate curves for experiments in Strategy B at 1200 bar..... | 87 |
| Figure 5.11 Combustion Images Sequence for B2 at 1200 bar..... | 88 |
| Figure 5.12 Flame Temperature and KL factor images sequence for B2 at 1200 bar | 90 |
| Figure 5.13 Combustion Images Sequence for B5 at 1200 bar..... | 91 |

| | |
|---|-----|
| Figure 5.14 Flame Temperature and KL factor images sequence for B5 at 1200 bar | 93 |
| Figure 5.15 Spray Images Sequence for C2 at 1200 bar | 94 |
| Figure 5.16 Injector signals and pressure wave at the injector for 1200 bar | 95 |
| Figure 5.17 Cylinder pressure traces for experiments in Strategy E at 1200 bar..... | 100 |
| Figure 5.18 Heat release rate curves for experiments in Strategy E at 1200 bar | 100 |
| Figure 5.19 Combustion Images Sequence Strategy E3 at 1200 bar | 101 |
| Figure 5.20 Flame Temperature and KL factor images sequence for E3 at 1200 bar .. | 103 |
| Figure 5.21 Cylinder pressure traces for experiments in Strategy A at 800 bar | 109 |
| Figure 5.22 Heat release rate curves for experiments in Strategy A at 800 bar..... | 109 |
| Figure 5.23 Combustion Images Sequence Strategy A1 at 800 bar..... | 110 |
| Figure 5.24 Flame Temperature and KL factor images sequence for A1 at 800 bar | 113 |
| Figure 5.25 Cylinder pressure traces for experiments in Strategy B at 800 bar | 117 |
| Figure 5.26 Heat release rate curves for experiments in Strategy B at 800 bar..... | 117 |
| Figure 5.27 Combustion Images Sequence Strategy B1 at 800 bar | 118 |
| Figure 5.28 Flame Temperature and KL factor images sequence for B1 at 800 bar | 120 |
| Figure 5.29 Cylinder pressure traces for experiments in Strategy C at 800 bar | 123 |
| Figure 5.30 Heat release rate curves for experiments in Strategy C at 800 bar..... | 123 |
| Figure 5.31 Combustion Images Sequence Strategy C3 at 800 bar | 124 |
| Figure 5.32 Flame Temperature and KL factor images sequence for C3 at 800 bar | 126 |
| Figure 5.33 Injector signals and pressure wave at the injector for 800 bar | 127 |
| Figure 5.34 Cylinder pressure traces for experiments in Strategy E at 800 bar..... | 130 |
| Figure 5.35 Heat release rate curves for experiments in Strategy E at 800 bar | 130 |
| Figure 5.36 Combustion Images Sequence Strategy E5 at 800 bar | 131 |
| Figure 5.37 Flame Temperature and KL factor images sequence for E5 at 800 bar | 133 |
| Figure 6.1 Schematic View of the Injection Rate Test Rig | 137 |
| Figure 6.2 Cylinder pressure traces for BTL 50 experiments in Strategy A at 1200 bar | 142 |

| | |
|--|-----|
| Figure 6.3 Heat release rate curves for BTL 50 experiments in Strategy A at 1200 bar | 142 |
| Figure 6.4 Combustion Image Sequence for BTL 50 experiment A1 at 1200 bar | 143 |
| Figure 6.5 Injection Rate Measurements for Strategy A, Base Diesel and BTL 50 | 145 |
| Figure 6.6 Cylinder pressure traces for BTL 50 experiments in Strategy B at 1200 bar | 148 |
| Figure 6.7 Heat release rate curves for BTL 50 experiments in Strategy B at 1200 bar | 149 |
| Figure 6.8 Combustion Image Sequence for BTL 50 B5 experiment at 1200 bar..... | 150 |
| Figure 6.9 Injection Rate Measurements for Strategy B, Base Diesel and BTL 50 | 151 |
| Figure 6.10 Cylinder pressure traces for BTL 50 experiments in Strategy E at 1200 bar | 154 |
| Figure 6.11 Heat release rate curves for BTL 50 experiments in Strategy E at 1200 bar | 154 |
| Figure 6.12 Combustion Images Sequence for BTL 50 E3 experiment at 1200 bar | 155 |
| Figure 6.14 Injection Rate Measurements for Strategy E Base Diesel and BTL 50..... | 157 |
| Figure 6.15 Cylinder pressure traces for BTL 46 experiments in Strategy A at 1200 bar | 160 |
| Figure 6.16 Heat release rate curves for BTL 46 experiments in Strategy A at 1200 bar | 160 |
| Figure 6.17 Cylinder pressure traces for BTL 46 experiments in Strategy B at 1200 bar | 163 |
| Figure 6.18 Heat release rate curves for BTL 46 experiments in Strategy B at 1200 bar | 163 |
| Figure 6.19 Cylinder pressure traces for BTL 46 experiments in Strategy E at 1200 bar | 166 |
| Figure 6.20 Heat release rate curves for BTL 46 experiments in Strategy E at 1200 bar | 166 |

Chapter 1 Introduction

1.1 Introduction

Diesel engines have become in recent years a very important part of the automotive industry in Europe. In their first years, diesel engines were mostly only employed for industrial applications but, due to their high thermal efficiency, the development of the diesel engine continued making them better, smaller and more compact. This allowed them to be used for a wider range of applications and even for passenger cars. Given the advantages of diesel engines over gasoline engines regarding efficiency and fuel economy, improvements have been made regarding noise and driveability and nowadays they represent a very important part of the market of car sales in the world.

Internal combustion engines' research has always been important in order to improve engines' performance, but since 1990s automotive research has been focused on reduction of pollutants emissions due to the more and more stringent regulations on vehicle emissions. In the last years organisations like the California Air Resources Board (CARB) or the Environmental Protection Agency (EPA) in the United States as well as the European Union have adopted regulations to reduce pollutants emissions in vehicles and, in particular, Nitrogen Oxides (NO_x) and soot emissions in diesel engines, since these pollutants represent the most important emissions in conventional diesel combustion.

The pollutant formation in diesel engines has been extensively studied and is well understood. Particulate matter in the exhaust consists mainly of soot; its formation occurs from the combustion of a richer than stoichiometric mixture. NO_x formation is associated to the combustion at high temperatures with an excess of oxygen and hydrocarbons that can be found in the diesel emission consist of decomposed fuel molecules or intermediate compounds; they are related to very lean regions, where the excess of air prevents combustion from initiating or progressing.

The invention of the common rail (CR) fuel injection equipment (FIE) in diesel engines has led to one of the biggest improvements in diesel engines. The CR FIE, using solenoid or piezoelectric injectors, has gained in accuracy as well as in variation regarding injection timing and fuel quantity. The flexibility in the injection system has made possible for researchers to investigate combustion modes different from the

conventional diesel combustion. These modes include homogeneous charge compression ignition (HCCI) combustion, premixed charge compression ignition (PCCI) or low temperature combustion (LTC) to achieve a diesel combustion capable of reducing the NO_x and soot emissions simultaneously. In order to achieve this, many different injection strategies have been investigated in recent years. Among these studies, the first investigations were related to pilot and main injection, later on a post injection was included and more recently strategies including three and four injections have been studied. Although big improvements have been made, there are still today some factors that need to be improved or controlled in diesel combustion.

In order to understand the effects of different parameters on combustion efficiency and pollutant formation during combustion, optical engines have been very useful. The application of optical techniques in internal combustion engines requires modification to enable optical access. This optical access can be provided using, for example, the glow plug bore and an endoscope-based system; this technique has the advantage that little modification must be done in the engine, however the view is limited and does not allow the application of laser techniques without further modifications. The most common optical arrangement in an engine is the “Bowditch” design, like in this study. The “Bowditch” design enables optical access from below as the ordinary steel piston is extended and on top of which a quartz window is mounted giving optical access to the combustion chamber. Two openings on opposite sides of the extended piston enable mounting a 45° mirror to ensure optical access from outside to the interior of the combustion chamber.

The diesel combustion is rather luminous and this luminosity is caused mainly by the radiation of soot particles at high temperature. Engines with optical access enable to see the combustion process dominated by the soot radiation. With the addition of laser, other techniques can be applied that allow the investigation of the spray and the subsequent mixing process as well as some intermediate products that are formed during the combustion and can give relevant information.

One of the optical techniques commonly applied in engines is called the “Two-Colour Method”; this technique exploits soot radiation in order to estimate the flame temperature and soot concentration during the combustion process. It has been applied with Intensified Charge-Couple Devices (ICCD) cameras due to their high spectral response within a wide range of wavelengths. However the main drawback of using this

type of camera is that, due to the image processing time of the camera, the images obtained are separated by many cycles. During this investigation, this method has been extended for the implementation of a high speed camera to obtain cyclic resolved in-cylinder soot and combustion temperature measurements in a single cylinder optical engine.

1.2 Aims and Objectives

The aim of this study is to investigate split injection strategies in combination with exhaust gas recirculation (EGR) in diesel engines by means of in-cylinder studies performed on a single cylinder engine with optical access. The main objectives of this investigation were to:

- ♦ Set up the single cylinder engine with the appropriate intake and Nitrogen flow to simulate EGR system
- ♦ Develop a high speed two-colour system and its application for in-cylinder soot and combustion temperature measurement
- ♦ Optimise the optical equipment for in-cylinder spray and combustion visualisation
- ♦ Investigate the effect of injection timing and dwell angle for split injection strategies on mixture formation and combustion process with the aim to achieve a reduction in emissions.
- ♦ Investigate the effect of biodiesels on the mixture formation and combustion process under the same conditions as for base diesel.

1.3 Thesis Outline

Following the introduction in Chapter 1, Chapter 2 gives a review of the literature available related to diesel combustion investigation and in-cylinder optical diagnostic techniques. The diesel combustion process is explained and new diesel combustion modes to achieve low emissions are described as well as injection strategies investigated by researchers with the aim of achieving the low emissions combustion modes mentioned earlier. Some of the optical techniques employed in the field of

combustion engines are presented and the techniques related to this investigation are discussed.

Chapter 3 explains the experimental setup and test facilities employed in this study, with a detailed description of the single cylinder engine with optical access; the optical techniques and equipment for their implementation are also described.

Chapter 4 presents the development and extension of the two-colour method for the use with a high speed camera. It explains the theory on which the method is based, as well as the implementation of the technique for the application of a high-speed two-colour system for in-cylinder diesel combustion temperature and soot measurements.

Chapter 5 presents the investigation of the effects of the split injection strategies. The details of the operating conditions are given and the results regarding efficiency and emissions are shown. The optical data obtained is presented and discussed in company with the data of engine performance and emissions.

Chapter 6 presents the investigation of the effect of the split injection strategies using biodiesels instead of the base diesel employed in the previous chapter. Performance and emissions data and optical data are presented and discussed.

Chapter 7 summarises the results obtained and states the recommendations for future work that can be performed in line with this investigation.

Chapter 2 Literature Review

2.1 Overview of Diesel Engines

The first diesel engine was created by Rudolph Diesel in 1897. Since then diesel engines have been evolving from those seen in industrial applications to those used in the automotive industry, and most recently even in motor sport. Diesel engines have always been characterized by their high thermal efficiency, reliability and fuel economy. These have been the main reasons for their development in the automotive industry. The improvement on fuel economy and noise reduction brought these engines to be used in passenger cars within the automotive industry. Thus, an increase of diesel engine sales with respect to gasoline engines has been experienced in Europe since the late 1990s. In the last year more than half (53%) of new cars in the European Union (EU) were sold with a diesel engine [1].

Due to the environmental concerns, countries like the United States, Japan and the European Union member states have introduced emissions regulations. For example, in the United States the Low Emissions Vehicle (LEV) legislation was introduced by the California Air Resources Board (CARB). The Environmental Protection Agency (EPA) introduced Tier 1 standards in 1998 followed by Tier 2 and Tier 3 emission standards that will take effect in 2012, followed by Tier 4 in 2015 [2]. In the European Union, the Euro 1 came into force in 1993, the current Euro 4 entered into force in 2005 with the Euro 5 coming in 2009 followed by Euro 6 in 2014. Table 2.1 shows the current and future permitted emissions levels within the EU for passenger cars [3].

Table 2. 1 Current and Future EU Legislated Emissions Levels for Passenger Cars [3]

| Euro Standard | Year | Engine Type | CO (mg/km) | THC (mg/km) | NMHC (mg/km) | NO _x (mg/km) | THC + NO _x (mg/km) | PM (mg/km) |
|---------------|------|-------------|------------|-------------|--------------|-------------------------|-------------------------------|------------|
| Euro 4 | 2004 | SI | 1000 | 100 | - | 80 | - | - |
| | | CI | 500 | - | - | 250 | 300 | 25 |
| Euro 5 | 2009 | SI | 1000 | 100 | 68 | 60 | - | 5 |
| | | CI | 500 | - | - | 180 | 230 | 5 |
| Euro 6 | 2011 | SI | 1000 | 100 | 68 | 60 | - | 5 |
| | | CI | 500 | - | - | 80 | 170 | 5 |

2.2 Diesel Engines Combustion and Emissions

Diesel engine emissions vary considerably depending on several factors such as speed, load, engine operating conditions and fuel properties. The load in a diesel engine is determined by the amount of fuel injected into the chamber. In order to identify the pollutant formation processes, it is important to understand first the combustion process in diesel engines. This process can be considered to consist of the following phases as shown by the heat release rate diagram in Figure 2.1 [4]:

- ♦ Ignition Delay (ID): It is the time between the start of injection (SOI) and the start of combustion (SOC). It is usually given in crank angle degrees (CA).
- ♦ Premixed combustion phase: In this phase the fuel that has mixed with the air burns rapidly producing high heat release rate.
- ♦ Mixing-controlled phase: In this phase, the heat release rate is controlled by the rate at which the fuel vapour and air mixing process takes place. The heat release rate is decreasing.
- ♦ Late combustion phase: This last phase continues in the expansion stroke, it is due to some fuel that has not been burnt or to some fuel energy released from soot.

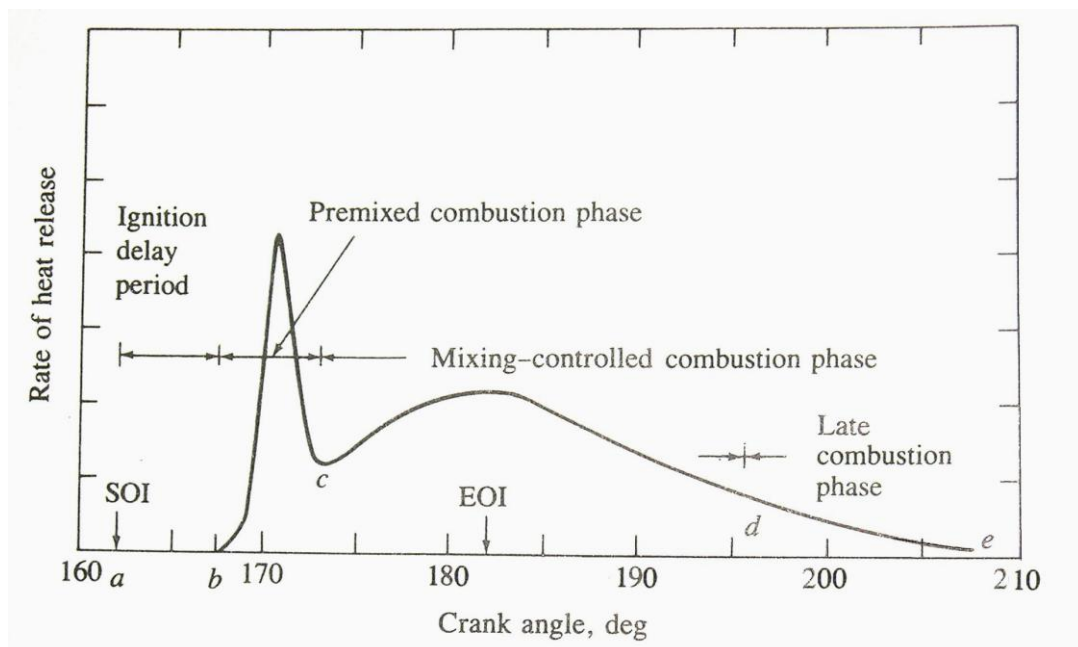


Figure 2.1 Heat release rate of diesel combustion [4]

The pollutant formation process is strongly dependant on fuel distribution during the combustion process, as explained above; the fuel distribution is not uniform inside the

chamber, consequently the pollutant formation varies with time depending on the combustion phase.

2.2.1 NO_x

One of the major pollutants in diesel engines is nitrogen oxides. Generally known as NO_x the oxides of nitrogen present in the exhaust gas consist of NO (around 70% to 90%) and NO₂ [5].

NO formation has been studied and is fully understood. It is accepted that NO is formed by the extended Zeldovich mechanism:



At high temperatures, when excess oxygen is exposed to N₂, NO is formed and an atom of N is left in an unstable state. This nitrogen atom combines with oxygen to form NO. Another source of NO explained by the Zeldovich mechanism is through the combination of radicals of OH that appear during combustion with atoms of nitrogen as shown in Equation 2.3

In diesel combustion NO_x formation is related to local high temperatures that occur in the premixed combustion phase. Shundoh et al. [6, 7] found that NO formation is related to the local oxygen concentration areas; this study showed that NO formation is related to the excess air ratio. Ropke et al [8] showed that the amount of oxygen was the main parameter on NO formation and how by increasing the amount of inert gases in the intake the NO formation decreased.

One of the major problems in conventional diesel engines is the NO_x-soot trade off. Premixed combustion is very important in NO formation where in-cylinder pressure and temperature are very high. Techniques to control NO_x formation are mainly focused on this stage and reducing the combustion temperatures. However by decreasing the combustion temperature, exhaust particulate matter emissions are increased.

2.2.2 Particulate Matter

By definition, particulate pollutants are components of the exhaust gas which are removed from the diluted exhaust gas at a maximum temperature of 325K (52° C) by means of the filters described in the test procedure for verifying average tailpipe

emissions [9]. The composition of the diesel particulates can be divided into carbonaceous or most commonly known as soot, sulphate particles and soluble organic materials. Figure 2.2 shows a schematic diagram of diesel engine exhaust particles [10].

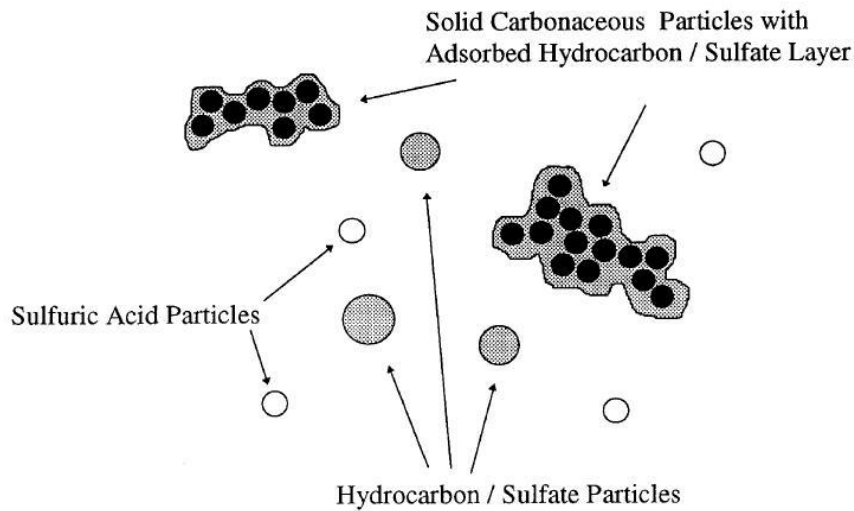


Figure 2.2 Schematic diagram of diesel engine exhaust particles [10]

Although most of the carbonaceous matter formed (80% to 98%) is oxidized during combustion [11], they still represent an important pollutant in diesel engines and therefore the importance of reducing their emissions.

Soot formation has been widely studied; Dec et al. worked on soot formation and distribution using laser imaging techniques such as Laser Induced Incandescence (LII) [12-14] (explained in Section 2.6.3). And based on this work, he developed a model for the soot formation during diesel combustion [15]. Figure 2.3 shows a schematic of this model.

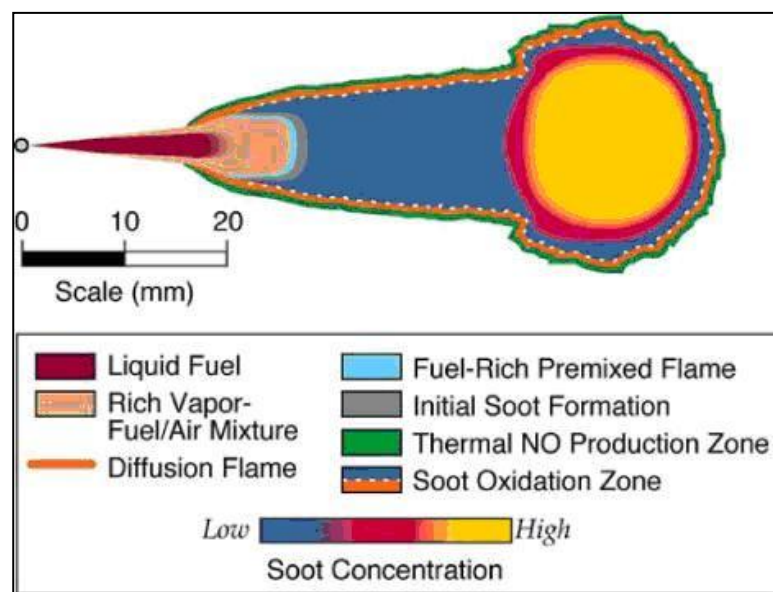


Figure 2.3 Schematic of the soot formation model [15]

Their findings show the small particles of soot form at the leading edge of the fuel jet where the premixed combustion occurs after the first mixing. The vast majority of soot particles are formed during the diffusion combustion phase at regions where the equivalence ratio is high such as in the periphery of the jet.

Similar findings were obtained by other researchers applying optical techniques in the investigation of soot formation. Senda et al. [16] applied Particle Image Velocimetry (PIV) and Laser-Induced Exciplex Fluorescence (LIEF) to present the dependency of soot formation on fuel vapour distribution. Inagaki et al. [17] using LII studied the concentration of soot during the combustion phases. The concentration of soot was small during the premixed combustion and it rapidly increased at the beginning of the diffusion combustion.

Lee et al. [18-20] developed a Forward Illumination Light Extinction (FILE) technique in a constant volume chamber to investigate soot formation in diesel engines. They suggested that soot formation consists of 3 stages: a rapid soot generation at the end of premixed combustion, a stable period of formation and oxidation before the end of injection and the latest period consisting mainly of oxidation of the latest fuel injected.

Reitz et al. [21-23] carried out a series of experiments on heavy duty diesel engines and developed a multi step model for HSDI engines for soot formation. Their findings were similar to those by Dec.

2.2.3 Unburned Hydrocarbons

The hydrocarbons that can be found in diesel emissions consist of decomposed fuel molecules or intermediate compounds. The unburned hydrocarbons are related to very lean regions, the excess of air prevents the combustion from starting or continuing. Historically diesel engines have had very low uHC emissions. In recent years searching for new types of combustion where both NO_x and PM emission could be decreased, an increase of uHC emissions has been observed [24, 25].

2.2.4 Effects of Diesel Pollutants

The complex composition of diesel pollutants has made very difficult to investigate the effects on human health. Diesel particulates are considered the most appropriate parameter to investigate the human health effects until more information about the mechanisms of toxicity of diesel emissions becomes available [26].

Diesel emission effects on human health can be classified in three groups:

- ♦ Short-term (e.g. episodic) effects: Some symptoms of diesel pollutant exposures are:
 - acute irritation (e.g. eye, throat, bronchial)
 - neurophysiological symptoms (e.g. nausea)
 - respiratory symptoms (cough, phlegm)

- ♦ Chronic (Long-Term Exposure) non-cancer respiratory effects: Information from the available human studies is inadequate for a definitive evaluation of possible non-cancerous health effects from chronic exposure to diesel emissions; some reports link exposure to risk of heart attacks but the evidence is not clear [27].

- ♦ Chronic (Long-Term Exposure) carcinogenic effects: In the last years, risk assessments carried out by the World Health Organisation (WHO) and the U.S. Environmental Protection Agency conclude that diesel emissions are “likely to be carcinogenic to humans by inhalation” [27].

2.3 Diesel Combustion

The combustion process for a conventional direct injection (DI) diesel engine has been explained in Section 2.2. The major drawback for diesel engines is the soot and NO_x emissions. Usually reducing one of these emissions leads to an increase of the other. However investigations have been carried out to find a combustion model in which both soot and NO_x emissions are reduced simultaneously compared to a conventional DI diesel engine.

2.3.1 Homogeneous Charge Compression Ignition

Homogeneous Charge Compression Ignition (HCCI) has become one of the most important alternatives for diesel combustion in the last few years. HCCI was proposed for its low soot and NO_x emissions from diesel engines [28]. Its principle is to get a homogeneous combustion of lean mixture, to avoid the production of NO_x related to high temperatures, but close to stoichiometric mixture in order to avoid the production of soot from rich mixtures.

HCCI combustion is dominated by local chemical-kinetic reactions with no requirement for flame propagation [29]; the main effect of this is that small changes of temperature inside the cylinder have considerable effects on combustion since chemical reactions are very sensitive to temperature. Related to this, Docquier and Bruneaux [30, 31]

experienced difficulties to control combustion timing in their investigations of HCCI combustion.

Another characteristic of the HCCI is that combustion occurs very rapidly. Due to this, although fuel air mixing is very important before the start of combustion, it is not during combustion itself [29]. It is known that the HC and CO emissions in HCCI combustion are higher than in traditional diesel combustion. The main challenges that HCCI has to overcome is to control the auto-ignition, achieving suitable fuelling rates for high loads conditions, and the reduction of HC and CO for low loads when after-treatment catalysts are not fully efficient.

One of the approaches to HCCI was to advance the injection timing [32]; although it produced combustion with low NO_x and soot emissions, it increased the unburned HC and fuel consumption due to wall wetting. In order to reduce unburned HC in HCCI combustion, Ra et al. [33] carried out investigations with Variable Geometry Spray (VGS), having narrow cone injectors to avoid wall wetting and therefore reducing the uHC emissions. Regarding uHC, Komminos et al. [34] developed a multi-zone model for HCCI combustion where they showed that during the “high temperature” combustion the fuel mass increased rapidly in the crevices area provoking a decrease in cylinder pressure and an increase in uHC.

Other investigations on HCCI [35, 36] showed that HCCI was achievable with split injection, high percentage of EGR and late inlet valve closure (IVC) or variable valve lift (VVL). A long ignition delay was achieved producing a premixed lean mixture. The use of EGR without cooling was proved to be efficient in reducing HC for low load conditions. However controlling the injections became a problem as the dwell angle was very short.

2.3.2 Premixed Charge Compression Ignition

Another combustion type for diesel engines to reduce soot and NO_x emissions is Premixed Charge Compression Ignition (PCCI). First investigations on PCCI were carried out by Takeda et al. [37] who called this combustion ‘premixed lean diesel combustion’ (PREDIC). It was based on very early injection timing and it produced a low temperature combustion leading to a reduction of NO_x emissions however the uHC and CO emissions were increased.

Simescu et al. (2003) carried out a series of investigations in a heavy duty diesel engine [38, 39] where PCCI was achieved by adding a port injector and injection quantities

between 10% and 70% of the total fuel. They obtained reduction in NO_x emissions except for low speed high load experiments; uHC and CO emissions were increased, however for port injection quantities higher than 60%, they found a decrease of CO emission probably due to the oxidation time being increased.

The “premixed lean diesel combustion” developed by Takeda, has led many researchers to base their investigations on PCCI on an early injection. Kook and Bae [40] applied two-stage injection on heavy duty engines, the main injection taking place around 100° CA BTDC and the post injection close to TDC. The auto-ignition was advanced due to the early injection and thus the combustion temperatures were low. It demonstrated a reduction of 90% NO_x emissions with respect to conventional diesel engines and an increase in IMEP but the uHC and CO were increased. Another problem was the post injection timing optimization because the intake temperature affected the auto-ignition.

Kanda et al. [41] applied the same concept of early injection with a narrow cone injector on their investigation of PCCI. The compression ratio was reduced to avoid too advanced auto-ignition and EGR was applied as well to retard the auto-ignition. Using an endoscope, they recorded combustion images. Although they found NO_x emissions reduction, HC, CO and soot were increased due to the formation of a fuel wall-film on the piston wall as vaporization was very poor at the moment of injection. In further investigations [42] they applied an injection close to TDC and this PCCI presented levels of NO_x very similar to PCCI with early injection and the advantage of reducing the rest of the emissions due to the elimination of the fuel wall film.

An extensive study of PCCI was carried out on a heavy duty engine by Hardy and Reitz [43-45]. Based on an early injection timing they found that high levels of EGR were needed to control the cylinder pressure and, therefore, auto-ignition and boosting were also required in order to keep the equivalence ratio low enough to decrease the soot emissions. Multiple injections were applied with the effect of wall wetting and consequently high uHC emissions. Lee and Reitz carried out investigation on the influence of spray targeting for PCCI on HSDI engines [46]; when the spray was targeted to the piston bowl edge it showed a good NO_x -soot trade off with low CO emissions. When targeting the bottom of the piston bowl, it showed better soot but worse CO emissions. This spray targeting was difficult to analyse when engine speed varied, as the mixing varied and therefore the start of combustion was different.

2.3.3 Low-Temperature Combustion (LTC)

Similar to HCCI and PCCI combustion, in trying to exploit the low temperature and with relatively low equivalence ratio, another combustion model was defined as Low-Temperature Combustion (LTC) [47] as Figure 2.4 shows:

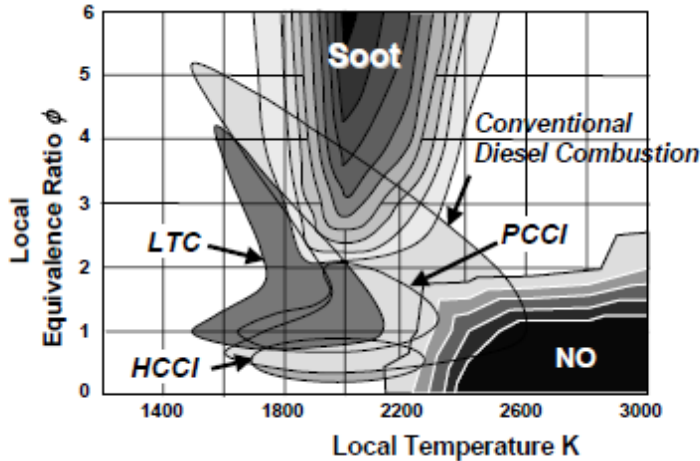


Figure 2.4 LTC concept on Φ - T [47]

They achieved LTC at low load by increasing the intake manifold temperature with the use of EGR without cooler. As for higher loads, in order to keep the combustion at low temperatures, cold EGR was applied. Alriksson and Denbratt [48] achieved LTC in a heavy duty engine using very high levels of EGR. Up to 50% EGR showed no increase in HC and CO, however at higher loads with an EGR increase of up to 65%, both the fuel consumption and HC emissions were compromised. Using a HSDI diesel engine Avolio et al. [49] achieved LTC with very high levels of cooled EGR. Current investigations on the use of high levels of EGR are being undertaken in order to achieve LTC to meet future emissions legislations.

2.4 Injection Strategies

With the introduction of the common rail in the middle 90s and engine electronic units (ECU) which open the injectors electronically, the diesel injection system gained injection precision as well as variation in injection timing and quantity. This was first utilized with solenoid valve injectors and lately with piezoelectric injectors for increased precision and injection fuel pressures up to 2000 bar.

Some of the first investigations on different injection strategies [50-53] were focused on pilot plus main injection or split injection with a fuel distribution 50%/50%. They found that by means of a pilot injection, the ignition delay was reduced and as a result the heat

release rate peak was reduced. General gas temperature was thus lower, reducing the NO_x emissions. Although the mixing controlled phase was increased, the soot emissions were not increased as split injection enhanced better mixing and air utilization.

Subsequent to the pilot plus main and the split injection methods, investigations on split injection including strategies with a post injection have been conducted [54, 55]. They found that when there was post injection, or split injection with the second injection quantity lower than the first injection quantity, there was a reduction of soot emissions. This was mainly because the post injection increased the combustion temperature during the diffusion phase and enhanced soot oxidation.

These first investigations on split injection namely pilot plus main or main plus post injection were extended with new studies exploring the combination of different factors such as split injection incorporating EGR levels [56, 57]. Montgomery and Reitz [56] investigated split injection in conventional heavy duty diesel engines with injection rates of 50%/50%, 55%/45% and 70%/30% with EGR levels between 10 to 25%. Their investigations showed that it was possible to reduced NO_x and soot emissions simultaneously as the NO_x reduction was related to the EGR levels and the soot reduction was enhanced by split injection due to improved the mixing process. In order to understand the mixing process, Zhang et al. [58, 59] carried out a series of investigations on the mixing process in diesel engines by means of laser absorption-scattering (LAS) for the spray visualization in a constant volume chamber. They compared the mixing process of single injection with split at 75%/25%, 50%/50% and 25%/75% injection rates, finding that the 75/25 strategy showed the best improvement regarding soot emissions for their engine conditions. This is explained as being due to the improved turbulence resulting from the second injection and therefore enabling the mixing process to obtain a more homogenous mixture. Similar results were obtained by Shayler and Ng [60] who compared single injection with split at 90%/10 and 60%/40% injection rates. They found that soot emissions were reduced when increasing the second injection quantity.

As injection systems became more flexible, investigations were carried out on triple injection strategies [55, 61] or pilot + main + post injection strategies [62, 63]. In these investigations they found that increasing the time between pilot and main injection would decrease NO_x emissions. However, after a certain dwell angle the soot emissions would increase. As stated previously the addition of the post injection would reduce soot but having the drawback of increased fuel consumption and HC emissions.

Investigations comparing 3 injection strategies namely pilot + second pilot + main and pilot + main + post, with the pilot + main and main + post injection strategies were carried out by Mallano et al. [64, 65] in HSDI diesel engines with addition of EGR levels between 10% and 40%. They found that for the two pilots + main injection strategy combustion noise was reduced as cylinder pressure was decreased, although an increase in emissions was observed. Some optical techniques such as combustion imaging with a Copper Vapour Laser as light source [63] or the Two-Colour Method [61], were used in these multiple injection strategies in order to analyse the mixing process and the flame temperature reached during combustion. LII has been applied to investigate the soot formation under different multiple injections [66], showing the reduction of soot formation during the diffusion combustion phase due to the improved mixing created by split injection.

In recent years, injection strategies have been investigated with up to 4 or 5 injections [67-69]. These researchers have focused their studies in order to achieve new combustion models like HCCI or LTC to reduce soot and NO_x simultaneously. Thus Reitz et al. found a reduction in NO_x and soot emissions with a four injection strategy but with the need of EGR to increase the ignition delay so that a leaner mixture would burn. In a similar way, Mendez and Thirouard [70] obtained emissions reduction without increasing fuel consumption but difficulties controlling the injection quantity were encountered due to the pressure wave created and the necessity to accurately inject the amounts required. For this purpose piezoelectric injectors were used.

Although split injection strategies have been investigated for a long time, scant investigations have been conducted regarding split injection with high levels of EGR. As stated previously, EGR has been proven responsible for the NO_x reduction in diesel engines. In addition, split injection strategies, where the first injection quantity is higher than the second injection, have shown a potential in reducing the soot emissions because of the improvement of the mixing process. Furthermore, most of the investigations available are simulations or experimental work based on conventional engines and few investigations have been focused on split injection strategies within an engine with optical access. Some researchers [71-73] investigated the pilot + main injection strategy and the effect of injection timing, pressure and dwell angle using optical techniques such as direct spray and combustion visualization and Mie scattering, showing the effect of the pilot injection to reduce NO_x emissions and how the dwell

angle between pilot and main injection would have an effect on soot emissions as well if pilot injection was taking place too early.

Park et al. [74] investigated pilot + main and main + post injection in an optical engine with injection pressures between 300 bar to 1200 bar in later investigations [40], where they applied optical techniques in the study of PCCI with an early main injection and late post injection. Other researchers [75-77] studied the effect of EGR levels within an optical engine, but these investigations were carried out with a single injection and in a later study with pilot + main injection strategy.

The present study attempts to resolve this question presenting an in-depth investigation of split injection strategies with high levels of EGR from an optical approach involving high speed direct visualization and the two-colour method.

2.5 Biodiesel Fuels

The first generation of biodiesel fuels are derived from renewable feedstock which can be vegetable oil or animal fat. The type of biodiesel fuels depends mainly on the different available biomass in each country. For example, the main biodiesel production in U.S is from soybeans while in Europe it is from rapeseed oil and in Brazil from sugar cane. Today there is a range of biodiesel fuels or blends of diesel with biodiesel available in the market. The increase on the use of this type of fuel was caused firstly by the need of replacing fossil fuels for the automotive industry and secondly by the obligation to meet the regulatory targets set by each government and the European Union. Thus many investigations have been carried out in recent years on combustion engines using this type of fuel. Earlier investigations [78-80] were focused on the development of the biodiesel and biodiesel blends from a chemistry point of view, and how composition would influence and could reduce emissions of diesel combustion. Grimaldi et al. [81] investigated spray penetration for different biodiesel blends derived from rapeseed oil compared to base diesel and found higher penetration for biodiesel. In later investigations [82], they compared three biodiesel fuels (methyl ester of rapeseed oil, soybean and waste cooked oil, obtained by transesterification process), and found high reduction in PM emissions for the three biodiesel fuels compared to the normal diesel, although the performance was also reduced. Applying pilot + main injection strategy and using biodiesel obtained by transesterification of an oil mixture consisting of 70% of rapeseed crude oil and 30% of waste vegetable oil [83, 84], they found that biodiesel presented similar performance and a reduction in HC and CO emissions. The

PM emissions were drastically reduced, but due to the higher vaporization of the biodiesel premixed combustion was increased leading to higher NO_x emissions. Other researchers [85, 86] have used different percentages of blends of biodiesel, such as soybean oil ester and waste-cooking oil methyl ester, finding similar results for CI engines.

2.5.1 Biomass to Liquid (BTL) fuels

The production process for BTL starts with the grinding of biomass. The biomass is subjected to a low-temperature gasification process and transformed into a synthetic gas mixture in a second step. After purification, the gas is liquefied in a so called “Fischer–Tropsch” reaction to obtain the end product (liquid fuel). More recent investigations [87] have shown an improvement in both NO_x and soot emissions in a conventional engine using BTL fuel compared to diesel fuel. They found as well an important reduction of CO₂ emissions, showing great potential although optimization of BTL is still needed (i.e. Cetane Number, lubricity, etc). Compared to the first generation of biodiesels, BTL can be produced a wider variety of biomasses.

In a recent PhD study at Brunel University, Gill [88] investigated three different BTL fuels with pilot + main injection strategy and multiple injection strategy to achieve HCCI combustion. For the pilot + main injection strategy, he found a considerable increase in performance and emissions (except NO_x) over base diesel. However for multiple injection strategies, the BTL fuels showed lower IMEP values than those achieved by base diesel. This study, consisting of split injection investigations, has employed two BTL fuels (BTL 46 and BTL50) as they have shown great potential in a previous study.

2.6 Optical Diagnostics

The diesel combustion process involves injecting fuel at a very high pressure into a high pressure high temperature atmosphere. Liquid has to atomize, vaporize to mix with the air before auto-ignition and combustion. This combustion is heterogeneous, unsteady and in three dimensions leading to a very complex process. Optical techniques to visualize the combustion and the injection process appeared in the 1960s in order to gain a better understanding of this complex process.

2.6.1 Injection Visualization

The injection process can be divided in 4 stages: fuel injection, atomization, vaporization and mixing with air. These four stages influence very importantly efficiency, emissions and fuel consumption. Therefore, in addition to cylinder pressure and heat transfer analysis, researchers need to “see” what happens inside the combustion chamber for a better understanding of the influence of the injection process on general performance.

Some of the methods that were developed or are currently in use are as follows:

- ▶ Schlieren Technique: This was the first method to visualize the injection process. It is an optical system that “projects line-of sight information on to a viewing screen or camera focal plane” [89]. It requires a light source and lens to focus the light that passes through the test region or area and the shadow created is focused to a screen or more recently to a CCD camera. Figure 2.5 shows the schematic diagram of the Schlieren Technique.

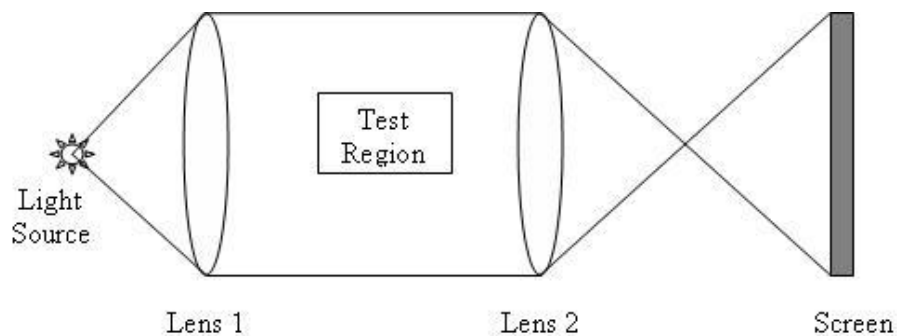


Figure 2.5 Diagram of a Simple Schlieren Technique

Shadowgraphy: It is a similar technique to Schlieren however it is not a focused optical technique and it is less sensitive. Figure 2.6 shows the schematic setup for shadowgraphy.

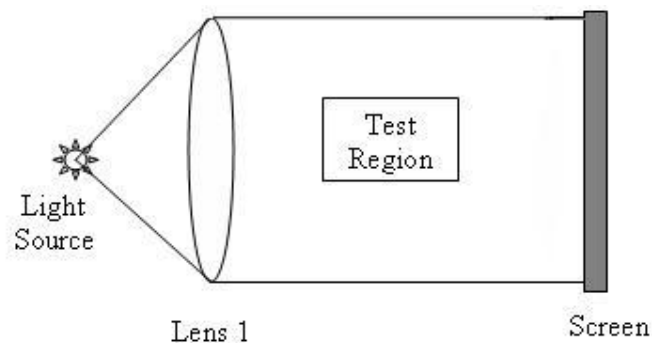


Figure 2.6 Diagram of Direct Shadowgraphy Technique

- ♦ Laser Rayleigh scattering (LRS). It is an elastic scattering process, which means that the scattered light has the same wavelength as the incident light. This method provides visualization of the gas phase of a mixture in the absence of liquid drops in order to detect the vapour phase efficiently. Another drawback of this method is that the scattered light from solid particles and from the walls can interfere with the Rayleigh light from the gas.
- ♦ Raman Scattering: Spontaneous Raman Scattering allows direct air/fuel ratio detection via simultaneous multiple-species measurements since spectral measurement of Raman scattered light can identify the molecular species. However, spontaneous Raman scattering is a very weak process and requires careful signal-to-noise consideration.
- ♦ Mie scattering: This method, as the LRS, is an elastic process of scattered light, and it provides an efficient view of the liquid drops of a fuel. It is not molecular number density or temperature dependence hence it can not provide that information. It is particle size dependent and as an elastic process there is no energy exchange, thus the scattered light has the same wavelength and is a strong signal.
- ♦ Laser Induced Fluorescence: This method was born as the idea of adding a visual tracer, so that the fluorescence emitted by this tracer is proportional to the concentration. This method is widely used for the detection of gas molecules, nonetheless the fluorescence emission of both liquid and vapour makes difficult to distinguish the distribution of the molecules in the gas phase, even if the images can be compared to the images of liquid obtained via Mie scattering.
- ♦ LIEF: Laser Induced Exciplex Fluorescence was developed due to the need to discriminate the fluorescence between the liquid and vapour phases of a fuel.

2.6.1.1 LIEF Laser Induced Exciplex Fluorescence

Various techniques were used in the field to analyse the temporal and spatial distribution of the in-cylinder mixture, which could quantify either the liquid or vapour fuel separately. The aspiration to understand completely this process, made Melton [90] develop a new technique called LIEF Laser Induced Exciplex Fluorescence in 1984, which provided images of liquid and vapour fuel simultaneously.

Exciplex fluorescence requires mixing a solvent with other two components: a fluorescent monomer and an appropriate partner. When excited by a laser beam at the right wavelength, the monomer associates with the partner and forms an excited state (Exciplex). See Figure 2.7:

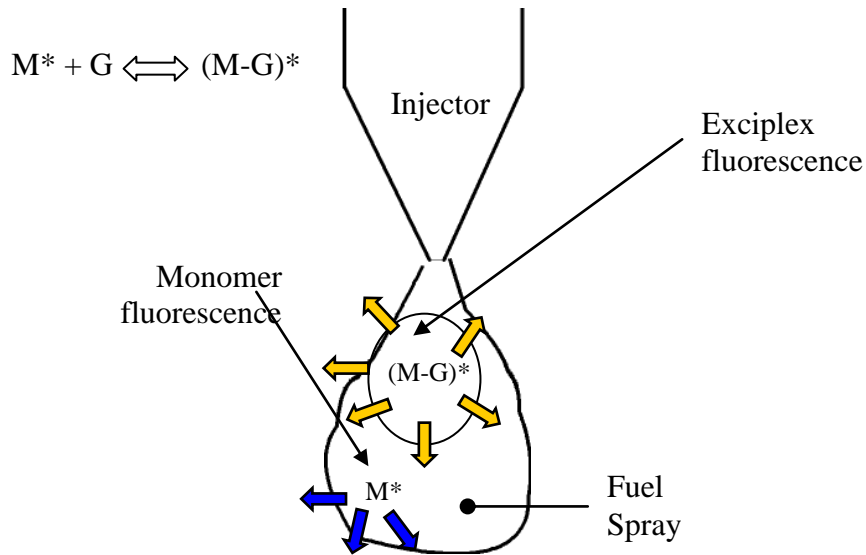


Figure 2.7 Exciplex Fluorescence

The fluorescence of the excited state is red-shifted compared to that monomer. Since the density of the liquid phase is high, there is a high probability of association between the monomer and the partner. Conversely there is little probability of association in the vapour phase because of the lower density. As a result the predominant fluorescent signal coming from the liquid phase is due to the Exciplex while the monomer fluorescence dominates the vapour phase.

The liquid phase is red shifted with respect to the vapour phase, although there is an area of the spectrograph in which vapour and liquid are seen simultaneously, as Figure 2.8 shows. With the use of the appropriate filters, it is possible to separate the vapour spectra from the liquid spectra.

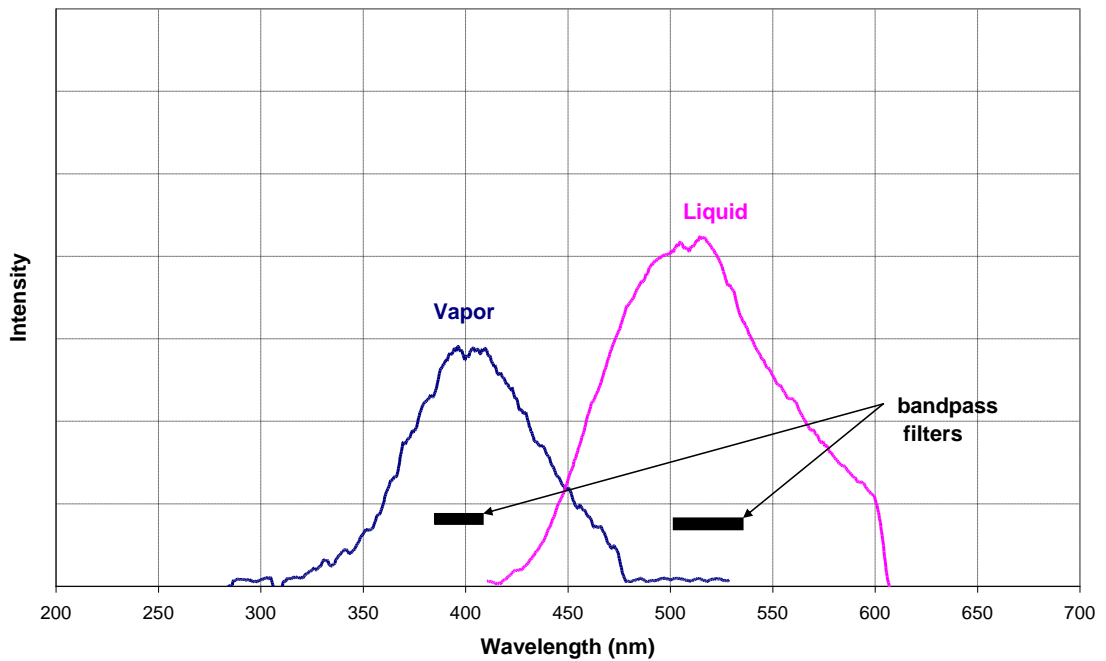


Figure 2.8 Vapour and Liquid Fluorescence Spectra

Melton [91] used the combination of hexadecane as solvent, tetramethyl-p-phenylene diamine (TMPD) as the monomer and naphthalene (Np) as the partner, 90% n-decane, 9% TMPD and 1% naphthalene. Melton asserted that this method could have the major advantage of being able to have quantitative analysis of the sprays as the fluorescence is proportional to the concentration. But he also indicated the drawbacks of this method. The scattering and absorption from the spray would mean that the part of the spray from which the laser enters would be excited more strongly than the part to which the laser leaves the spray. The other very important phenomenon influencing LIEF is the quenching by O_2 of the vapour molecules, for which the solution was to use N_2 atmosphere for experiments.

Melton [92] proposed a quantitative analysis of the vapour and liquid images based on light absorption and quantum yields for emissions, as Exciplex fluorescence was proportional to concentration and did not depend on droplet size distribution. Melton summarised the procedure and the photo physical function/parameter methods in a “user’s manual”. However this procedure proved difficult to perform [93].

Senda et al. [94] developed a method for the quantitative analysis of the vapour images using a high pressure constant volume vessel. This method was based on Lambert-Beer’s law to measure the TMPD concentration from the fluorescence intensity and correcting the intensity for the effect of the quenching, the ambient temperature and fuel

mixture concentration. This process was carried out assuming that the solvent, monomer and partner saturated temperatures and evaporating rates were the same. For the calculation of the fuel temperature two assumptions were taken into account: the mixing between the fuel and air was adiabatic and it occurred at constant pressure. Ghandhi and Kim [95] produced a series of experiments of LIEF in a constant volume chamber, developing a technique to analyze quantitatively the vapour concentration in sprays. This method was based in photophysics, for which several statements/assumptions had to be taken into account as follows:

- ♦ TMPD concentration is indicative of the total vapour concentration and that there is no cross-talking between the liquid and the vapour phase fluorescence. This means that this method is just as reliable in the areas of the spray where there is only a vapour phase.
- ♦ Variation of photophysical parameters depending on temperature, pressure and quenching by molecular collisions.
- ♦ Absolute calibration between TMPD concentration and fluorescence. Before every test run a known concentration of TMPD was injected so that they could calculate the calibration constant K.

Since the LIEF technique was used for the first time by Melton, there have been many studies of injection in constant volume combustion chambers and in optical engines.

2.6.2 Combustion Imaging

The diesel combustion has been optically observed for many years. It is recognised that during the diffusion phase of combustion, the soot radiation gives quite a luminous flame which can be recorded with CCD cameras or high speed cameras. Generally, the premixed combustion has too low luminosity but with the addition of a light source some of the premixed phase as well as the liquid spray of the injection can be recorded. The use of a copper vapour laser (CVL) as a light source, like in this study, has been applied in recent years to film the diesel combustion and the liquid spray in which spray penetration measurements have been obtained [96-99].

2.6.3 Laser Induced Incandescence (LII)

Melton first proposed Laser Induced Incandescence (LII) as a technique for soot concentration measurements [100]. LII involves the heating of soot particles to temperatures above the surrounding gas by a short laser pulse and subsequently detection of the radiation emitted by the soot particles at elevated temperatures. Soot volume fraction and soot particle size can be calculated applying energy and mass balance equations. However this technique presents some drawbacks or assumptions for the soot particle measurements. When heating particles up to a high temperature by a laser, some particles may vaporize causing the particle size distribution being measured to differ from that originally present. Other factors that affect the LII signal and should be considered for quantitative soot measurements are the laser fluence and laser beam profile. If low laser fluence is applied the relation between particle size and LII signal is not longer valid as the soot particles are not heated up near the vaporization temperatures. For quantitative soot size measurements, in situ soot temperature will be required and can be obtained by the two-colour method. Using Gaussian profile beam results in a longer rise time near the edge of the laser which may result in erroneous measurements [92]. In recent years, many researchers have applied successfully this technique to soot particle sizing in diesel engines [101-103] and it can be a method for soot measurements in new combustion modes aiming the reduction of soot particles.

2.6.4 Two-Colour Method

The Two-Colour Method was developed in 1932 by Hottel [104] in search of finding the flame temperature in industrial furnaces, but it was Matsui et al [105-107] who developed this technique further and presented the first flame temperature and soot concentration images in a diesel engine.

The two-colour method is based on optical pyrometry which, in this case, it is based on the radiation of the soot particles during combustion. The radiation is measured at two different wavelengths from which two apparent temperatures are calculated. From these apparent temperatures which correspond to the two different wavelengths, the flame temperature and the soot concentration can be estimated. It is important to highlight that despite the fact that with this method the temperature estimated is from the soot, it is generally accepted that the temperature difference between the soot and the surrounding gases is less than 1K.

Zhao and Ladommatos [108, 109] created a guide for the two-colour method, from the theory on which this technique is based on, to calibration and implementation. This guide “standardized” this method and therefore significant parameter values like alpha have generally been accepted since then.

The two-colour method has been investigated with many different optical configurations. Using an optical engine of “Bowditch” design, many researchers [105-107, 110] have employed CCD cameras. This provides a full view of the combustion chamber, but the combustion itself may differ from a standard production engine as the in-cylinder conditions are difficult to replicate in optical engines. A less interfering way of applying this method is by means of fibre optics [111, 112] or by using endoscopic visualization [113, 114]. Using a two-stroke optical diesel engine Tominaga et al. [115] applied this method with a CMOS high speed video camera. However this was done at a very low engine speed of 345 rpm and 1,000 frames per second of recording speed.

In this study, a single cylinder optical research engine of “Bowditch” design was used, and the two-colour method was applied with a high speed video camera with CMOS sensor at a recording speed of 10,000 frames per second with an engine speed of 2000 rpm for all experiments. This represents an advancement for the two-colour method application in combustion engines, achieving cyclic resolved in-cylinder soot and combustion temperature measurements.

The theory of this technique as well as its implementation for the use with high speed cameras will be explained in detail in Chapter 4.

2.7 Summary

Nowadays, diesel engines research is driven by the environmental legislation to reduce pollutants emissions in vehicles. This chapter has explained the investigations related to pollutants formation in diesel engines and their emissions. It has stated the main research approaches regarding new types of diesel combustion as well as injection strategies that can help to achieve the low emissions combustion modes. Finally optical techniques related to this investigation have been described with specific reference to the two-colour method, the state of this technique and its application in internal combustion engines.

Chapter 3 Experimental Setup

3.1 Introduction

This chapter presents the experimental setup and test facilities used for this study. It starts with a detailed description of the single cylinder engine with optical access and the associated equipment to obtain and analyse the data. The optical techniques and their implementation are then discussed.

3.2 Single Cylinder Research Engine with Optical Access

3.2.1 General Description

All experimental testing in this study was completed in a single cylinder Ricardo Hydra engine, designed to be representative of a typical modern high-speed direct injection (HSDI) diesel engine. The engine specifications are detailed in Table 3.1. The engine is mounted on a Cussons Technology single cylinder engine test bed consisting of a seismic mass engine mounting, 30 kW DC dynamometer, engine coolant and engine oil circuits.

Table 3.1 Engine Specifications

| Ricardo Hydra Single-Cylinder Engine | |
|---|-------------------------------|
| Bowditch System: imaging through piston bowl | |
| Bore | 86 mm |
| Stroke | 86 mm |
| Swept Volume | 499 cm ³ |
| Compression Ratio | 16.0:1 |
| Piston Bowl Diameter/Depth | 43.4/11.6 mm, Cylinder Shaped |
| Swirl Ratio | 1.4 |
| Engine Speed for Testing | 2000 rpm |

The engine consists of a Ricardo Hydra crankcase, an extended cylinder block and a cylinder head platform. The cylinder block has an upper and lower part that allows space to mount an extended piston and also features three cylinder wall cut-outs where glass windows can be fitted to gain optical access through the side. The engine is mounted with a standard production cylinder head and a common-rail fuel injection system.

As the operating time of optical engines is very short, the coolant and lubrication systems are heated before each engine run in order to have adequate engine temperatures. The coolant system consists of a testbed mounted electric pump and a thermostat controlled immersion heater. The lubrication system consists of a wet sump, test bed mounted gravity-fed pressure pump driven by an electric motor and two immersion heaters in the sump. Oil is drawn from the sump and pumped through a filter before being fed to the main oil gallery in the crankcase which supplies the crankcase and cylinder head. The oil is fed to the crankshaft, big end bearing and camshaft bearings. The lower piston and cylinder wall are lubricated by oil thrown up by the action of the crankshaft. The upper cylinder block and piston cannot be lubricated by oil due to the rapid contamination of the optical surfaces that would result. Therefore, the upper piston is lubricated by two carbon rings made of Le Carbone Lorraine grade 5890 carbon. Two conventional steel compression rings are fitted for sealing, lubricated by carbon deposited on the cylinder walls by the carbon rings as well as lubrication paste that is applied to these rings during each rebuild.

The 30 kW DC dynamometer motors the engine and acts as a brake when the engine is firing. The dynamometer control system allows a set engine speed point to be set and automatically maintained by driving or braking the engine as necessary.

Figures 3.1 and 3.2 illustrate a general view of the test facility and a front view of the Ricardo Hydra engine.

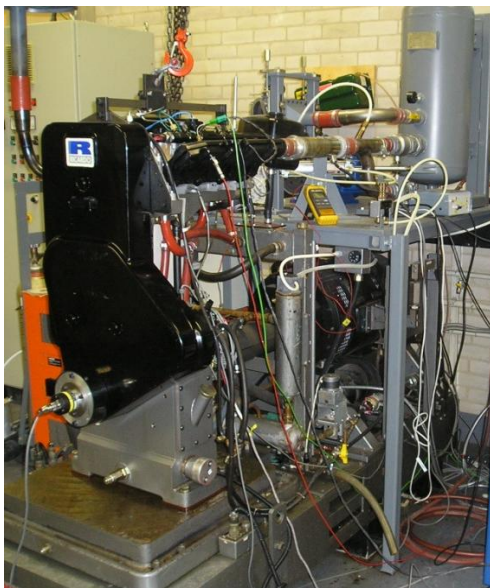


Figure 3.1 Engine Test Facility

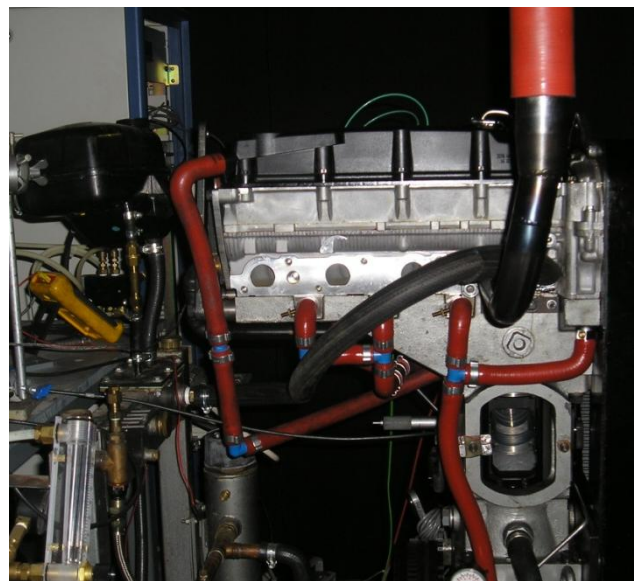


Figure 3.2 Front View of Ricardo Hydra engine

3.2.2 Cylinder Head

The Ricardo Hydra engine was designed to allow the use of a standard production four-cylinder head. The cylinder head is from a production Ford 2.0 litre ZSD 420 Duratorq turbocharged engine. The cylinder head includes 4 valves, a centrally located injector and a glow plug. For this study, as the glow plug is not required, a Kistler 6125 piezoelectric pressure transducer for measuring in-cylinder pressure is positioned instead.

3.2.3 Optical Arrangement

Optical access is provided by the Bowditch method, which allows the combustion chamber to be viewed through a window mounted in the base of the piston bowl. This glass window is made of fused silica. In order to visualize the chamber, an extended piston and extended cylinder block are required. A 45° angled mirror is located between the upper and lower part of the extended piston, as shown in Figure 3.3. The mirror is made of glass with an aluminized front surface.

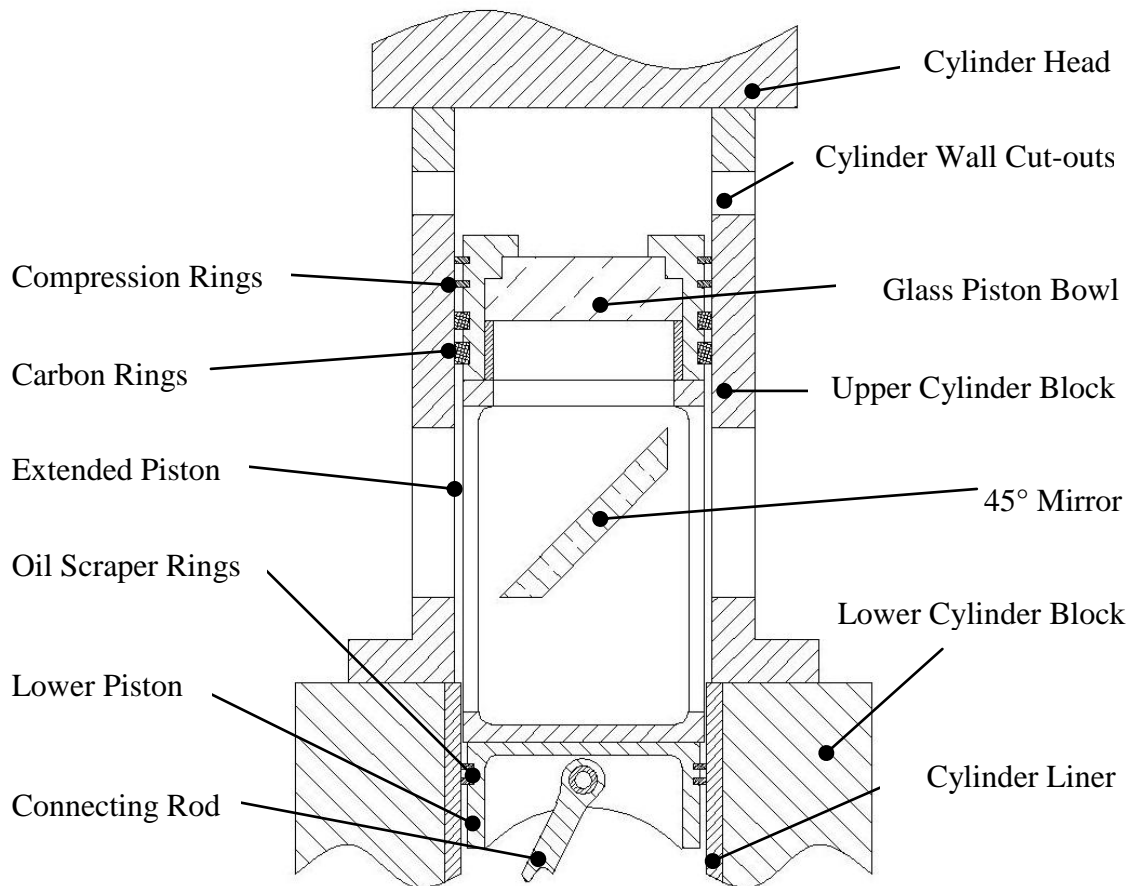


Figure 3.3 Sectional Schematic View of the Optical Layout

3.2.3.1 Optical Windows

The upper part of the cylinder block has three rectangular cut-outs, where glass windows made of fused silica can be fitted for side optical access. Two of these windows are in the same plane, which allows the use of laser by using one window for the laser to enter the chamber and the other to leave the chamber where a beam dumper can be placed. The third window is placed at 90°, which can be used to place the detector. During this study, metal blanks were installed in place of the optical windows and they provided convenient access for cleaning the piston window between each experiment. Figure 3.4 shows a 3D schematic view of the chamber with its 3 side windows.

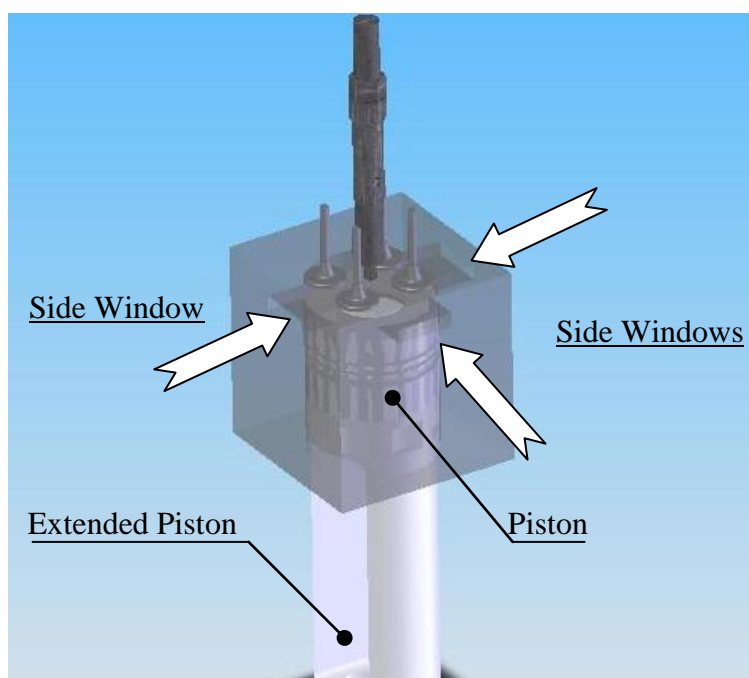


Figure 3.4 3D schematic view of side windows

The optical access for the experiment in this study was through the piston. At the bottom of the piston bowl a glass window made of fused silica was fitted. In order to obtain a good seal while preventing the damage of the window, a graphite gasket is fitted between the window and the upper piston and a carbon gasket between the window and a spacer ring, which is sealed against the extended piston (see Figure 3.5).

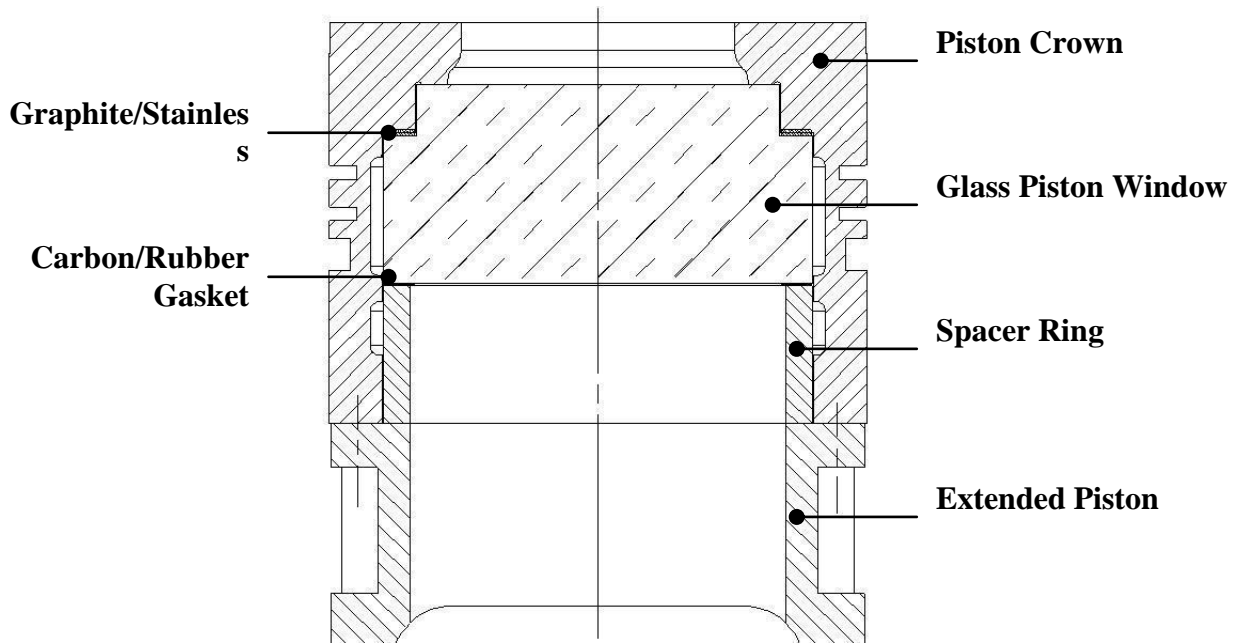


Figure 3.5 Sectional Schematic View of the Piston Window

3.2.4 Crankshaft Position System

In order to detect the angular position of the crankshaft a shaft encoder is fitted to the crankshaft. The shaft encoder transmits two output signals: one pulse per revolution and 1800 pulses per revolution. Both signals are sent to the Electronic Control Unit (ECU) that controls the injection system and to the data acquisition system. The single pulse signal is also used to illuminate an LED in front of the 45° mirror to show TDC as a visual mark on the high speed videos. Figure 3.6 shows the location of the LED.

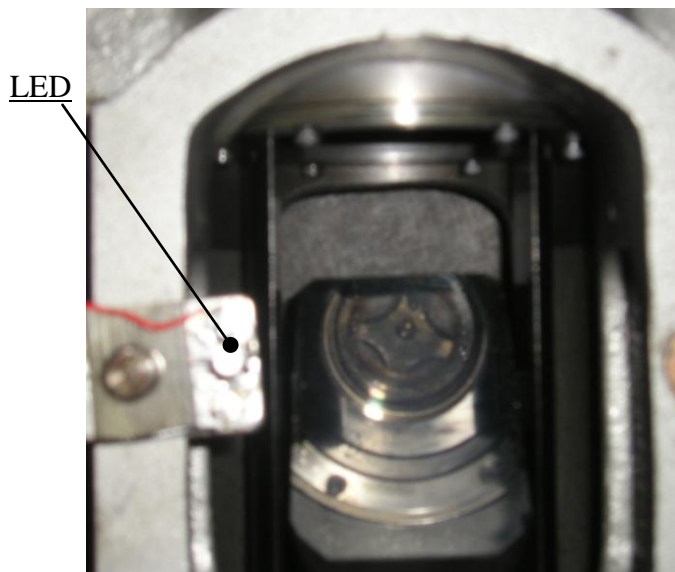


Figure 3.6 LED position

3.2.4 Fuel Systems

The fuel injection system in this study was based on the common rail fuel injection concept. This system is commonly used for direct injection diesel engines as it gives great flexibility regarding injection quantity, timing and number of injections, which are controlled electronically. Figure 3.7 shows a schematic view of the injection system used for this study.

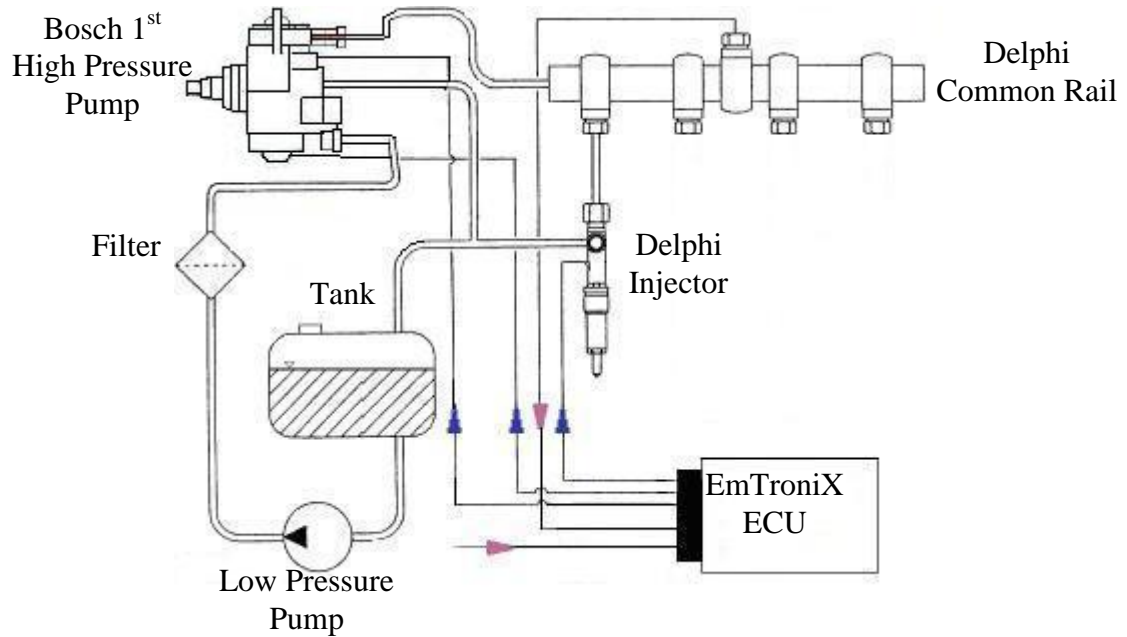


Figure 3.7 Schematic of the Fuel System [116]

A 12V low pressure pump supplies fuel from the tank through a filter and regulator to the high pressure pump. The high pressure pump is a production Bosch 1st generation common rail pump driven by the engine. The fuel is supplied to a Delphi HP common rail through a single thick-wall steel pipe. The common rail is fitted with a Delphi rail pressure sensor whose signal is sent to the ECU to control the injection pressure. The common rail has four outlets, three of which are blanked off and the remaining one connects the rail with the injector.

The injector used for this study was a Delphi multihole injector. Table 3.2 shows the specification of the injection system and injector.

Table 3.2 Injection System and Injector Specifications

| Injection System | |
|---|------------------|
| 1 st generation common rail system | |
| Injection Pressures | 800 bar/1200 bar |
| Delphi Wide Angle Injector | |
| Number of Holes | 6 |
| Hole Size | 0.123 mm |
| Cone Angle | 155° |
| Flow rate | 557 cc/min |
| Type | Microsac |

The flow rate graph of the injector is shown in Appendix A.

The injection system is controlled by an ECU supplied by EmTroniX. This ECU is operated with a software called EC-Lab installed in a PC. The ECU receives input signals from the shaft encoder and rail pressure. Via the EC-Lab, injection pressure, number of injections, timing and quantity can be adjusted. The ECU generates two output signals, the first one to the high pressure pump to control the injection pressure and the second to the injector driver which generates the appropriate signal sent to the injector. A screen shot of the user interface is shown in Appendix A.

3.2.5 Intake System

The single cylinder engine has been set up to work naturally aspirated or supercharged when required. It can also simulate EGR by injecting nitrogen into the intake system. Figure 3.8 shows the intake system of the Hydra engine.

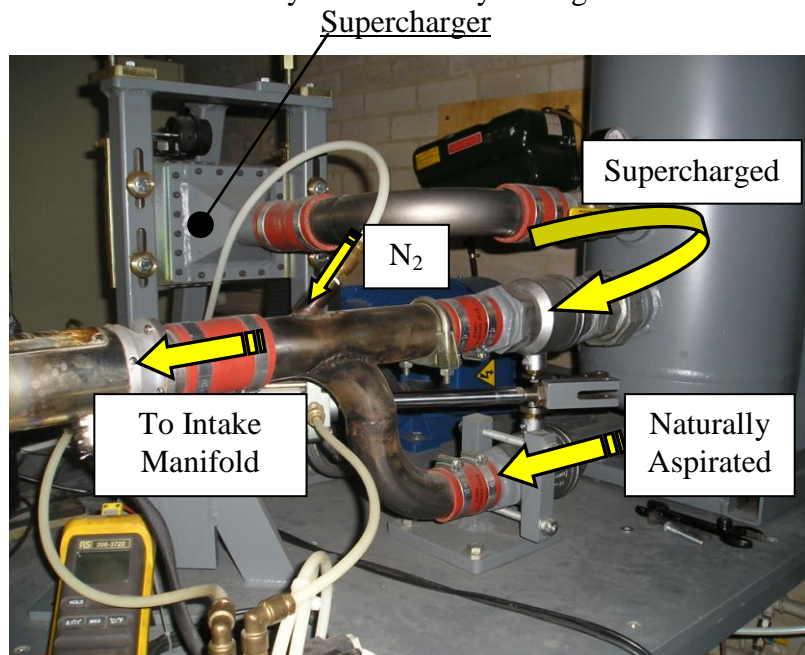


Figure 3.8 Intake System for the Hydra engine

3.2.5.1 Forced Induction

A forced induction system is fitted to the engine to allow boosting of the intake pressure if necessary. An Eaton M45 supercharger is used. The supercharger is a positive displacement roots type blower and it is driven by an AC motor at 2600 rpm. It incorporates a bypass valve so that the boost can be reduced from the maximum boost pressure which is 0.5 bar when the valve is fully closed. Figure 3.9 shows the supercharger and bypass valve.

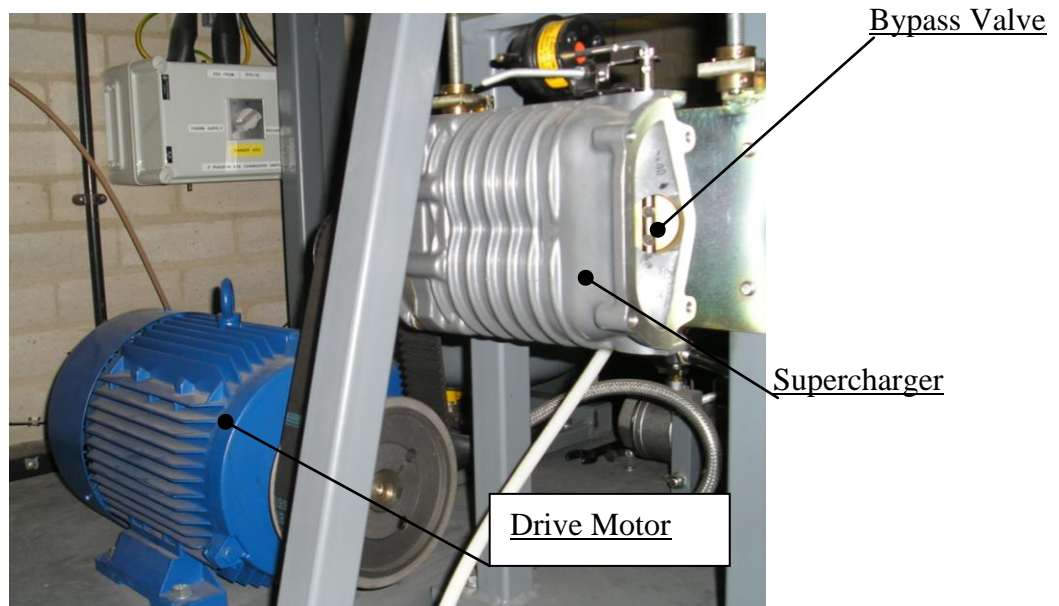


Figure 3.9 Supercharging System

A Kistler 4045A5 piezo-resistive pressure transducer is mounted in the intake manifold. The pressure transducer is connected to a Kistler 4618A2 piezo-resistive amplifier, from which the intake manifold pressure is determined and recorded by a digital oscilloscope. By opening or closing the bypass valve the required boost can be adjusted.

3.2.5.2 EGR system

EGR is simulated by using N_2 as inert gas: the N_2 flows from the compressed bottle to the intake manifold via a flowmeter, where the required amount can be set. In the case of this study 60% EGR was simulated. As an attempt to reduce both NO_x and soot emissions, very high levels of EGR are used in this investigation. It was chosen to correspond to a typical part-load condition at which low temperature diluted combustion was studied on a multi-cylinder engine by IFP and Renault as part of the EU NICE project. The air and N_2 flow rate chart for different engine speeds and temperatures are shown in Appendix B.

3.2.5.1 Intake Heating

In order to replicate the typical HSDI diesel operating conditions, intake air is heated by a 3kW heater installed before the intake manifold. A thermocouple is mounted to the intake manifold and sends the signal to a home-built heater control box. The control box turns the heater on and off and keeps it at a constant temperature. A temperature of 140°C was set in the heater control box for this study. Figure 3.10 shows the intake manifold and heater.

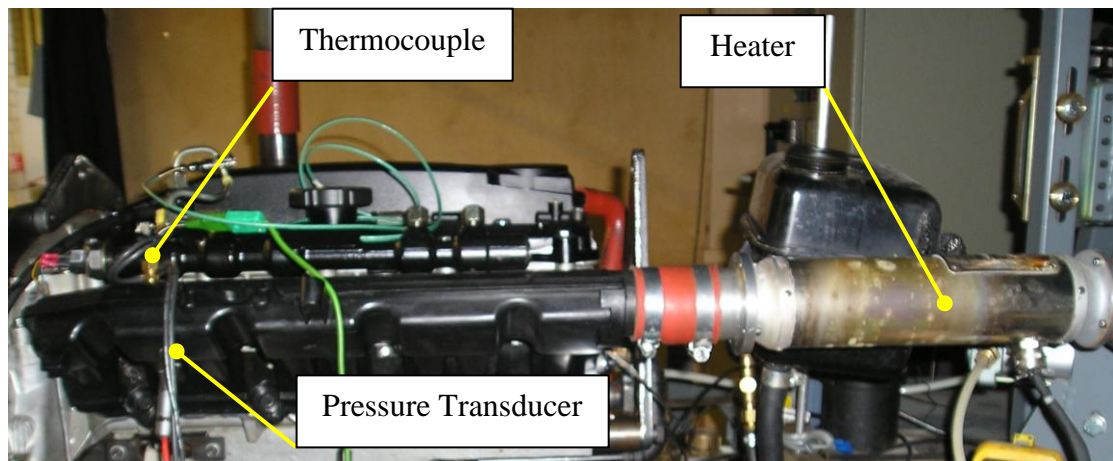


Figure 3.10 Intake Heating System

3.3 Cylinder Pressure Data Acquisition Systems

The heat release analysis, which is based on the collected cylinder pressure, is a powerful tool to understand the diesel engine combustion process. Hence the principle and implementation of the cylinder pressure measurement and heat release analysis are given in the following sections.

3.3.1 Cylinder Pressure Measurement

As stated in Section 3.2.2, A Kistler 6125A piezoelectric pressure transducer is mounted in place of the glow plug. The pressure transducer is connected to a Kistler 5011 charge amplifier, which sends an amplified signal to the data acquisition system.

3.3.2 Data Acquisition System

The data acquisition system consists of a National Instruments (NI) data acquisition card and interface board and a software written in LabVIEW by John Williams,

formally at Brunel University. The software is provided with the shaft encoder signals, thus these signals and the signal from the charge amplifier are connected to the National Instruments BNC-2110 board, which in turn is connected to the National Instruments PCI-MIO-16E data acquisition card installed in the PC.

The software uses the 1800 pulses per revolution signal from the shaft encoder as a reference signal. These signals are the clock that the software uses to record the data, therefore the data is recorded with 0.2 crank angle intervals. The software records the values of cylinder pressure which are thereafter taken to Microsoft Excel to calculate IMEP and heat release rate. A screen shot of the LabVIEW program is shown in Appendix B.

3.3.3 Experimental Procedure

Before all experiments could commence, the coolant and lubrication systems were switched on and left approximately for 1 hour. The first step before motoring the engine was to turn the low pressure pump on to make sure that the high pressure pump was lubricated. Then the engine was motored and the intake heater turned on. Just before reaching the required temperature, the engine was speeded up to the required speed. A button in the EC-Lab software was pressed to start injection and combustion in the cylinder.

To record the cylinder pressure data, the “Run” button in the LabVIEW program was pressed to allow recording and saving the cylinder pressure data of 20 cycles.

At the start of every session the motoring pressure was recorded. This was a diagnostic tool to check that the starting conditions were similar for every test and to check if the piston window seals were worn and the engine needed to be rebuilt.

3.4 Optical Set-Ups

The optical techniques applied in this study consist of high speed combustion imaging and the two-colour method, which has been developed for the use of high speed video cameras. Details of the two-colour method theory and implementation are explained in Chapter 4.

3.4.1 Combustion Imaging

High Speed Imaging was used to record videos of combustion and also of the fuel spray during the injection period. In order to visualize the injection spray a CU15 Oxford Lasers copper vapour laser was used. Table 3.3 gives the specifications of the copper vapour laser.

Table 3.3 Specifications of copper vapour laser

| copper vapour laser | |
|----------------------------------|-------|
| Type: CU15 Oxford Laser | |
| Wavelength (nm) | 511 |
| Average Power (W) | 8.5 |
| Pulses Width (ns) | 10-40 |
| Pulse repetition frequency (kHz) | 10 |

The high speed video camera used is a NAC Memrecam FX6000 which is equipped with a high speed colour CMOS sensor. The frame rate used in this study was 10,000 frames per second; this means that one frame is equal to 1.2 CA at the engine speed of 2000 rpm. The image resolution depends on the frame rate, thus for a 10,000 frames per second the resolution was 512 x 248 pixels. A Nikon 50mm f.1.4 lens was used in this study.

The camera is connected to a monitor in order to visualize the videos in real time, as well as after it had been recorded. The selected frames are then downloaded into a PC through an Ethernet cable.

3.4.1.1 Combustion Imaging Procedure

The laser beam was directed into the chamber by means of a fibre optics cable mounted in front of the 45° angled mirror. The high speed video camera was placed in front of the 45° angled mirror to allow the combustion chamber to be viewed. When firing, the camera was triggered manually and it recorded 12,000 frames before stopping automatically. This equals around 20 cycles at the engine speed of 2000 rpm used during these experiments. The video also captured the flashing of a LED which was triggered by the shaft encoder single signal, to identify the position of TDC.

3.5 Exhaust Emissions Measurements

The exhaust emissions measurements of CO, CO₂, O₂, uHC, NO and NO_x were taken by means of a Horiba MEXA-7170DEGR analyser and soot emissions were measured using an AVL 415 smoke meter.

3.5.1 Horiba MEXA-7170DEGR Emissions Analyser

The Horiba MEXA-7170DEGR is built with four modules in a compact cabinet with a PC as the main control unit. The screen displays instantaneous emissions and the values are stored in the computer in which variables are sample rate and measuring time. The four modules perform the actual emissions based on different techniques.

3.5.1.1 Horiba AIA-72X Series: CO and CO₂ measurement

A Horiba AIA-72 was used to measure the CO and CO₂ concentrations using a non dispersive infrared (NDIR) method. It is based on the fact that different molecules absorb infrared radiation at different wavelength and the absorption is an expression of the concentration of the molecules. Figure 3.13 shows a NDIR analyser.

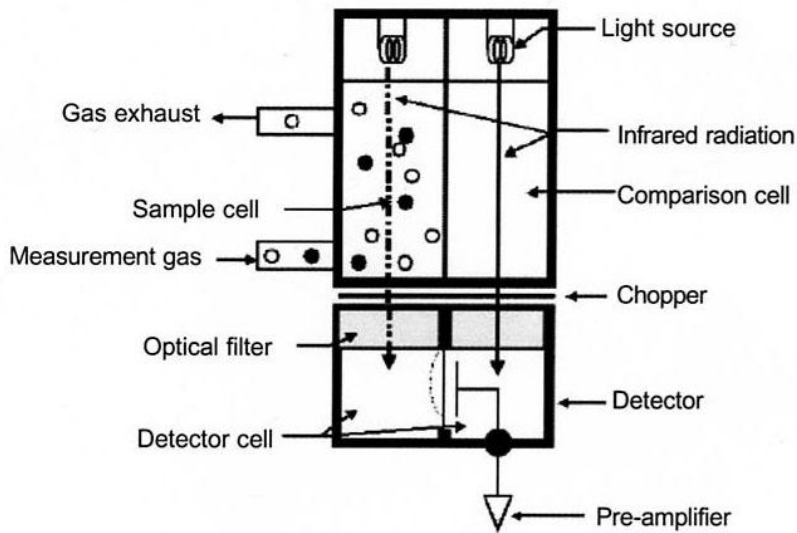


Figure 3.11 NDIR analyser (Horiba Instruments Ltd)

The analyser consists of a chamber with two sealed cells, sample cell and comparison cell separated by a membrane. An infrared light passes through the cells, the comparison cell containing nitrogen and the sample cell containing the measurement gas. As the gas enclosed in the cell absorbs infrared light, its temperature increases and

therefore expands. The movement of the membrane is detected as an electrical signal proportional to the gas concentration.

An optical filter between the sample cell and detector cell is used to block the transmission of wavelength absorbed by other species.

A light chopper is employed so that infrared light is transmitted intermittently enabling the detection of the changes in the gas concentration.

3.5.1.2 Horiba MPA-720: O₂ measurement

The Horiba MPA-720 magneto-pneumatic analyser was used to measure the O₂ concentration. It is based on the principle of paramagnetism, which is a magnetism that occurs in selected molecules when an external magnetic field is applied. The principle of a magneto-pneumatic oxygen analyzer is shown in Figure 3.14.

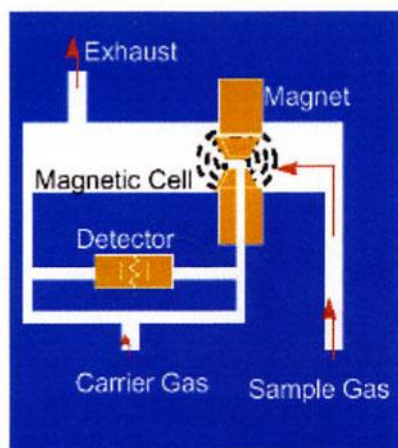


Figure 3.12 Configuration of magneto-pneumatic oxygen analyser (Horiba Instruments Ltd)

When an AC current flows in the electromagnet, an electromagnetic field is created around the poles which attract the oxygen molecules; this provokes a pressure rise around the poles proportional to the concentration of the oxygen. This pressure change is detected by a condenser microphone creating an output electrical signal.

3.5.1.3 Horiba FIA-720: Unburnt Hydrocarbon measurement

The Horiba FIA-720 Flame Ionisation Detector was used to measure the unburnt hydrocarbons (uHC). The detector works on the principle that when a gas containing hydrocarbons is burnt, ions are produced. Figure 3.15 shows a diagram of a FI Detector.

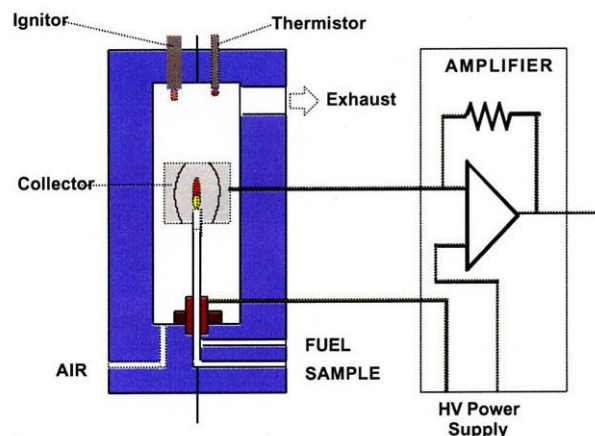
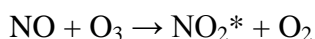


Figure 3.13 Schematic diagram of a (FID) Flame Ionisation Detector (Horiba Instruments Ltd)

The sample gas is burnt with hydrogen as a fuel due to the minimal ionisations that occurs during its combustion, and with high purity air. The ions are produced by thermal dissociation during the combustion. Two electrodes are fitted on each side of the flame, then a high DC voltage is applied provoking the ions to move to one of the electrodes producing an electric current which is proportional to the ionisation, proportional to the number of carbon atoms present. Thus this method can only measure the total hydrocarbons present without discriminating between components.

3.5.1.4 Horiba CLA-720A: NO and NO_x measurement

The Horiba CLA-720A Chemiluminescence analyser was used to measure the concentrations of NO and NO_x. The chemiluminescence method uses the reaction of NO with ozone (O₃):



A portion of the NO₂ generated as the result of this reaction becomes excited NO₂*. As these excited molecules return to the ground state, chemiluminescence is generated. The light intensity is proportional to the concentration of NO molecules and by measuring it, the NO concentration of the sample gas can be measured.

3.5.2 AVL 415 Soot Measurements

The AVL 415 smokemeter was used to measure the exhaust gas soot contents. The process is performed automatically by the smoke meter when the exhaust gas is passed through a paper filter. Using a reflectometer, the reflectance of the blackened filter is compared with a clean paper. The values given by the smoke meter following the ISO 10054:1998-Measurement apparatus for smoke from engines operating under steady-state conditions: Filter type smokemeter- and are as follows:

Smoke Value: 0 to 10 FSN

Which is equivalent to:

Soot Concentration: 0 to 32000mg/m³

3.6 Data Analysis

3.6.1 Cylinder Volume Calculation

The cylinder volume is calculated via the engine geometry for any crank angle using the following equations:

$$V = V_c + \frac{\pi B^2}{4} (l + a - s) \quad (3.1)$$

and

$$s = a \cos \theta + \sqrt{l^2 - a^2 \sin^2 \theta} \quad (3.2)$$

Where:

- V Cylinder Volume
- V_c Clearance Volume
- B Cylinder Bore
- l Connecting Rod Length
- a Crank Radius

- s Distance between Crankshaft and piston pin axes
- θ Crank Angle Relative to vertical

Applying the following equations for compression ratio and ratio of connecting rod to crank radius:

$$r_c = \frac{V_d + V_c}{V_c} \quad (3.3)$$

Where:

- r_c Compression Ratio
- V_d Displacement Volume

$$R = \frac{l}{a} \quad (3.4)$$

- R Ratio of Connecting Rod Length to Crank Radius

Equation 3.1 can be rearranged to:

$$V = V_c \left\{ 1 + \frac{1}{2} (r_c - 1) [R + 1 - \cos\theta - \sqrt{(R^2 - \sin^2\theta)}] \right\} \quad (3.5)$$

3.6.2 Engine Combustion Heat Release Analysis

From the cylinder pressure data, the engine output and combustion characteristics can be calculated using a program written in Microsoft Excel.

3.6.2.1 Indicated Mean Effective Pressure

Indicated mean effective pressure (IMEP) is the theoretical pressure that would have to be present in the cylinder during the power stroke to generate the maximum power possible. It is calculated from the pressure-volume diagram. Gross IMEP is the area enclosed between the compression and expansion strokes; negative work is done during the exhaust and intake strokes. Net IMEP is the result of subtracting the negative work from the gross IMEP. Thus IMEP is calculated by integrating the pressure on the piston over the compression/expansion cycle of the p-V diagram:

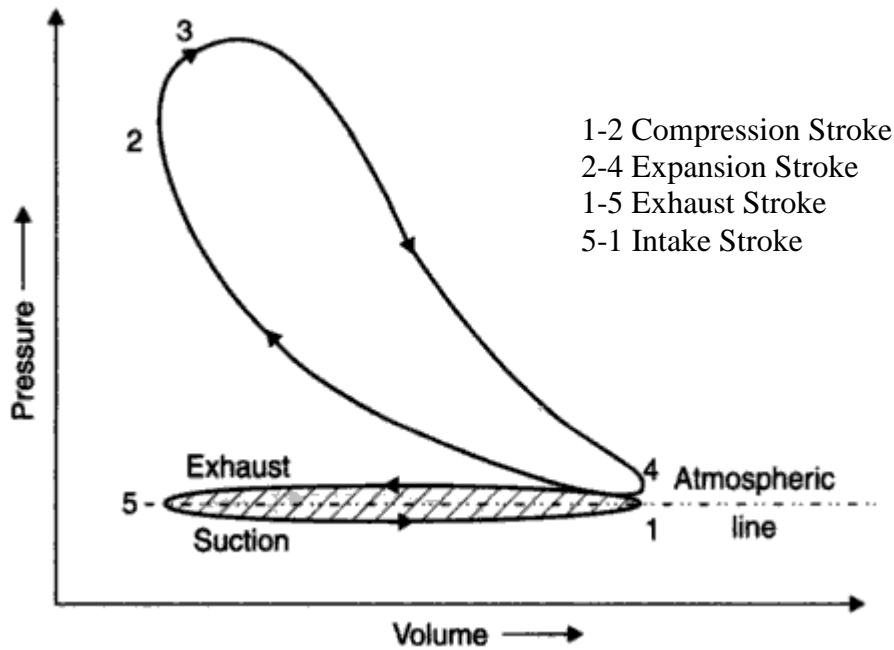


Figure 3. 14 p-V diagram for an actual diesel engine [113]

$$\text{IMEP} = \frac{1}{V_d} \int p dV \quad (3.6)$$

3.6.2.2 Indicated Specific Fuel Consumption

Indicated Specific Fuel Consumption (ISFC) is calculated as the fuel mass flow rate divided by the work output:

$$\text{ISFC} = \frac{\dot{m}_f \times \text{speed}}{\text{IMEP} \times V_d} \quad (3.7)$$

Where:

\dot{m}_f Mass flow rate of fuel

3.6.2.3 Heat Release Rate

To calculate the heat release rate, the one-zone model is used which considers the gases within the cylinder as homogenous, without distinguishing between burned and unburned gases. This model simplifies the calculation of heat release rate. The energy generated from the combustion process is considered as a separate additional source of

energy. To calculate the heat release, the combustion chamber is taken as an open system and the first law of thermodynamics applies as:

$$\frac{dQ}{dt} - p \frac{dV}{dt} + \sum_i \dot{m}_i h_i = \frac{dU}{dt} \quad (3.8)$$

Where:

$\frac{dQ}{dt}$ Rate of heat release transfer into system across boundary

$p \frac{dV}{dt}$ Rate of work transfer by system to the mobile boundary

\dot{m}_i Mass flow rate into system at location i

h_i Enthalpy of flux i

$\frac{dU}{dt}$ Internal energy of the charge

Once the intake and exhaust valves are closed, the mass which flows through the boundary is only the fuel and the crevice flow. Considering that the combustion takes place while the intake and exhaust valves are closed, and neglecting the crevice flow, Equation 3.8 becomes:

$$\frac{dQ}{dt} - p \frac{dV}{dt} + \dot{m}_f h_f = \frac{dU}{dt} \quad (3.9)$$

U is taken as the sensible internal energy of the in-cylinder charge, h_f is the sensible enthalpy of the injected fuel and $h_{s,f}$ is neglected. Then dQ/dt becomes the net heat release rate dQ_n/dt which is the difference between the heat release from the combustion of the fuel and the heat transfer from the system.

$$\frac{dQ_n}{dt} = \frac{dQ_{ch}}{dt} - \frac{dQ_{ht}}{dt} = p \frac{dV}{dt} + \frac{dU_s}{dt} \quad (3.10)$$

Considering the charge as an ideal gas, Equation 3.10 is written as follows:

$$\frac{dQ_n}{dt} = p \frac{dV}{dt} + mc_v \frac{dT}{dt} \quad (3.11)$$

Where:

c_v Specific heat at constant volume

T Absolute temperature

Considering the ideal gas law, $pV=mRT$, with R assumed constant:

$$V \frac{dp}{dt} = p \frac{dV}{dt} + mR \frac{dT}{dt} \quad (3.12)$$

Combining Equation 3.11 and 3.12:

$$\frac{dQ_n}{dt} = \left(1 + \frac{c_v}{R}\right) p \frac{dV}{dt} + \frac{c_v}{R} V \frac{dp}{dt} \quad (3.13)$$

Writing $\gamma = \frac{c_p}{c_v}$, the final equation is equivalent to:

$$\frac{dQ_n}{dt} = \frac{\gamma}{\gamma-1} p \frac{dV}{dt} + \frac{1}{\gamma-1} V \frac{dp}{dt} \quad (3.14)$$

Where

γ Ratio of specific heats, c_p/c_v

Equation 3.14 provides a simple way of calculating the heat release rate in a diesel engine. The value of γ is not constant during the different stages of the engine cycle, but generally, the values for air before combustion are around 1.35 and for the burned gases around 1.28-1.30 [4]. For diesel heat release analysis, a single value of γ is used, for this project γ was 1.3.

3.6.2.4 Cumulative Heat Release

The cumulative heat release can be determined from the heat release rate by:

$$CHR_n = HR_{n-1} + (HR \times \Delta\theta) \quad (3.15)$$

Where:

HR Heat release rate

$\Delta\theta$ Change in crank angle

3.6.2.5. Combustion Efficiency

The combustion efficiency can be calculated from the cumulative heat release and the heating value of the fuel:

$$\eta_c = \frac{\sum \frac{dQ_n}{dt}}{\dot{m}_f Q_{HV}} \quad (3.16)$$

Where:

dQ_n/dt Heat release rate

Q_{HV} Lower heating value of fuel

3.6.2.6 Ignition Delay

Ignition Delay is defined as the delay in crank angle between the start of injection (SOI) and start of combustion (SOC). The start of combustion (SOC) is determined from the heat release rate graph, and it is considered as the point where the rate begins to increase. The start of injection (SOI) is normally the timing of the main injection. For this study, where split injection was investigated, it was the start of the first injection.

3.7 Summary

This chapter has detailed the specification of the research engine and the equipment used to control the engine and gathering the data. The equipment used for the optical techniques has also been described as well as the apparatus for the emissions analysis and the fundamentals on which the measurement techniques are based on.

Chapter 4 Two-Colour Method for High Speed Camera

4.1 Introduction

As mentioned in Chapter 2, the two-colour method was developed by Matsui et al. [105] with the objective of estimating the flame temperature and soot concentration inside the combustion chamber of diesel engines.

It is well known that combustion in diesel engines is rather luminous, and this luminosity is caused mainly by the radiation of soot particles at high temperature. The two-colour method exploits the radiation emitted by the soot to measure the flame temperature as well as the KL factor or soot concentration.

This chapter contains the theory on which the two-colour method is based as well as the details of its implementation and the calibration in an optical engine. It has been developed for the use of high speed cameras, having the great advantage of obtaining the flame temperature and soot concentration during the whole process of combustion during a cycle, being possible to record up to 16 consecutive cycles.

4.2 Theory of the Two-Colour Method

During combustion soot emits radiation. The two-colour method is based on the measurement of this radiation at two different wavelengths to estimate the flame temperature and the soot concentration. Although the two-colour method estimates the flame temperature through the radiation emitted by soot, it is recognised that the temperature difference between the soot and the surrounding gases is only around 1K [105-107].

The blackbody radiation described by the Planck's law which states that the radiation intensity from a blackbody depends on the temperature of the blackbody at a given wavelength (Equation 4.1).

$$E_{b,\lambda}(T) = \frac{C_1}{\lambda^5 [e^{(C_2/\lambda T)} - 1]} \quad (4.1)$$

Where:

$E_{b,\lambda}$ = blackbody radiation intensity at temperature T, (Wm^{-3})

λ = Wavelength of the radiation

C_1 = first Planck's constant ($C_1 = 2\pi \cdot c^2 h = 3.7510^{-16} \text{Wm}^2$)

C_2 = second Planck's equation ($C_2 = \frac{h_c}{k} = 1.4210^{-2} \text{ mK}$)

T = temperature of the blackbody (K)

In the Planck's equation the term blackbody is introduced. A blackbody is an object that absorbs all incident light and emits radiation over a range of wavelengths. The radiation intensity at a determined wavelength depends on the temperature of the blackbody. However, a real body will emit always less radiation than a blackbody at a given temperature and wavelength, therefore the definition of emissivity appears as:

$$\varepsilon_\lambda = \frac{E_\lambda(T)}{E_{b,\lambda}(T)} \quad (4.2)$$

Where, $E_\lambda(T)$ is the monochromatic emissive power of a non-blackbody and $E_{b,\lambda}(T)$ is the monochromatic emissive power of a blackbody, at the same temperature and wavelength.

4.2.1 Flame Temperature Estimation

In the two-colour method, blackbody and non-blackbody radiation can be related by introducing the concept of apparent temperature T_a , which is defined as the temperature of a blackbody that will emit the same amount of radiation as a non-blackbody at temperature T . From this definition:

$$E_{b,\lambda}(T_a) = E_\lambda(T) \quad (4.3)$$

As the emissivity of a non-blackbody is always less than 1, it follows that $T > T_a$. Combining Equations 4.2 and 4.3:

$$\varepsilon_\lambda = \frac{E_{b,\lambda}(T_a)}{E_{b,\lambda}(T)} \quad (4.4)$$

Combining Equations 4.1 and 4.4:

$$\varepsilon_\lambda = \frac{e^{(C_2/\lambda T)} - 1}{e^{(C_2/\lambda T_a)} - 1} \quad (4.5)$$

ε_λ is estimated for soot particles using the empirical correlation developed by Hottel and Broughton [104], i.e.

$$\varepsilon_\lambda = 1 - e^{-(KL/\lambda^\alpha)} \quad (4.6)$$

Where:

K = an absorption coefficient proportional to the density of soot.

L = the geometric thickness of the flame along the optical axis of the detection system.

The parameter α is a value that depends on the physical and optical properties of the soot in the flame. The selection of α will be discussed later.

Combining Equations 4.5 and 4.6 obtains:

$$KL = -\lambda^\alpha \ln \left[1 - \left(\frac{e^{(C_2/\lambda T)} - 1}{e^{(C_2/\lambda T_a)} - 1} \right) \right] \quad (4.7)$$

The unknown product KL can be eliminated from Equation 4.7 by applying it for two apparent temperatures at different wavelengths λ_1 and λ_2 :

$$\left[1 - \left(\frac{e^{(C_2/\lambda_1 T)} - 1}{e^{(C_2/\lambda_1 T_{a1})} - 1} \right) \right]^{\lambda_1^{\alpha_1}} = \left[1 - \left(\frac{e^{(C_2/\lambda_2 T)} - 1}{e^{(C_2/\lambda_2 T_{a2})} - 1} \right) \right]^{\lambda_2^{\alpha_2}} \quad (4.8)$$

The flame temperature can be calculated from the above equation if the apparent temperatures T_{a1} , T_{a2} are obtained. These can be estimated prior to two-colour measurement through a calibration system by means of a tungsten calibration lamp. This will be explained in Section 4.3.3 of this chapter.

4.2.2 KL factor and Soot Concentration Estimation

Once the value of the flame temperature T is calculated through Equation 4.8, it is taken to Equation 4.7 to calculate the value of KL which is proportional to the soot concentration.

An estimate of the volumetric density of soot (C_v) which is the volume of particles in a unit gas volume can be obtained through the following equation:

$$C_v = \frac{1}{6\pi L \text{Im} \left(\frac{m^2 - 1}{m^2 + 2} \right)} \frac{KL}{\lambda^\alpha} \quad (4.9)$$

Where:

m = is the complex refractive index of the soot particle

I = is given by Lambert-Beer law

$$I = I_0 \exp \left(\int K_{\text{ext}} dx \right) \quad (4.10)$$

Where:

I_0 = the incident light intensity (Wm^{-2})

K_{ext} = the extinction coefficient for a cloud of particles (m^{-1})

L = the path length of the light beam (m)

It is also possible to estimate the soot gravimetric concentration C_m , which is the mass of soot per unit gas volume as follows:

$$C_m = \rho C_v \quad (4.11)$$

Where:

ρ = soot density

However, the estimation of the soot density requires knowledge of the composition of the soot particles.

4.3 Implementation

As explained previously, the flame temperature can be estimated through Equation 4.8 for which it is necessary to calculate the apparent temperatures at two different wavelengths and to define the parameter α .

4.3.1 Selection of Parameter α

The estimation of the flame temperature and the KL factor depends on the selection of a suitable value for α . The value of α depends on the light wavelength, soot particle size and the refractive index of soot. In the selection of α , it is less critical for the estimation of the flame temperature if the wavelengths selected are in the visible range of the spectra. This can be seen in Figure 4.1:

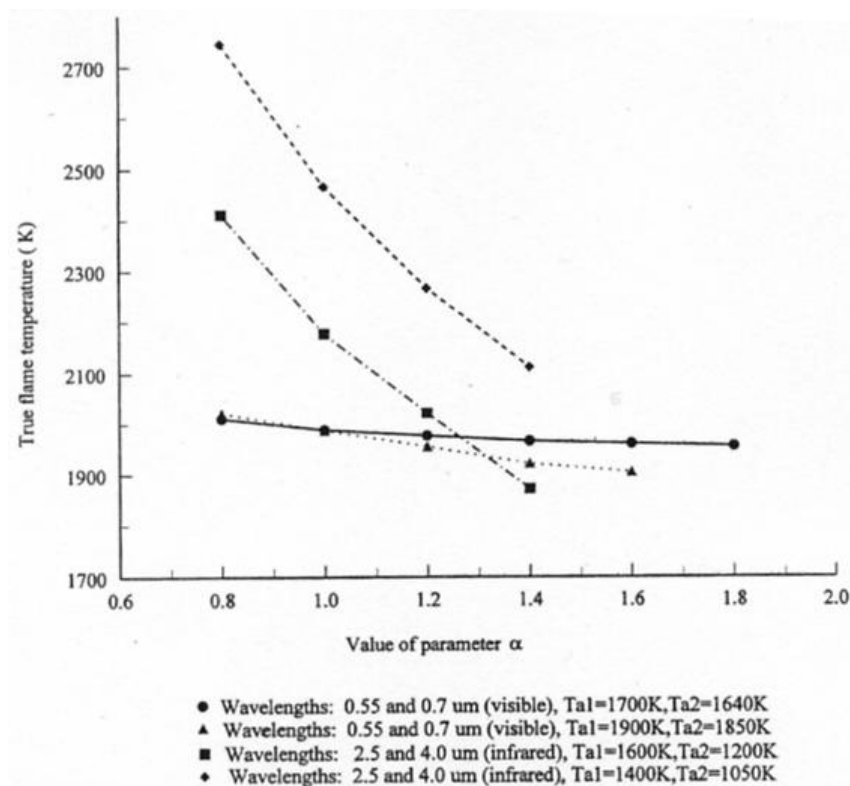


Figure 4.1 The effect of the value of parameter α on the estimated temperature [93]

Zhao and Ladommatos made a compilation of the values of the parameter alpha used in the literature, which can be seen in Table 4.1. It can be noticed that for a selection of wavelengths in the visible region, the value of the parameter alpha recommended is 1.39 [108, 109]; this value can be used for most fuels.

Table 4.1 Compilation of values of parameter alpha in the Hottel and Broughton correlation for soot emissivity (Zhao and Ladommatos [93])

| Visible Wavelengths | Infrared Wavelengths | | Fuel or Flame Type | Reference |
|---------------------|------------------------------------|-----------------------------|-----------------------|-----------------------------|
| 1.39 | 0.95 | $\lambda > 0.8 \mu\text{m}$ | Steady luminous flame | Hottel and Broughton (1932) |
| 1.38 | 0.91 – 0.97 | $\lambda > 0.8 \mu\text{m}$ | Diesel engine flame | Matsui et al. (1980) |
| 1.39 | | | Diesel engine soot | Yan and Boreman (1988) |
| - | 0.94 – 0.97 | $\lambda > 0.8 \mu\text{m}$ | | Libert and Hibbard (1970) |
| - | 0.89 , 1.00 | $\lambda > 1-7 \mu\text{m}$ | Amyl acetylene | Siddell and McGrath (1963) |
| - | 0.77 | $\lambda > 1-7 \mu\text{m}$ | Kerosene | |
| - | 0.94 , 0.95 | $\lambda > 1-7 \mu\text{m}$ | Benzene | |
| - | 0.93 | $\lambda > 1-7 \mu\text{m}$ | Candle | |
| - | 0.96 , 1.14 , 1.25 | $\lambda > 1-7 \mu\text{m}$ | Furnace samples | |
| - | 1.06 | $\lambda > 1-7 \mu\text{m}$ | Petrotherm | |
| - | 1.00 | $\lambda > 1-7 \mu\text{m}$ | Propane | |
| - | $\alpha = 0.91 + 0.28 \ln \lambda$ | $\lambda > 1-7 \mu\text{m}$ | Various fuels | |
| 1.43 | - | | Acetone | Rossler and Behrens (1950) |
| 1.39 | - | | Amyl acetate | |
| 1.29 | - | | Coal gas/air | |
| 1.23 | - | | Benzene | |
| 1.14 | - | | Nitrocellulose | |
| 0.66 – 0.75 | - | | Acetylene/air | |

In the last 15 years, the two-colour method has been widely employed in the estimation of flame temperature in diesel engines, and the value of 1.39 for the parameter alpha has been commonly applied [1013, 118-120]. The same value of 1.39 for the parameter alpha was employed in this project.

4.3.2 Choice of Wavelengths

In the two-colour method, detection at two wavelengths is necessary to solve Equation 4.8. The radiation can be detected in the visible and infrared regions [121, 122]. Visible wavelengths are preferred due to the sensitivity of the measuring system to changes in flame temperature being greater than in the infrared region because the rate of change of

spectral radiance with respect to temperature ($dI\lambda/dT$) is larger in the visible range than in the infrared region (see Figure 4.2).

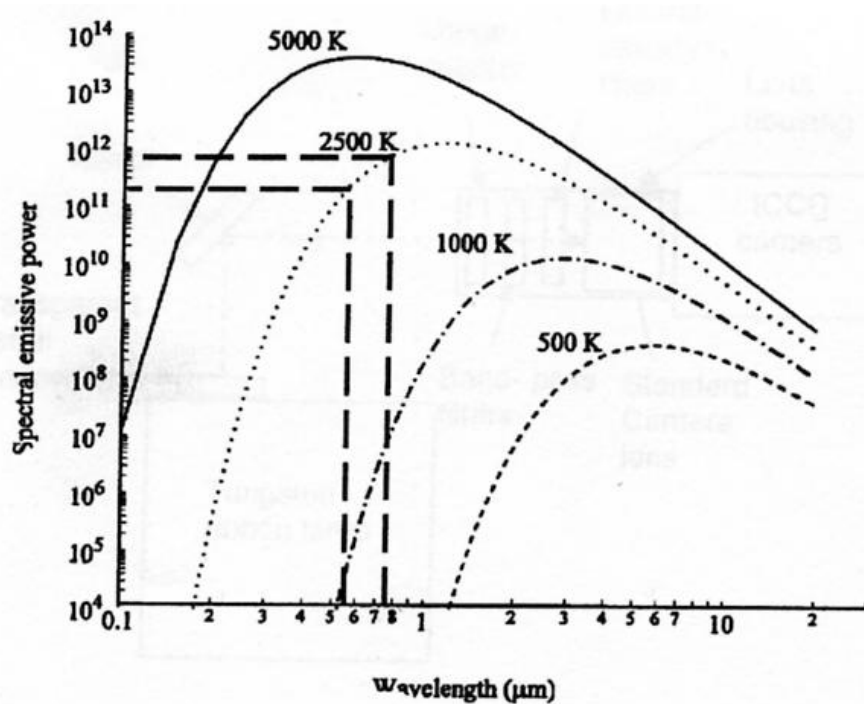


Figure 4.2 The spectral radiance of a blackbody as a function of temperature (Zhao and Ladommatos [93])

During combustion in diesel engines there is thermal radiation from the soot particles and radiation emissions from gases. Another reason for which the visible region is preferable over the infrared is that in the infrared region radiation or absorption from gases as such as CO_2 , CO , water vapour and even fuel vapour may take place.

The two-colour method with an ICCD camera was implemented at Brunel University by Sison [123]. For the reasons mentioned before, and due to the spectral response of the ICCD camera, the selection of wavelengths was 550nm and 750nm. The same wavelengths were chosen for this project, although different modifications had to be implemented in the instrumentation as explained in the following section.

4.3.3 Instrumentation, Use of High Speed Camera

The two-colour method was extended in this study for the use of high speed video cameras, allowing the estimation of flame temperature and soot concentration for the whole combustion process in a cycle. Figure 4.3 shows the schematic of the two-colour

experimental set-up. Using the Ricardo Hydra engine with optical access of the “Bowditch” design, the optical set-up consists of a high speed camera NAC Memerecam FX6000, a DRS intensifier ILS-3-11 and a standard Nikon 60mm f2.8 lens. In front of the lenses, a mounting was created to hold an image doubler where two half-circumference bandpass filters at 550nm and 750nm were fitted.

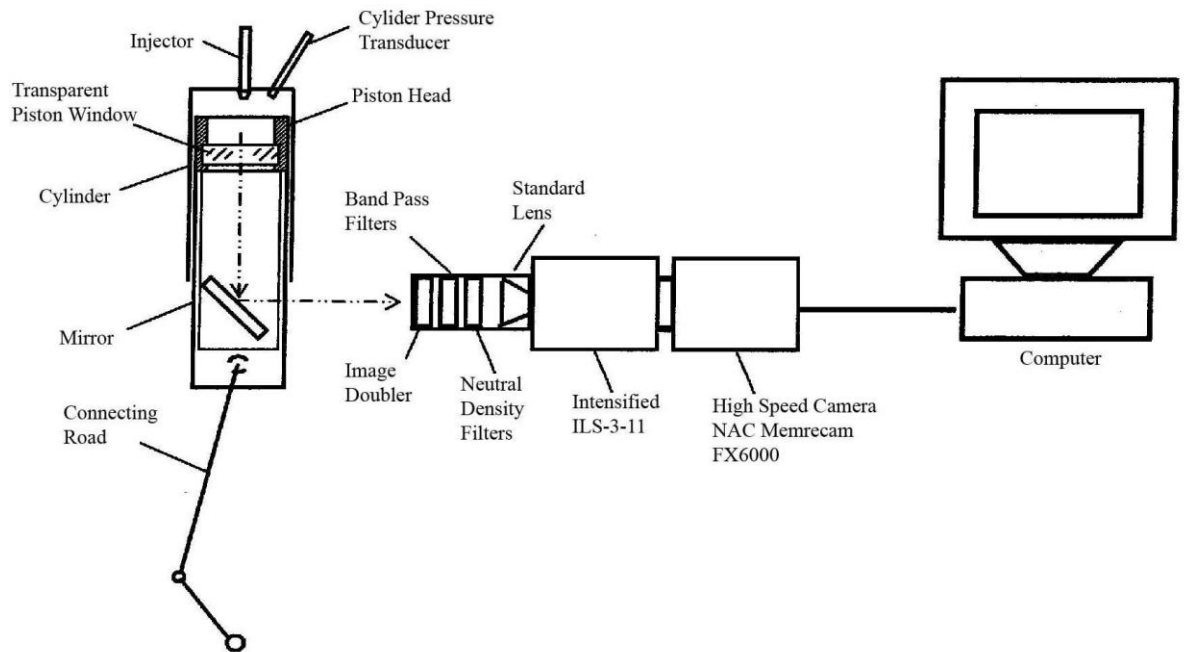


Figure 4.3 Schematic of the Two-Colour Experimental Set-up

Two neutral density filters were placed in front of the 550nm bandpass filter so that the radiation intensities at 550nm and 750nm were approximately of the same range. (The spectral emissivity of the system is determined by the spectral response of the NAC Memerecam FX6000 high speed camera and the DRS intensifier ILS-3-11). Figure 4.4 and Figure 4.5 show the spectral response for the NAC Memerecam FX6000 high speed camera and the DRS intensifier ILS-3-11. As seen in the figures below the total spectral response of the system at 750nm is very low compared to 550 nm which justifies the use of these density filters.

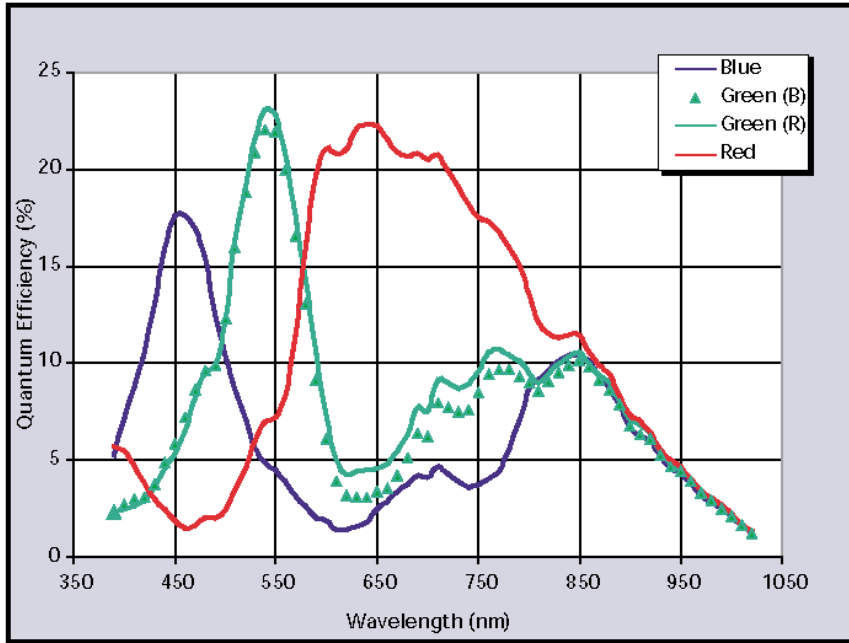


Figure 4.4 Spectral Response of the High Speed Camera

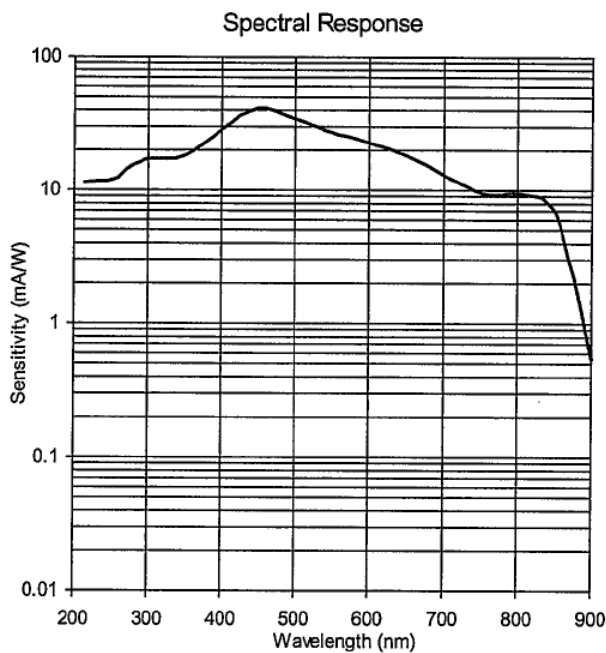


Figure 4.5 Spectral Response of the intensifier

4.3.3.1 Intensifier Lens System

The lens intensified system used for this study was Type ILS-3-11. This range of Intensified Systems is designed to provide light intensification, high speed shuttering and UV to visible conversion for use with a range of high speed cameras and video systems. It allows high speed imaging up to approximately 100,000 frames per second. It is fitted with a standard Nikon objective F-mount to accept standard Nikon lenses.

The ILS system is triggered externally through a BNC cable connected to the TTL input signal connector, which comes from the high speed camera.

4.3.3.2 Image Doubler and band pass filters

As the two-colour method requires capturing two images of combustion, a Hoya Vari-Multivision image doubler was used for this study.

Two TFI Technologies Inc. band pass filters were used in this study. The filters are specially cut into two semi-circles in order to fit with the image doubler. Figure 4.6 shows the image doubler and band pass filters, whose specifications are given in Table 4.2.

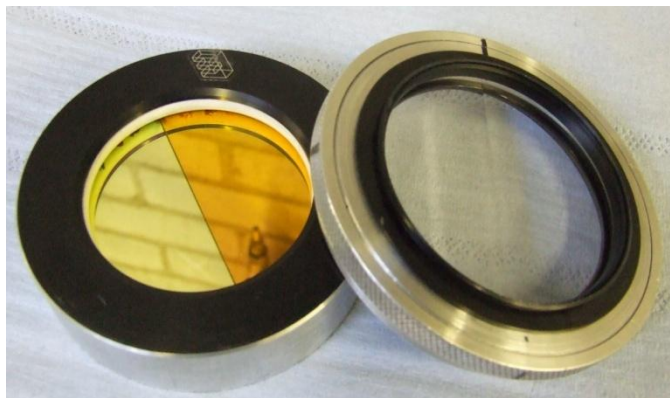


Figure 4.6 Band pass filters and image doubler

Table 4.2 Specifications of band pass filters

| TFI Band pass filter 550-40 | | TFI Band pass filter 750-40 | |
|--|---|--|---|
| CWL | 550nm +/- 8nm | CWL | 750 +/- 8nm |
| FWHM | 40nm +/- 8nm | FWHM | 40 +/- 8nm |
| T | >70% @peak | T | >=75% @peak |
| B | >=OD4, UV-1150nm (dielectric blocking) | B | >=OD4, UV-1150nm (dielectric blocking) |
| Size | 50mm diam. +0/-0.25mm | Size | 50mm diam.+0/-0.25mm |
| Tk | <6.3mm | Tk | <6.3mm |
| AOI | 0 degrees | AOI | 0 degrees |

4.3.3.3 Neutral Density Filters

Two Kodak Wratten neutral density filters with 10% transmission were used in front of the 550nm band pass filter to reduce the intensity; thus the intensity at both 550nm and 750nm were of the same magnitude.

4.3.3.4 Two-Colour technique procedure

As for the combustion imaging, the high speed camera is triggered manually when the engine is firing allowing the recording of several cycles. The intensifier is triggered externally by the high speed camera via a BNC cable. The high speed camera records a movie of combustion at a rate of 10,000 frames per second. Each frame is then processed in order to estimate the flame temperature and KL factor (the image processing method is explained in Section 4.3.5 of this chapter). Finally all the frames are put together to complete the flame temperature and KL factor movies. Figure 4.7 shows the equipment used for this technique.

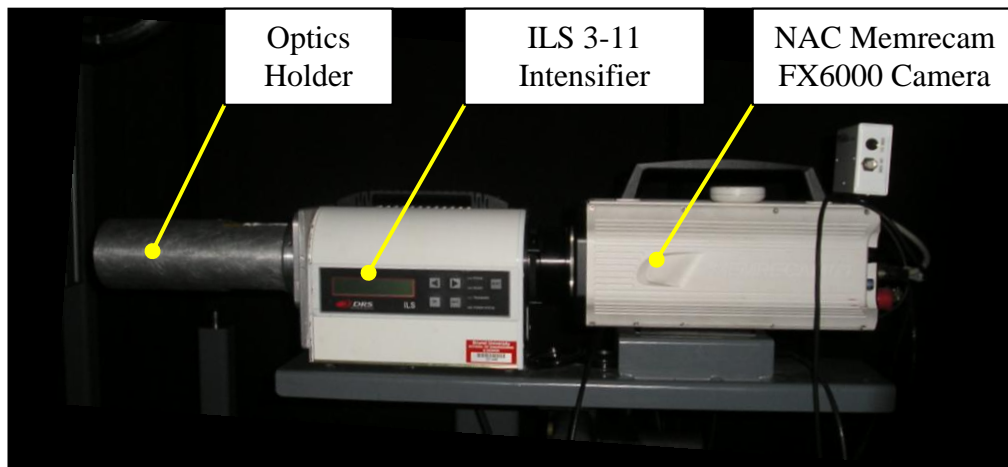


Figure 4.7 The Two-Colour Setup

4.3.4 Calibration

The two-colour method is based on the estimation of two apparent temperatures. After calculating these apparent temperatures, through Equations 4.7 and 4.8 the flame temperature and KL factor can be estimated. With this setup, every frame is analysed pixel by pixel giving intensity values. Hence the system must be calibrated so that the pixel values correspond to the apparent temperatures. This calibration can be done using a blackbody and a calibration curve can be obtained for the two wavelengths selected.

For this project, as a blackbody was not available, a calibrated tungsten lamp was used. This tungsten lamp is calibrated in terms of apparent temperature and current supplied (see Appendix C for the calibration table) which was carried out at 660nm, but it is usually adequately accurate at wavelengths near 660nm [108].

Figure 4.8 shows a schematic diagram of the setup for the calibration.

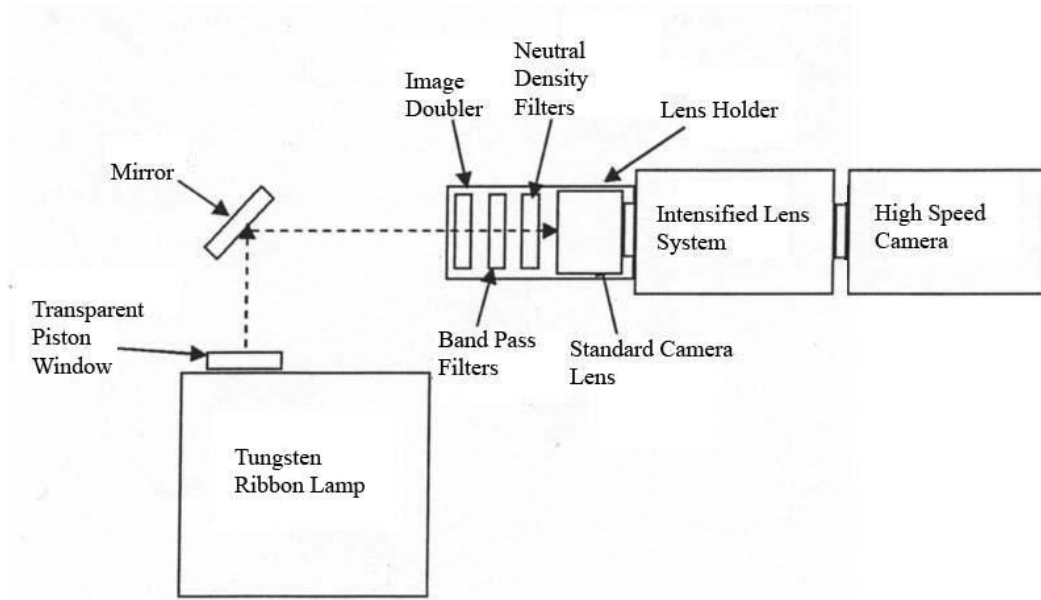


Figure 4.8 Schematic Setup of the Two-Colour Calibration with Tungsten Lamp

As Figure 4.8 illustrates, the setup for the calibration follows the same setup as the one used in the single cylinder optical engine for the experiments. A 45 degree mirror is placed to simulate the mirror under the glass piston window and in front of the lamp a transparent piston window is placed, exactly the same as in the single cylinder engine.

The tungsten lamp is calibrated by the manufacturer against a standard blackbody, where the blackbody radiance temperature was accurately related to the current supplied to the lamp filament, which is shown in Figure 4.9.

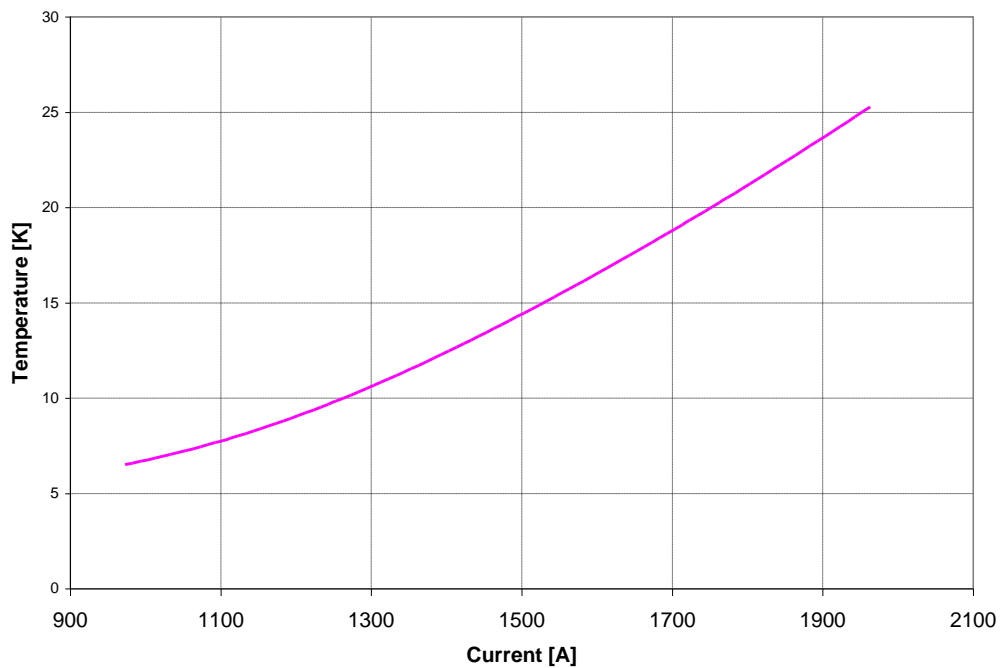


Figure 4.9 Calibration Curve for Tungsten Ribbon Lamp

This tungsten lamp was calibrated at a wavelength of 660nm. Therefore in order to calculate the apparent temperatures at 550nm and 750nm, the emissivity values at these wavelengths were needed. Larrabee et al. [124] presented the relationship between the apparent temperature and emissivity. By interpolation using the emissivity values of 540nm and 560nm for the 550nm wavelength and 740nm and 760nm for the 750nm wavelength, the emissivity values for 750nm and 550nm were obtained, as shown in Table 4.3. After obtaining the values of emissivity, the apparent temperatures were calculated through Equation 4.12.

$$T_{a1} = \frac{\epsilon_{550}}{\epsilon_{660}} T_{660} \quad \text{and} \quad T_{a2} = \frac{\epsilon_{750}}{\epsilon_{660}} T_{660} \quad (4.12)$$

Table 4.3 Emissivity Table [109]

| Wavelength (nm) | Temperature [K] | | | | |
|-----------------|-----------------|---------------|---------------|---------------|---------------|
| | 1600 | 1800 | 2000 | 2200 | 2400 |
| 540 | 0.453 | 0.451 | 0.448 | 0.446 | 0.443 |
| 550 | 0.4525 | 0.4500 | 0.4470 | 0.4445 | 0.4420 |
| 560 | 0.452 | 0.449 | 0.446 | 0.443 | 0.441 |
| 740 | 0.430 | 0.426 | 0.422 | 0.419 | 0.415 |
| 750 | 0.4285 | 0.4245 | 0.4210 | 0.4175 | 0.4140 |
| 760 | 0.427 | 0.423 | 0.420 | 0.416 | 0.413 |
| 660 | 0.441 | 0.436 | 0.432 | 0.428 | 0.424 |

A relationship between RGB colour intensity pixels values from the frames and the apparent temperatures was found. This calibration was carried for three different shutter positions of the Nikon lens as well as for three different intensity gains in the intensifier. Consequently it could be possible to study combustion of different luminosity. Table 4.4 illustrates the condition matrix for the calibration carried out.

Table 4.4 Calibration Matrix

| Shutter Lens | Intensified Gain (%) | | | | |
|--------------|----------------------|----|----|----|----|
| f 2.8 | 55 | 60 | 65 | 70 | 75 |
| f 4 | 60 | 65 | 70 | 75 | 80 |
| f 5.6 | 70 | 75 | 80 | 85 | 90 |

The high speed camera takes movies, with 10 frames selected for every calibration point, so that the pixel values were averaged. During this calibration it was found that at low values of apparent temperatures, the difference of pixel values between frames was considerably high due to the low signal to noise ratio. However, as apparent

temperatures increased, the difference decreased. Therefore a cut-off pixel value was introduced in the relationship between pixel values and apparent temperatures, below which the apparent temperature was considered zero. By means of using these cut-off values the error of averaged intensity values for the 10 frames selected for every calibration was below 5%. As a result, the first few frames just after start of combustion and the last few frames of combustion were not analysed and therefore these flame temperatures and KL factors were not possible to be included in the flame temperature and KL factor movies.

The final relationship between the pixel values and the apparent temperatures can be found in Appendix D.

4.3.5 Data Analysis

The movies taken with the high speed camera show two images of combustion. These two images correspond to the two different wavelengths and therefore to two apparent temperatures. Through Equations 4.7 and 4.8, the flame temperature and KL factor were then estimated.

In order to obtain these estimations, every frame of the movie had to be saved in Bitmap (.bmp) format and then processed using LabVIEW. Two programs were written by K. Sison [123] a former PhD student at Brunel University, the first one called “align and crop.vi” allows the images to be aligned and then cropped so that the main image post-processing program can analyse them. The second program “2 colour method.vi” allows the flame temperature and KL factor calculation to be carried out pixel by pixel. At each pixel two apparent temperatures are provided and then the true temperature is estimated. As Equation 4.8 cannot be solved analytically, a numerical method based on the Newton-Raphson iteration is used, based on a method developed by Yan [125]. The calculation involves an estimation of the apparent temperature at the first wavelength T_{a1} and assumed T (the adiabatic flame temperature is T 3000 K) and a measured apparent temperature at the second wavelength T_{a2} . The temperature T_{a1} is calculated iteratively until the difference between the calculated temperature T_{a1} and the measured temperature T_{a1} is less than 0.1°C . Each iteration was calculated for a new estimated true temperature T found by linear interpolation.

4.3.5.1 Calculation of Flame Temperature and Soot Concentration

The variation of T_{a1} with T at a given T_{a2} is approximately linear for a short temperature range, so rearranging Equation 4.8

$$\frac{1}{T_{a1}} = \frac{\lambda_1}{C_2} \ln \left[1 + \left(\frac{e^{(C_2/\lambda_1 T)} - 1}{A} \right) \right] \quad (4.12)$$

Where

$$A = 1 - \ln \left[1 - \left(\frac{e^{(C_2/\lambda_2 T)} - 1}{e^{(C_2/\lambda_2 T_{a2})} - 1} \right)^{\frac{\alpha_2}{\alpha_1}} \right] \quad (4.13)$$

Through Equation 4.8 and 4.12, the flame temperature was calculated using the iterative method explained below. This procedure was inserted in the program “2 colour method” in order to calculate simultaneously flame temperature and KL factor.

Figure 4.10 is a schematic example for solving the flame temperature, where the curve between point 1 and point 2 represents the point's location at T_{a2} constant.

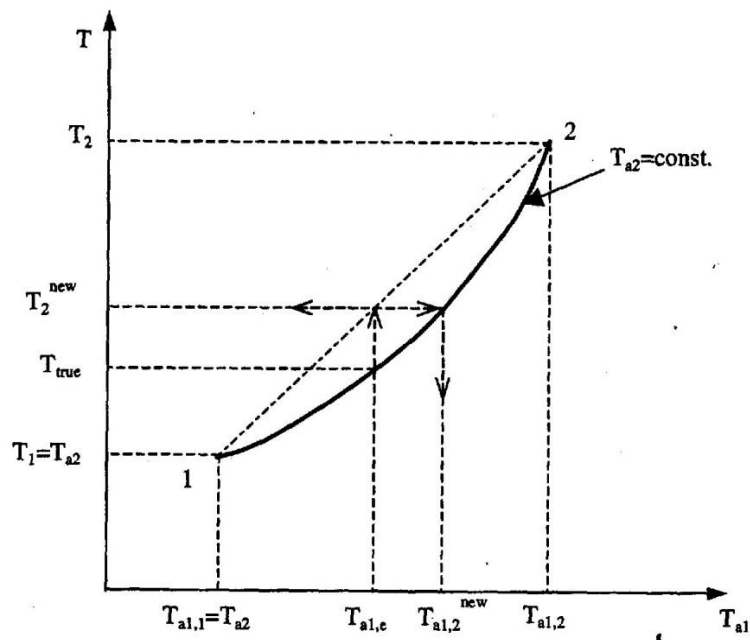


Figure 4.10 Schematic of the Numerical Scheme for Solving Equation 4.8 (Zhao & Ladommatos, [82])

Steps for solving the flame temperature:

1. True temperature is assumed to be between points 1 and 2 in Figure 4.10. Point 1 (P1) in Figure 4.10 is assigned to the measured apparent temperature, which is the apparent temperature T_{a2} at the longer wavelength. Point 2 (P2) is selected to be greater than the true temperature, which in this case is assumed to be 3000 K.
 - a. T_1 (point 1) is assigned to the measured temperature to T_{a2} at the longer wavelength
 - $T_{a1,1}$ is the apparent temperature $T_{a1,1} = T_{a2}$
 - $T > T_1 = T_{a2}$

2. The true flame temperature is assumed to be T_2 . In a diesel engine the flame temperature is around 2500 K, so T_2 is assumed to be 3000 K for the start of the iteration.

$$T_2 = 3000\text{K} > T$$

3. The flame temperature is higher than its apparent temperature.

$$T > T_{a1} > T_{a2}$$

4. Through Equation 4.12 a first value of apparent temperature (at shorter wavelength) $T_{a1,2}$ is calculated using the known T_{a2} value and the assumed first value T_2 .

$$T_{a1,2} > T_{a1,m}$$

5. Once the two points in the graph P1 (T_{a2} ; T_{a2}) and P2 ($T_{a1,2}$; T_2) are known, a linear interpolation was done to estimate the new flame temperature.

$$T_2^{new} = T_1 + \frac{(T_2 - T_1)(T_{a1,m} - T_{a2})}{(T_{a1,2} - T_{a2})} \quad (4.14)$$

6. A point 4 can be found on the curve at T_{a2} constant. Using the new flame temperature calculated T_2^{new} and the constant value T_{a2} , a new second iterative apparent temperature $T_{a1,2}^{new}$ has been calculated by Equation 4.14.

7. The new temperature on the ordinate axis calculated $T_{a1,2}^{new}$ is compared with the measured temperature T_{a1} .

- a. If the different between the two temperatures is less than 0.1 K, then T_2^{new} is the solution to the true flame temperature for the two apparent temperatures measured.
- b. If not then, $T_{a1,2}$ is replaced with the point 4 ($T_{a1,2}^{new}$, T_2^{new}) and steps 5, 6 and 7 are repeated until a convergent solution is found.

8. When the true flame temperature T_2^{new} is found, it is used to calculate the KL factor

4.3.6 The LabVIEW and MATLAB Programs

As previously explained, LabVIEW was used for image post-processing. The two programs used were written by a former PhD student at Brunel University however modifications had to be done to be adapted for the high speed movies' frames.

4.3.6.1 Align and Crop

As the two images for 550nm and 750nm must be aligned accurately in order to perform analysis on a pixel by pixel basis, this program was created so that a correlation coefficient was used to show if the alignment was precise. This correlation coefficient could be from 0 to 1 when the images were absolutely identical. There were two cursors that could be moved to the centre of each image and when the value of the correlation factor was greater than 0.95, the program would automatically stop and crop the images. A small modification had to be made, as the original program was to analyse pictures taken by the ICCD camera, which were in greyscale values 8-bit whereas the frames saved from the videos were in RGB colour 32-bit.

Figure 4.11 shows a screenshot of the align and crop LabVIEW program.

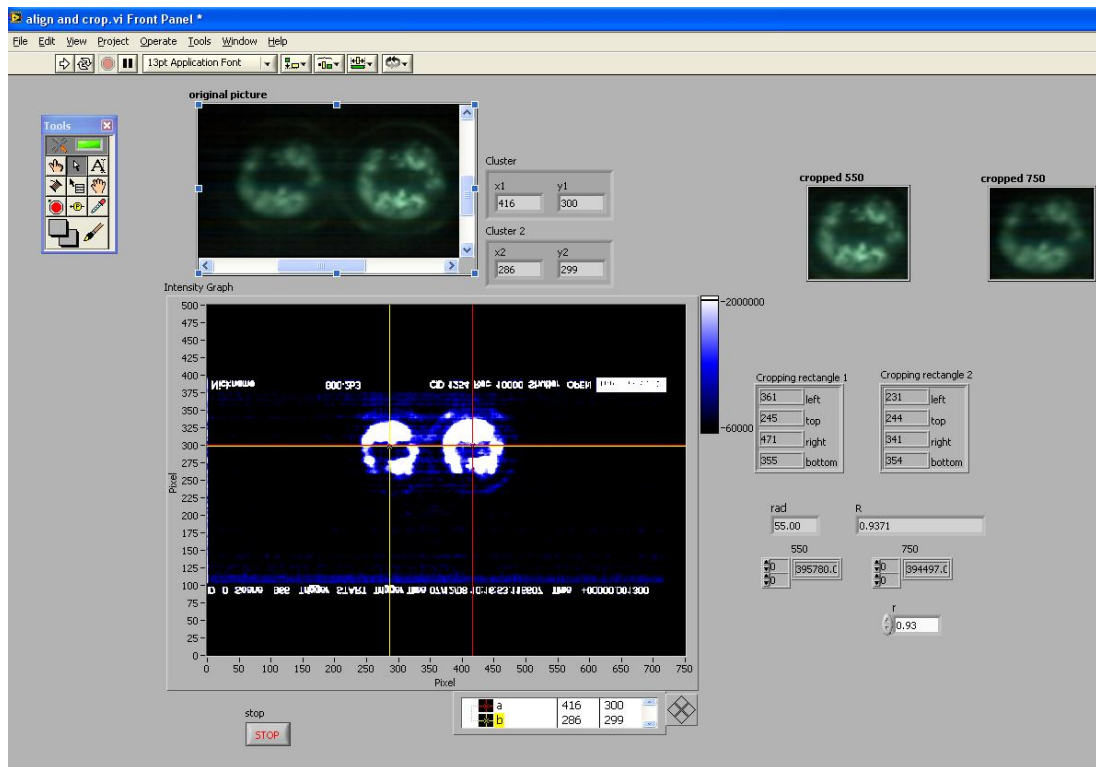


Figure 4.11 Front Panel of Align and Crop LabVIEW program

4.3.6.2 The Two-Colour program

The “two-colour.vi” program performs calculations on the images produced by align and crop.vi on a pixel by pixel basis, and hence generates the flame temperature and soot concentration maps. This program was modified so that the calibration equations were added as well as the cut-off pixel values for which the analysis would be performed, as explained before. The “two-colour.vi” could be used to display the maps as well as save them as bmp format. Another modification was made in order to save the flame temperature and soot concentration as two dimensional matrices. This was done so further analysis could be carried out. In the case of this project, this data was exported to MATLAB so that it would show the flame temperature and soot concentration contour maps with the isolines.

Figure 4.12 illustrates the screenshot of the two-colour.vi

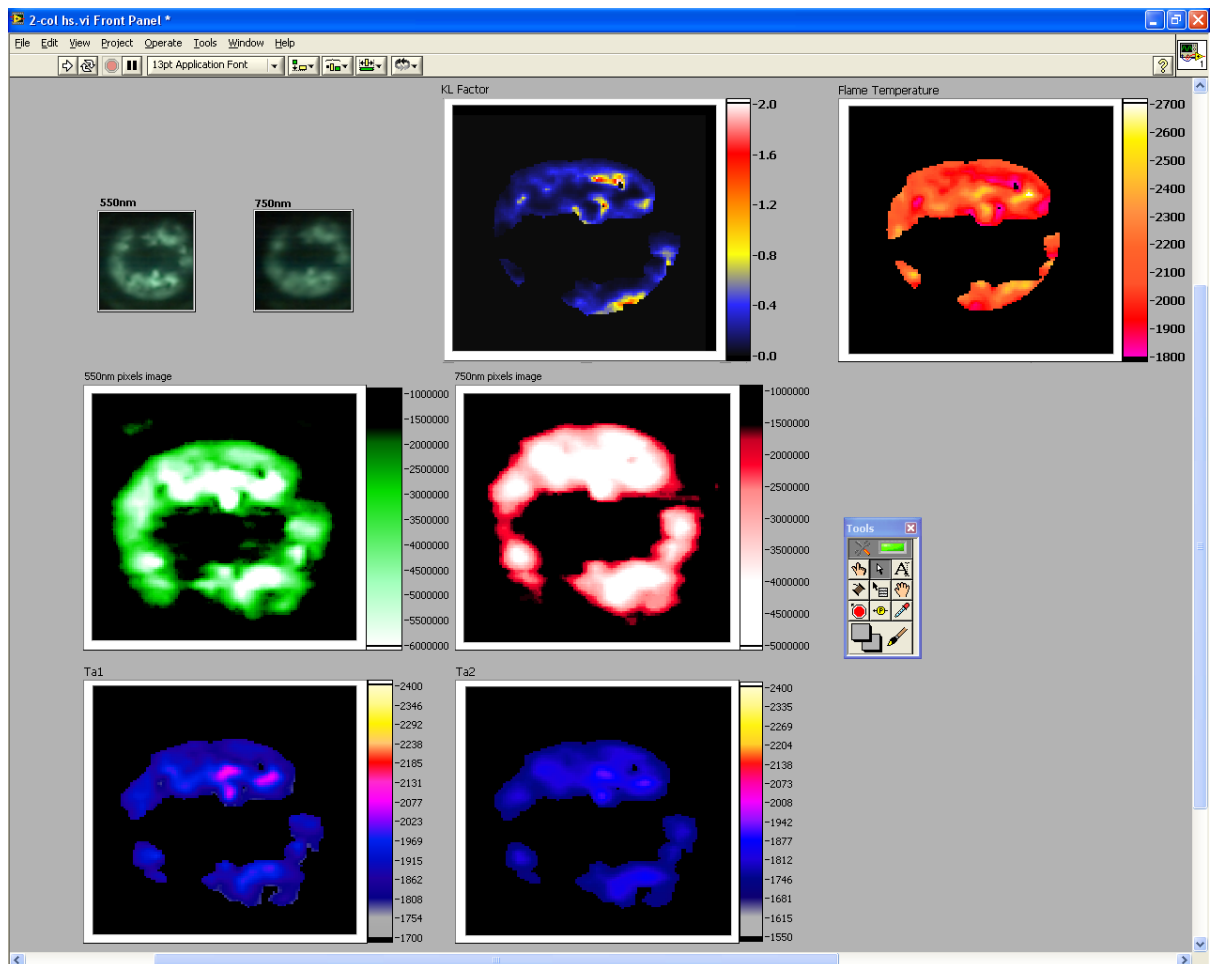


Figure 4.12 Front Panel Two-Colour.vi

4.3.6.3 Contour map with MATLAB

The 2D matrices of flame temperature and soot concentration were exported to MATLAB and display them as contour maps showing the isolines. Figure 4.13 shows an example of one frame after being displayed by MATLAB.

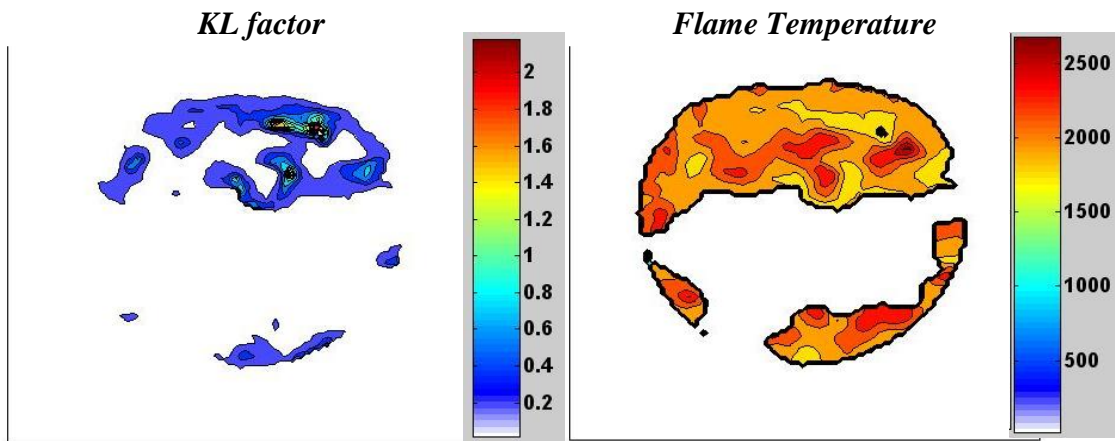


Figure 4.13 Flame Temperature and KL factor Colour maps from MATLAB

The last step for this technique was to put all the frames together in order to create two movies for the flame temperature and the soot concentration.

4.4 Summary

This chapter describes the two-colour method as applied in this project. It presents the theory of the technique and the procedure for the capture of the radiance emitted by the soot particles during combustion and their subsequent conversion into flame temperature and soot concentration. It also describes the implementation of this technique for the use of a high speed camera to obtain cyclic resolved in-cylinder soot and combustion temperature measurements in a single cylinder optical engine.

Chapter 5 Split Injection Studies for Diesel Fuel

5.1 Introduction

This chapter details the investigation carried out for split injection using base diesel as fuel. The following sections first present the different split injection strategies and different injection timings per strategy. The effect of split injection strategies on mixture formation, combustion and heat release rate, as well as exhaust emissions, are then analysed by means of in-cylinder pressure measurements and high speed optical techniques.

For the strategies analysed, cylinder pressure data was recorded from which heat release rate was calculated. Emissions and soot tests were also carried out to assess the effect on performance and emissions of different injection strategies. Based on these results, optical techniques, including high speed imaging and two-colour method, were applied to selected strategies in order to gain a better understanding of the combustion characteristics. The two-colour method has been extended by the author so that it would work with a high speed intensified video camera, from which the time history of flame temperature and soot concentration (KL factor) distributions could be obtained for several consecutive cycles.

5.2 Test Conditions

The initial tests carried out in this study were part of an EU funded project, New Integrated Combustion System for future Passenger Cars Engines (NICE project). Thus different split injection strategies were investigated at a part load operating condition at 2000rpm specified by the sub-project co-ordinator, Renault. It is worthwhile to note that such an engine speed is higher than those reported for most other optical engines. In addition, the boost pressure and intake air temperature were controlled to achieve the same in-cylinder conditions (compression pressure and temperature of 33 bar and 715 K) and ignition delay (ID=16 CA) in the single cylinder optical engine as the multi-cylinder engine at Renault.

The test conditions for this study are detailed in Table 5.1

Table 5.1 Test Conditions

| Test Conditions | |
|------------------------|--|
| Engine Speed | 2000 rpm |
| Intake Air | 140°C |
| | 0.5 bar boost |
| EGR | 60% (N ₂) |
| Fuel | Commercially Available 49.1 CN Diesel |
| Fuelling | 9.25 mm ³ total (70%/30%) |
| Injection duration | 4.5° CA 1 st injection |
| | 3.8° CA 2 nd injection |
| Air flow rate | 323 l/min |
| Nitrogen flow rate | 200 l/min |
| Load | ≈27 % of full load |
| Injection Pressure | 800 bar, 1200 bar |
| Piston Bowl | Glass (optical techniques) Metal (emissions) |

As seen in Chapter 3, the glass piston bowl was flat so that optical techniques could be applied without having optical aberrations. When measuring the exhaust emissions, a metal piston was used in order to preserve the glass window. A shallow bowl was machined in the crown to give comparable effective compression ratio. This implies that for this study the in-cylinder flow was different than in current diesel engines where the bowl shape is used in order to enhance the mixing process. Consequently the mixing process, combustion characteristics and exhaust emissions were affected by this.

During the experiments, the intake air was boosted by 0.5bar and heated to 140°C so that the in-cylinder temperature at the time of injection (715 K) was similar to that measured in the multi-cylinder engine at Renault and IFP.

When measuring the exhaust emissions, the flat piston window was replaced with a metal blank of same dimensions in order to achieve prolonged engine operation. However, due to better sealing of the metal blank, the in-cylinder pressure and temperature were higher. The intake air was not boosted but still heated to 140°C so that the ignition delay was matched to the multi-cylinder engine.

The total amount of fuel injected was set at 9.25mm³. The percentage of EGR was set to 60% for all the experiments by replacing part of the air with Nitrogen gas as detailed in Chapter 3.

Injection pressure was varied and the experiments were carried out for 800bar and 1200 bar (See Table 3.2 for details). The use of 1200 bar was limited by the current FIE with common rail installed in the Hydra engine. The 800 bar injection pressure was used in order to study the effect of injection pressure on the mixing process compared to the 1200 bar. Although the maximum injection pressure is lower than the state-of-art fuel injection systems used in the most recent diesel engines, the injection pressure used are similar to those used for part-load operations as the case of the current studies.

5.3 Injection Strategies

Five different dwell-angle split injection strategies were investigated for each injection pressure. In addition, five injection timings were investigated for each strategy forming the base matrix of this study. Table 5.2 shows the matrix of these experiments.

Table 5.2 Experimental Matrix for Diesel Fuel

| 1200 bar Injection Pressure | | | | 800 bar Injection Pressure | | | |
|-----------------------------|------------------|---------------------------|---------------------|----------------------------|------------------|---------------------------|---------------------|
| Test Number | Dwell Angle (CA) | Split Injection (CA BTDC) | | Test Number | Dwell Angle (CA) | Split Injection (CA BTDC) | |
| | | 1 st SOI | 2 nd SOI | | | 1 st SOI | 2 nd SOI |
| A | 8 | 19 | 11 | A | 8 | 19 | 11 |
| | | 17 | 9 | | | 17 | 9 |
| | | 15 | 7 | | | 15 | 7 |
| | | 13 | 5 | | | 13 | 5 |
| | | 11 | 3 | | | 11 | 3 |
| B | 10 | 19 | 9 | B | 10 | 19 | 9 |
| | | 17 | 7 | | | 17 | 7 |
| | | 15 | 5 | | | 15 | 5 |
| | | 13 | 3 | | | 13 | 3 |
| | | 11 | 1 | | | 11 | 1 |
| C | 12 | 21 | 9 | C | 12 | 21 | 9 |
| | | 19 | 7 | | | 19 | 7 |
| | | 17 | 5 | | | 17 | 5 |
| | | 15 | 3 | | | 15 | 3 |
| | | 13 | 1 | | | 13 | 1 |
| D | 14 | 23 | 9 | D | 14 | 23 | 9 |
| | | 21 | 7 | | | 21 | 7 |
| | | 19 | 5 | | | 19 | 5 |
| | | 17 | 3 | | | 17 | 3 |
| | | 15 | 1 | | | 15 | 1 |
| E | 16 | 25 | 9 | E | 16 | 25 | 9 |
| | | 23 | 7 | | | 23 | 7 |
| | | 21 | 5 | | | 21 | 5 |
| | | 19 | 3 | | | 19 | 3 |
| | | 17 | 1 | | | 17 | 1 |

As part of the NICE project, split injection investigation at 1200 bar with high levels of EGR was investigated for a dwell angle of 12°. In order to study the effect of the dwell angle, four more strategies were investigated, two by decreasing the dwell angle and two by increasing it. In order to reduce NOx emission injection is usually retarded and therefore the combustion pressure and temperature are decreased. Based on this concept, five injection timings were chosen where the second injection took place close to TDC. Finally, these experiments were repeated at 800 bar injection pressure in order to assess the effects of injection pressure.

5.4 Strategies at Injection Pressure 1200 bar

5.4.1 Strategy A

5.4.1.1 Effects of Injection Timing on Performance and Emissions

Table 5.3 shows the Injection timings used in strategy A and the corresponding combustion characteristics and emissions. Concerning engine performance, the IMEP values for each experiment are shown. Combustion characteristics include Ignition Delay (ID) as the time between start of injection (SOI) and start of combustion (SOC) and combustion duration (given by the heat release rate as the time until 90% of fuel is burnt).

Table 5.3 Injection, Combustion and Emissions Characteristics of Strategy A, 1200 bar

| Strategy A | | | | | | | | | | | |
|--------------------|--------------------|--------------------------------------|---|-------------------|-------------------|-------------------------------|-------------------------------|----------------------|------------------|------------------|-------------------|
| Dwell Angle | Test Number | SOI (1st injection) (CA BTDC) | SOI (2nd injection) (CA BTDC) | IMEP (bar) | Combustion | | | | EMISSIONS | | |
| | | | | | SOC | 1st ID (CA) | 2nd ID (CA) | Duration (CA) | HC (ppm) | NOx (ppm) | Soot (FSN) |
| 8 | A1 | 19 | 11 | 1.6 | 2.6 BTDC | 16.4 | 8.4 | 24.8 | 703 | 60 | 1.37 |
| | A2 | 17 | 9 | 2.2 | 0.6 BTDC | 16.4 | 8.4 | 25.4 | 706 | 58.5 | 2.15 |
| | A3 | 15 | 7 | 2.1 | TDC | 15 | 7 | 26.0 | 707 | 51 | 2.25 |
| | A4 | 13 | 5 | 2.2 | 1.2 ATDC | 14.2 | 6.2 | 25.8 | 798 | 48 | 3.05 |
| | A5 | 11 | 3 | 2.7 | 3.6 ATDC | 14.6 | 6.4 | 25.6 | 740 | 43 | 2.67 |

Figure 5.1 shows the cylinder pressure averaged over 20 cycles for strategy A. For the first set A1, the cylinder pressure follows the line of the motoring pressure until 5.4° CA BTDC, when it starts to increase steadily over the motoring pressure until 2.6° BTDC. It then experiences a rapid increase, reaching a peak value of 42.5 bar at 6.4° ATDC, from this point the cylinder pressure drops rapidly over the expansion stroke giving an IMEP value of 1.6 bar. In the case of A2 experiment, the cylinder pressure follows the motoring pressure line until 3.4° CA BTDC, at this point there is a first increase of pressure until 0.6° BTDC when it experiences a rapid rise. The peak cylinder pressure is reached at 10.4° ATDC, 4° CA after A1 was peaked, giving a value of 41.5 bar. The peak cylinder pressure seems to be lower than for A1 as the premixed combustion occurs while the piston is descending after TDC. After the peak value, the cylinder pressure remains higher than for A1 therefore its IMEP value of 2.2 bar is higher than for A1. As injection timing is retarded the change in the slope of the pressure is delayed, thus for A3 it occurs right before TDC and for A4 at 1° CA ATDC. After the first change of the slope there is a quick increase of the pressure which takes place at 5.2° and 7.6° CA ATDC, respectively, however the peak values are much lower than the first two strategies at values of 38 and 36 bar, respectively, which represent 10 and 15 % less than the first strategy. After reaching their peaks the firing pressures equalize for the rest of the expansion stroke, having higher values than the strategy A1. The final values of IMEP for A3 and A4 are 2.1 and 2.2 bar respectively. Similar to A2, A3 and A4 have higher pressure values over the expansion stroke; this is the reason why their IMEP's are higher than A1. Strategy A5 follows the motoring pressure beyond TDC, it is at 3.4° CA ATDC when a first rise in the slope occurs, and it goes higher than the motoring pressure up to 10.6° CA ATDC, when there is a sharp increase of the cylinder pressure due to the premixed combustion. The cylinder pressure peaks at 17.2° CA ATDC with a value of slightly lower than 34 bar, very close to the motoring pressure of 33 bar. After reaching the peak, the decrease in pressure occurs at a slightly faster rate than the others over the expansion stroke. The IMEP value for the A5 experiment is 2.7 bar, which is an increase of almost 70% with respect to A1.

Figure 5.2 illustrates the heat release rates for the five experiments in strategy A. For A1 the first noticeable event occurs at 14.5° BTDC, where there is a decrease in the heat release rate. This is due to the cooling effect right after the first injection takes place and it lasts until 11.4° CA BTDC. After this point, just before the start of the second injection, there is a slight increase in the heat release rate, this is likely to be due to the

cool flames reactions. This rise is interrupted at 6.8° CA BTDC when there is a second, but minor decrease caused by the cooling effect of the second injection. At 4° CA BTDC there is a rapid increase of the heat release rate, due to the premixed combustion, where fuel that has mixed with the air burns rapidly within a high temperature combustion; this occurs until 8.2° CA ATDC. From this point onwards, the mixing-controlled or diffusion combustion starts; this combustion phase is controlled by the rate of the fuel and air mixing. It can be seen that the heat release rate reaches a second peak at 11° CA ATDC, this one much lower than the peak of the premixed combustion. After this second peak, the heat release rate decreases gradually, the diffusion combustion ends at around 18° CA ATDC. After this point, the late combustion phase starts where there is still some heat released that is likely to come from a fraction of the fuel or partially oxidised hydrocarbons and CO that at this stage have not been burnt yet or from some remaining energy present in the soot.

The heat release rate for A2 shows similar trend to the line of A1, as the first injection takes place 2 crank angles after A1; the first decrease of the heat release occurs at 12.4° CA BTDC as a consequence of the cooling effect from the first injection. At 8.4° CA BTDC there is a rise in the heat release rate, probably produced by the cool flame reactions, which peaks at 4° CA BTDC when the cooling effect from the second injection causes a decrease of the heat release until 1.4° CA BTDC. At this point the rapid increase of heat release rate due to the premixed combustion takes place. It reaches a peak at 7.2° CA ATDC, and then it decreases to a value of 11.6° CA ATDC when the premixed combustion phase finishes. Similar to A1, the diffusion combustion phase starts with an increase in the heat release rate showing a peak at 14.2° CA ATDC. After the peak, it slowly decreases. The diffusion combustion finishes at approximately 21° CA ATDC, when the late combustion phase starts. This strategy shows the combustion slightly longer than for A1.

Experiments A3 and A4 follow similar pattern in their heat release rates. There is no apparent cooling effect after the first injection; however it can be seen that at approximately 4° CA after the end of the first injection, at 6.4° CA BTDC for A3 and 4.6° CA BTDC for A4, first cool flame reactions take place, which increases the heat release peaks at 2.4° CA BTDC and 0.8° CA BTDC, respectively. After this peak, both strategies show a very slow decrease almost like a plateau which is a consequence of the cooling effect after the second injection. At TDC for A3 and 1.4° CA ATDC for A4, there is a rapid increase of the heat release rate, as premixed combustion starts. The

peak heat release rate is reached at 8.4° CA ATDC and 9.8° CA ATDC, respectively. It seems that after this point, and while still in the premixed phase, mixing-controlled combustion reactions start taking place and the two phases appear combined in the heat release rate, in contrast to the first two strategies where the premixed and diffusion phases were easily identified. The diffusion combustion finishes at about 22° CA ATDC for A3 and 24° CA ATDC for A4. This shows as well that the combustion duration for both strategies is nearly the same.

Experiment A5's injection timing is 11° CA and 3° CA BTDC; the heat release rate shows a slow increase from 12° CA BTDC up to 2.2° CA BTDC, this means that no cooling effect is noticeable after the first injection. At 2.2° CA BTDC there is a small, but rapid increase in the heat release until 1.4° CA ATDC, when the cooling effect of the second injection provokes a decrease until 3.6° CA ATDC, when the combustion starts. Initially the rise is gradual until 8° CA ATDC, which implies diffusion combustion. From 8° CA ATDC, the rise occurs rapidly, typical from premixed combustion reaching a peak at 13.2° CA ATDC. The decrease in the heat release rate is similar to A3 and A4 where the end of the premixed combustion and diffusion combustion are mixed. In this case, the diffusion combustion appears to be even longer than in the previous cases, although the total combustion duration is about the same. The maximum heat release rate is reached at 2.8° CA ATDC, from that point onwards there is a decrease as the premixed fuel is almost fully burnt. At 7.4° CA ATDC it reaches a nadir, at this point the diffusion combustion starts, fuel that is mixing with the air starts burning producing a lower temperature combustion. In this case the diffusion combustion shows a second peak on the heat release rate at 10.4° CA ATDC.

The first injection timing has the longest ignition delay and more fuel burns in premixed combustion, as injection is retarded, the ignition delay is shorter and less fuel burns in premixed combustion and diffusion combustion is longer. In order to gain a better understanding of strategy A, combustion imaging and the two-colour method measurements were carried out for experiments A1, A3 and A5. By selecting these injection timings the effect of the injection timing will be further explain.

Cylinder Pressure Strategy A

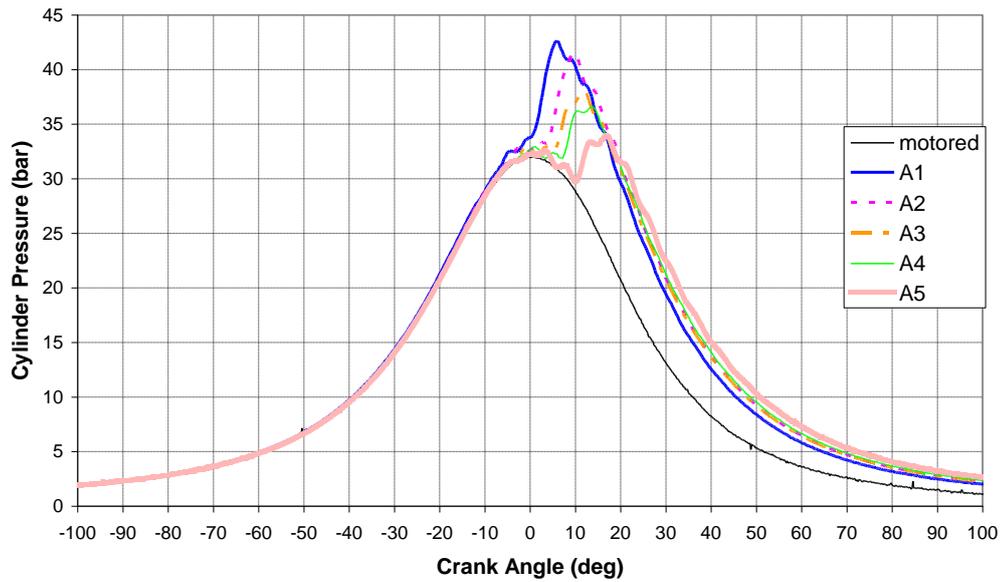


Figure 5.1 Cylinder pressure traces for experiments in Strategy A at 1200 bar

Heat Release Rate Strategy A

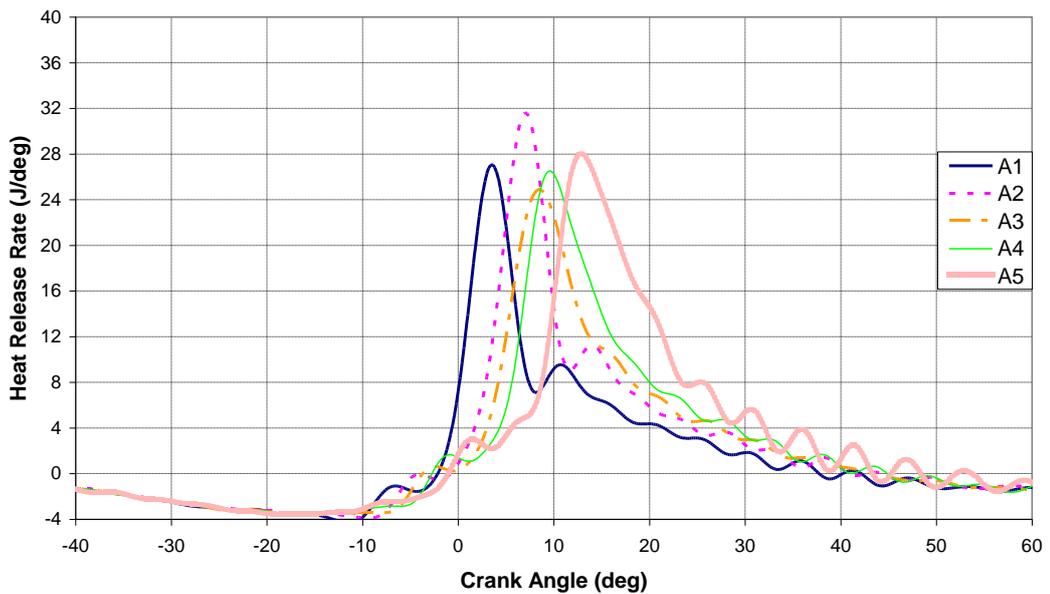


Figure 5.2 Heat release rate curves for experiments in Strategy A at 1200 bar

5.4.1.2 A1 Injection and Combustion Visualization

Figure 5.3 shows the sequence of images from the start of injection to the end of combustion for A1. During the first injection it can be seen in frame 16.2 BTDC that the tip of the fuel spray is almost reaching the piston bowl wall. For the second injection the spray penetration is slightly less due to the higher in-cylinder charge density. At 3.6 BTDC the first flames appear, this corresponds exactly with the heat release rate data. It

can be seen that four ignition sites appear slightly downstream of the spray in the direction of swirl. At TDC combustion has expanded to larger regions, one at the top and the other at the bottom. The colour difference between the combustion regions can be related to the combustion process. For example, the top less luminous combustion indicates a more premixed combustion while at the bottom the high luminosity is caused by the burning of carbon particles which is more typical of diffusion combustion. In the next frames, it can be seen that the combustion regions follow the in-cylinder swirl motion and smaller burning regions turn more luminous due to the soot radiation characteristic of diffusion combustion. Visible frames appear vanishing around 16° CA ATDC showing the end of the diffusion combustion phase.

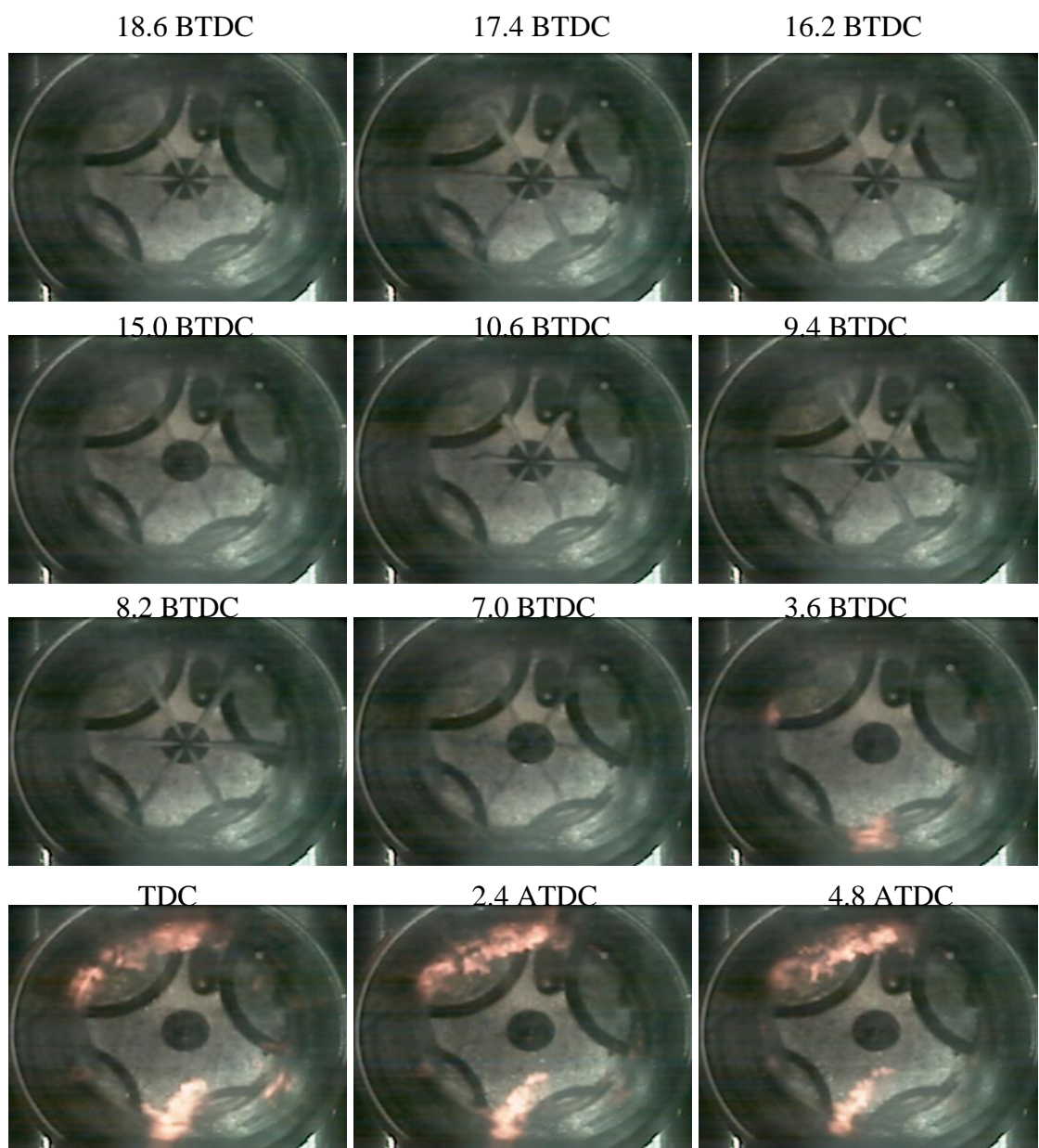


Figure 5.3 Combustion Images Sequence for experiment A1 at 1200 bar



Figure 5.3 Combustion Images Sequence for A1 injection timing at 1200 bar (cont'd)

5.4.1.3 A1 Flame Temperature and Soot Concentration (KL factor) Measurements

Figure 5.4 presents the image sequence for the flame temperature and the soot concentration given by the KL factor for the A1 injection timing. Although the first flames in Fig.5.3 were seen at 3.6° CA BTDC, the first visible two-colour images start to appear around TDC. In the temperature images, it can be seen that there are four main focal points where the flame temperature is high, reaching 2500 K. Looking at the KL factor image at TDC, it can be noticed that soot is produced at this stage but at very low concentrations. This agrees with the combustion images where the premixed combustion could be noticed at TDC. At 1.2° CA ATDC, the flame temperature is higher at more areas, while the soot concentration is very low. This is typical of premixed combustion where higher temperatures are produced and small soot particles form at the leading edge of the flame front. Up to 7.2° CA ATDC, the flame temperature at some specific points remains quite high. During the premixed combustion, NO_x is produced at high temperature regions, therefore it could be expected some NO_x formation in the exhaust emissions. Table 5.3 shows the emissions values for strategy A. NO_x emissions are very low compared to conventional diesel combustion with a single injection. However, experiment A1 indicates a relatively high value with 60 ppm at the exhaust. The next frames show the decrease of the flame temperature and a small increase of the soot formation. For this particular strategy the value of smoke given by FSN was 1.37.

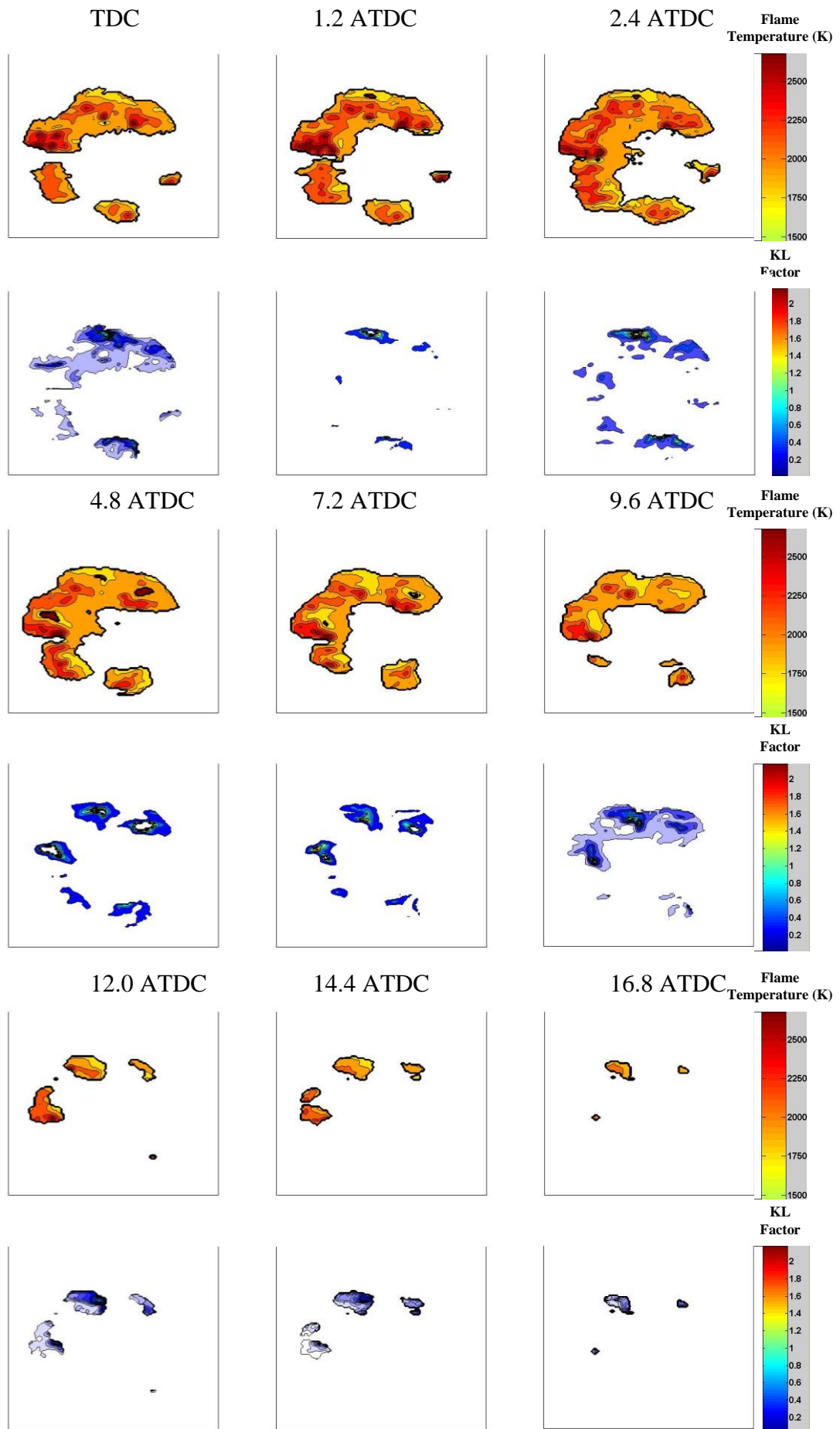


Figure 5.4 Flame Temperature and KL factor images sequence for A1 at 1200 bar

5.4.1.4 A3 Injection and Combustion Visualization

Figure 5.5 shows the injection and combustion imaging for experiment A3. This strategy produced an IMEP 30% higher than A1, with lower NO_x emissions. The injection timings were 15° CA BTDC and 7° CA BTDC. In this case, it is clear that the liquid penetration for the second injection is less than for the first injection (frames 5.6 and 4.4° CA BTDC). The first visible flames appear at TDC in the form of premixed combustion. These ignition spots appear slightly downstream of the spray in the direction of the swirl, and six different spots can be easily identified (compared to four combustion regions in A1). From frame 4.8 ATDC, the luminosity of the flames indicates diffusion combustion with the formation of soot. From frame 13.2° CA ATDC, the flames appear to subside, but are still being uniformly distributed within the cylinder.

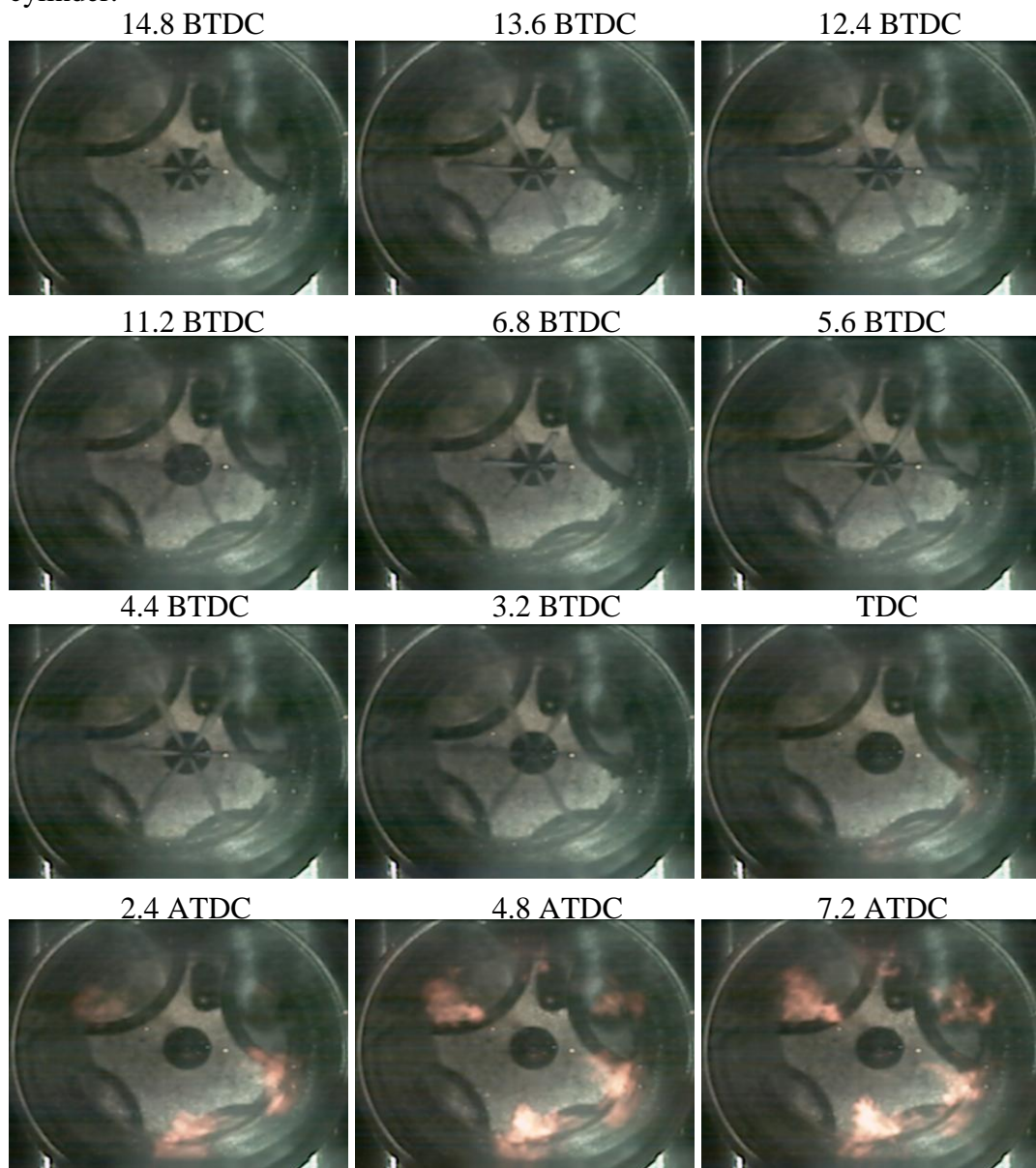


Figure 5.5 Combustion Images Sequence for experiment A3 at 1200 bar



Figure 5.5 Combustion Images Sequence for experiment A3 at 1200 bar (cont'd)

5.4.1.5 A3 Flame Temperature and Soot Concentration (KL factor) Measurements

Figure 5.6 shows the flame temperature and KL factor for A3 injection timing. As seen in the combustion sequence, the first flames spots that appear at TDC have little luminosity. Hence the first frame for flame temperature and KL factor shows a very small flame and the production of soot is very low. From frame 2.4 ATDC, it can be seen that combustion takes place consistently within the cylinder. The main flames have a temperature about 2500 K, but rapidly decrease from 6.0° CA ATDC onwards. The decrease of flame temperature below 2200K would suggest that combustion is taking place out of the NO_x formation temperature region. This strategy had a NO_x emissions value of 50 ppm, which equals to 15% less than strategy A1. The main drawback for this strategy was the soot production as it could be expected from the lower temperature combustion. From the images of KL, it shows that from 4.8° CA ATDC soot is produced evenly inside the cylinder, and from 7.2° CA ATDC when the temperature has dropped the concentration of soot is higher. During the last stages of combustion, the KL factor is still high as the soot oxidation is low due to the lower temperatures. Soot emissions given in FSN can be seen in Table 5.3; strategy A3 has a value of 2.25 FSN which corresponds to an increase of 60% with respect to A1.

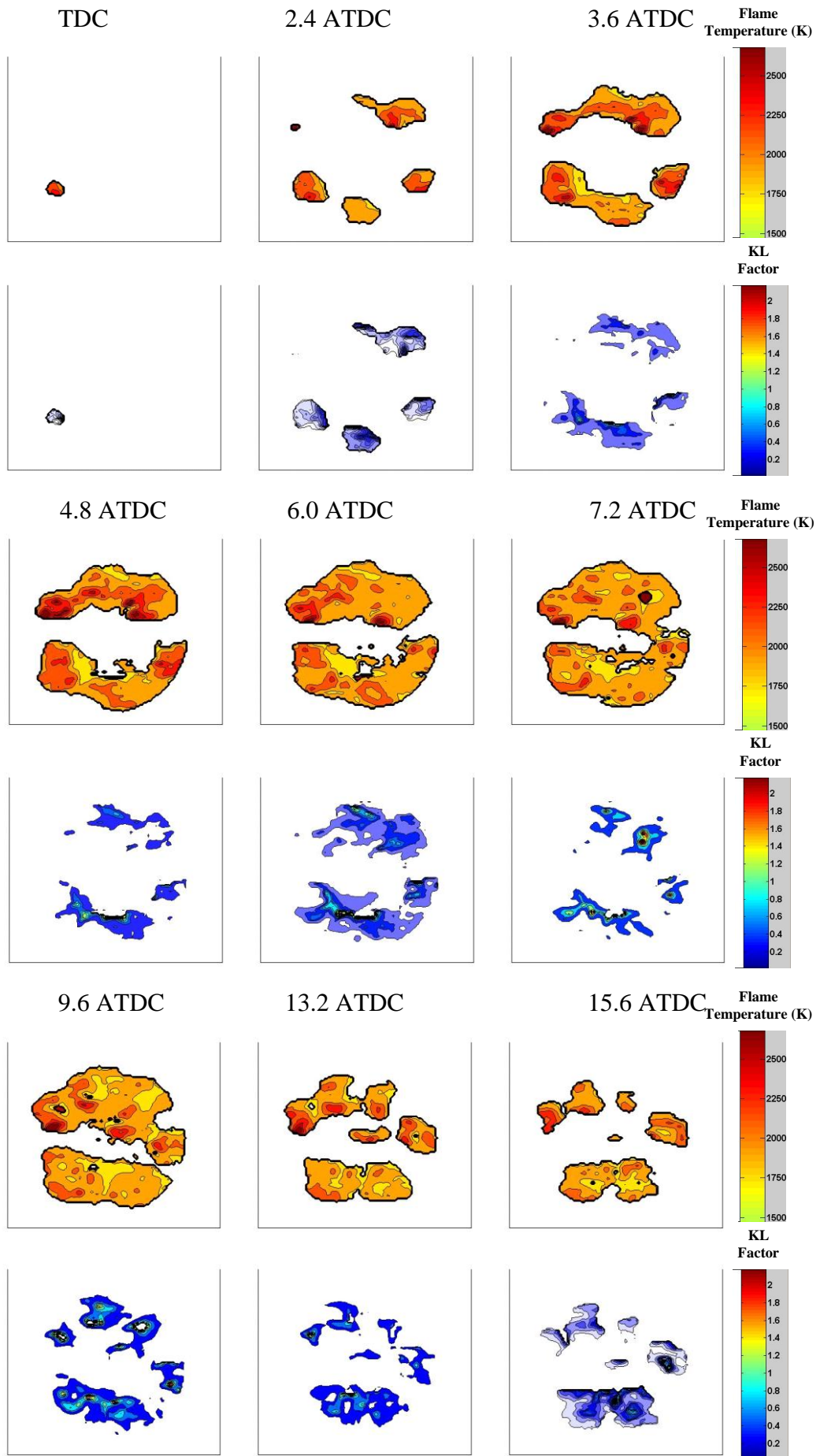


Figure 5.6 Flame Temperature and KL factor images sequence for A3 at 1200 bar

5.4.1.6 A5 Injection and Combustion Visualization

Within the five experiments in strategy A, A5 had the most retarded injection timing. As explained in Section 5.4.1.1 combustion takes place well after TDC, this gives an IMEP value of 2.7 bar, 70% higher than A1. From the heat release rate, the start of combustion is at 3.6° CA ATDC; however from Figure 5.7 the chemiluminescence's image is at 5.6° CA ATDC. Six flame spots appear uniformly distributed following the swirling motion. From frame 8.0° CA ATDC; it can be seen that the six flame spots spreads towards the centre of the cylinder as rich diffusion combustion. The ignition delay for this strategy is 14.6° CA, compared to 15° CA for A3 and 16.4 for A1. As the ignition delay is less, the fuel has less time to mix with the air and richer combustion occurs. From frame 15.6° CA ATDC the diffusion combustion is of low intensity and decreasing, but it fills the entire cylinder.

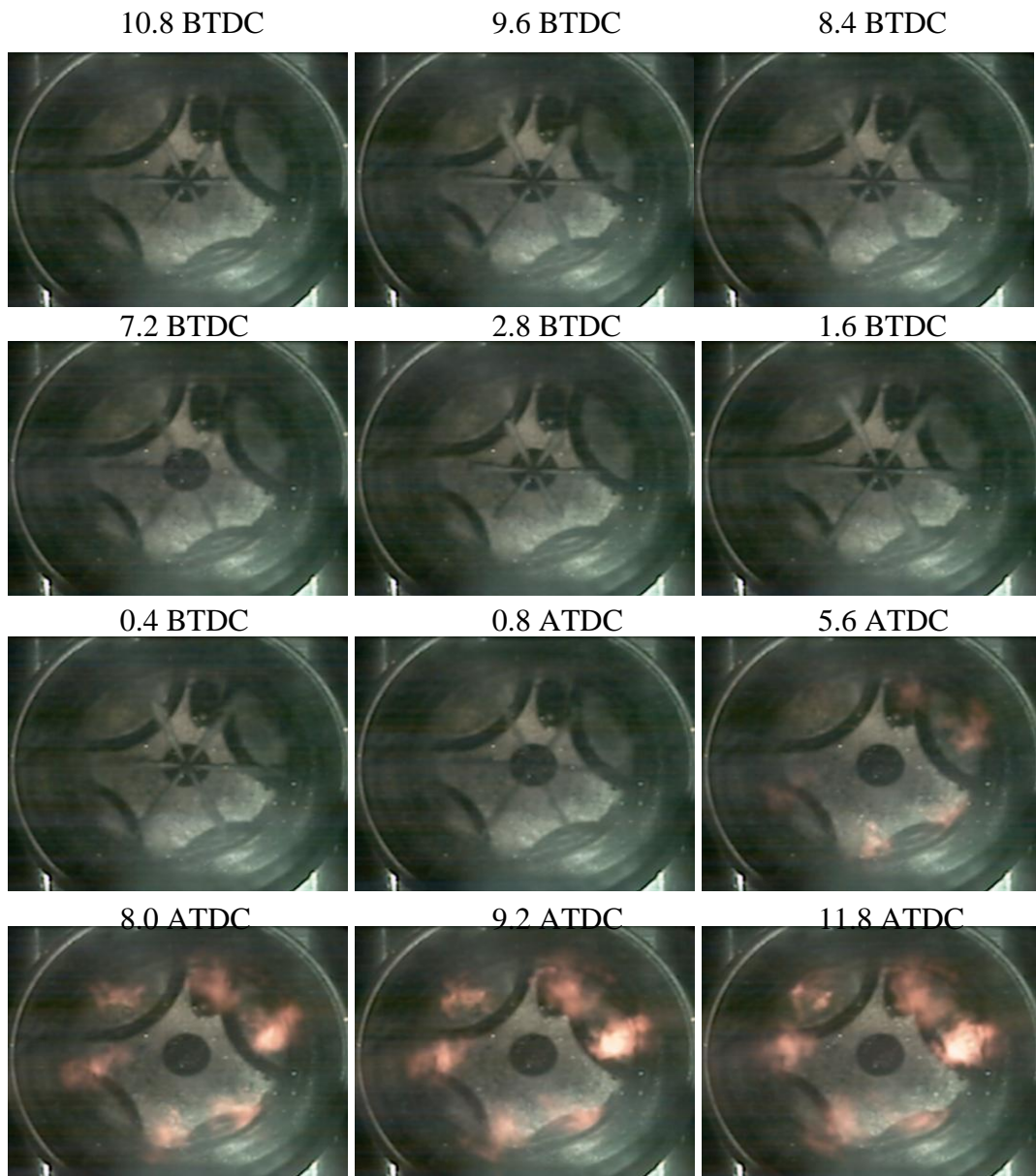


Figure 5.7 Combustion Images Sequence for experiment A5 at 1200 bar

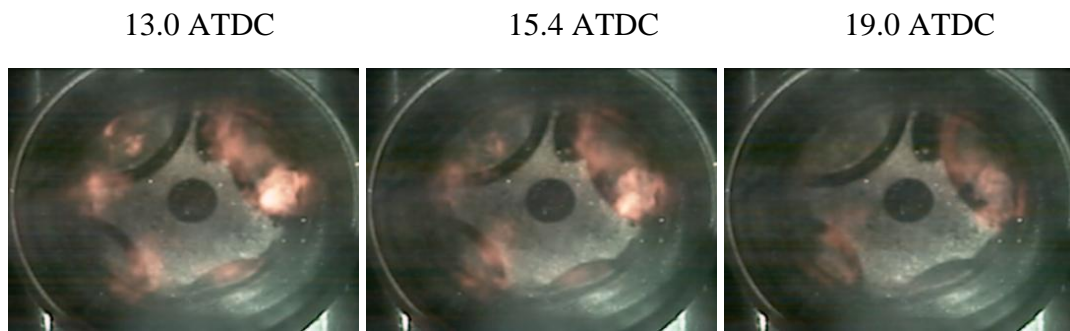


Figure 5.7 Combustion Images Sequence for experiment A5 at 1200 bar (cont'd)

5.4.1.7 A5 Flame Temperature and Soot Concentration (KL factor) Measurements

Figure 5.8 shows the flame temperature and KL factor images sequence for experiment A5. From the first frames (6.8 and 8.0° CA ATDC) it can be seen that the flame temperature is quite well distributed inside the cylinder, surrounding the injection spray. The temperatures shown at this stage are not very high, approximately 2300 K, and from 9.2° CA ATDC onwards clearly lower than this which indicates that combustion takes place out of the temperature region where NO_x is normally formed. Table 5.3 shows that the value of NO_x emissions for this strategy is 43ppm, a reduction of 30% with respect to strategy A1. As it was shown in the combustion images, the flame temperature propagates towards the centre of the cylinder, thus frame 10.4° CA ATDC shows the flame temperature covering almost the whole of the chamber. As a consequence of the shorter ignition delay and lower combustion temperatures, the soot formation is much higher than for the rest of the experiments in strategy A as shown by the soot images from frame 5.6° CA ATDC to frame 10.4° CA ATDC. From frame 11.6° CA ATDC the KL factor appears even higher as soot oxidation rate reduces due to the lower temperatures. The final value of smoke emissions for this strategy from Table 5.3 is 2.67 (FSN) which represents an increase of 100% with respect to A1.

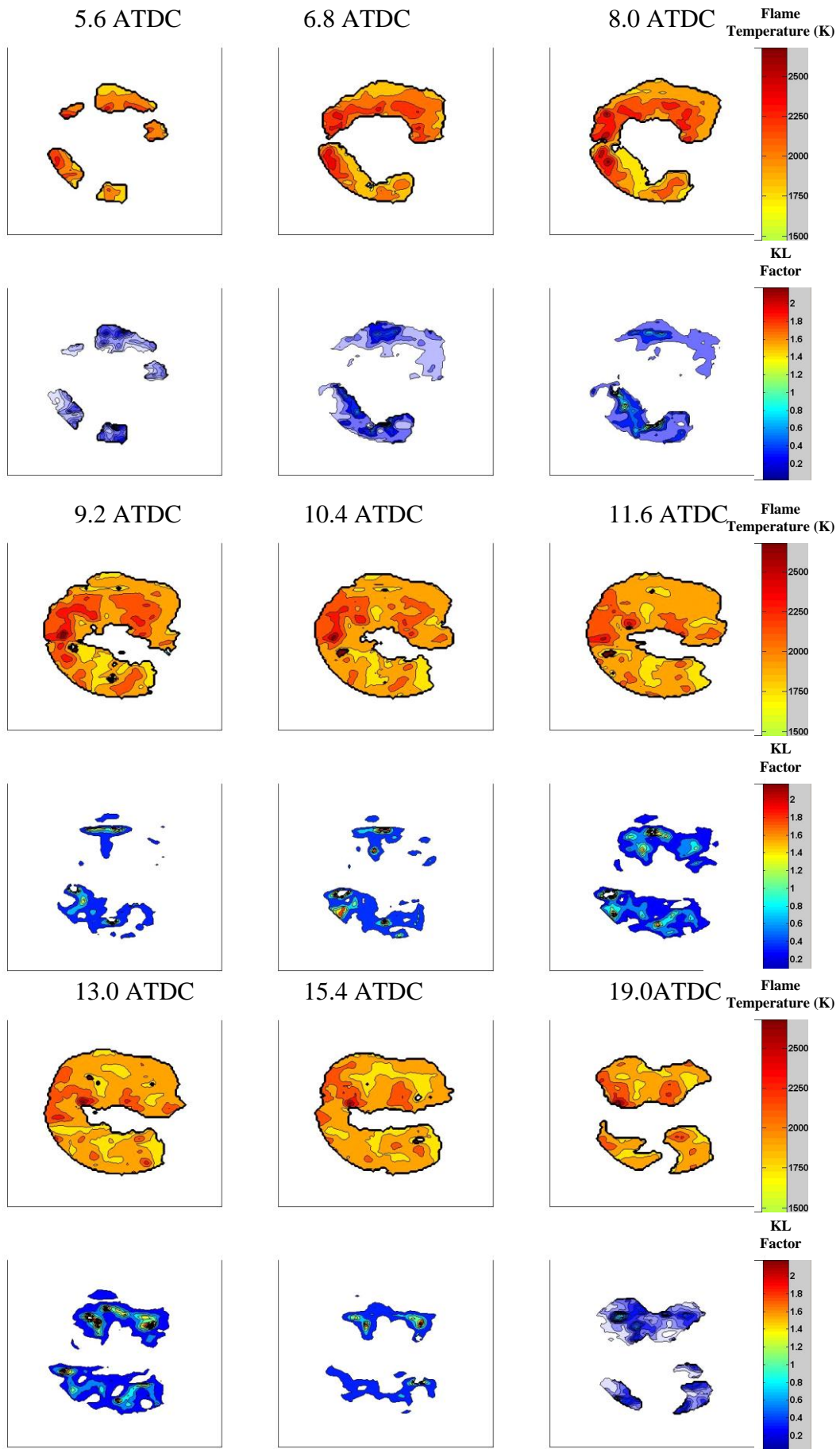


Figure 5.8 Flame Temperature and KL factor images sequence for A5 at 1200 bar

5.4.2 Strategy B

The next strategy in this study had an increase of 2° CA with respect to strategy A.

5.4.2.1 Effects of Injection Timing on Performance and Emissions

Table 5.4 summarises the injection and combustion characteristics for five different injection timings for the 10° CA dwell angle strategy. The performance and emissions of the strategies are also included.

.

Table 5.4 Injection, Combustion and Emissions Characteristics of Strategy B, 1200 bar

| Strategy B | | | | | | | | | | | |
|--------------------|--------------------|---|---|-------------------|-------------------|-------------------------------|-------------------------------|----------------------|------------------|------------------|-------------------|
| Dwell Angle | Test Number | SOI (1st injection) (CA BTDC) | SOI (2nd injection) (CA BTDC) | IMEP (bar) | Combustion | | | | EMISSIONS | | |
| | | | | | SOC | 1st ID (CA) | 2nd ID (CA) | Duration (CA) | HC (ppm) | NOx (ppm) | Soot (FSN) |
| 10 | B1 | 19 | 9 | 2.0 | 3.0 BTDC | 16 | 6 | 28.4 | 340 | 46 | 0.13 |
| | B2 | 17 | 7 | 2.5 | 1.4 BTDC | 15.6 | 5.6 | 28.2 | 310 | 45 | 0.42 |
| | B3 | 15 | 5 | 2.3 | 0.2 BTDC | 14.8 | 4.8 | 28.2 | 298 | 41 | 0.47 |
| | B4 | 13 | 3 | 1.9 | 2.4 ATDC | 15.4 | 5.4 | 26.0 | 320 | 36 | 1.05 |
| | B5 | 11 | 1 | 2.1 | 3.8 ATDC | 14.8 | 4.8 | 25.6 | 360 | 36 | 1.35 |

Figure 5.9 shows the cylinder pressure for strategy B; B1 follows the line of motoring pressure until 15° CA BTDC, at this point the increase of pressure is higher than for the motoring pressure. It follows this trend until 2.8° CA BTDC when it experiments a rapid rise following the start of premixed combustion. It reaches a cylinder peak pressure value of 43.4 bar at 5.2° CA ATDC. This value is slightly higher compared to strategy A1. The pressure drops quickly after the peak; however, it stays much higher than the motoring pressure. As a consequence the IMEP is 2.0 bar, 25% higher than for A1. Experiment B2 follows the trend of B1, going along with the motoring pressure until 15° CA BTDC when it starts increasing slightly faster until 1.4° CA BTDC. At this point, there is a very steep increase of the pressure reaching a maximum of 46 bar at 6.8° CA ATDC. It experiences a drop similar to B1 with slightly higher values of pressure during the expansion stroke. The IMEP value for B2 is 2.5, 25% higher than for B1. As in the previous strategies, B3 goes along the motoring pressure until 10° CA BTDC when it starts increasing at slightly higher rate than the motoring pressure. It follows this trend until 0.2° CA ATDC when a quick increase of pressure occurs due to the main combustion. The maximum is reached at 8.8° CA ATDC with a value of 42 bar, lower than the previous strategies. During the expansion stroke, the pressure values decrease to a value between B2 and B1 results, therefore the final IMEP value given by this strategy is between B2 and B1 at 2.3 bar. The firing pressure for experiments B4 and B5 have similar trends as they both follow the motoring pressure until 10° CA BTDC; from that point onwards, they have higher pressure and they go after TDC. There is a first peak at 2.4° CA ATDC for B4 and at 4° CA ATDC for B5, the pressure decreases over the next several crank angles until 5° CA ATDC and 7.4° CA ATDC, respectively, when the rapid pressure rise occurs. The second peak and maximum value of pressure is reached at 12 and 14° CA ATDC, respectively. The pressure drop occurs at a lower value than for B1 during the first part of the expansion stroke. However, after 30° CA ATDC approximately the pressure values are higher than for B1, although lower than B2. The IMEP values for these two experiments are 1.9 and 2.1, respectively. These values are 16 and 24% lower than B2, which has the highest IMEP values of 2.5 bar amongst all the experiments in strategy B.

In general, experiments in strategy B show better IMEP values than those in strategy A, probably due to the longer dwell angle. As the dwell angle increases, better fuel air mixing occurs and hence the improved IMEP.

Figure 5.10 shows the heat release rate for B1 to B5. The heat release rates for all strategies are very similar at the beginning of compression stroke and they start differing from each other after the first injection takes place. Accordingly B1 experiences a slight drop of the heat release at 14° CA BTDC, which is approximately when the first injection has finished. This lasts for only 3° CA when it starts increasing probably due to the pre-combustion reactions. These reactions are stopped at 5.2° CA BTDC exactly after the second injection finishes due to its cooling effect. At 3° CA BTDC there is a rapid and very steep rise of the heat release rate, as combustion takes place. This sharp increase is provoked by the burning of the fuel that has already mixed with the air inside the cylinder, producing rapid and high temperature combustion. The peak heat release is achieved at 3° CA ATDC. There is then a steep decrease typical of the end of premixed combustion until 7.8° CA ATDC; after this point it is only diffusion combustion that takes place. In the case of B1 a second peak is reached at 10.8° CA ATDC, after this point there is a gradual reduction of the heat release rate as it goes into the expansion stroke. The end of combustion is considered to happen at 25.4° CA ATDC, which gives a combustion duration of 28.4° CA.

Comparing the heat release rate of experiments A1 and B1, it can be seen that although both present very similar curves, the peak heat release rate of A1 is higher than for B1. This would indicate higher combustion temperatures and therefore higher NO_x emissions for A1. Another difference is the combustion duration, since the dwell angle is longer, the mixing for B1 is longer and therefore improved combustion is achieved. Looking at the unburned hydrocarbons emissions from Table 5.3 and Table 5.4, it can be seen that B1 gives 340 ppm which is 50% less than that in A1 due to the improved fuel/air mixing providing a more complete combustion.

The heat release rate for B2 shows no apparent cooling effect after the first injection. However, first combustion reactions from the first injection occur at 8.4° CA BTDC. As the second injection takes place at 7° CA BTDC, its cooling effect stops the pre-combustion reactions at 3.6° CA BTDC and it continues reducing the heat release rate until 1.6° CA BTDC. At this point, the sharp increase of heat release rate occurs due to the premixed combustion phase. The maximum heat release rate is reached at 5° CA ATDC, with a value of $35 \text{ J}/^\circ \text{ CA}$ which is the highest of all 5 experiments in strategy B. Following the peak, there is a rapid decrease of the heat release corresponding to the end of the premixed combustion. The diffusion combustion provokes another rise of the heat release achieving a second peak at 12.4° CA ATDC which is much lower than the

first peak belonging to the premixed combustion. Compared to B1, B2 follows the same trend, however a much higher peak is achieved in the premixed combustion; this could be due to the optimum timing for this split injection at 2000 rpm and the lack of the cooling effect after the first injection.

Similar to B2, B3 shows no cooling effect after the first injection and the pre-combustion reactions provoke a rise in the heat release rate at 6.6° CA BTDC lasting until 2.2° CA BTDC, when the cooling effect of the second injection reduces the heat release until 0.2° CA BTDC. At this moment, the premixed combustion causes the rapid increase in the heat release rate achieving a maximum at 6.8° CA ATDC. The decrease of the heat release rate occurs more gradually than for strategies B1 and B2, this is due to the diffusion combustion that has already started. Different from B1 and B2, the early stages of the diffusion combustion appear more like a plateau before it starts decreasing slowly.

Similar to the cylinder pressure data, the heat release rates for B4 and B5 are very similar. After the start of the first injection, there is a gradual increase of the heat release rate. A few crank angles after the end of the first injection and when some mixing has occurred, at 4° CA BTDC and 2° CA BTDC respectively, the increase is steeper. The cooling effect of the second injection stops this rise and provokes a decrease in the heat release rate. During this time, the fuel is mixing with air and gets to ignite starting combustion at 2.4° CA ATDC for strategy B4 and 3.8° CA ATDC for strategy B5. The curve of the heat release rate shows a more diffusion controlled combustion in these two cases, as combustion starts well after TDC. At this time, combustion temperatures are expected to be lower and therefore NO_x emissions as well compared to the previous strategies.

Looking at the data from strategies A and B, it can be seen that strategy B, having greater dwell angle, has better IMEP and also lower uHC emissions. Fuel/air mixing is improved and combustion duration is longer, having more time to burn more fuel. Another characteristic that can be noted from Tables 5.3 and 5.4 is that strategy B has also lower soot emissions. It is probable that the longer dwell time produces a much leaner combustion as there is more time for mixing and that is why less soot is produced.

The combustion characteristics of B2 and B5 will be further discussed in the following sections as examples to get a better understanding of strategy B.

Cylinder Pressure Strategy B

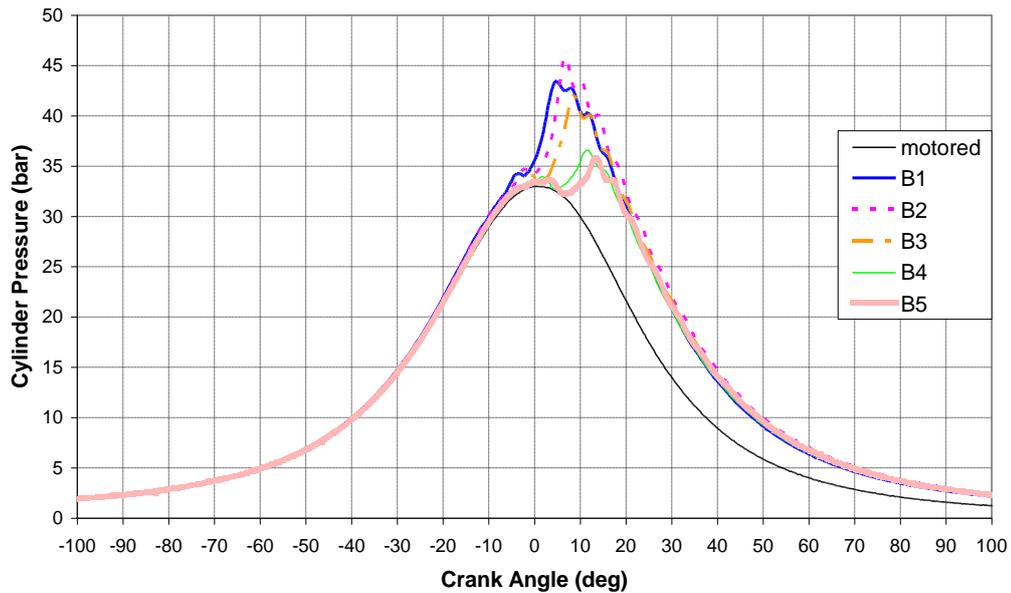


Figure 5.9 Cylinder pressure traces for experiments in Strategy B at 1200 bar

Heat Release Rate Strategy B

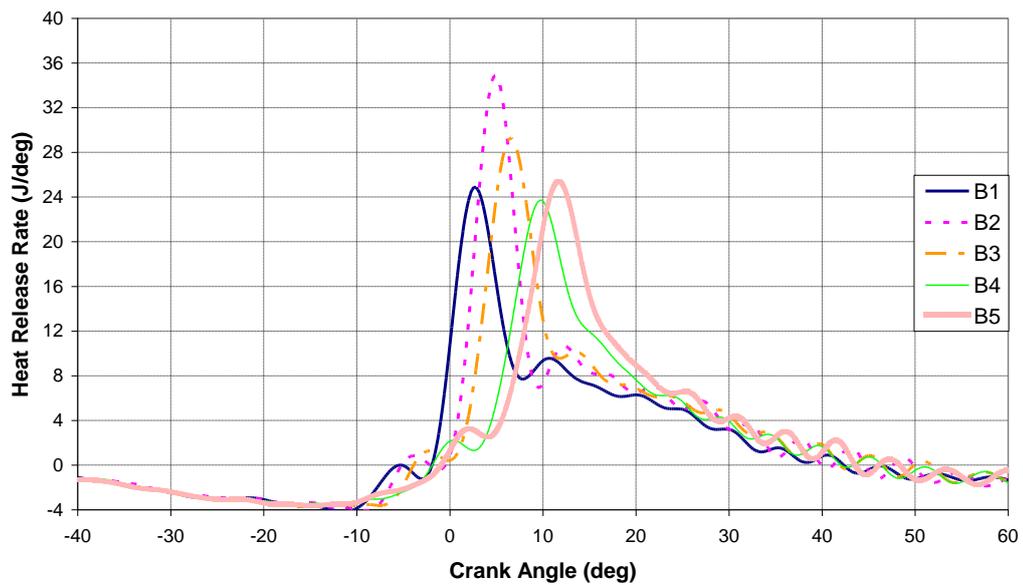


Figure 5.10 Heat release rate curves for experiments in Strategy B at 1200 bar

5.4.2.2 B2 Injection and Combustion Visualization

Figure 5.11 shows the combustion images sequence for the B2 injection timing. The start of injection occurs at 17° CA BTDC and the first frame in which the injection can be seen is at 16.6° CA BTDC. The second injection follows the same pattern as the first one, with the spray penetrations being similar in both cases. At the end of the second injection at 3.2° CA BTDC, the first chemiluminescence flames appear. When it reaches TDC, it can be seen that flames are occurring close to the cylinder walls and occupying almost the complete circumference of the cylinder. This shows that, as the dwell angle

increases from strategy A, the mixing improves and therefore there is more fuel already mixed with the air and ready to burn. The frame at 3.6° CA ATDC shows the combustion filling up a big part of the cylinder and always close to the cylinder walls; this corresponds with the peak of the heat release rate and the peak temperatures of premixed combustion. From the 6° CA ATDC until the end of combustion, it can be seen that the combustion area is reduced due to the diffusion combustion, as the rest of the fuel is mixing before burning takes place. Although combustion is present in less area, the luminosity is still high which is characteristic of diffusion combustion where soot is formed that emits radiation. This image sequence shows a more complete combustion hence the lower uHC emissions compared to the experiments in strategy A, as mentioned before.

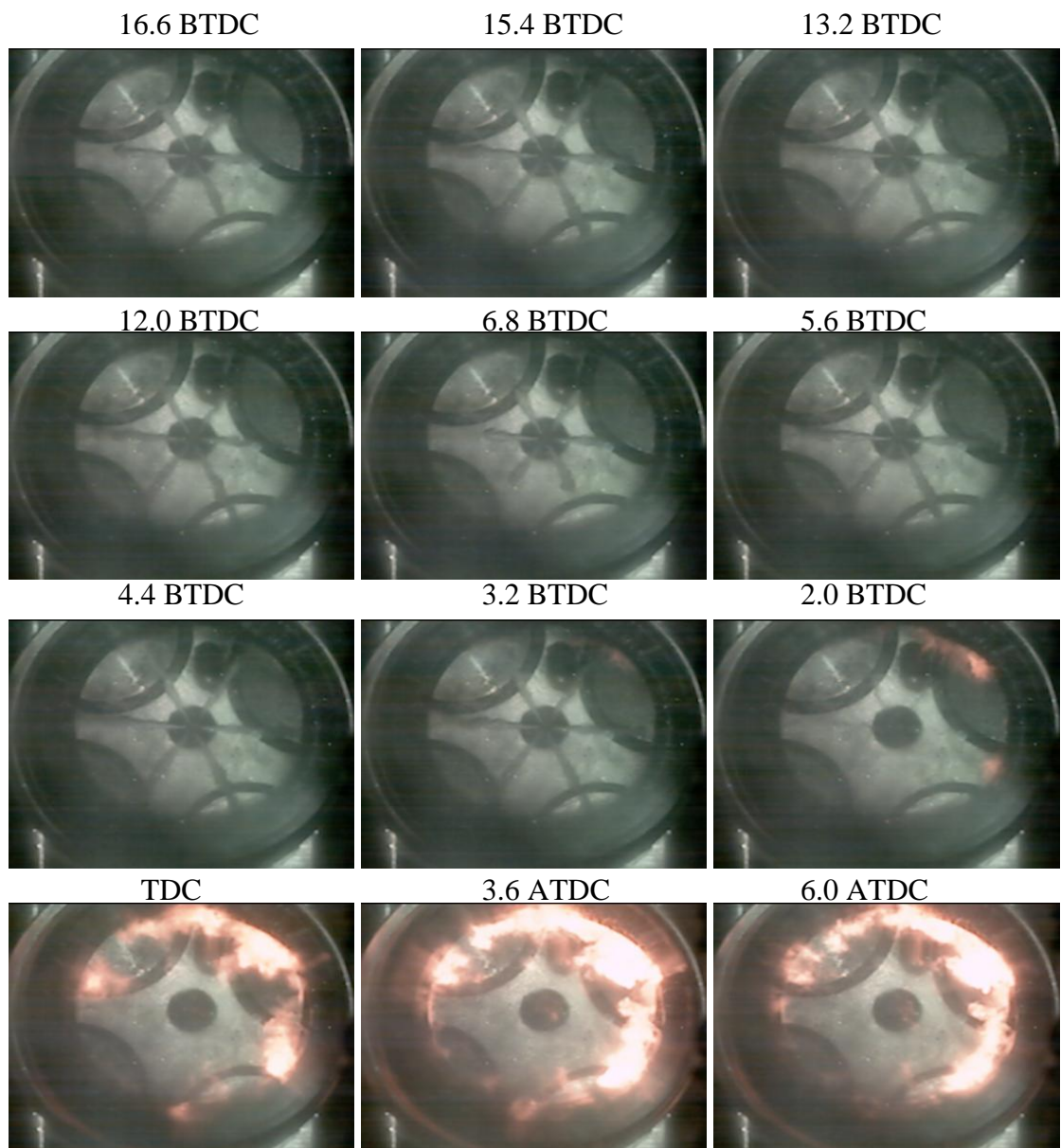


Figure 5.11 Combustion Images Sequence for B2 at 1200 bar



Figure 5.11 Combustion Images Sequence for B2 at 1200 bar (cont'd)

5.4.2.3 B2 Flame Temperature and Soot Concentration (KL factor) Measurements

Figure 5.12 shows the flame temperature images sequence as well as the KL factor images for B2 injection timing. As alluded to previously, the first flames that appear in the combustion images are due to chemiluminescence and as a result there is no radiation produced by the soot. Consequently, small flame spots appear around the cylinder wall in the first frames of the flame temperature. By 2.4° CA ATDC, it can be seen how the flames are distributed uniformly around the cylinder, with the maximum temperature reached by these flames of about 2300K. Strategy B2 is shown as combustion with high IMEP and low uHC due to its combustion completeness. In addition, due to the lower flame temperatures mostly out of the NO_x formation region, the NO_x emissions show very low values. From Table 5.4 it can be seen that the NO_x emissions for B2 are 45 ppm. Looking at the KL factor images in Figure 5.12, it is noted that during the premixed combustion little soot is formed. As combustion advances, the soot formation increases. However, due to its better mixing compared to strategy A, the fuel/air mixture is leaner and therefore the soot formation is lower. Compared with strategy A, the fact that this combustion is at lower temperature as seen in Figure 5.12, gives lower NO_x emissions. Furthermore, the soot formation in the diffusion combustion phase is also lower due to the better premixed leaner mixture associated with the longer dwell angle. From Table 5.4 it can be seen that B2 gives a FSN number of 0.42 compared to 1.37 that was the lowest value amongst strategies A; this represents a reduction of more than 70%.

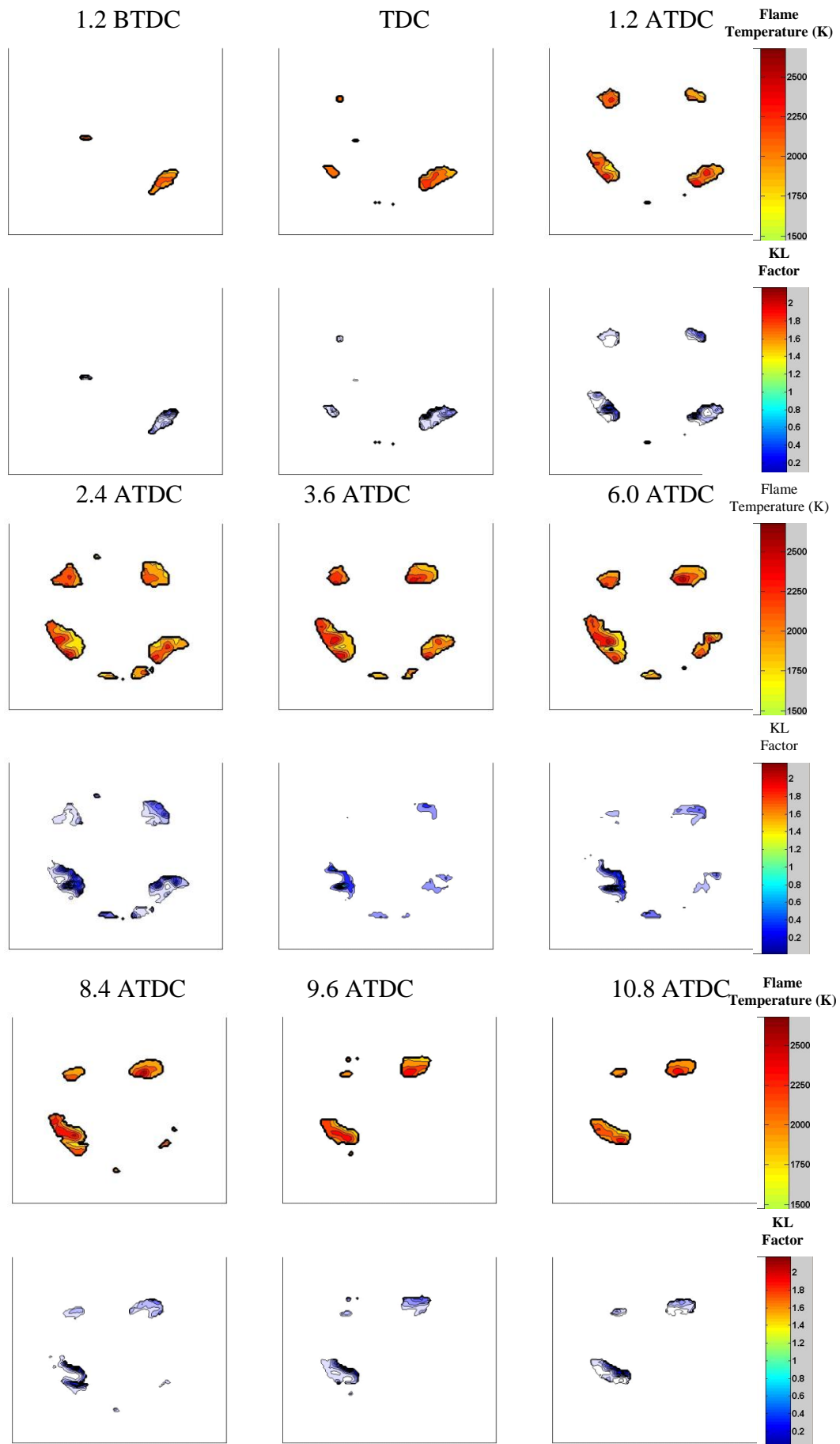


Figure 5.12 Flame Temperature and KL factor images sequence for B2 at 1200 bar

5.4.2.4 B5 Injection and Combustion Visualization

Figure 5.13 shows the images sequence for B5. As stated in Section 5.4.2.1, B5 injection timings is 6° CA later than in B2. Although the uHC emissions are of the same order, the NO_x emissions are 20% less but the soot emissions are three times higher. B5 is presented in order to analyse the influence of injection timing on the combustion performance and emissions. According to the images sequence, the start of combustion appears at 3.6° CA ATDC, which corresponds to the data from the heat release rate. In the frames of 6.0° CA and 8.4° CA ATDC, it can be seen that premixed combustion takes place uniformly and is distributed close to the cylinder walls. At 12° CA ATDC the luminosity of the flames is higher than that during the premixed combustion. At this stage the diffusion combustion is predominant and its luminosity is due to the soot radiation. From 18° CA ATDC the luminosity starts decreasing and from 24° CA ATDC it can be clearly seen that the flames start extinguishing.

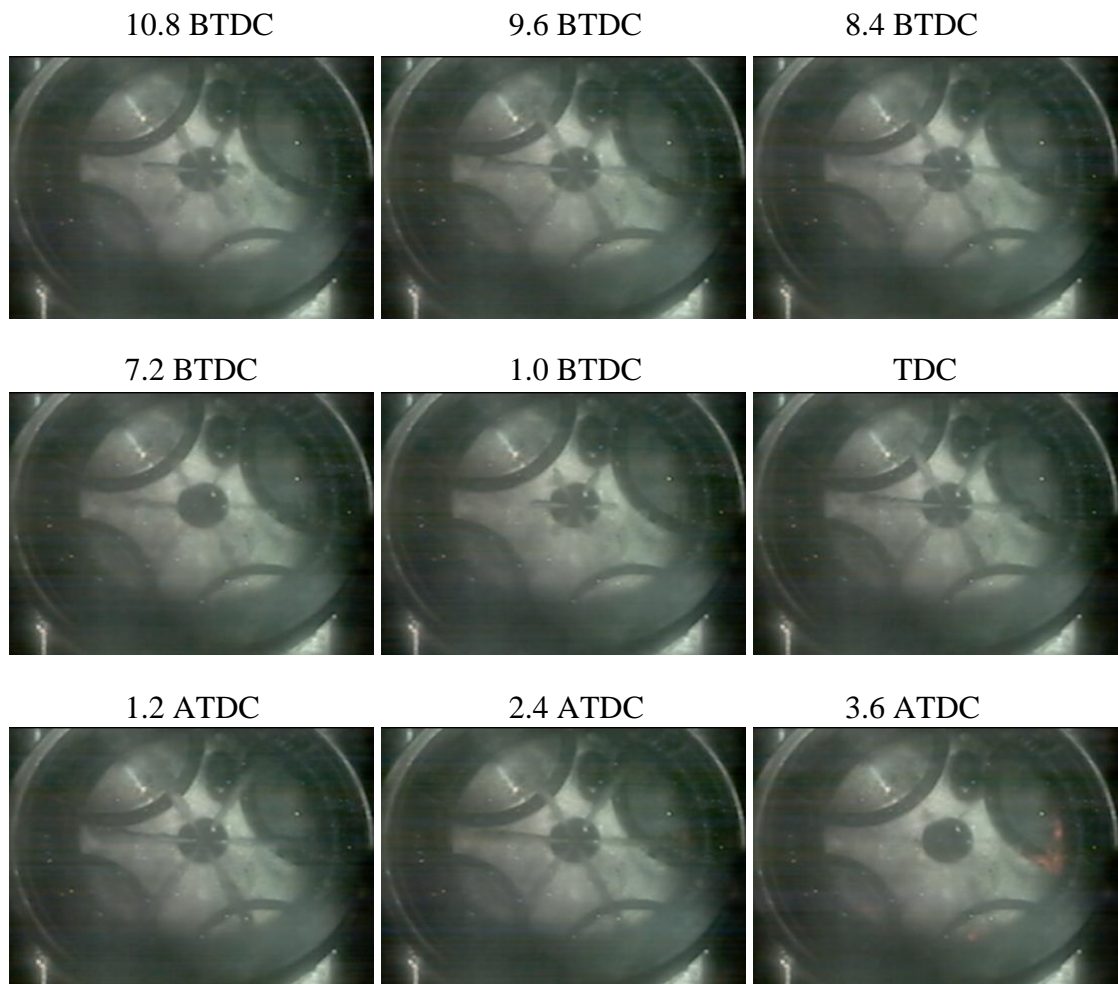


Figure 5.13 Combustion Images Sequence for B5 at 1200 bar

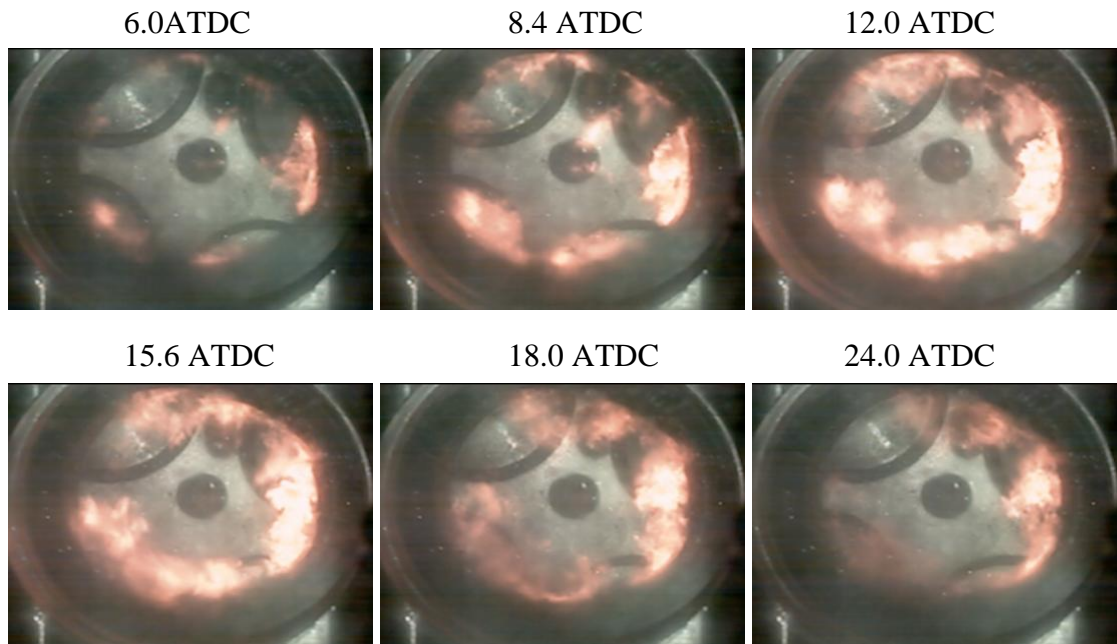


Figure 5.13 Combustion Images Sequence for B5 at 1200 bar

5.4.2.5 B5 Flame Temperature and Soot Concentration (KL factor) Measurements

Figure 5.14 shows the flame temperature images sequence for B5. In the frames 7.2 and 8.4° CA ATDC it can be seen that the combustion takes place near the cylinder walls, and also that there are some points at which the temperature is relatively high, 2250K, while the rest of the flame is at lower temperature. At 12° CA ATDC, which is after the peak heat release rate, the hot spots have reduced their temperature. From 14.4° CA ATDC, which is well into the diffusion combustion, it can be seen that most of the flame temperature is below 2000K, and it stays at this value until the end of combustion. At this flame temperature region, NO_x is not formed. Compared with B2, premixed combustion occurs at lower temperature, as most of the flame is below 2000K and just a few combustion sites are at higher temperature. The diffusion combustion starts earlier and it also takes longer; this explains the NO_x reduction with respect to B2.

As shown by the KL factor images in Figure 5.14, at 7.2 ATDC when premixed combustion takes place, there is very low concentration of soot; soot is formed at the tip of the leading spray where mixing with air takes place. From frame 12 ATDC, there is evidence of typical soot formation from diffusion combustion. Frames 14.4 to 18° CA ATDC show quite high soot concentration; this is probably due to the low temperature combustion which does not allow oxidation of the soot that is formed. As this strategy's injection timing is retarded with respect to B2, the start of combustion takes place well after TDC and the combustion temperature is lower than B2 which explains the increase of soot emissions shown in Table 5.4.

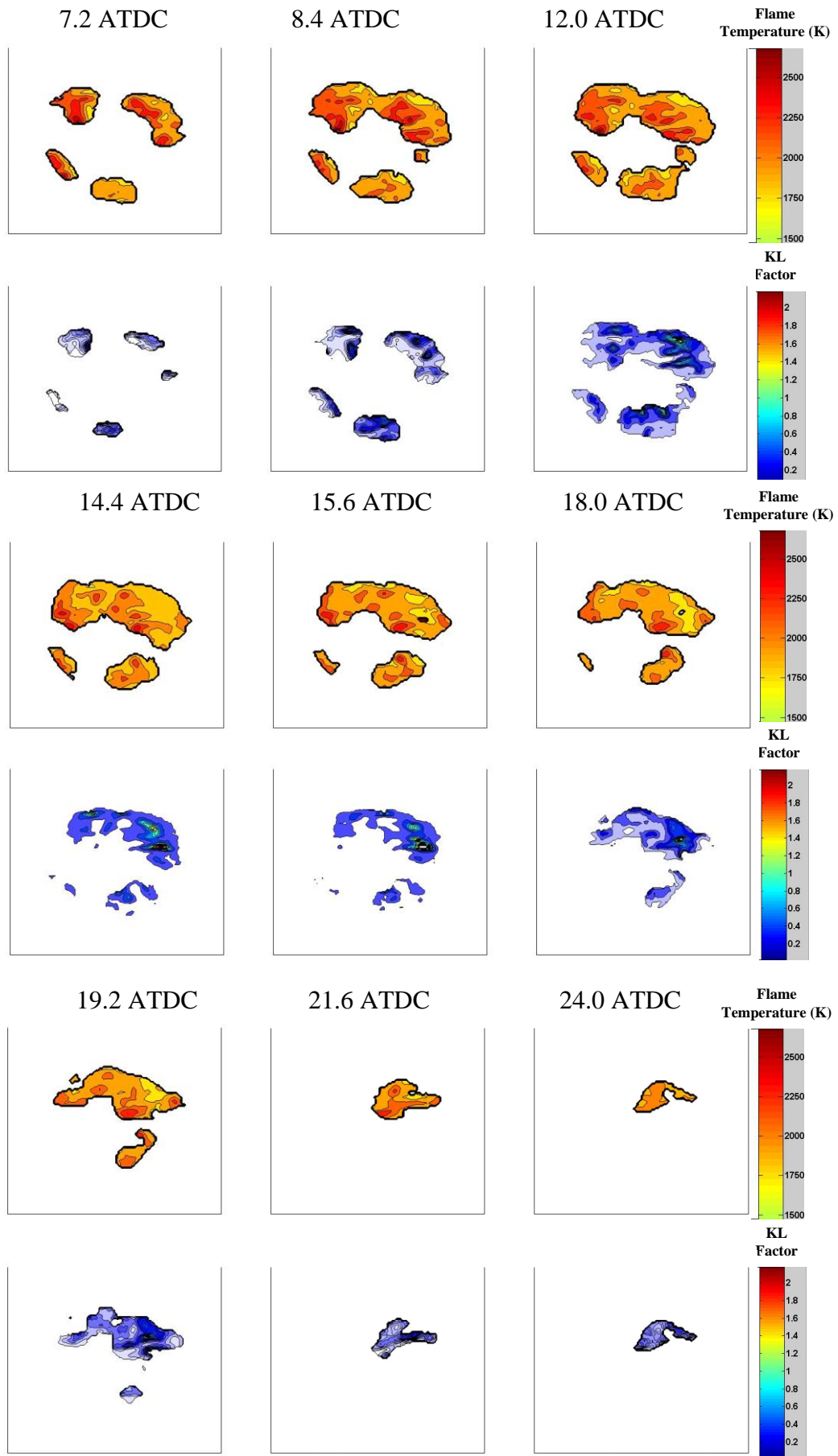


Figure 5.14 Flame Temperature and KL factor images sequence for B5 at 1200 bar

5.4.3 Strategy C and Strategy D

Table 5.2 showed the experimental matrix created for this study. For the strategies of 12 and 14° CA of dwell angle, strategies C and D, during the cylinder pressure data and heat release analysis it appeared that no combustion was taking place. High speed imaging was applied for different injection timings from strategy C and strategy D which showed that only the first injection was taking place instead of the split injection as it was expected.

Figure 5.15 shows an example of these high speed images sequence taken for strategies C and D. The sample corresponds to C2 where the injection timings are 19 and 7° CA BTDC; as expected the first injection occurs normally but the second injection never appears and the images show just a single injection without combustion.

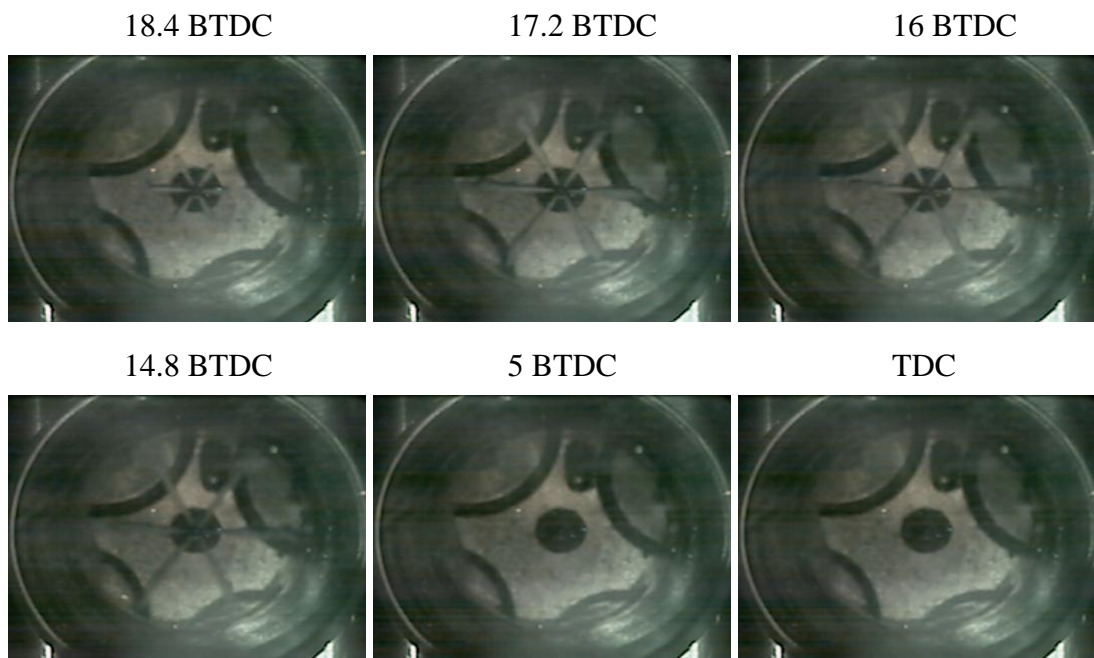


Figure 5.15 Spray Images Sequence for C2 at 1200 bar

During the injection process, when the needle goes down and closes the nozzle at the end of an injection, a pressure wave is created. For split injection investigations, the second injection takes place close to the first injection, and therefore it is influenced by the pressure wave created from the end of the first injection.

In order to gain a better understanding of the effect of the pressure wave, the pressure in the high pressure pipe was analysed. A Kistler piezoresistive high pressure sensor was located in the high pressure pipe at 250 mm from the nozzle approximately. Figure 5.16

shows the signal in voltage sent from the injector driver to the injector (picked up with a current probe) for the five different dwell angle injection cases. The pressure wave is plotted as well as the start of injection timing mark. As the pressure wave travels along the pipe at the speed of sound, the delay between the nozzle and the location of the pressure sensor is taken into account as follows; The speed of sound in a fluid can be obtained through the following equation:

$$c = \sqrt{\frac{B}{\rho}} \quad (5.1)$$

Where c = speed of sound in m/s

B = the bulk modulus in MPa

ρ = fuel density

The bulk modulus vary with pressure, thus at 1200 bar we can obtain from [126] that $B = 2600$ MPa and $\rho = 880$ Kg/m³. This gives the speed of sound equal to approximately 1.7mm/us.

As the sensor is at located 250mm from the nozzle, it results to a delay of 145 μ s approximately. The position of the first pressure trough shows a total delay of about 350 μ s. The additional 205 μ s delay is caused by the response time of the solenoid and the injector needle after receiving the driving current. Therefore, in the case of strategy C and D, the nozzle opening time would be 1350 μ s and 1500 μ s respectively, which correspond to the second pressure trough seen on the diagram.

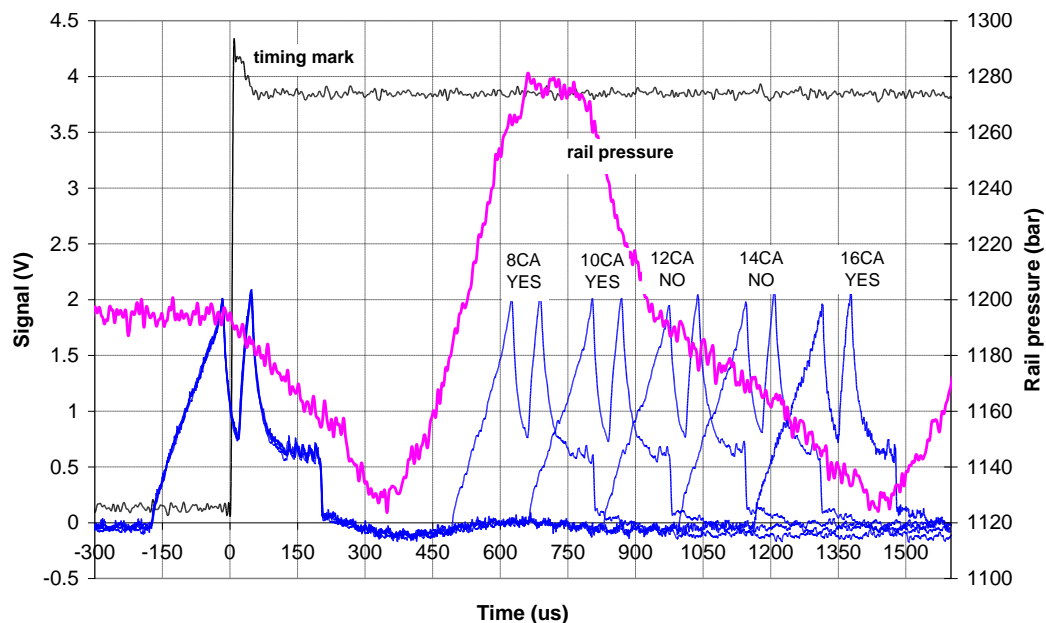


Figure 5.16 Injector signals and pressure wave at the injector for 1200 bar

The blue line represents the signal sent by the injector driver to the injector detected with a current probe. The black line is the reference timing signal from the ECU to indicate the timing of the first injection. The pink line represents the fuel pressure in the high pressure line between the injector and common rail.

As the graph shows, for strategies A and B of 8° CA and 10° CA dwell angles, respectively, the injector solenoid lifts the needle at the peak of the pressure wave. For strategies C and D, with 12° and 14° CA dwell angles, respectively, the solenoid tries to open the needle during the falling of the pressure wave and fails to open and therefore to inject fuel. The manufacturer of the injectors alludes to this pressure fall and the type of injector as the main reason for the failure in providing second injector. The second injection for the last strategy with a 16° CA dwell angle is still in the falling edge of pressure wave and it produces second injection. However, this injection is shorter than expected, probably due to the needle lifts later than expected as it passes the falling pressure

As a consequence, and in order to be able to work with close split injections, in practice the ECU would have been programmed to compensate for the pressure effect by altering the driving current characteristics. In this study, the Emtronix ECU and injector driver did not have the capability to take into account and overcome this pressure wave in order to lift the needle, consequently strategies C and D were not investigated further.

5.4.4 Strategy E

5.4.4.1 Effect of Injection Timing on Performance and Emissions

Table 5.5 shows the combustion characteristics for strategy E with a 16° CA dwell angle; it includes injection timing and quantity as well as performance and emissions for each of the five experiments investigated.

Table 5.5 Injection, Combustion and Emissions Characteristics of Strategy E, 1200 bar

| Strategy E | | | | | | | | | | | |
|--------------------|--------------------|---|---|-------------------|-------------------|-------------------------------|-------------------------------|----------------------|------------------|------------------|-------------------|
| Dwell Angle | Test Number | SOI (1st injection) (CA BTDC) | SOI (2nd injection) (CA BTDC) | IMEP (bar) | Combustion | | | | EMISSIONS | | |
| | | | | | SOC | 1st ID (CA) | 2nd ID (CA) | Duration (CA) | HC (ppm) | NOx (ppm) | Soot (FSN) |
| 16 | E1 | 25 | 9 | 0.6 | 3.4 BTDC | 21.8 | 5.8 | 28.2 | 620 | 44 | 2.20 |
| | E2 | 23 | 7 | 0.4 | 3.0 BTDC | 20 | 4 | 28.0 | 612 | 42 | 3.09 |
| | E3 | 21 | 5 | 1.1 | 2.6 BTDC | 18.4 | 2.4 | 27.4 | 420 | 41 | 3.56 |
| | E4 | 19 | 3 | 1.1 | 1.8 BTDC | 17.2 | 1.2 | 26.8 | 440 | 40 | 3.85 |
| | E5 | 17 | 1 | 1.0 | 0.8 BTDC | 16.2 | 0.2 | 25.8 | 450 | 35 | 3.47 |

Figure 5.17 illustrates the cylinder pressure data for strategy E and its 5 injection timings. Results of E1 and E2 follow the line of motoring pressure until about 12° CA BTDC, when both E1 and E2 experience a higher increase than the motoring pressure. This relatively rapid increase slows down after TDC to reach a peak at 7.2° CA ATDC for E1 and 5.4° CA ATDC for E2 giving pressure values of 34 bar. The peak of cylinder pressure stays over a short period of time before it starts decreasing. The two pressure lines decrease at a similar rate and from approximately 15° CA ATDC they coincide during the expansion stroke, but always at higher level than the motoring pressure. E1 gives a low IMEP of 0.6 bar and E2 a lower one of 0.4 bar. The difference between these two is that for E1 the peak cylinder pressure is slightly higher than E2. Similar to the first two, E3 and E4 have matching trends in their pressure lines. They go along the motoring pressure until approximately 11° CA BTDC when from that moment onwards the increase of pressure is higher and around TDC they start approaching a plateau where they reach the peak cylinder pressure. This occurs at 10.8° CA and 12° CA ATDC, respectively, where they reach values of 35 bar of pressure. The decrease occurs rapidly and from 17° CA ATDC both cylinder pressures go along the expansion stroke at higher level this time than in the first two injection timings E1 and E2. This difference of pressure over the expansion stroke is probably the reason why E3 and E4 give a higher IMEP than the first two, with a value of 1.1 bar. The last experiment studied for the 16° CA dwell angle was E5 where its pressure line goes along the motoring pressure until 10° CA BTDC, from where it experiments a higher increase. This rise tops around 5° CA ATDC with a value of just below 35 bar. Then the pressure decreases along the expansion stroke at similar values like E3 and E4. This strategy gives an IMEP of 1.0 bar, slightly lower than E3 and E4 as it peaks at lower values, but considerably higher than E1 and E2 as the values during the expansion stroke are much higher.

Comparing strategy E with the previous A and B, the IMEP given by strategy E is at least 50 % lower than A and B. In the following sections, by means of optical analysis an explanation is provided.

Figure 5.18 illustrates the heat release rate for all cases in strategy E. As for the cylinder pressure data analysis, the heat release rate curves of E1 and E2 follow similar trends and the three remaining cases of E3, E4 and E5 give identical shapes with a delay of 2° CA which is the injection timing difference. Thus E1 and E2 suffer a first decrease of the heat release rate at approximately 21° CA and 19° CA BTDC, respectively; this is

caused by the cooling effect of the first injection (SOI 25° CA and 23° CA BTDC). The fall in the heat release stops at 18 and 17° CA BTDC when it reaches a plateau while the fuel is mixing with the air. At 14° CA BTDC for E1 and 12.6° CA BTDC for E2, the first increase in the heat release rate occurs; this rise is probably due to the first combustion reactions with peaks at 10.4 and 8.8° CA BTDC, respectively. The heat release drops again while the second injection takes place and at 7.2° CA BTDC and 5.8° CA BTDC a steady increase occurs, which determines the start of combustion. This increase is slower than a typical premixed combustion and more like diffusion combustion. This combustion starts before the end of the second injection for this reason it produces a very rich diffusion combustion. The heat release rate curves for E3, E4 and E5 do not show apparent cooling effect after the first injection. It can be seen, however, that at around 2° CA after the end of the first injection the heat release rate increases rapidly; this is probably after some fuel from the first injection has mixed with air and pre-combustion reactions take place. For these three cases, 7° CA later this rise is stopped and a rapid but small decrease occurs at 7, 5 and 3° CA BTDC. A very rapid and steep increase in the heat release rate takes place for the three strategies immediately after the beginning of the second injection, this is at 4.6, 2.8 and 1 CA BTDC. The rapid rise of the heat release corresponds to initiation of combustion. However in the middle of the rise, it is interrupted for few crank angles to continue increasing until its maximum heat release rate which is reached at 8.4° CA ATDC for E3, 10.2° CA ATDC for E4 and 12.2° CA ATDC for E5. The heat release rates for these strategies indicate three diffusion phase combustions, which explains the high values obtained for the soot emissions shown in Table 5.5.

After looking at Table 5.5 showing the values of performance and emissions and Figures 5.16 and 5.17, several conclusions can be reached for strategy E which are as follows:

The first two cases show quite high uHC emissions compared to the last three and also lower IMEP. As the first injection takes place earlier, the fuel air mixing is poorer and therefore more fuel is burned in the fuel rich region resulting in higher UHC emissions and lower IMEP.

The NO_x emissions values obtained for strategy E are generally very low, which indicates that when low temperature combustion occurs, the soot emissions are very high. As explained before, combustion starts during the second injection which leads to a very rich combustion producing high concentrations of soot. As the temperature is

then relatively low, soot oxidation is rather weak, leading to high exhaust soot emissions.

High speed imaging, flame temperature and KL factor results for E3 are shown in the following sections as means for providing a better understanding of strategy E.

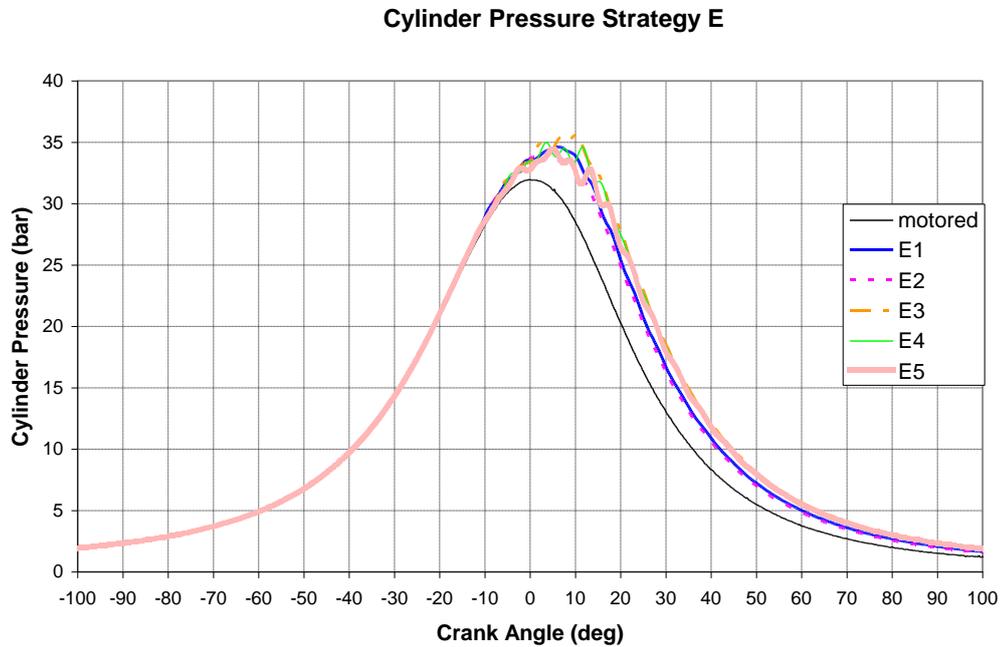


Figure 5.17 Cylinder pressure traces for experiments in Strategy E at 1200 bar

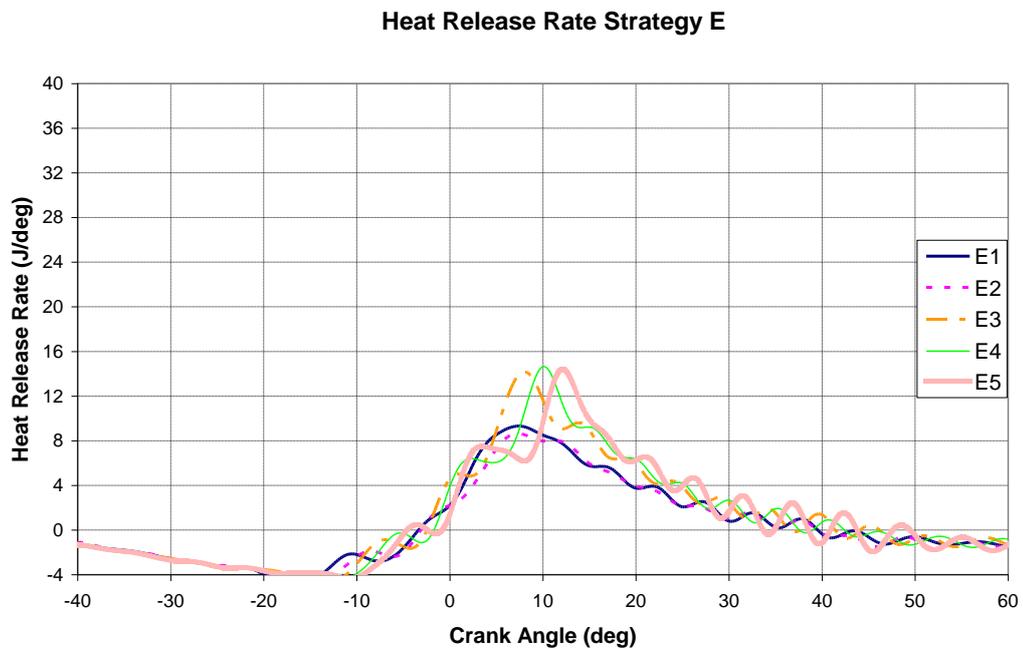


Figure 5.18 Heat release rate curves for experiments in Strategy E at 1200 bar

5.4.4.2 E3 Injection and Combustion Visualization

Figure 5.19 illustrates the high speed movie for case E3 where the injection timings were 21 and 5° CA BTDC. Frame 21 BTDC shows the start of the first injection; by the time it reaches frame 17.4 BTDC, which represents almost the end of injection and when the needle is fully open, the fuel almost reaches the piston bowl wall which could lead to some of the measured uHC, as explained previously. Frame 4.2° CA BTDC shows the start of the second injection which should be at 5° CA BTDC according to the injection setup. The injection duration is 313 μ s and at 2000 rpm this corresponds to 3.7° CA. It is clear that, due to the pressure wave, the injector needle lifts a bit later than the demand value. The second injection duration is shorter and it is finished by frame 0.6° CA BTDC, when the first luminous flame spots appear at the tip of the spray characteristic of the rich diffusion combustion. The following frames show six different combustion sites that occur in line with the fuel sprays and spreading in the direction of the swirl; the flames are very luminous as a consequence of rich diffusion combustion where high concentration of soot is produced.

This combustion images sequence explains the difference of IMEP between strategies A, B and E. Although strategy E with the longer dwell time shows poor mixing and therefore poor combustion, the fuel quantity injected is the major reason why IMEP does not reach higher values.

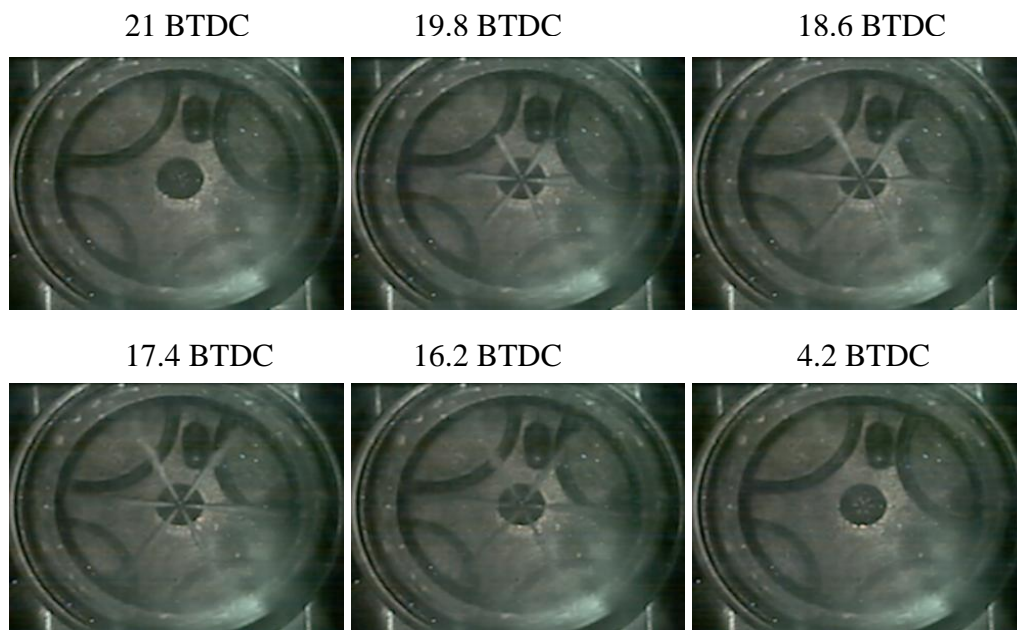


Figure 5.19 Combustion Images Sequence Strategy E3 at 1200 bar

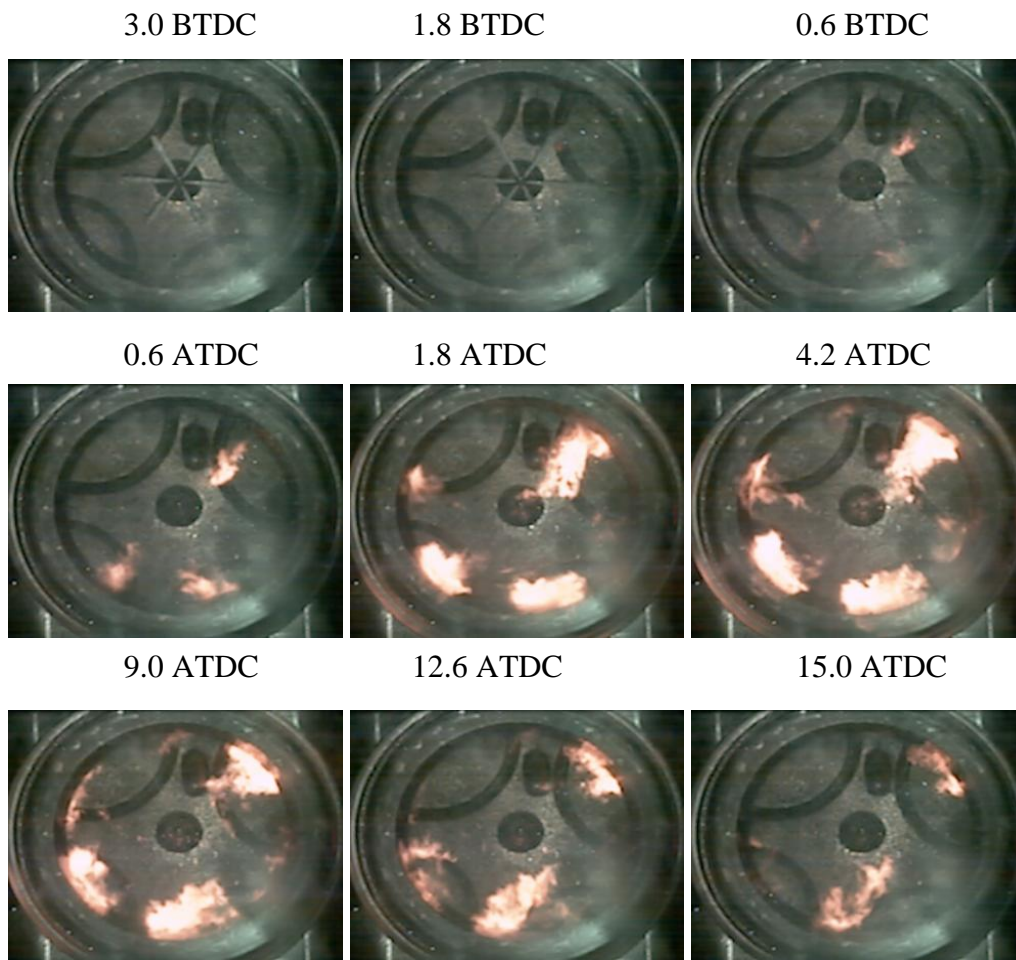


Figure 5.19 Combustion Images Sequence Strategy E3 at 1200 bar (cont'd)

5.4.4.3 E3 Flame Temperature and Soot Concentration (KL factor) Measurements

Figure 5.20 shows the flame temperature and KL factor images for E3. Looking at the flame temperature frames, at TDC and 2.4 ATDC, it can be seen that some of the flames are quite hot reaching values of 2400K; however, from that point onwards the flame temperature during combustion is much lower. Frame 4.8° CA ATDC shows some hot spots where the flame temperature is high but the rest of it is around 2000K and below. From frame 8.4° CA ATDC until the end of combustion, the flames temperature is mostly below 2000K which explains the low NO_x emissions shown in Table 5.5. As for soot concentration, it is seen in the combustion images that the flame has five or six combustion sites that line up with the injection spray; in the KL factor images it can be seen that the formation of soot follows the same pattern and it concentrates at different areas. Due to the low temperature combustion, soot oxidation is rather limited, leading to very high values of soot emissions as shown in Table 5.5.

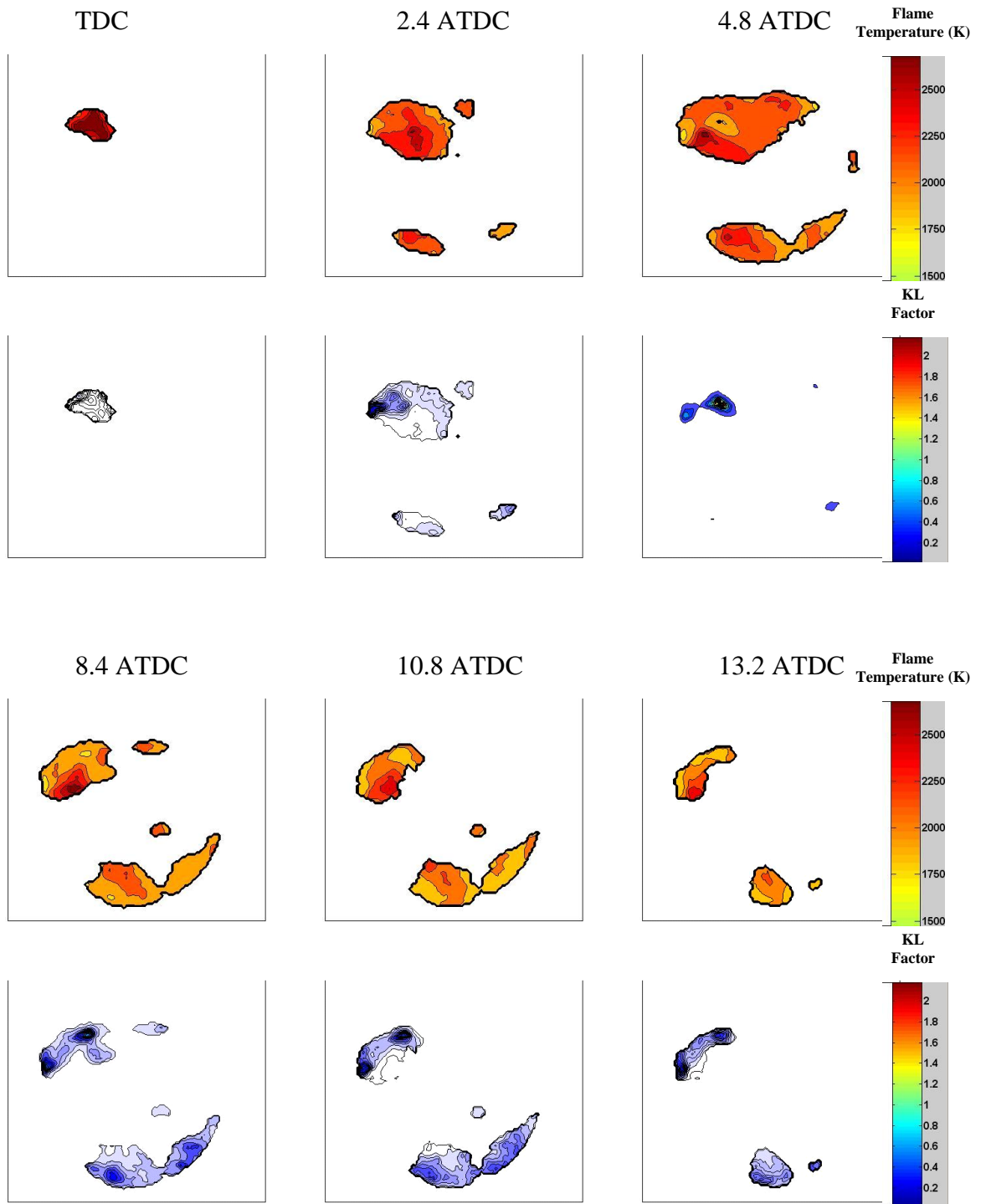


Figure 5.20 Flame Temperature and KL factor images sequence for E3 at 1200 bar

5.4.5 Conclusions for Strategies at 1200 bar

From the previous sections, the following conclusions can be reached regarding split injections at 1200 bar.

- Strategy A has the shortest dwell angle among the strategies studied. It shows good IMEP and low NO_x emissions. However due to the short time between injections the fuel/air mixing is poor, leading to high uHC emissions. This can be seen in the high speed combustion imaging where six flame spots spread following the swirl motion. The movies show high luminosity flames characteristic of fuel rich mixture. The other major drawback related to poor mixing is the high soot emissions. The combustion in the diffusion phase involves a rich mixture which causes high soot production while the flame temperature is not high enough to oxidise most of it. This has been noticed in the flame temperature and soot concentrations measurements given by the two colour method.

- Strategy B with its slightly longer dwell angle shows a big improvement compared to strategy A. The IMEP values are similar and in some cases even higher, but overall the emissions are much lower. For instance, the uHC emissions are decreased by about 50% and the soot emissions by 70%. As the dwell angle increases, mixing improves and therefore more fuel is burnt and the much leaner flames lead to this emissions' reduction. This is confirmed by the combustion images in which the combustion sites spread almost the complete circumference of the cylinder. NO_x emissions are also reduced by a small percentage as combustion temperature decreases.

- Strategy C and D end up as single injection due to the developing pressure wave, and no combustion is produced.

- Strategy E gives the lowest IMEP values among the strategies studied. This is caused primarily by the reduced amount of the second injection due to negative effect of the pressure wave generated from the first injection. Due to the greater dwell angle, as seen in the high speed combustion imaging, start of combustion takes places during the second injection, when the rich mixture burning gives high exhaust soot emissions. This is verified by the two colour measurements where high soot formation and low soot oxidation due to the lower combustion temperature are observed.

5.5 Strategies at Injection Pressure 800 bar

As stated previously, in order to study the effect of injection pressure, the same five strategies were investigated at 800 bar injection pressure, (as shown in Table 5.2 in Section 5.4). At this low pressure, fuel atomization is not so efficient and therefore vaporization and fuel/air mixing would be expected to be poor, leading to more incomplete combustion than at 1200 bar injection pressure. However, lower injection pressure would incur less parasitic loss from the high pressure fuel pump and hence would be desirable if it can be used. At 800 bar injection pressure, in order to keep the amount of fuel injected constant, the injection duration is increased by approximately 10%. Table 5.6 shows the test conditions for the strategies investigated at 800 bar.

Table 5.6 Test Conditions for 800 bar injection pressure experiments

| Test Conditions | |
|------------------------|--|
| Engine Speed | 2000 rpm |
| Intake Air | 140°C |
| | 0.5 bar boost |
| EGR | 60% (N ₂) |
| Fuel | Commercially Available 49.1 CN Diesel |
| Fuelling | 9.25 mm ³ total (70%/30%) |
| Injection duration | 5.2° CA 1 st injection |
| | 4.3° CA 2 nd injection |
| Air flow rate | 323 l/min |
| Nitrogen flow rate | 200 l/min |
| Load | ≈27 % of full load |
| Injection Pressure | 800 bar |
| Piston Bowl | Glass (optical techniques) Metal (emissions) |

5.5.1 Strategy A

5.5.1.1 Effects of Injection Timing on Performance and Emissions

Table 5.7 shows the injection characteristics as well as the combustion and emissions results for strategy A.

Table 5.7 Injection, Combustion and Emissions Characteristics of Strategy A, 800 bar

| Strategy A | | | | | | | | | | | |
|-------------|-------------|-------------------------------|---|------------|------------|-------------------------|-------------------------|---------------|-----------|-----------|------------|
| Dwell Angle | Test Number | SOI (1st injection) (CA BTDC) | SOI (2 nd injection) (CA BTDC) | IMEP (bar) | Combustion | | | | EMISSIONS | | |
| | | | | | SOC | 1 st ID (CA) | 2 nd ID (CA) | Duration (CA) | HC (ppm) | NOx (ppm) | Soot (FSN) |
| 8 | A1 | 19 | 11 | 1.0 | 1.8 BTDC | 17.2 | 9.2 | 27.0 | 240 | 19 | 0.22 |
| | A2 | 17 | 9 | 0.4 | 0.4 BTDC | 16.6 | 8.6 | 24.6 | 244 | 20 | 0.77 |
| | A3 | 15 | 7 | 0.5 | 1 BTDC | 14.0 | 6.0 | 23 | 252 | 15 | 0.75 |
| | A4 | 13 | 5 | 0.9 | 0.8 BTDC | 12.2 | 4.2 | 28.4 | 277 | 11 | 0.63 |
| | A5 | 11 | 3 | 0.1 | 0.6 BTDC | 10.4 | 2.4 | 28.4 | 401 | 5 | 0.47 |

Figure 5.21 illustrates the cylinder pressure traces of the experiments of strategy A with an injection pressure of 800 bar. The cylinder pressures for all 5 injection timings follow similar trend, they follow the motoring pressure line until approximately the first injection timing when the slope becomes slightly steeper than the motoring pressure. For A1, it increases at higher rate until 5° CA ATDC when it reaches a maximum point with a value of 34 bar of firing pressure. From this point onwards the cylinder pressure decreases gradually until 17° CA ATDC when it experiences a rapid drop of pressure over the expansion stroke. Since there is no steep pressure rise from the premixed combustion near TDC, the final IMEP value for injection timing A1 is just 1 bar. The rest of the experiments for strategy A show similar cylinder pressure traces; there is no rapid pressure increase, the peak is reached near TDC with low values and the cylinder pressure over the expansion stroke decreases at a similar rate to the motoring pressure although with higher values. These injection timings give a poorer engine output performance and their IMEP varies between 0.9 and 0.1 bar.

When comparing the IMEP of strategy A at 800 bar with strategy A at 1200 bar, it shows that at 800 bar the IMEP is much lower, the best injection timing for 800 bar, A1, gives an IMEP 37% lower than that at 1200 bar. For the rest of injection timings the IMEP is reduced at an average value of 80%. This could be explained because at the 1200 bar injection pressure, as the mixing process improves, there is much more fuel that burns in the premixed combustion phase, giving a high IMEP. At 800 bar injection pressure the cylinder pressure data shows no important premixed combustion due to the poor fuel/air mixing process. This will be investigated by means of the heat release rate analysis and optical techniques in the following sections.

The heat release rate curves for the experiments of strategy A at 800 bar injection pressure are shown in Figure 5.22. It is interesting to notice that although the injection timing is retarded by 2° CA for each experiment, the SOC takes place within the interval of 1° CA for all the experiments. The heat release rate for these experiments does not show any cooling effect after the first or second injection. This is probably because at 800 bar the injection rate is much slower than at 1200 bar and therefore no apparent effect can be seen in the graph. The heat release rate for A1 starts showing an increase around 14° CA BTDC, which is after the first injection has finished and this rise is gradual until approximately 4° CA BTDC when a steep rise takes place due to the premixed combustion reactions as the fuel that has already mixed with the air starts burning. This increase lasts only a few crank angles and the heat release rate slows

down at around 3° CA ATDC. At 7° CA ATDC the heat release rate experiments show another increase which peaks at 14° CA ATDC. This rise is typical of diffusion combustion or mixing controlled combustion. It decreases then rapidly until 20° CA ATDC when the last phase or late combustion starts as the remaining fuel keeps burning well over the expansion stroke.

As injection timing is retarded, it can be seen in the heat release rate curves that the premixed combustion phase is reduced and the diffusion combustion phase is increased. For A5 the heat release rate increases gradually from the start of combustion as mainly diffusion combustion takes place.

As seen in Figure 5.22 the heat release rate for strategy A at 800 bar injection pressure shows essentially short premixed combustion compared with the well defined premixed combustion phase in strategy A with 1200 bar injection pressure. This could explain the difference on IMEP values between the injection pressure strategies. From Tables 5.3 and 5.7, it can be seen that the uHC emissions for strategy A at 800 bar are reduced by more than 50%. This is because the combustion duration is longer (around 3 CA with respect to strategy A at 1200bar, see Table 5.3 and Table 5.7) which allows more time for the burning of more fuel.

In order to obtain a better understanding in the mixing process and combustion performance for strategy A, high speed imaging as well as Flame temperature and KL factor measurements for experiment A1 (with the highest IMEP values) are shown in the following sections.

Cylinder Pressure Strategy A

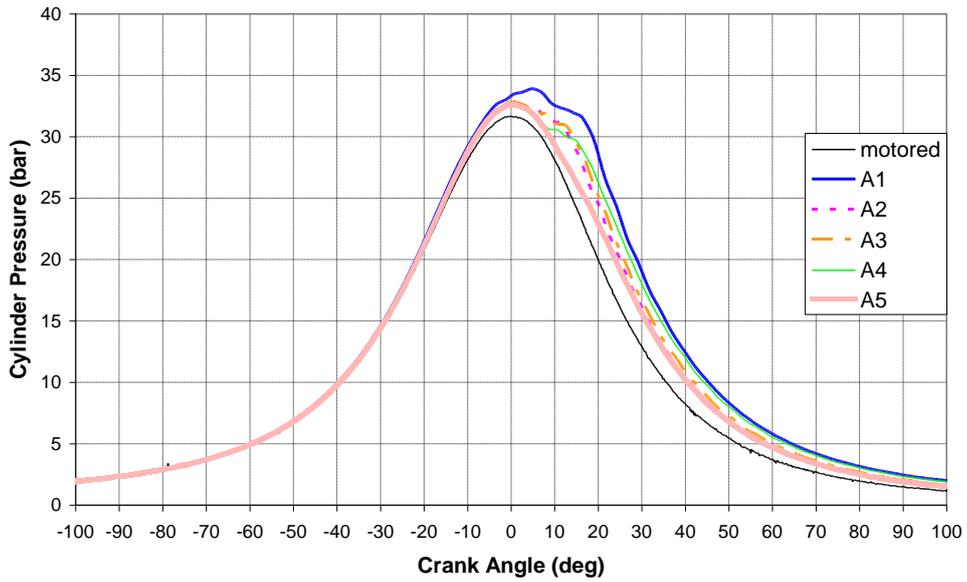


Figure 5.21 Cylinder pressure traces for experiments in Strategy A at 800 bar

Heat Release Rate Strategy A

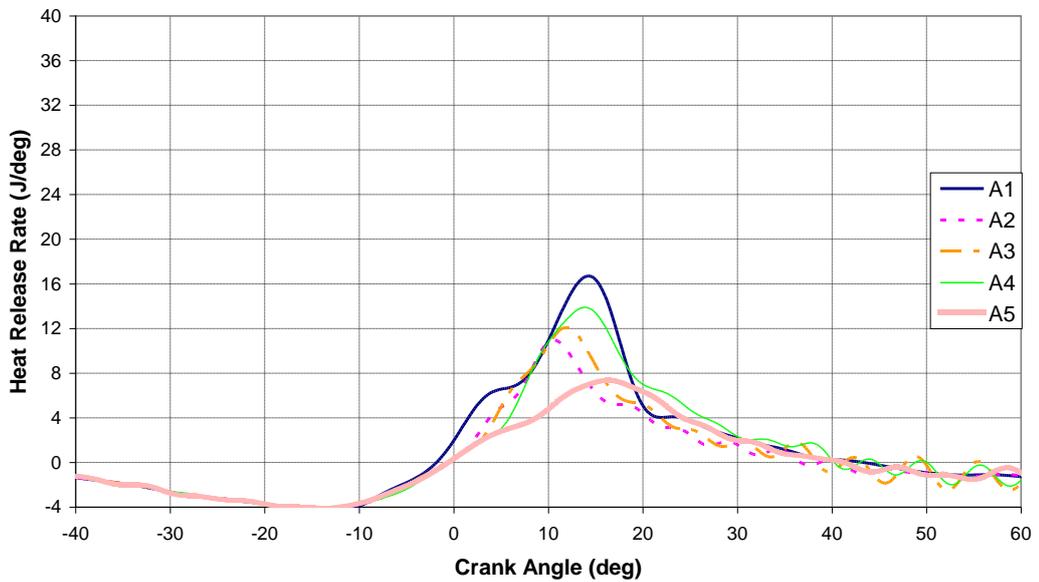


Figure 5.22 Heat release rate curves for experiments in Strategy A at 800 bar

5.5.1.2 A1 Injection and Combustion Visualization

Figure 5.23 shows the images sequence from the start of injection until the end of combustion with injection timing A1 at 800 bar. The first 5 frames illustrate the first injection where it can be clearly seen that the spray penetration is lower than at 1200 bar injection pressure when it was almost reaching the cylinder walls. The spray penetration for the two injections is lower (as seen in the figure), which could explain the reduction of uHC emissions shown in Table 5.7, as there is less liquid fuel impingement. Although SOC according to the heat release analysis is at 1.8° CA BTDC, the first ignition spots due to chemiluminescence appear a bit earlier at 2.4° CA BTDC. At TDC it can be seen that there are several flame spots of very low luminosity which indicates the premixed combustion phase. However, it can be seen that in the centre of the cylinder a much brighter flame is present as some of the fuel is mixing and burning in a diffusion flame. By 3.6° CA ATDC diffusion combustion covers almost the whole cylinder. From this point onwards, diffusion combustion continues where flame luminosity is high due to the radiation emitted by soot. From frame 18 ATDC, the combustion burning is at a lower rate as it is entering the last stage of combustion.

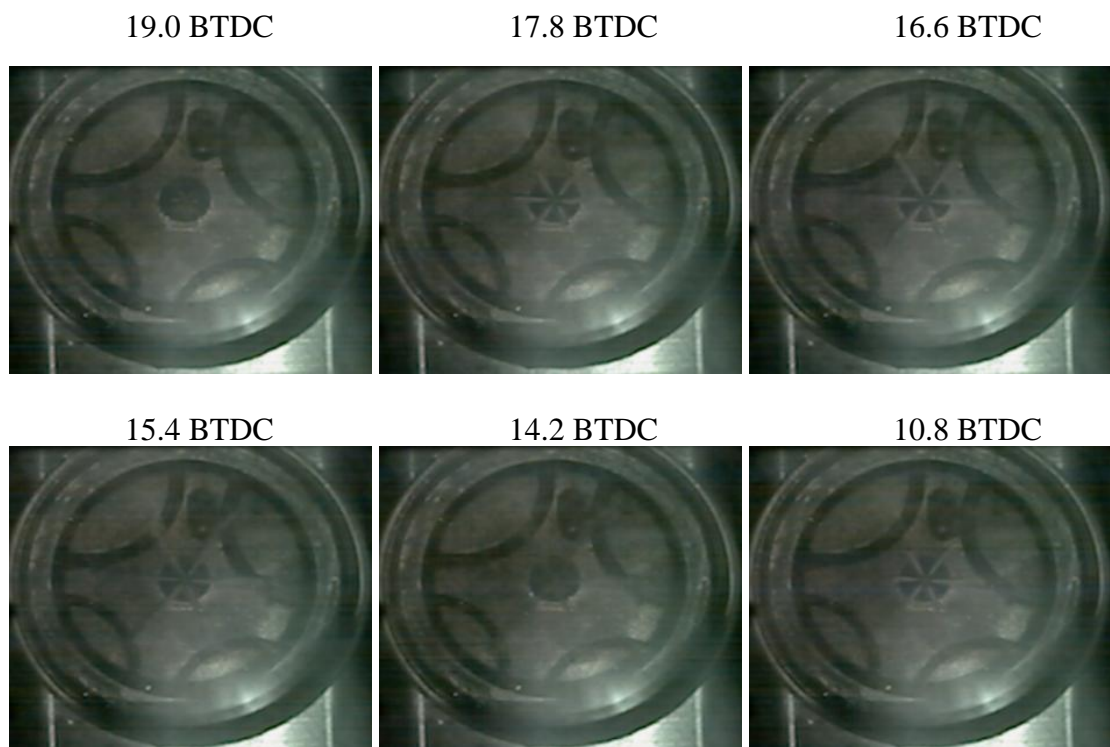


Figure 5.23 Combustion Images Sequence Strategy A1 at 800 bar

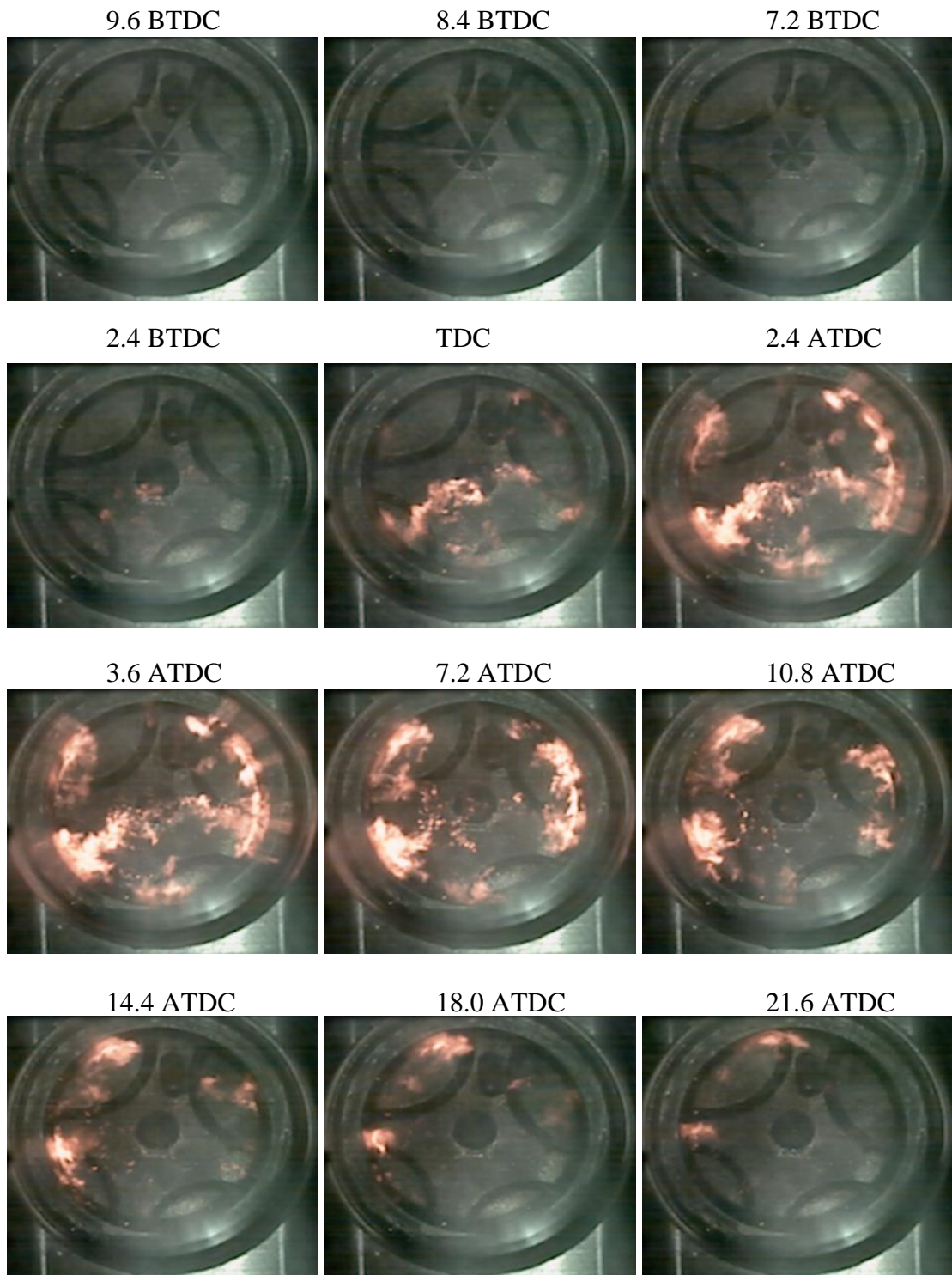


Figure 5.23 Combustion Images Sequence Strategy A1 at 800 bar (cont'd)

5.5.1.3 A1 Flame Temperature and Soot Concentration (KL factor) Measurements

Figure 5.24 depicts the flame temperature and soot concentration (KL factor) measurements taken in a high speed imaging sequence. The flame temperature frames show that at TDC and 1.2 ATDC there are some flame spots with a high temperature of around 2500K; this matches the heat release rate information where premixed

combustion is taking place. It can be clearly seen from frame 3.6 ATDC onwards that the flame temperature decreases to around 2000K for the rest of combustion as it is in the diffusion phase. From the flame temperature measurements and the heat release rate, it can be argued that the premixed combustion phase is reduced at the 800 bar injection pressure and the diffusion phase increases, hence the flame temperature is generally lower and, as a consequence, the NO_x emissions for strategy A at 800 bar are reduced by 50% compared to strategy A at 1200 bar injection pressure.

Looking at the soot concentration (KL factor) measurements in Figure 5.24, at frames TDC and 1.2 ATDC the first soot formation appears at the edges of the flames during the premixed combustion and from 3.6 ATDC, as diffusion combustion takes over the concentration of soot increases. However during the rest of combustion the soot concentration is not very high probably due to the combustion temperature being high enough to oxidise soot. Tables 5.3 and 5.7 show the ignition delay for the 800 bar injection pressure being longer than that for 1200 bar. As there is more time for mixing combustion burns in a leaner mixture during the diffusion phase producing less amount of soot than for the 1200 bar injection pressure strategy. The total amount of soot produced in strategy A at 800 bar is reduced by more than 60% compared with strategy A at 1200 bar injection pressure.

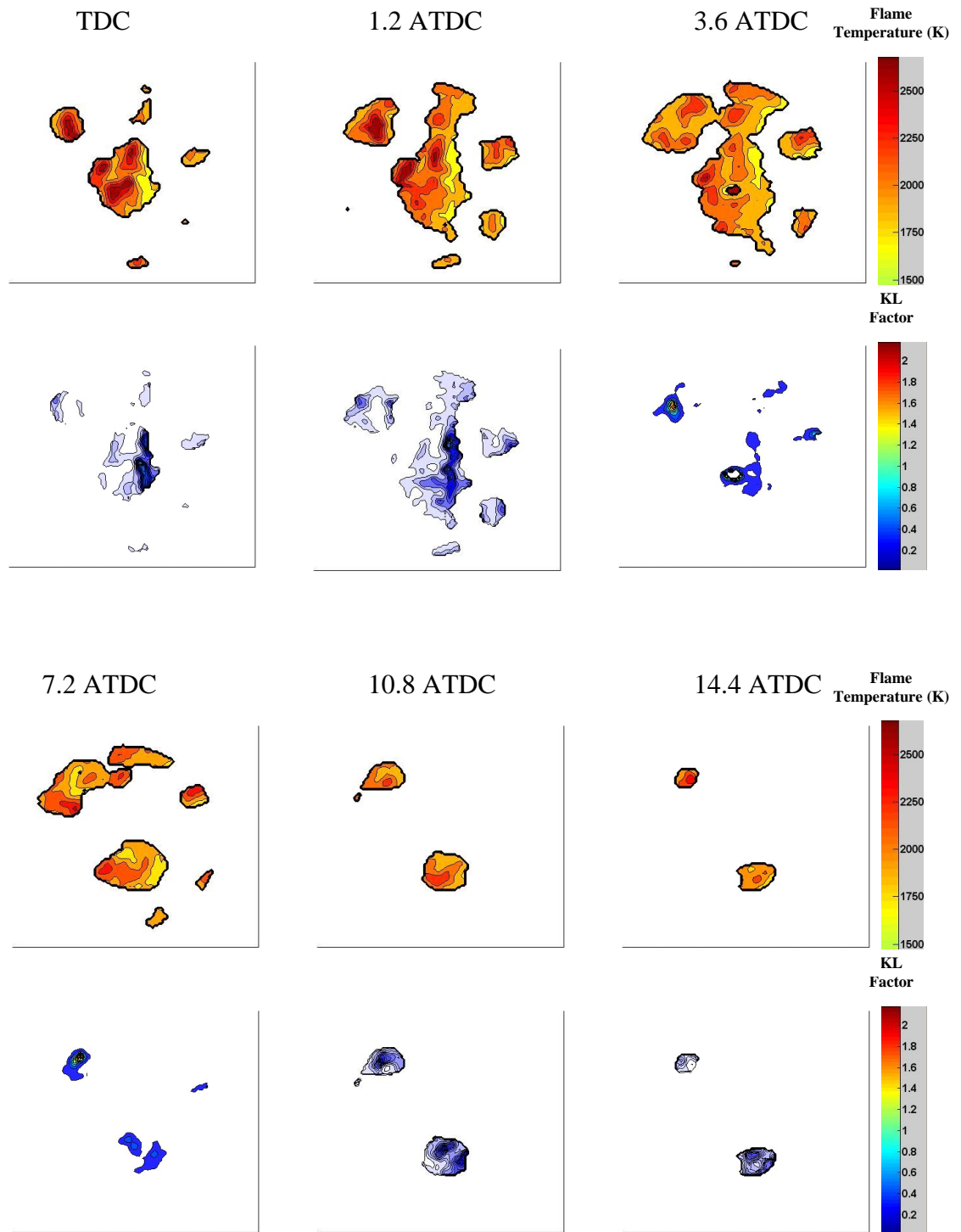


Figure 5.24 Flame Temperature and KL factor images sequence for A1 at 800 bar

2 Strategy B

5.5.2.1 Effects of Injection Timing on Performance and Emissions

Table 5.8 summarises the injection and combustion characteristics for five different injection timings for the 10° CA dwell angle strategy with an injection pressure of 800 bar. The table includes the emissions and engine performance measurements.

Table 5.8 Injection, Combustion and Emissions Characteristics of Strategy B, 800 bar

| Strategy B | | | | | | | | | | | |
|--------------------|--------------------|--------------------------------------|---|-------------------|-------------------|-------------------------------|-------------------------------|----------------------|------------------|------------------|-------------------|
| Dwell Angle | Test Number | SOI (1st injection) (CA BTDC) | SOI (2nd injection) (CA BTDC) | IMEP (bar) | Combustion | | | | EMISSIONS | | |
| | | | | | SOC | 1st ID (CA) | 2nd ID (CA) | Duration (CA) | HC (ppm) | NOx (ppm) | Soot (FSN) |
| 10 | B1 | 19 | 9 | 0.75 | 2.0 BTDC | 17.0 | 7.0 | 26.0 | 284 | 28 | 0.44 |
| | B2 | 17 | 7 | 0.60 | 1.4 BTDC | 15.6 | 5.6 | 25.0 | 250 | 18 | 0.71 |
| | B3 | 15 | 5 | 0.15 | 1.6 BTDC | 13.4 | 3.4 | 26.2 | 266 | 12 | 0.56 |
| | B4 | 13 | 3 | 0.20 | 1.8 BTDC | 11.2 | 1.2 | 26.8 | 273 | 12 | 0.83 |
| | B5 | 11 | 1 | 0.1 | 1.4 BTDC | 9.6 | - | 27.2 | 300 | 16 | 1.45 |

Figure 5.25 illustrates the cylinder pressure traces for strategy B. Amongst the injection timings studied for this strategy, it can be seen that there are two trends in the cylinder pressure lines. B1 and B2 follow the line of the motoring pressure until TDC and 0.8° CA ATDC respectively when they experience an increase in pressure due to the premixed combustion. For B1 this rise occurs rapidly and peaks at 7.4° CA ATDC with a relatively low peak cylinder pressure value of 37 bar, while for B2 the increase of pressure is more gradual achieving its maximum value of just 35 bar at 8.8° CA ATDC. After peaking the B1 and B2 pressure lines go along during the expansion stroke with higher values than the motoring pressure. Among the injection timings investigated for this strategy at 800 bar injection pressure, the B1 and B2 injection timings show the highest IMEP values respectively of 0.7 and 0.6 bar. The rest of the injection timings go along with the motoring pressure until they pass TDC and there is no rapid increase of pressure due to the premixed combustion. However during the expansion stroke their pressure values are higher than the motoring pressure due to combustion but lower than B1 and B2. The final IMEP values for these experiments are very low varying between 0.1 and 0.2 bar.

Similarly to strategy A for the 800 bar injection pressure, the mixing process is worse than that for the 1200 bar and, therefore, less fuel burns in the premixed phase. The air/fuel mixing ratio controls the diffusion combustion over the expansion stroke. As most of the fuel is burned during the expansion stroke, when the piston is moving downwards, the work done on the piston by combustion is not very efficient and hence the low IMEP values for this strategy B.

Comparing with strategy B at 1200 bar injection pressure, the engine output values for the first two B1 and B2 timings represent 30% of the values for 1200 bar. This is because at 1200 bar the mixing process improves and more combustion takes place in the premixed phase near TDC leading to higher engine output.

The heat release rate of strategy B is shown in Figure 5.26. For the first two injection timings, B1 and B2, the heat release rate curves are similar. The lines coincide until approximately 10° CA BTDC when they experience an increase of the heat release. This rise is due to the pre-combustion reactions after the first injection. It is interesting to notice that there is no cooling effect from the first injection. This, similar to strategy A, is due to the lower injection rate that occurs at 800 bar. The increase of the heat release rate is slowed down at 6° CA BTDC in the case of B1 and at 4° CA BTDC for

B2 due to the cooling effect of the second injection. This cooling effect lasts only for a few crank angles and at 3° CA and 2° CA BTDC, respectively, a rapid increase of the heat release occurs due to the premixed combustion. Injection timing B1 reaches a maximum heat release rate at 4° CA ATDC. It can be seen that for B2, where injection timing is retarded 2° CA with respect to B1, the rise in the heat release rate is at a lower rate and it peaks later at 6.6° CA ATDC. This phenomenon has been noticed before: as injection timing is retarded more diffusion combustion occurs and this can be seen associated with more gradual rate of the heat release. This is because the ID decreases and therefore there is less time for the fuel to mix with the air and burn in the premixed phase. After reaching their maximum values, the heat release lines for B1 and B2 decrease quickly due to the end of the premixed combustion until 8 and 10° CA ATDC when the rate decreases more gradually as a consequence of the diffusion combustion. The next three experimental cases (B3-B5) have similar heat release rates. They initially have a rise at between 14° and 12° CA BTDC, with the first increase due to the pre-combustion reactions. After the second injection, there is a minor cooling effect and then the start of combustion occurs around TDC for B3 and B4 and well after TDC for B5 when the pressure and temperature inside the cylinder are already decreasing. The heat release rate increases after TDC for these three experiments which indicates that more diffusion combustion is taking place. They achieve a maximum heat release with a very low value of about 8 J/deg and then they decrease gradually over the expansion stroke at a rate controlled by the fuel mixing with the air inside the cylinder.

Having the highest IMEP value among the injection timings for strategy B, combustion imaging and flame temperature and KL factor measurements for B1 are shown below.

Cylinder Pressure Strategy B

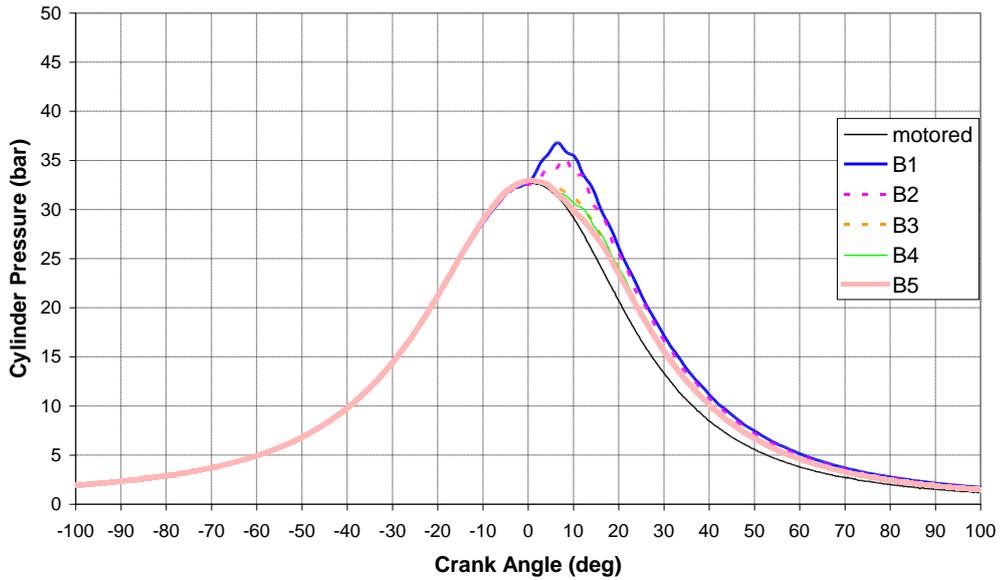


Figure 5.25 Cylinder pressure traces for experiments in Strategy B at 800 bar

Heat Release Rate Strategy B

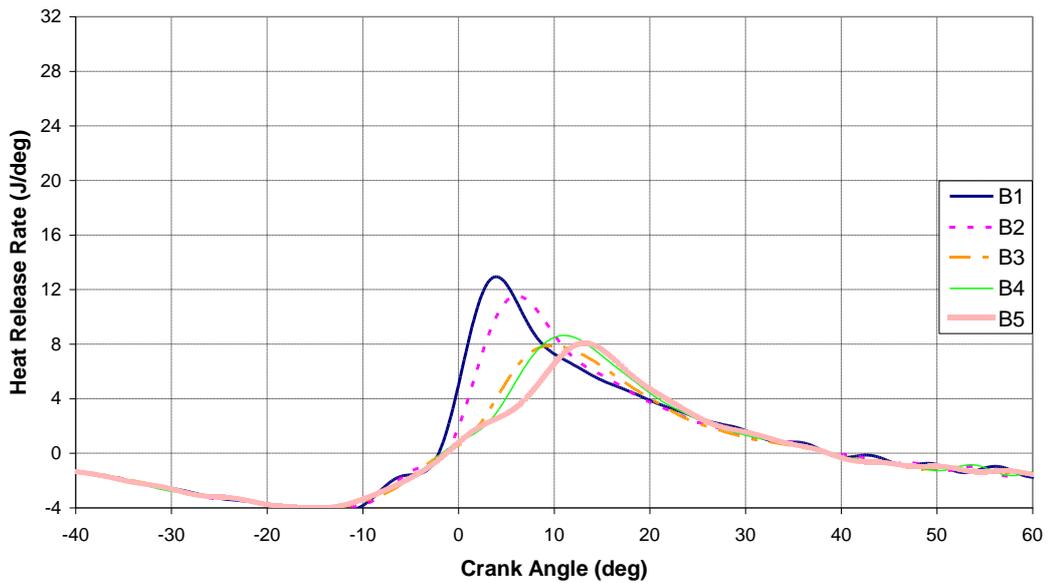


Figure 5.26 Heat release rate curves for experiments in Strategy B at 800 bar

5.5.2.2 B1 Injection and Combustion Visualization

The combustion imaging for experiment B1 is shown in Figure 5.27. During the first several frames the two injections show that the spray penetration is reduced compared to the 1200 bar injection pressure. After the injection, frame 2.4 BTDC shows the first flame spots if with very low luminosity indicative of premixed combustion. At frame

2.4 ATDC some flame points of very low luminosity can be seen as premixed combustion reaching its maximum, some high luminosity flames and starts appearing more typical of diffusion combustion. Frames 4.8 and 6.0 ATDC show the diffusion flames being spread following the swirl motion; they do not show very high luminosity which indicates that the soot formation rate is not very high. The following frames show the flames persisting until the end of combustion.

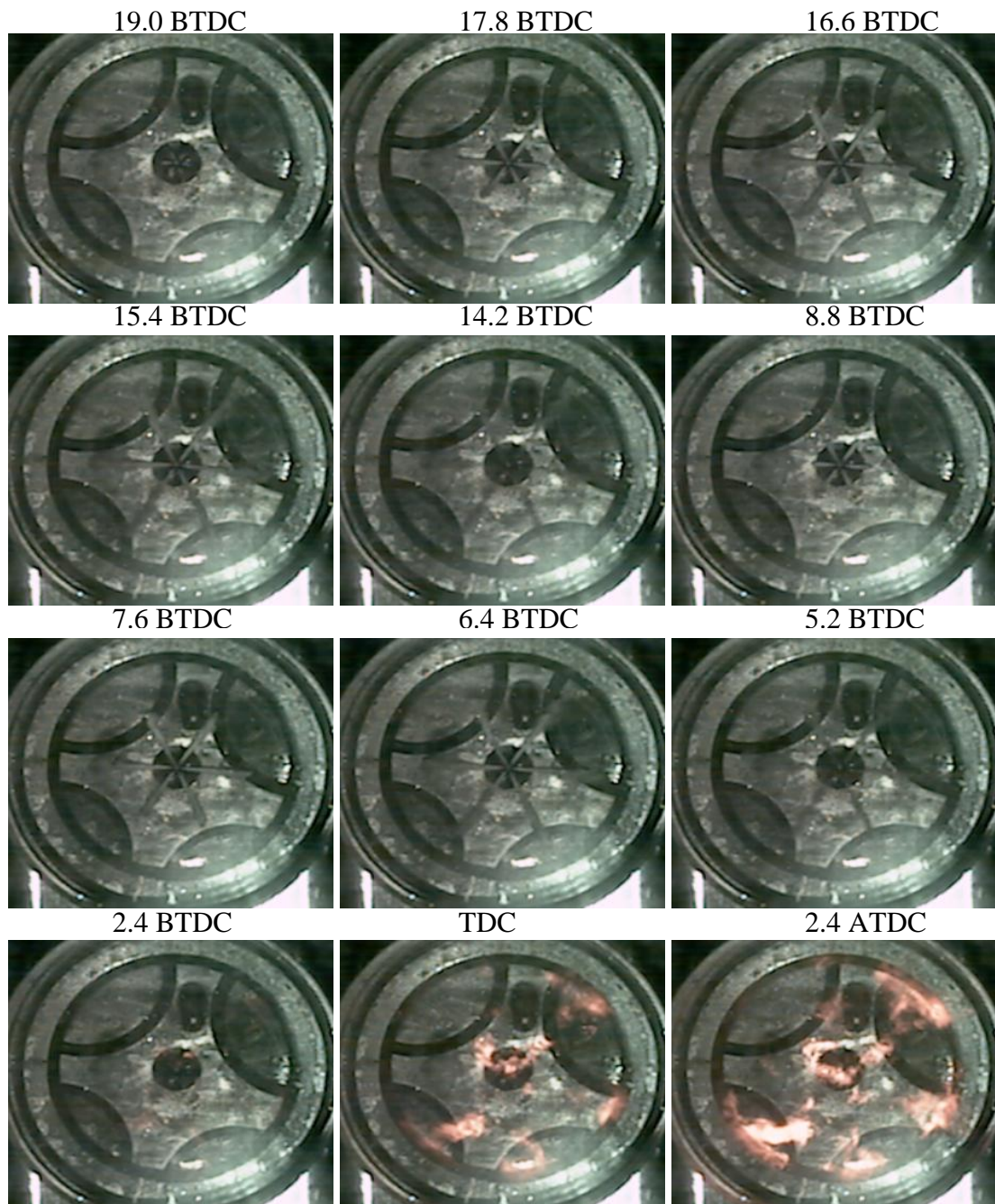


Figure 5.27 Combustion Images Sequence Strategy B1 at 800 bar

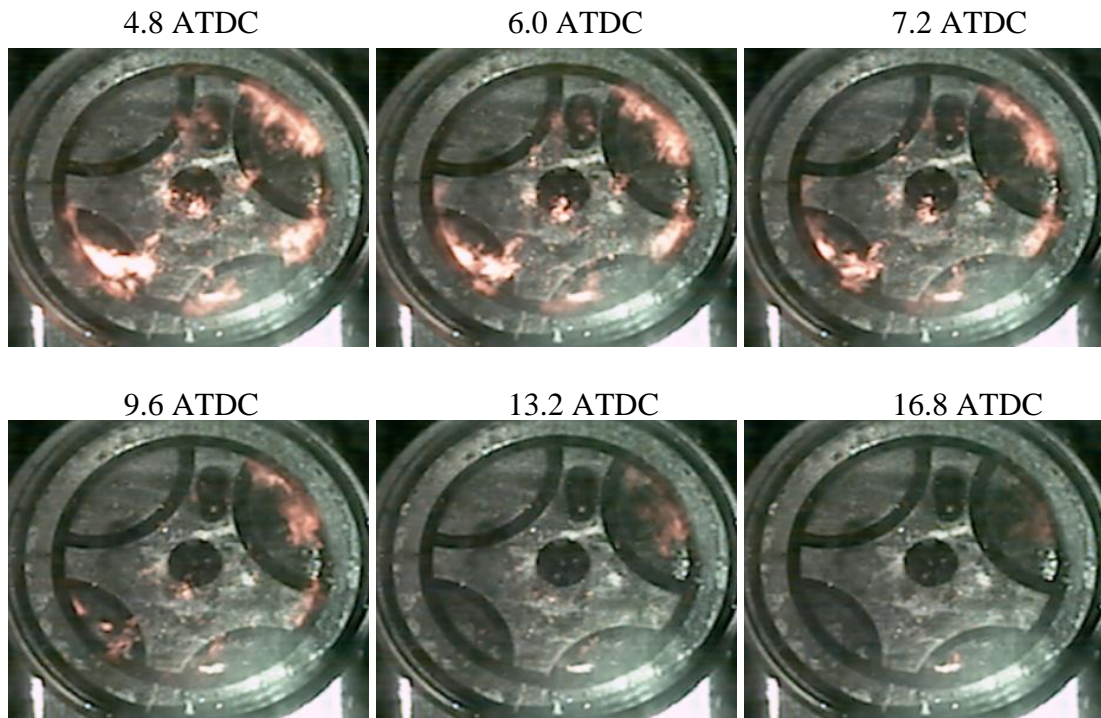


Figure 5.27 Combustion Images Sequence Strategy B1 at 800 bar (cont'd)

5.5.2.3 B1 Flame Temperature and Soot Concentration (KL factor) Measurements

Figure 5.28 illustrates the images sequence of the flame temperature and KL factor measurements for experiment B1. From frame 1.2 BTDC until 2.4 ATDC the flame temperature shown is quite high reaching over 2500K in some points. This coincides with the premixed combustion where the highest temperatures are reached. Although these temperatures would indicate high NO_x emissions, Table 5.8 shows very low NO_x emissions produced for all injection timings of strategy B. This can be explained by looking at the next flame temperature frames where the flame temperature has dropped below 2000K for almost the whole flame. Thus the NO_x formation lasts only for few crank angles.

The KL factor measurements show low soot formation during premixed combustion. At frame 2.4 ATDC it can be seen an area where soot formation occurs which corresponds with the leading edge of diffusion combustion. This agrees with the high speed combustion images where diffusion combustion could be seen starting around 2.4° CA ATDC. During the rest of combustion, KL factor measurements show some soot formed which at the end of the diffusion combustion is reduced probably by means of soot oxidation.

Comparing the values of soot emissions with the same strategy at 1200 bar injection pressure, it can be seen in Tables 5.4 and 5.8 that at 800 bar injection pressure they

show a moderate increase probably due to the poorer mixing and therefore richer diffusion combustion.

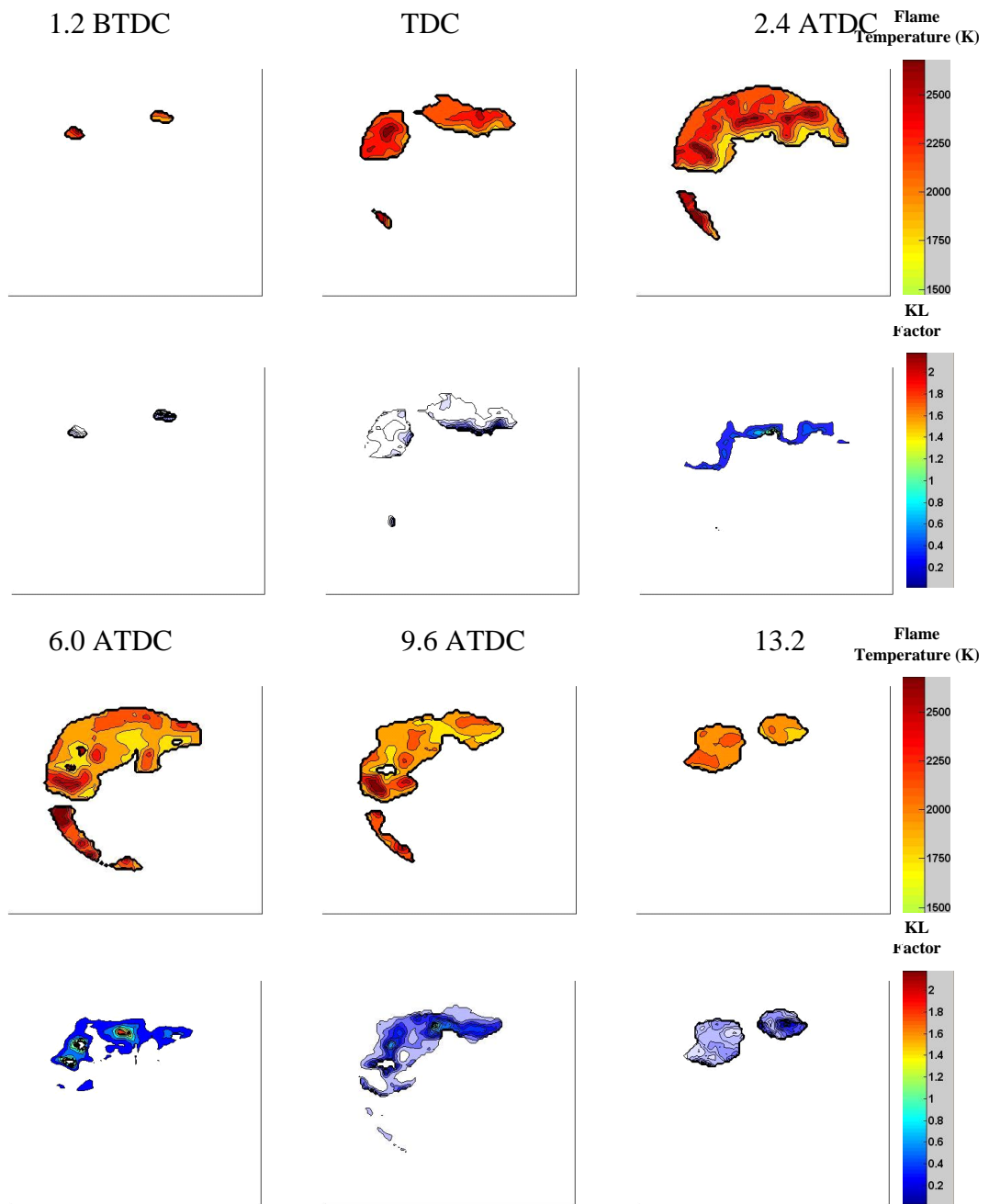


Figure 5.28 Flame Temperature and KL factor images sequence for B1 at 800 bar

5.5.3 Strategy C

5.5.3.1 Effects of Injection Timing on Performance and Emissions

Table 5.9 shows the injection and combustion characteristics for strategy C, which is by increasing the dwell angle by two with respect to strategy B. Engine output and emission values are also shown.

Table 5.9 Injection, Combustion and Emissions Characteristics of Strategy C, 800 bar

| Strategy C | | | | | | | | | | | |
|-------------|-------------|-------------------------------|---|------------|------------|-------------------------|-------------------------|---------------|-----------|-----------|------------|
| Dwell Angle | Test Number | SOI (1st injection) (CA BTDC) | SOI (2 nd injection) (CA BTDC) | IMEP (bar) | Combustion | | | | EMISSIONS | | |
| | | | | | SOC | 1 st ID (CA) | 2 nd ID (CA) | Duration (CA) | HC (ppm) | NOx (ppm) | Soot (FSN) |
| 12 | C1 | 21 | 9 | 0.1 | 6.4 BTDC | 14.6 | 2.6 | 16.0 | 282 | 15 | 0 |
| | C2 | 19 | 7 | 0.1 | 5.2 BTDC | 13.8 | 1.8 | 17.0 | 254 | 13 | 0.18 |
| | C3 | 17 | 5 | 0.43 | 5.0 BTDC | 12.0 | - | 17.2 | 254 | 21 | 0.01 |
| | C4 | 15 | 3 | 0.1 | 2.8 BTDC | 12.2 | 0.2 | 17.2 | 247 | 10 | 0.41 |
| | C5 | 13 | 1 | 0.1 | 1.6 ATDC | 14.6 | 2.6 | 17.0 | 262 | 14 | 0.37 |

Strategy C for the 1200 bar injection pressure (Section 5.4.3) showed no second injection due to the negative effect of the pressure wave created after the first injection. However, at the 800 bar injection pressure, the second injection was detected and therefore the full investigation was carried out for strategy C. In Table 5.9 above, the IMEP values for the different injection timings were very low implying very poor performance which probably indicates a problem with the injection process.

Figure 5.29 shows the cylinder pressure traces for strategy C; the five injection timings investigated coincide with the motoring pressure until approximately 3°CA BTDC . At this point experiments C1 and C2 continue with the pressure increasing at the same rate and separating from the motoring pressure as this is slowing down closer to TDC. C1 and C2 peak around 4°CA ATDC with pressure values of 39 and 37 bar, respectively. Injection timing C3 experiences a more rapid rise of pressure at 2°CA BTDC , it then reaches a maximum value of pressure of 41 bar at 4°CA ATDC . Experiments C4 and C5 show a small increase of pressure after TDC, achieving very low pressure values at their peaks. All injection timings except C3, have a very rapid decrease of pressure after the peak with values slightly higher than for the motoring pressure. Therefore the engine out values for these strategies are very low. Only C3 has slightly higher values of pressure than the motoring line during expansion and it gives an IMEP value of 0.5 bar.

The heat release rate curves for the experiments of strategy C are shown in Figure 5.30. It can be noticed that as injection is retarded the SOC is retarded, thus experiments C1 and C2 have most of the combustion before TDC; C4 and C5 show that combustion occurs after TDC and it is injection timing C3 that shows most of the combustion occurring at TDC and therefore maximising the work done over the piston. This is why strategy C3 differs from the other injection timings among strategy C and shows the highest IMEP value. Looking at C3's heat release rate traces, it shows a little increase after the first injection has finished due to the pre-combustion reactions. This rise slows down for few crank angles until the rapid increase of the heat release starts due to the main combustion. This first phase is mainly premixed combustion, peaking at TDC as previously explained. It then decreases quite rapidly until 4°CA ATDC when the mixing-controlled combustion starts. At about 10°CA ATDC the heat release rate starts decreasing again as combustion is entering the last phase.

Due to its highest IMEP value, high speed imaging, flame temperature and KL factor results for C3 are shown in the following sections as an example for a better understanding of strategy C.

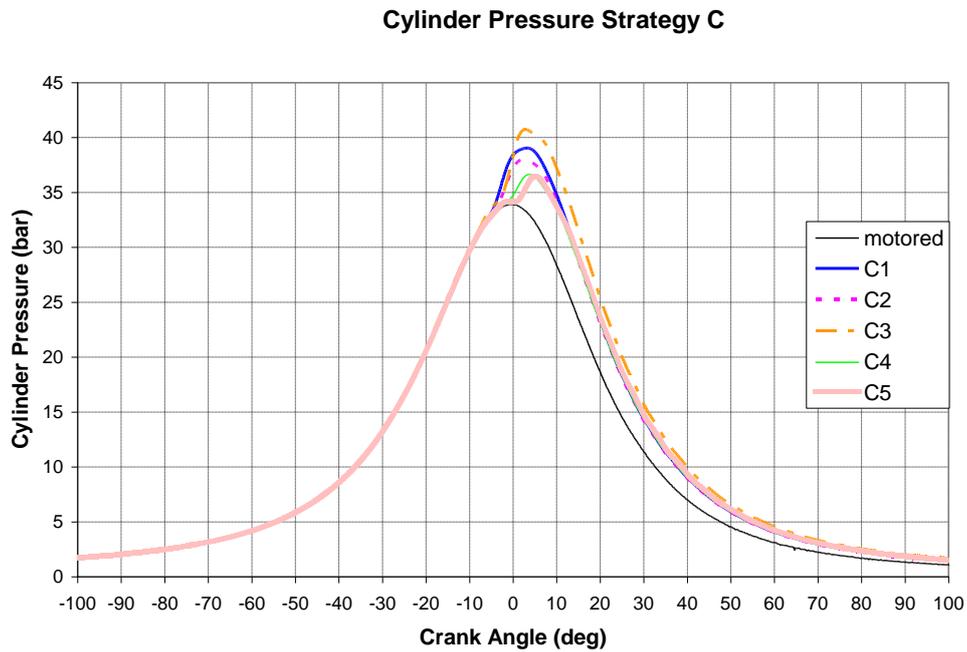


Figure 5.29 Cylinder pressure traces for experiments in Strategy C at 800 bar

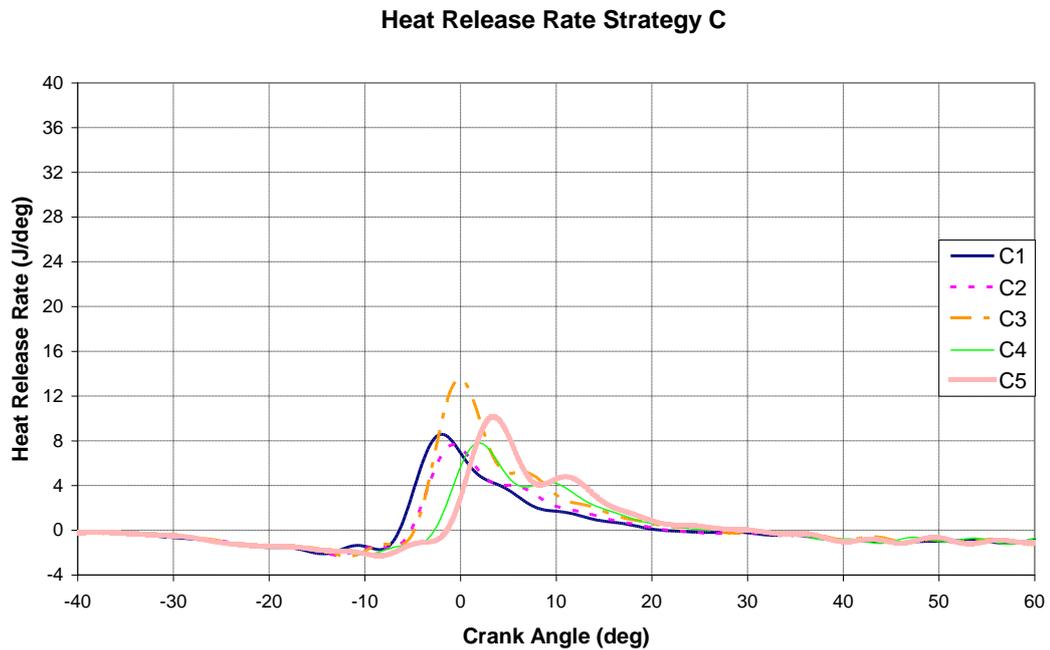


Figure 5.30 Heat release rate curves for experiments in Strategy C at 800 bar

5.5.3.2 C3 Injection and Combustion Visualization

The high speed injection and combustion imaging sequence for experiment C3 is shown in Figure 5.31. The first injection appears normal in the images as in the other cases with 800 bar injection pressure, with less spray penetration than for an injection

pressure of 1200 bar. The second injection is detected at 3.6° CA BTDC when it should be at 5° CA BTDC and by frame 1.2 BTDC it has already finished. This reduction of injection duration and therefore quantity injected into the cylinder is due to the negative effect of the pressure wave created after the first injection (see Section 5.5.4). As predicted previously and as evidenced by the low IMEP values measured for this strategy, the fuel quantity injected during the second injection is much lower than expected and therefore poor combustion and performance is shown for this strategy of the 12° CA dwell angle at the 800 bar injection pressure.

Looking at the combustion images, the first flames appear at 1.2 BTDC, a few crank angles later than the SOC shown in the heat release rate. By TDC, some very low luminosity flames are present in the cylinder (characteristic of the premixed combustion) which is in agreement with the heat release rate analysis. At TDC some more luminous flames appear due to the more diffusive combustion. By 4.8 ATDC frame, six flames spots appear slightly downstream of the spray following the swirl motion with high luminosity as at this crank angle, combustion is in the full diffusion phase, which agrees with the heat releases rate traces. From 8.4 ATDC frame, combustion is entering its last phase and it starts extinguishing.

From Table 5.9 it can be seen that the value of the uHC emission is very low, which means that most of the fuel has burned during combustion. The high speed imaging shows that the amount of fuel injected is much lower than expected and hence the very low values of IMEP.

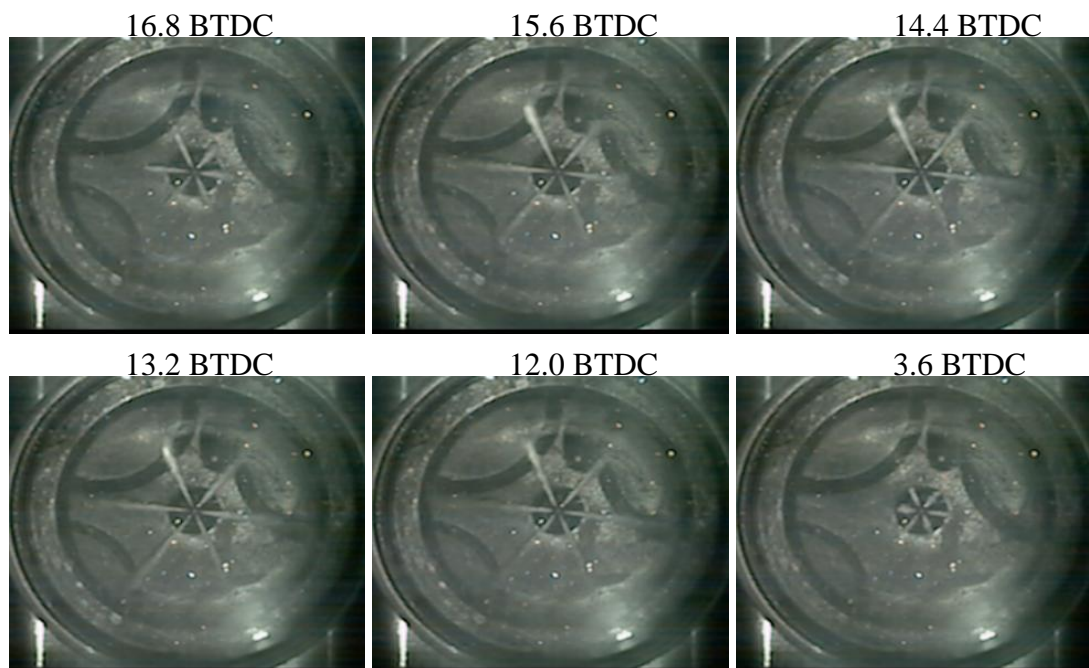


Figure 5.31 Combustion Images Sequence Strategy C3 at 800 bar

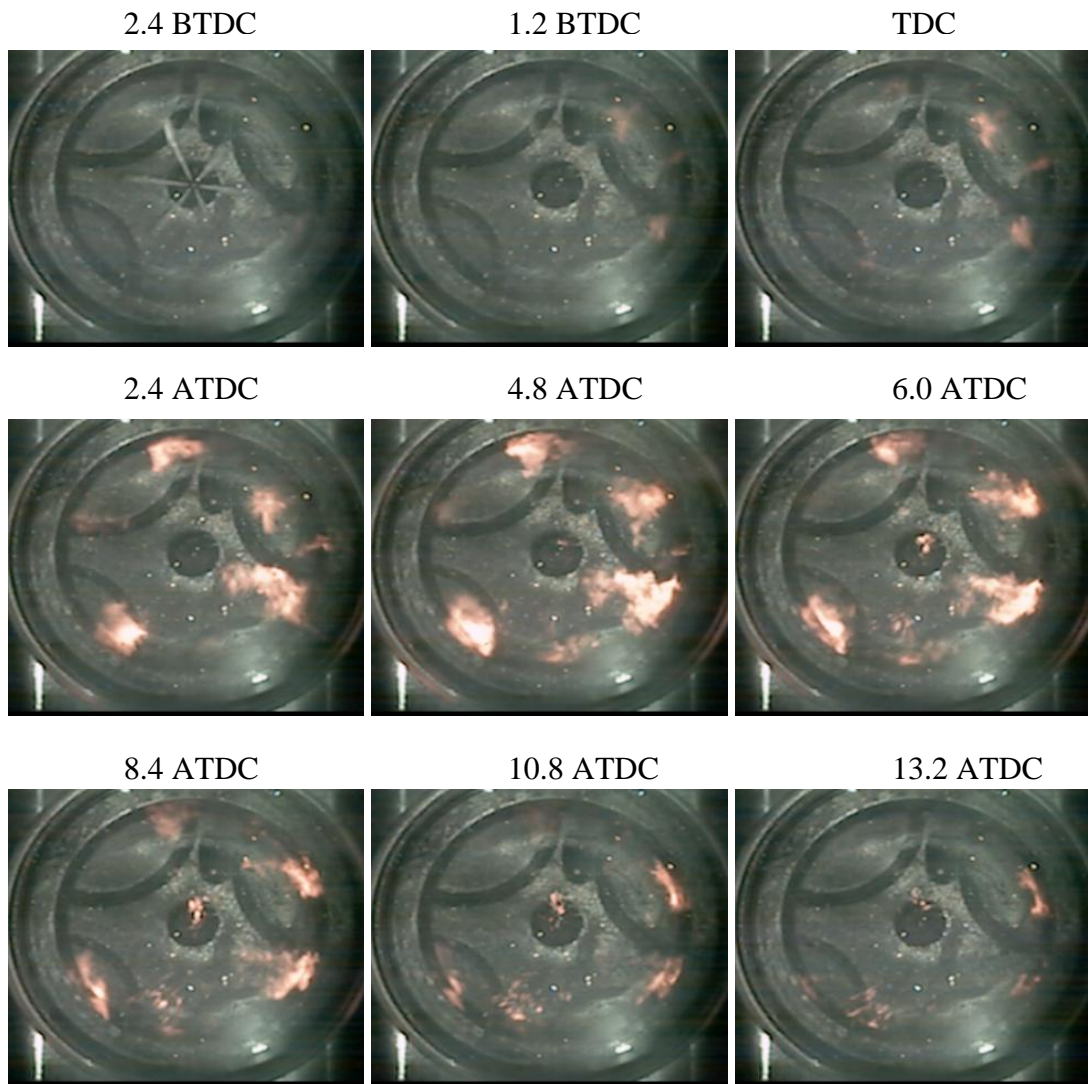


Figure 5.31 Combustion Images Sequence Strategy C3 at 800 bar (cont'd)

5.5.3.3 C3 Flame Temperature and Soot Concentration (KL factor) Measurements

Figure 5.32 shows the flame temperature and KL factor measurements for injection timing C3, as part of the 12°CA dwell angle strategy. The first luminous flames in the high speed imaging appear from 1.2° CA BTDC onwards, which matches with the results obtained by the two-colour method. These first stages of combustion are dominated by the premixed phase where high flame temperatures are prevailing. This is shown in frames TDC and 1.2 ATDC where there are some flame spots at which the flame temperature reaches around 2500 K. From 4.8 ATDC frame (when the diffusion combustion has already started) it can be seen that the flame temperature is mostly below 2000 K. The KL factor measurements show almost no soot formation during the premixed combustion but from 4.8° CA ATDC onwards there are some points in which

there is some soot forming. These are probably rich mixture regions during the diffusion combustion phase.

The soot and NO_x emission values for strategy C are generally very low because the combustion taking place is burning less fuel than expected. The highest NO_x emissions are shown in injection timing C3, as it is the experiment producing more complete combustion around TDC and with higher temperatures.

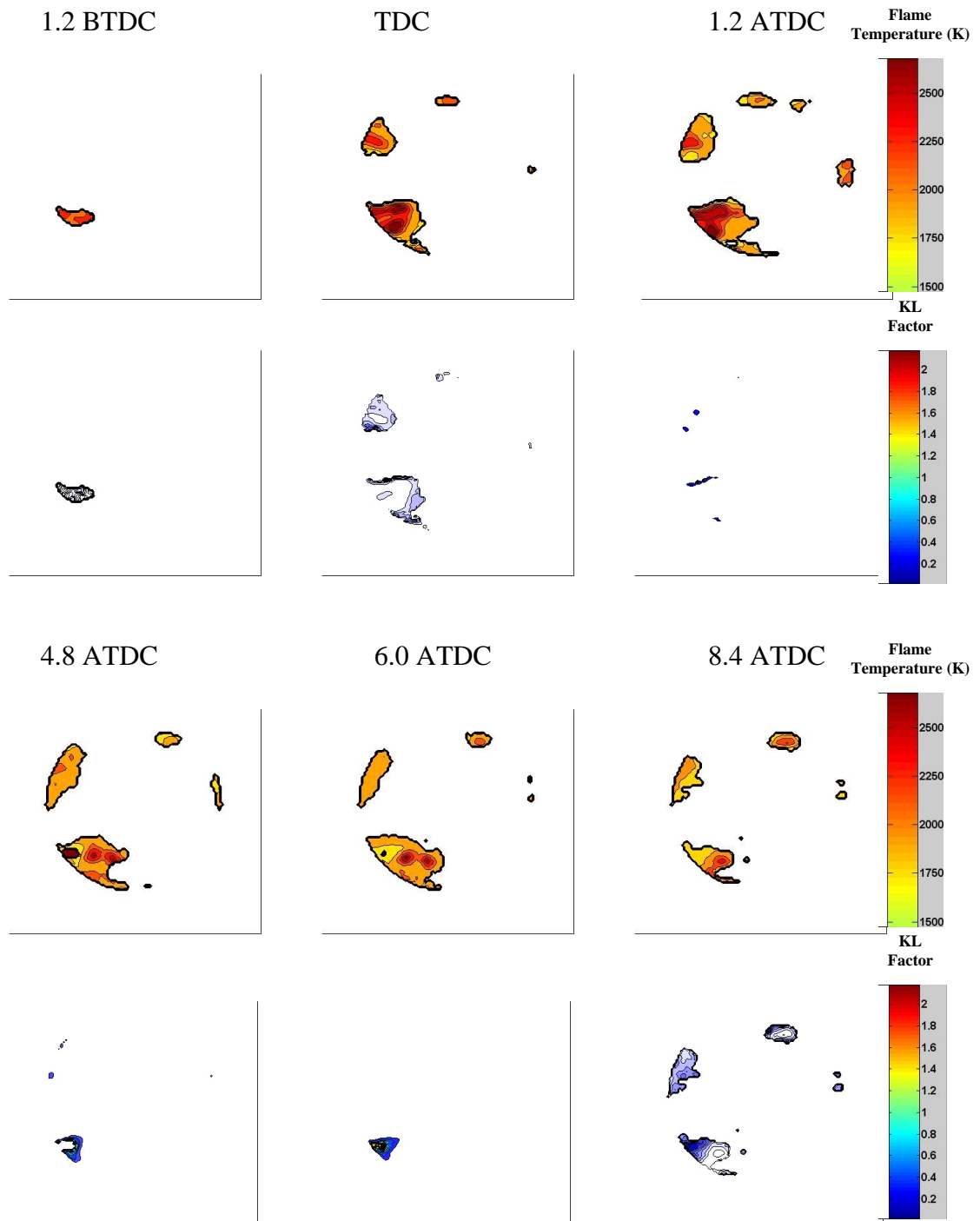


Figure 5.32 Flame Temperature and KL factor images sequence for C3 at 800 bar

5.5.4 Strategy D

As discussed in Section 5.4.3, the pressure wave created in the injector after the end of the first injection led to the inability of a second injection at 1200bar. A similar phenomenon was also experienced at 800bar. Figure 5.33 shows the pressure wave and injector signals for the five timings of strategy D at 800 bar. Strategy D shows no second injection and for strategy C, although it shows second injection as seen in the previous section, less fuel enters into the chamber and at a later time than expected. For both strategies, the injection signal for the second injection occurs at the lower edge of the pressure wave.

Strategy E showed second injection during this test. However, similar to strategy C, during the high speed imaging, the second injection appears later than expected (see Section 5.5.5).

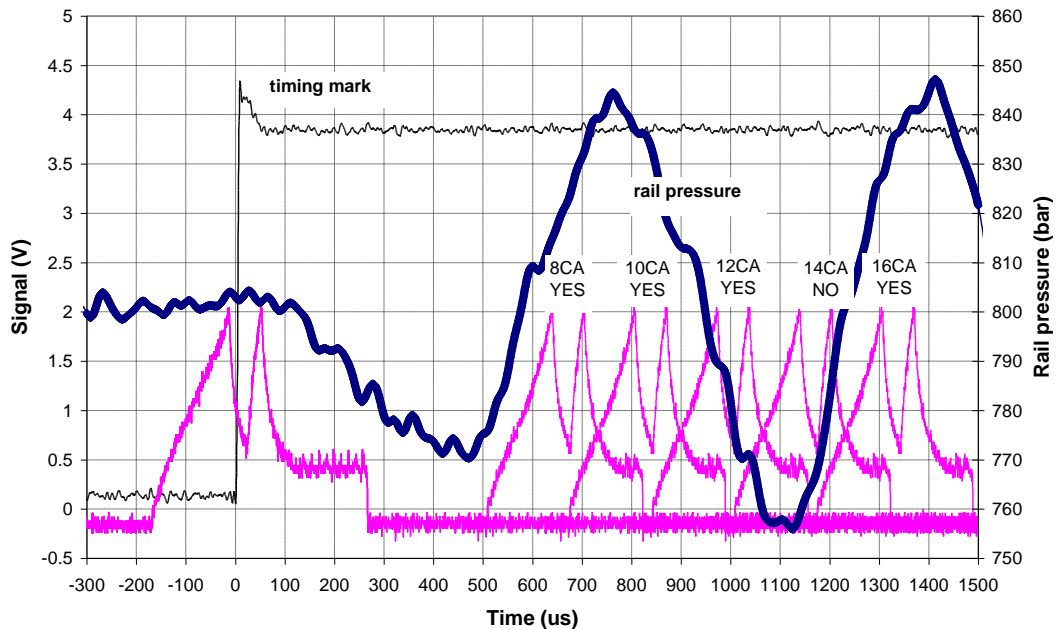


Figure 5.33 Injector signals and pressure wave at the injector for 800 bar

As stated in Section 5.4.3, the injection timing and quantity is affected by the pressure wave. Although it is not clear by the pressure wave measurements, the falling pressure apparently and according to the injection system’s manufacturer is the cause of the injection problem. According to this, at 800 bar, the pressure wave created is of less magnitude and therefore, injection takes place in more strategies but with an effect in quantity.

5.5.5 Strategy E

5.5.5.1 Effects of Injection Timing on Performance and Emissions

The combustion characteristics, engine output and emissions values for strategy E are shown in Table 5.10.

Table 5.10 Injection, Combustion and Emissions Characteristics of Strategy E, 800 bar

| Strategy E | | | | | | | | | | | |
|-------------|-------------|-------------------------------|---|------------|------------|-------------------------|-------------------------|---------------|-----------|-----------|------------|
| Dwell Angle | Test Number | SOI (1st injection) (CA BTDC) | SOI (2 nd injection) (CA BTDC) | IMEP (bar) | Combustion | | | | EMISSIONS | | |
| | | | | | SOC | 1 st ID (CA) | 2 nd ID (CA) | Duration (CA) | HC (ppm) | NOx (ppm) | Soot (FSN) |
| 16 | E1 | 25 | 9 | 0 | 4.0 BTDC | 21.0 | 7.0 | 28.8 | 506 | 5 | 0 |
| | E2 | 23 | 7 | 0 | 4.4 BTDC | 18.6 | 4.6 | 29.2 | 383 | 9 | 0.04 |
| | E3 | 21 | 5 | 0.2 | 3.4 BTDC | 17.6 | 3.6 | 27.4 | 343 | 15 | 0.11 |
| | E4 | 19 | 3 | 0.2 | 3.0 BTDC | 16.0 | 2.0 | 26.8 | 322 | 15 | 0.03 |
| | E5 | 17 | 1 | 0.3 | 1.6 BTDC | 15.4 | 1.4 | 26.2 | 305 | 4 | 0.19 |

From Table 5.10 it can be seen that for all injection timings of strategy E, the engine output is zero or very low which indicates almost no combustion. In Section 5.5.5 it was indicated that second injection was detected for this strategy. However in the following sections it will be shown that injection is negatively influenced by the pressure wave. Similarly to strategy C, the start of the second injection takes place later than expected and almost no fuel enters into the chamber; this is why there is almost no combustion.

Looking at the cylinder pressure traces from Figure 5.34, it can be noticed that for the first four injection timings the cylinder pressure follows the motoring pressure until almost TDC; it then continues at the same rate before stopping and decreasing following the motoring pressure again. Only experiment E5, which is the most retarded injection timing, shows a quick increase of the pressure after TDC due to the premixed combustion. This rise lasts for only 3° CA to reach a maximum, following similar trends to the other experiments.

Figure 5.35 illustrates the heat release rates for strategy E. The first injection timing E1 shows the SOC around 4° CA BTDC and the increase in the heat release is determined by diffusion combustion since no rapid rise of the premixed combustion is observed. As injection is retarded, the premixed combustion phase last longer. For experiment E5, the heat release rate shows a quite rapid increase from the SOC at 1.6° CA BTDC until 3° CA ATDC which is characteristic of premixed combustion; it then decreases before starting to increase again at 7.2° CA ATDC as diffusion combustion takes place. However, the heat release rate of this experiment is very low and its peak is only 8 J/deg; from 20° CA ATDC the last combustion phase occurs where the remaining available fuel burns.

The high speed imaging sequence for this injection timing is shown in the next section, where the problem of the second injection is confirmed.

Similar to strategy E at 1200 bar, at this dwell angle the first experiments with earlier injection show very poor combustion. The mixing process is poor and this explains the higher uHC emissions and minimum IMEP. As injection is retarded, the fuel enters into the cylinder where gas is at higher temperature and pressure which improves the mixing process and, therefore, combustion. Table 5.10 shows that for the last 3 experiments of this strategy the uHC emissions are reduced compared to the first two injection timings. However compared with strategy E at 1200 bar, the IMEP values are reduced on average by 70%. Part of this low performance is due to the poorer mixing processes that

take place at 800 bar injection pressure and it also can be due to the different quantity of fuel injected due to the adverse effect of the pressure wave.

Comparing this strategy with strategy A and B at 800 bar, it shows the lowest IMEP values probably due to the lower amount of fuel injected during the second injection and the poorer mixing process as dwell angle is increased.

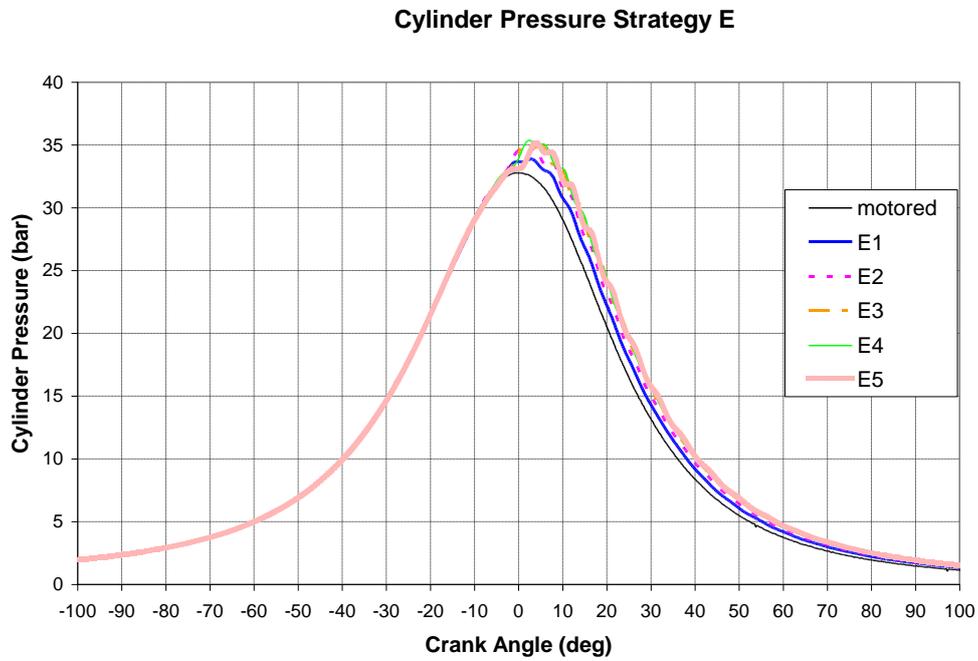


Figure 5.34 Cylinder pressure traces for experiments in Strategy E at 800 bar

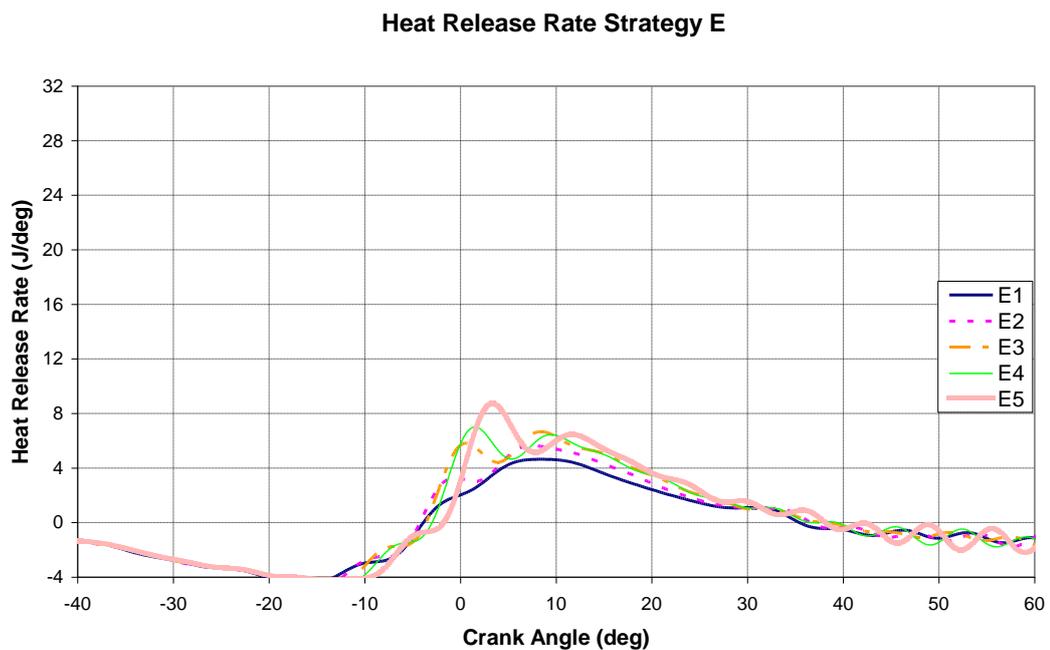


Figure 5.35 Heat release rate curves for experiments in Strategy E at 800 bar

5.5.5.2 E5 Injection and Combustion Visualization

Figure 5.36 displays the injection and combustion imaging sequence for experiment E5 at 800 bar. The frames show the first injection where it can be noticed that the spray penetration is much lower than for the 1200 bar injection pressure experiments. Frame 1.2 BTDC shows the start of the premixed combustion. At TDC the second injection should be seen, however the start of the second injection is seen after TDC. This delay in the start of the second injection is caused by the negative effect of the pressure wave. At frames 2.4 and 3.6 ATDC some small spots of premixed combustion can be noticed in the cylinder which show the injection spray burning in an over rich diffusion combustion. From frame 7.2 ATDC, as the heat release rate shows, only rich diffusion combustion takes place until approximately 18° CA ATDC when the burning rate slows down as the available fuel is reduced.

Due to the reduction of the fuel injected in the second injection the IMEP values achieved for this experiment and for strategy E are in general very low. The rich diffusion combustion leads to higher soot emissions and, although for injection timing E5 the soot emissions are low, they are the highest among the experiments within this strategy.

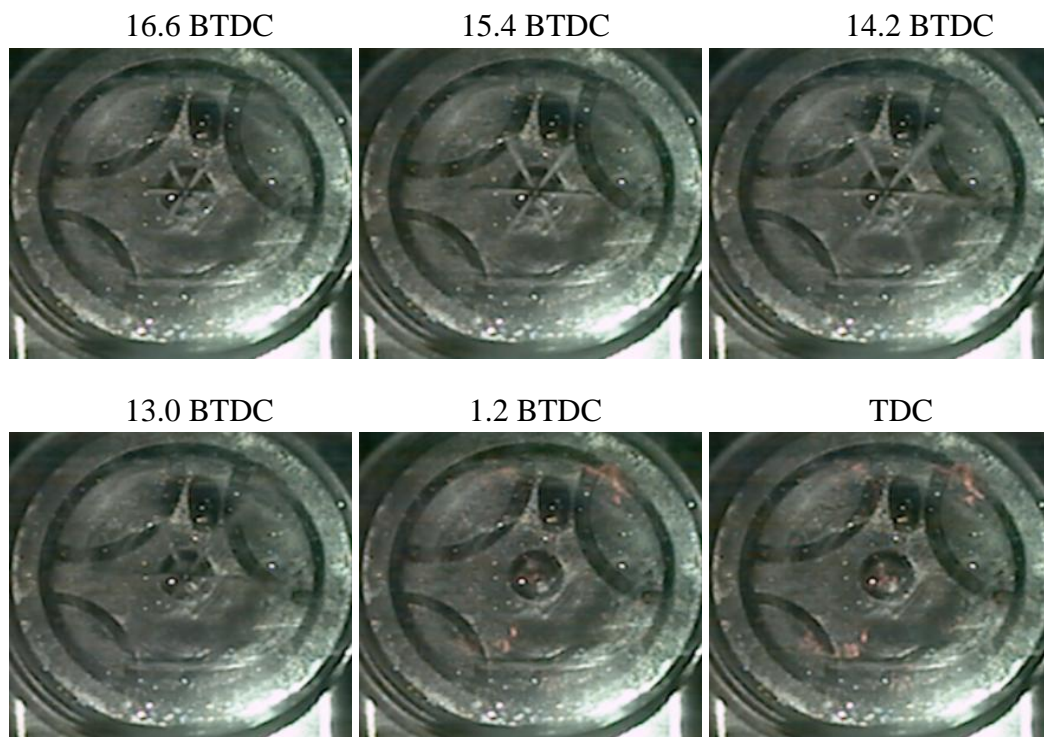


Figure 5.36 Combustion Images Sequence Strategy E5 at 800 bar

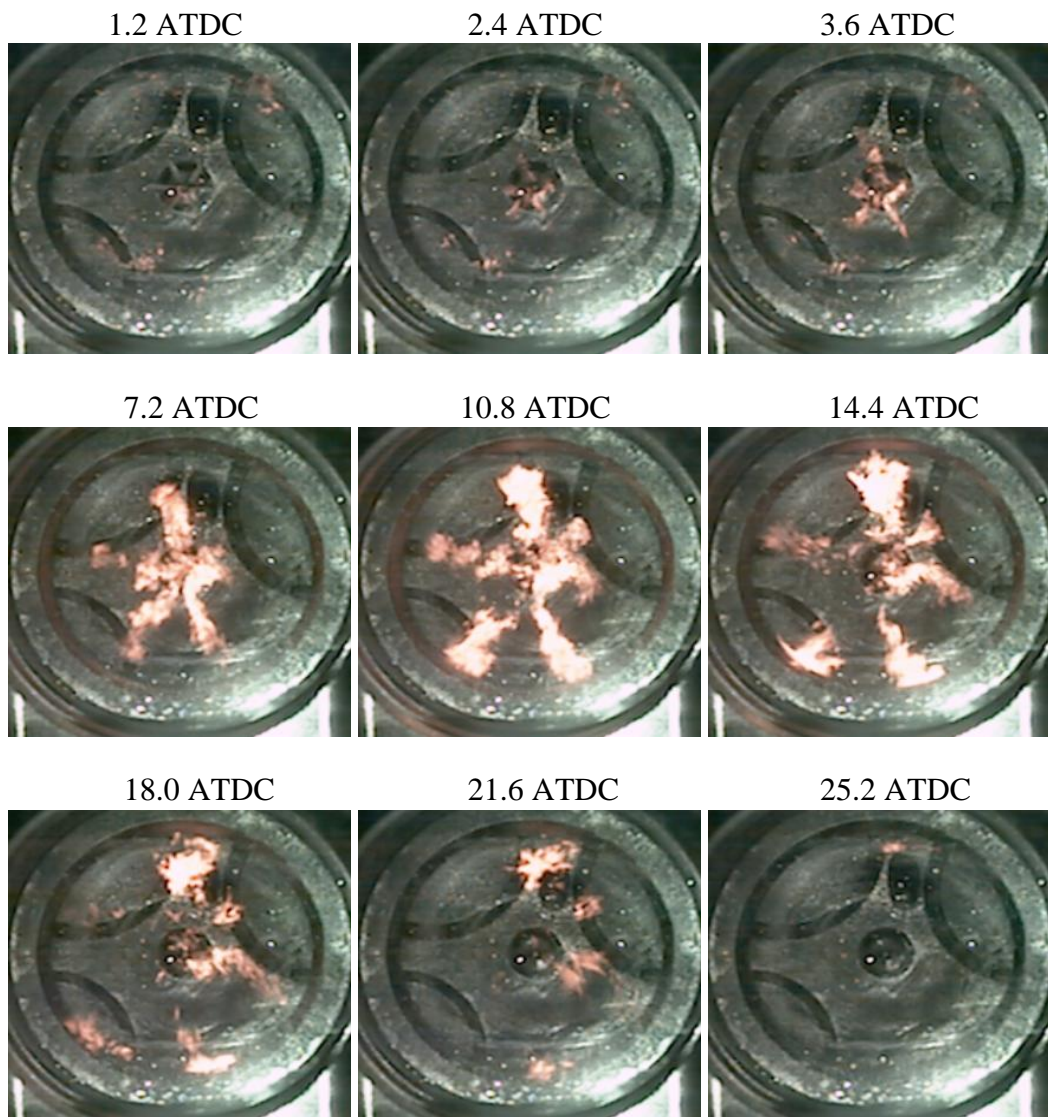


Figure 5.36 Combustion Images Sequence Strategy E5 at 800 bar (cont'd)

5.5.5.3 E5 Flame Temperature and Soot Concentration (KL factor) Measurements

The two-colour method was applied for this experiment in order to estimate the flame temperature and soot concentration as given by the KL factor which are shown in Figure 5.37. The first stages of the premixed combustion where very little soot radiation is emitted show a very small flame at high temperature. At frame 3.6 ATDC when the heat release rate analysis showed the peak, the flame temperature reaches the highest value of over 2500K located near the injector downstream of the spray. Although high flame temperatures are shown, they occur at over rich areas and therefore no much NO_x is formed as seen in Table 5.10.

The KL factor images sequence show soot formation at the leading edges of the diffusion combustion, but without reaching very high values probably because the amount of fuel injected during the second injection and its burning is lower than expected.

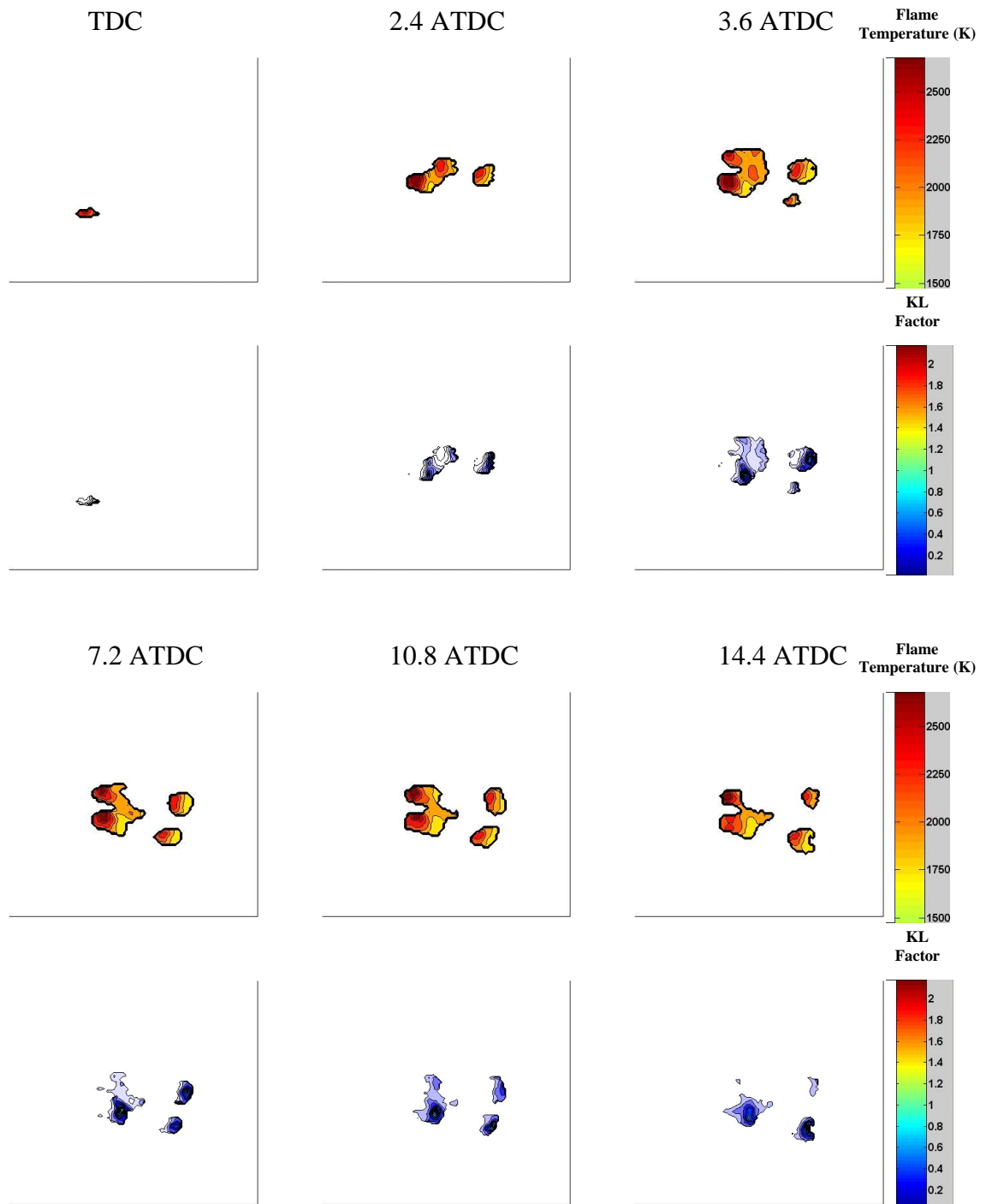


Figure 5.37 Flame Temperature and KL factor images sequence for E5 at 800 bar

5.5.6 Conclusions for Strategies at 800 bar

- Strategy A. Among the strategies investigated at the 800 bar injection pressure, A shows the highest IMEP values. Compared with strategy A at 1200 bar, it shows very inferior performance. The mixing process at 800 bar injection pressure is very poor, leading to a very small amount of fuel mixed during the premixed combustion while most of the fuel burns in the diffusion phase during the expansion stroke when the piston is moving downwards and the engine is not getting the most efficient work out of its motion.
- Strategy B. Experiments B1 and B2 show the highest IMEP values among strategy B, where there is more premixed combustion and more efficient work is done over the piston; however these injection timings represent a reduction of about 25% in IMEP with respect to the best injection timing among strategy A. As injection is retarded, more diffusion combustion occurs and lower IMEP values are obtained.
- Strategy C shows poor engine output due to the failure to produce the right amount of fuel during the second injection; this is due to the negative effect of the pressure wave. Injection timing C3 showed the highest IMEP values among the experiments for the 12 CA dwell angle as the main combustion takes place around TDC maximising the work done on the piston.
- Strategy D, similarly to the 1200 bar injection pressure, showed no second injection at all and it did not produce any combustion.
- Strategy E, shows minimum performance for the first experiments where the mixing process is very poor. As injection timing is retarded the temperature and pressure in the cylinder are higher and the mixing process improves increasing the engine output. However, overall the engine output is lowest which can be caused primarily by the reduced amount of fuel in the second injection due to the negative effect of the pressure wave generated from the first injection.

The split injection strategies investigated in this study involved low dwell angles and injections close to TDC. In order to perform properly it is very important to maximise the fuel/air mixing rate. Due to the low mixing rate, the 800 bar injection pressure proved not to be convenient for the split injection applications.

Chapter 6 Split Injection Studies for Bio-diesel Fuels

6.1 Introduction

This chapter details the investigation carried out with split injection using two bio-diesel fuels. The experimental techniques employed for this investigation are the same as the techniques for the base diesel explained in Chapter 5.

6.2 Alternative Fuels

Currently, bio-diesel fuels are based on vegetable or plant oils and they are known as the first generation bio-diesels. In order to minimise their interference with food supply and to widen their source of supply, second generation bio-diesel fuels will be produced from bio-mass that is non-edible and is more abundant. For this investigation two such bio-diesel fuels have been studied; these bio-diesels are called BTL (Biomass to liquid fuels), in which the biomass is gasified to syngas before being converted into liquid hydrocarbons by the Fischer-Tropsch process which is a catalyzed chemical reaction in which carbon monoxide and hydrogen are converted into liquid hydrocarbons of various forms. Generally the catalysts used are based on iron and cobalt.

The tested fuels are BTL 46 and BTL 50, both supplied as part of the EU NICE project by Brunel University's sub-project group partner.

In order to investigate the same dwell angle strategies, the injection timings were kept constant throughout the experiments. It is important to highlight that due to the differences in density and calorific value between the fuels, the amount of energy injected in the cylinder was not constant and this could influence the engine performance and combustion characteristics.

Table 6.1 shows the fuel properties of these fuels, as well as the amount of energy injected for each fuel. It is important to notice some major differences regarding the physical properties of these BTL fuels with respect to base diesel. These bio-diesel fuels are more volatile with much lower boiling temperatures which improves fuel vaporization after injection and therefore fuel/air mixing. Other important physical properties are the sulphur content and the aromatic compounds content, the former has an important effect reducing the sulphur oxides emissions; however, fuel injection equipments (FIE) are lubricated by the diesel fuel and the reduction of sulphur content may affect the durability and functionality of the equipment. Similarly, the aromatic compounds have an effect on the lubricity of the fuel. The advantage of the reduction of

the aromatic compounds in the fuel can be expected in the soot exhaust emissions. During the combustion, pyrolysis processes form aromatics that grow to form polycyclic aromatic hydrocarbons (PAHs) which grow to form soot particles. As the aromatic compounds percentage of the BTL fuels investigated in this study is zero, very low soot exhaust emissions should be expected.

Table 6.1 Fuel Properties

| | Base Diesel | BtL 46 | BtL 50 |
|--|-------------|--------|--------|
| Cetane Number | 49.1 | 46.0 | 50.0 |
| CV [MJ/kg] | 42.50 | 43.58 | 43.54 |
| Density [kg/m ³] | 853.8 | 703.9 | 711.1 |
| Kinematic Viscosity at 40°C [mm ² /s] | 2.56 | 0.58 | 0.76 |
| Sulphur Content [ppm] | 1900 | 6 | <1 |
| Aromatics [%] | 25.1 | 0 | 0 |
| Saturates [%] | 72.4 | 81.9 | 81.9 |
| Flash Point [°C] | 71 | -15 | -18 |
| Initial Boiling Point [°C] | 169.0 | 51.2 | 57.1 |
| 10% Volume Recovered @ °C | 213.5 | 87.8 | 93.9 |
| 50% Volume Recovered @ °C | 279.0 | 118.8 | 123.5 |
| 90% Volume Recovered @ °C | 343.0 | 150.1 | 164.2 |
| Final Boiling Point [°C] | 371.5 | 175.8 | 225.3 |
| Total Injection Quantity [mm ³] | 9.25 | 9.25 | 9.25 |
| Total Energy Injected [J/inj.] | 335.6 | 283.7 | 286.4 |

6.3 Test Conditions

Test conditions were the same as for the investigations with base diesel. Due to limited BTL fuel quantities, optical studies were performed at a few selected conditions based on engine experiments with the metal piston. Table 6.2 lists the test conditions for the detailed in-cylinder study.

Table 6.2 Test Conditions for alternative fuels investigation

| Test Conditions | |
|--------------------|--|
| Engine Speed | 2000 rpm |
| Intake Air | 140°C 0.5 bar boost |
| EGR | 60% (N ₂) |
| Fuel | BTL50 AND BTL 46 |
| Fuelling | 9.25 mm ³ total (70%/30%) |
| Injection duration | 4.5° CA 1st injection 3.8° CA 2nd injection |
| Air flow rate | 323 l/min |
| Load | ≈27 % of full load |
| Injection Pressure | 800 bar, 1200bar |
| Piston Bowl | Glass (optical techniques) Metal (emissions) |

6.4 Injection Rate Experiments

The bio-diesels investigated here have different properties compared to the base diesel fuel. Some properties like the bulk modulus, density or viscosity, can influence the amount of fuel injected. Therefore, measurements of the fuel injection rate were carried out in an injection rig that was developed at Brunel based on the Zeuch method [127].

In the Zeuch method, the amount of fuel injected can be calculated under constant volume conditions by measuring the increase of pressure through the following equation:

$$Pr = K \frac{V}{V_o} \quad (6.1)$$

Where:

Pr: pressure rise

K: bulk modulus

V_o : volume of chamber

The injection rate dV/dt is calculated by differentiating Equation 6.1 with respect to time t , as follows:

$$\frac{dV}{dt} = \frac{V_o}{K} \frac{dPr}{dt} \quad (6.2)$$

6.4.1. Injection Rate Test Rig

The experiments were carried out in a recently developed test rig at Brunel University. A schematic of the test rig and its components can be seen in Figure 6.1

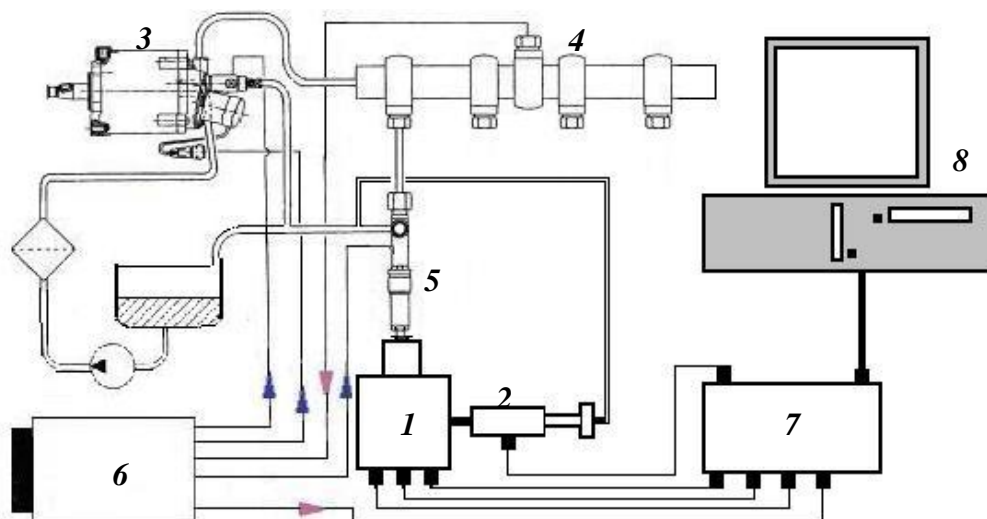


Figure 6.1 Schematic View of the Injection Rate Test Rig

The components and the procedure of the experiments are as follows:

- Constant volume high pressure chamber (1): 3 pressure sensors measure the back pressure as well as the pressure rise (high and low sensitive pressure rise that allows measuring the pressure of single or split injection). A solenoid valve (2) keeps the pressure in the chamber and closes just before each injection in order to capture the pressure rise.
- Fuel system consisting of a high pressure pump (3): a common rail (4) and injector (5). The high pressure pump is driven by an AC electric motor.
- EmtroniX ECU (6): the motor and injection system are controlled by the ECU via a PC. The ECU operates in the simulation mode that generates the engine speed required for the experiments. As in the experiments in the single cylinder optical engine, the EmtroniX controls the injection pressure as well as the injection timing and duration.
- The data acquisition system: the pressures are recorded by a NI interface board (7) and A/D card using a LabVIEW program (8). The program is triggered by the ECU, which then sends the signal to close the solenoid valve just before the injection and the pressure rise, back pressure, rail pressure and injection timing are recorded and saved in an excel file for further analysis.

6.5 Injection Strategies Studied for BTL 50

From Chapter 5, where all strategies were investigated, strategies A, B and E at 1200 bar injection pressure were selected to be investigated for the alternative fuels BTL 46 and BTL 50. Strategy A represents the smallest dwell angle of 8° CA and strategy B corresponds to an increase of 2° CA and finally strategy E has a 16° CA dwell angle.

6.5.1 Strategy A

6.5.1.1 Effect of Injection Timing on Performance and Emissions

Table 6.3 shows the details of strategy A, injection timing, combustion performance and emissions.

Table 6.3 Injection, Combustion and Emissions Characteristics of Strategy A for BTL 50, 1200 bar

| Strategy A | | | | | | | | | | | |
|--------------------|--------------------|---|---|-------------------|-------------------|-------------------------------|-------------------------------|----------------------|------------------|------------------|-------------------|
| Dwell Angle | Test Number | SOI (1st injection) (CA BTDC) | SOI (2nd injection) (CA BTDC) | IMEP (bar) | Combustion | | | | EMISSIONS | | |
| | | | | | SOC | 1st ID (CA) | 2nd ID (CA) | Duration (CA) | HC (ppm) | NOx (ppm) | Soot (FSN) |
| 8 | A1 | 19 | 11 | 2.4 | 3.8 BTDC | 15.2 | 7.2 | 21.6 | 441 | 50 | 0.35 |
| | A2 | 17 | 9 | 1.8 | 3.2 BTDC | 13.8 | 5.8 | 17.8 | 390 | 43 | 0.07 |
| | A3 | 15 | 7 | 1.4 | 1.4 BTDC | 13.6 | 5.6 | 15.2 | 400 | 32 | 0 |
| | A4 | 13 | 5 | 1.2 | 0.2 ATDC | 13.2 | 5.2 | 14.2 | 590 | 26 | 0.01 |
| | A5 | 11 | 3 | 1.6 | 1 ATDC | 12.0 | 4.0 | 17 | 630 | 28 | 0 |

Figure 6.2 shows the cylinder pressure data obtained for strategy A. The pressure line of strategy A1 follows the motoring pressure until 0.4° CA BTDC where it experiences a very rapid increase due to the premixed combustion. This very quick increase peaks at 3.4° CA ATDC with a value of almost 53 bar. Pressure decreases rapidly until 15° CA ATDC and then falls gradually afterwards. This strategy gives the highest IMEP value recorded of 2.4 bar. Strategy A2 follows the motoring pressure until 0.4° CA BTDC, exactly at the same point as the previous strategy, but the pressure rise is slightly slower and reaches a lower peak pressure of 48 bar at 7.2° CA ATDC. The decrease of pressure occurs in a similar way like A1 but with lower values during the expansion stroke; this explains the lower IMEP value of 1.8 bar. Looking at the rest of the strategies, they all follow similar trends in the expected ignition delay as injection is retarded 2° CA in each case. A3 shows the first rapid increase at 1.8° CA ATDC while A4 and A5 at 3.8 and 5.2° CA ATDC respectively. The rise is slower and A3 peaks at 7.4° CA ATDC while A4 and A5 achieve the maximum pressure at 9.2 and 10.8° CA ATDC. The values of the maximum pressure decrease from 44 bar for A3 to 41 bar for A4 and 40.5 bar for A5. Pressure traces in these three cases follow the same line over the expansion stroke. As a consequence the IMEP values are lower than in the first two strategies, with 1.4 bar, 1.2 bar and 1.6 bar for A3, A4 and A5, respectively.

Comparing cylinder pressure data from BTL 50 fuel with base diesel for strategy A shows that the increase in pressure due to the premixed combustion occurs more rapidly with BTL 50, reaching higher values. This is probably because more fuel has mixed before the SOC and, therefore, more fuel burns in the premixed phase. This is consistent with the combustion duration results in Tables 5.3 and 6.3, which show that for BTL 50 combustion duration is a few crank angles shorter than for base diesel. As stated in Table 6.1 the amount of energy introduced in the chamber for the BTL 50 experiments is 286.4 J/inj. which represents a reduction of 15% compared with the base diesel. For strategies A2 to A5, BTL 50 gives lower IMEP values than base diesel representing a reduction between 20% and 45%. However, for A1 the IMEP is higher since at this injection timing the peak cylinder pressure for BTL 50 was 53 bar which represents a 25% increase with respect to A1 with base diesel.

Figure 6.3 shows the heat release rate for strategy A. Similarly to the cylinder pressure, experiment A1 clearly differs from the rest of the experiments in that its heat release rate exhibits a first increase approximately at 11° CA BTDC, although it corresponds to the second injection timing, it is probably due to the pre-combustion reactions of the

fuel injected during the first injection. This increase lasts until 7.2° CA BTDC, when the second injection has finished and its cooling effect starts taking place. At 4.6° CA BTDC a rapid increase of heat release rate due to the premixed combustion is evident. It reaches a peak at 1° CA ATDC achieving a value of $46\text{J}/^\circ$ CA and then it decreases rapidly as the premixed phase is decaying. After the premixed combustion, the heat release rate increases to reach a second peak, but this time a very low one compared to the first peak of the diffusion combustion. Experiments A2 to A4 show a similar pattern in their heat release rate curves. There is no apparent cooling effect after the first injection and the first noticeable effect is a small and slow increase due to the pre-combustion reactions. This rise is inhibited by the cooling effect of the second injection which lasts for about 3° CA until the heat release rate curves show a rapid increase at $4.6, 2.4, 0.8^\circ$ CA BTDC for A2, A3 and A4 and at 0.8° CA ATDC for A5. The increase for A2 is quite rapid similar to A1 although it reaches a much lower value of just $33\text{ J}/^\circ$ CA. As injection timing is retarded, the slope of the rise becomes less steep as if the premixed combustion phase is shorter and more is fuel burnt as diffusion combustion. This can be explained in Table 6.3; as injection timing is retarded the ignition delay decreases which implies that less fuel is available to burn as premixed combustion and more fuel burns during diffusion combustion. As expected, NO_x emissions are reduced as injection timing is retarded.

Results in Table 6.3 show that the IMEP values for strategy A (except A1) are lower than for base diesel. A small reduction is expected due to the lower energy injected inside the cylinder, but the reduction in performance is quite higher. However, the emissions values are decreased. The uHC emissions are approximately 400 ppm while for the base fuel they are about 700 ppm. Due to the more volatile nature of BTL50 fuel, more combustion takes place in the premixed phase. The soot emissions for this strategy are unnoticeable and only A1 injection timing shows a FSN number of 0.35. The NO_x emissions are also very low, ranging from 50 to 30 ppm, which represents a reduction between 15 and 30 % compared to strategy A with base fuel.

As A1 demonstrates the highest IMEP among strategy A experiments, it was chosen for further analysis of combustion by means of flame visualization and by the two-colour method for flame temperature and soot concentration (KL factor) measurements.

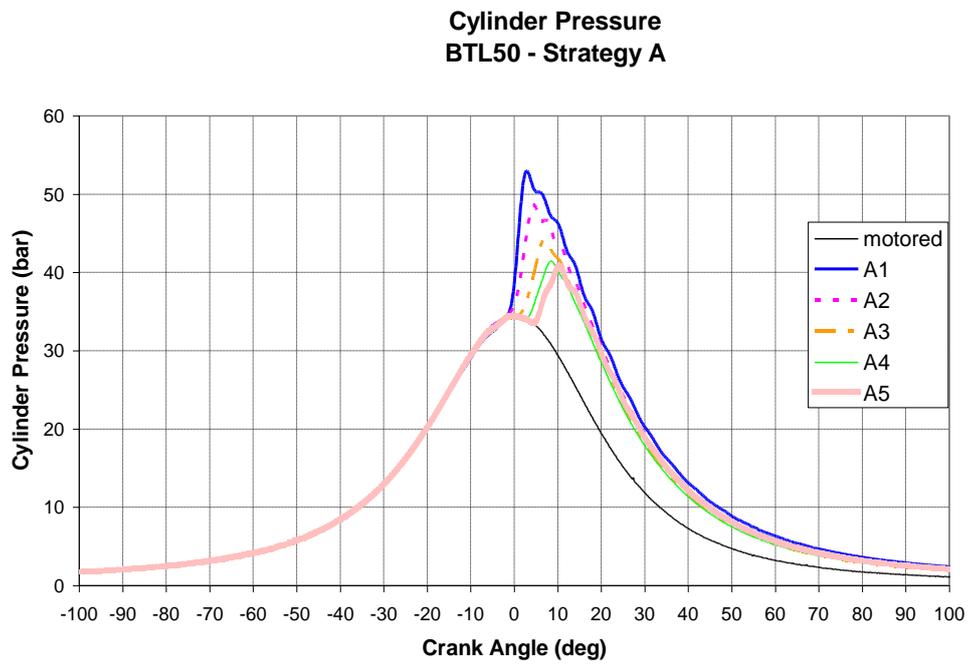


Figure 6.2 Cylinder pressure traces for BTL 50 experiments in Strategy A at 1200 bar

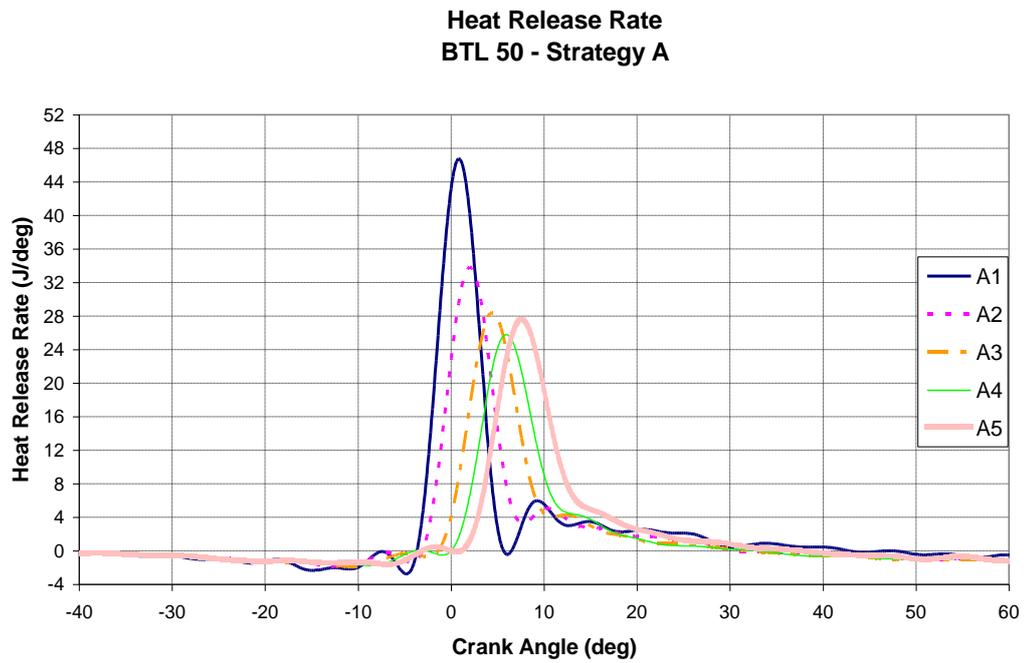


Figure 6.3 Heat release rate curves for BTL 50 experiments in Strategy A at 1200 bar

6.5.1.2 A1 Injection and Combustion Visualization

Figure 6.4 shows the combustion images of BTL50 fuel at A1 injection timing. As mentioned earlier, the injection duration was set to 4.5 and 3.8° CA for the first and the second injection, respectively. It can be seen in this figure that the first injection duration is slightly shorter than expected and the same phenomenon occurs for the second injection. This could be due to the nature of the fuel and its properties such as sulphur content, aromatic compounds percentage or bulk modulus. The firsts affect the lubricity and may have a negative effect in the needle movement. After the second injection the first flames become visible at 2.4° CA BTDC. From this point and until 3.6° CA ATDC, combustion appears to be rather homogeneous within the cylinder but with a very low luminosity that is characteristic of homogeneous premixed combustion. Towards the end of combustion, as shown in frames at 8.4 and 12.0 ATDC some fuel dribbling from the nozzle is burned in a rich diffusion flame. Compared with the same strategy with base fuel (Figure.5.3), combustion of BTL50 fuel occurs more homogeneously with faster burning.

Although experiments were planned and carried out to obtain flame temperature and soot concentration (KL factor) measurements for A1, the low soot concentration and low luminosity rendered the two-colour method redundant.

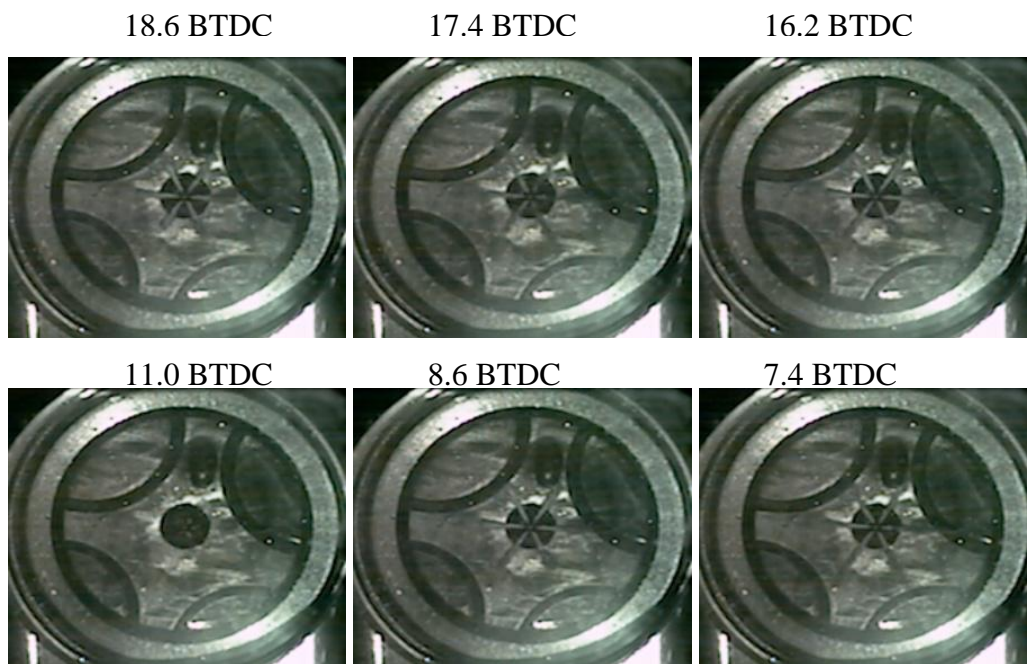


Figure 6.4 Combustion Image Sequence for BTL 50 experiment A1 at 1200 bar

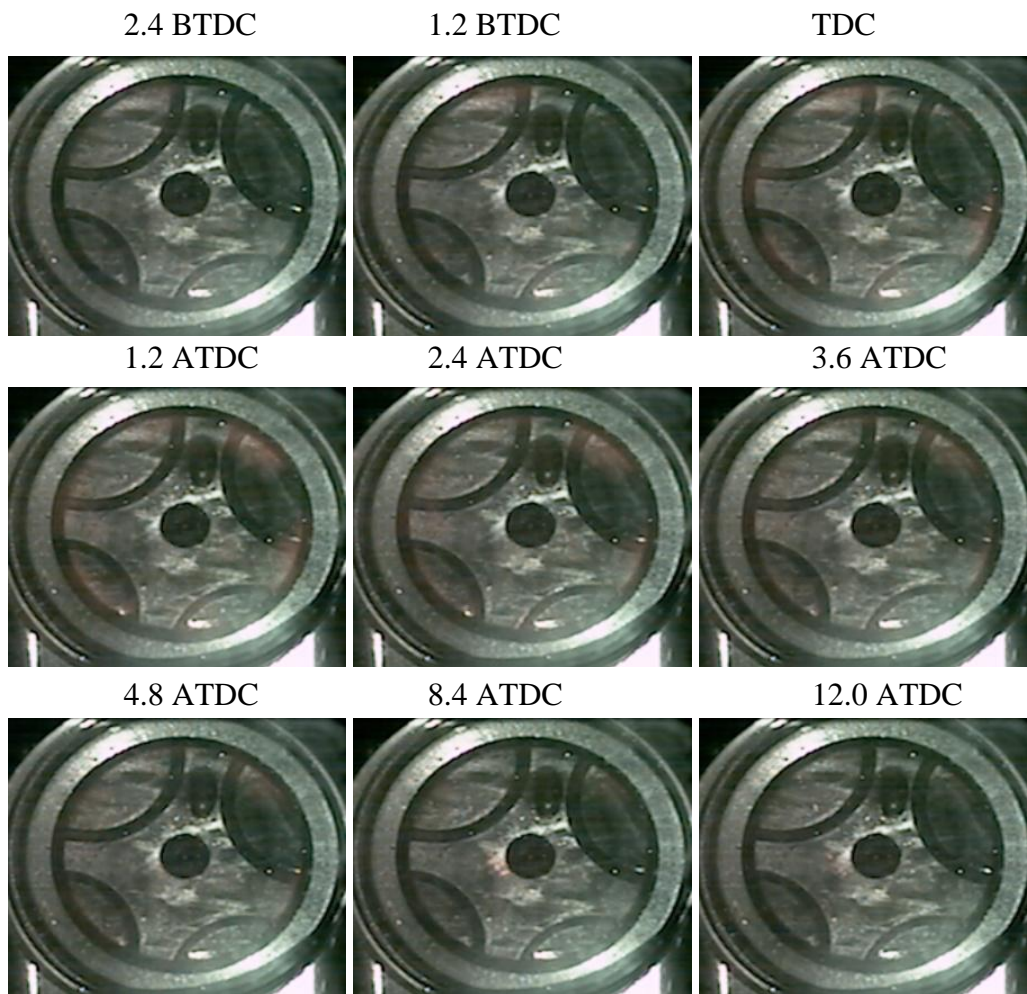


Figure 6.4 Combustion Image Sequence for BTL 50 experiment A1 at 1200 bar (cont'd)

6.5.1.3 Injection rate measurements for strategy A

As previously explained, injection rate measurements were carried out in order to understand the behaviour of the BTL fuel during injection. Figure 6.5 shows the injection rate for strategy A with the base diesel and the BTL fuel. The injector signals are also included in the graph as a reference when the injection is taking place. It is important to highlight that the injector signals do not correspond to the needle lift and are solely used as a reference point.

Injection Rate Strategy A

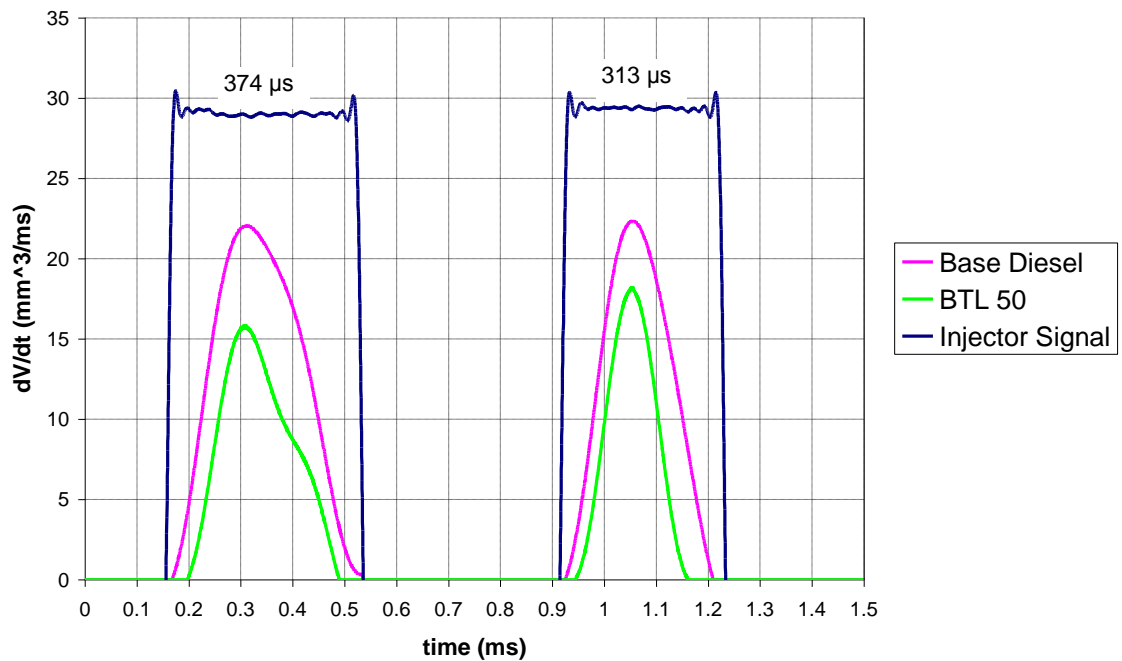


Figure 6.5 Injection Rate Measurements for Strategy A, Base Diesel and BTL 50

The graph clearly shows that the injection duration for the BTL fuel is shorter than expected which matches with the high speed images seen in Figure 6.4. This could be explained by the properties of BTL and its lower lubricity which may affect the opening and closing of the needle. The higher bulk modulus could influence on the injection quantity; the injection rate for diesel shows 5.5 and 3.2 mm^3 for the first and second injection, respectively. The injection rate for BTL is estimated using the same values of bulk modulus as diesel. As indicated in Equation 6.1 a higher bulk modulus value gives a lower injected quantity. The values estimated for BTL 50 are 3.7 and 2.2 mm^3 for the first and second injections which represent 70% of the base diesel injected. This explains the low performance obtained by this fuel in strategy A.

6.5.2 Strategy B

6.5.2.1 Effect of Injection Timing on Performance and Emissions

Table 6.4 summarises the injection and combustion characteristics for 5 different injection timings for the 10° CA dwell angle strategy with BTL 50 fuel. Table 6.4 also includes performance and emissions values for this strategy.

Table 6.4 Injection, Combustion and Emissions Characteristics of Strategy B for BTL 50, 1200 bar

| Strategy B | | | | | | | | | | | |
|--------------------|--------------------|---|---|-------------------|-------------------|-------------------------------|-------------------------------|----------------------|------------------|------------------|-------------------|
| Dwell Angle | Test Number | SOI (1st injection) (CA BTDC) | SOI (2nd injection) (CA BTDC) | IMEP (bar) | Combustion | | | | EMISSIONS | | |
| | | | | | SOC | 1st ID (CA) | 2nd ID (CA) | Duration (CA) | HC (ppm) | NOx (ppm) | Soot (FSN) |
| 10 | B1 | 19 | 9 | 1.0 | 3.8 BTDC | 15.2 | 5.2 | 14.0 | 595 | 30 | 0 |
| | B2 | 17 | 7 | 1.1 | 2.6 BTDC | 14.4 | 4.4 | 14.2 | 575 | 27 | 0 |
| | B3 | 15 | 5 | 1.1 | 1.6 BTDC | 13.4 | 3.4 | 15.2 | 584 | 25 | 0.03 |
| | B4 | 13 | 3 | 1.2 | 0.6 ATDC | 13.6 | 3.6 | 14.6 | 580 | 26 | 0 |
| | B5 | 11 | 1 | 1.3 | 0.8 ATDC | 11.8 | 1.8 | 16.8 | 670 | 23 | 0.11 |

Figure 6.6 shows the cylinder pressure traces for the 5 injection timings studied in strategy B for BTL 50 fuel; table 6.4 includes the calculated ignition delays for the 5 cases. As expected, ignition delays associated with both the first and second injected fuel decrease with retarded injection timing. As the injection timing is retarded the peak cylinder pressure drops but the higher expansion pressure results in greater expansion work and hence higher IMEP values.

Figure 6.7 shows the corresponding heat release rate curves for the five injection timings within strategy B for BTL 50. Following the cylinder pressure traces, the heat release rate curves of the five injection timings are very similar to each other though they are shifted towards the expansion stroke. After the first injection it is very difficult to notice any charge cooling effect. At approximately 6° CA after the start of the first injection, pre-combustion reactions provoke the first and slight increase of the heat release rate. This rise is interrupted by the start of the second injection and as soon as this starts the heat release commences to decrease. The fall of the heat release lasts approximately 2° CA, while fuel from the second injection is mixing with air and getting ready to burn. At this stage is where the different experiments differ slightly. For example, B1 starts increasing rapidly due to the premixed combustion at 4.6° CA BTDC and it reaches the maximum value at 1.8° CA ATDC. It then decreases rapidly until 7° CA ATDC when some diffusion combustion starts that keeps the heat release rate values for a few more crank angles until at 12° CA ATDC in the late combustion phase the heat release decreases gradually. The other noticeable event is that as injection timing is retarded the slope of the heat release rate becomes less steep. This is probably because more diffusion combustion now takes place as ignition delay is shortened.

Comparing strategy A and B, it can be seen in Table 6.3 and Table 6.4 that the IMEP values for strategy B are much lower than for strategy A. Looking at the ignition delays for both strategies, the first ignition delay is very similar in both cases. As the first injection timings are the same, the autoignition is controlled by the mixing process of the fuel injected during the first injection. As the dwell angle for strategy B is 2 CA longer, the mixing time for the fuel injected during the second injection is much shorter. This means that the mixing process at the shorter dwell angle is better leading to more complete combustion and higher IMEP values. Another fact explaining the difference between strategy A and strategy B is the values of combustion duration and uHC emissions shown in Tables 6.3 and 6.4. The combustion duration for strategy B is much

shorter, and the values of uHC emissions are higher which confirms that strategy A offers a better fuel/air mixing and more complete combustion process.

Comparing BTL with base diesel, strategy B for BTL 50 results in lower NO_x and soot emissions. NO_x emissions are reduced by approximately 35% with respect to the base diesel experiments. However, the engine output and the uHC are worse; for instance the IMEP values decrease by an average of 50%. As seen in Table 6.1, the amount of energy put in the cylinder per injection is 15% less than for base diesel, which would lead to a reduction of performance. However the IMEP values show lower values than expected. The ignition delay for BTL 50 is shorter than the base diesel fuel, probably due to its faster evaporation associated with its lower boiling temperatures shown in Table 6.1. The short ignition delay could lead to more fuel rich combustion, hence higher uHC emissions.

Injection timing B5 shows the highest IMEP value with similar emissions and therefore it was chosen for further in-cylinder injection and combustion analysis using high speed imaging and the two-colour method.

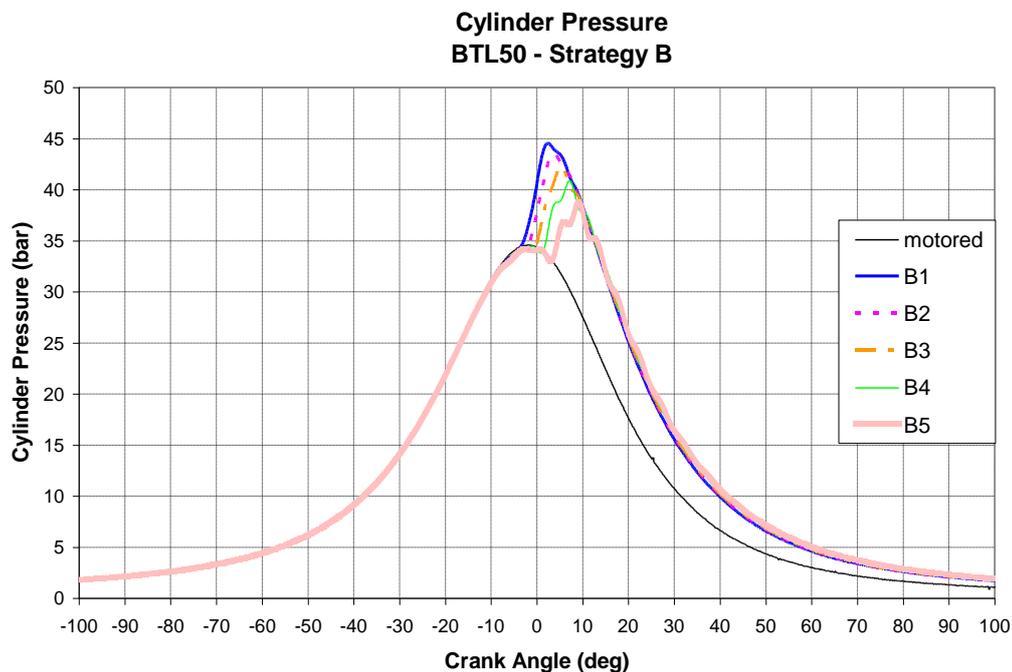


Figure 6.6 Cylinder pressure traces for BTL 50 experiments in Strategy B at 1200 bar

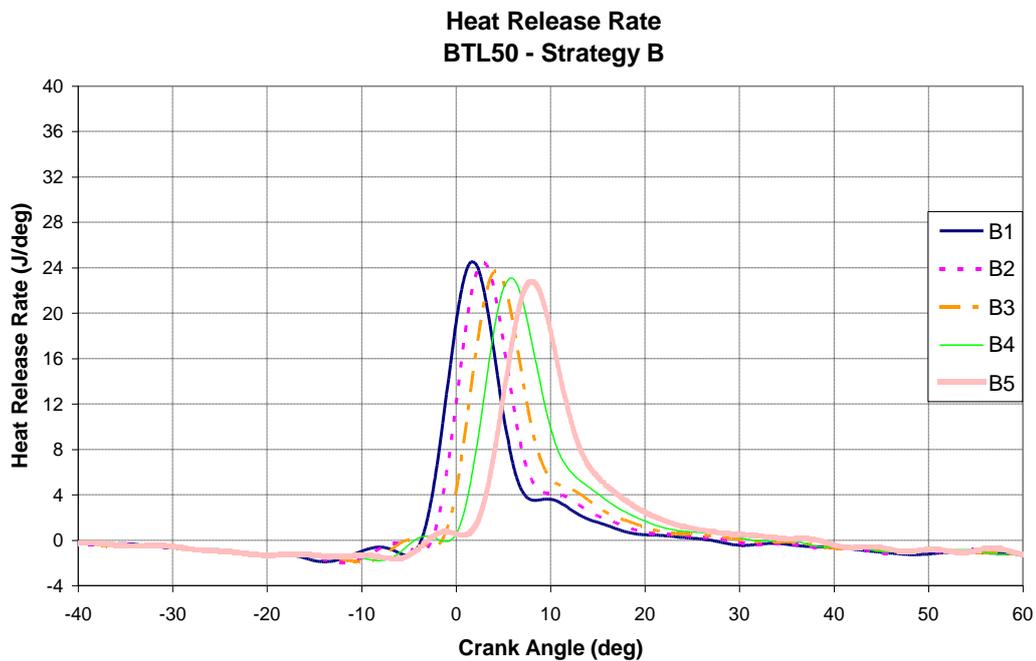


Figure 6.7 Heat release rate curves for BTL 50 experiments in Strategy B at 1200 bar

6.5.2.2 B5 Injection and Combustion Visualization

Figure 6.8 illustrates the high speed imaging of the B5 experiment, from the start of injection until the end of combustion. Similar to the imaging sequence from the experiment chosen among the strategy A, the injection duration for the first and the second injection is shorter than expected. As this problem appears with different strategies and it does happen in the first injection (where there is no pressure wave), the most probable reason is the physical properties of the biodiesel BTL itself. This injection problem is analysed in Section 6.5.2.3.

The first ignition spots appears at frame 0.6 BTDC, it is of very low luminosity and downstream of the sprays following the swirling motion. By 5.4° CA ATDC, there are six flame spots uniformly distributed, but with very low luminosity. At this stage the premixed combustion predominates and leads to very low soot formation. From frame 7.8 ATDC, it can be seen that the combustion flames cover almost the whole cylinder. The luminosity has increased as more diffusion combustion occurs at this point, as seen in the heat release rate curves in Figure 6.5. In front of the tip of the nozzle, a much brighter flame can be seen, like in the A1 experiment. This is probably due to the unatomised fuel from the sac that enters into the cylinder and is burned in a diffusion flame, which could be a source of soot formation. As this flame appears towards the end of combustion where flame temperatures are lower than the premixed flames, the soot

produced may not be oxidised and could lead to some soot emissions in the exhaust as confirmed in Table 6.4. Although the two-colour method was intended to be used for this injection timing, it was not possible to apply the technique because of the low luminosity during combustion.

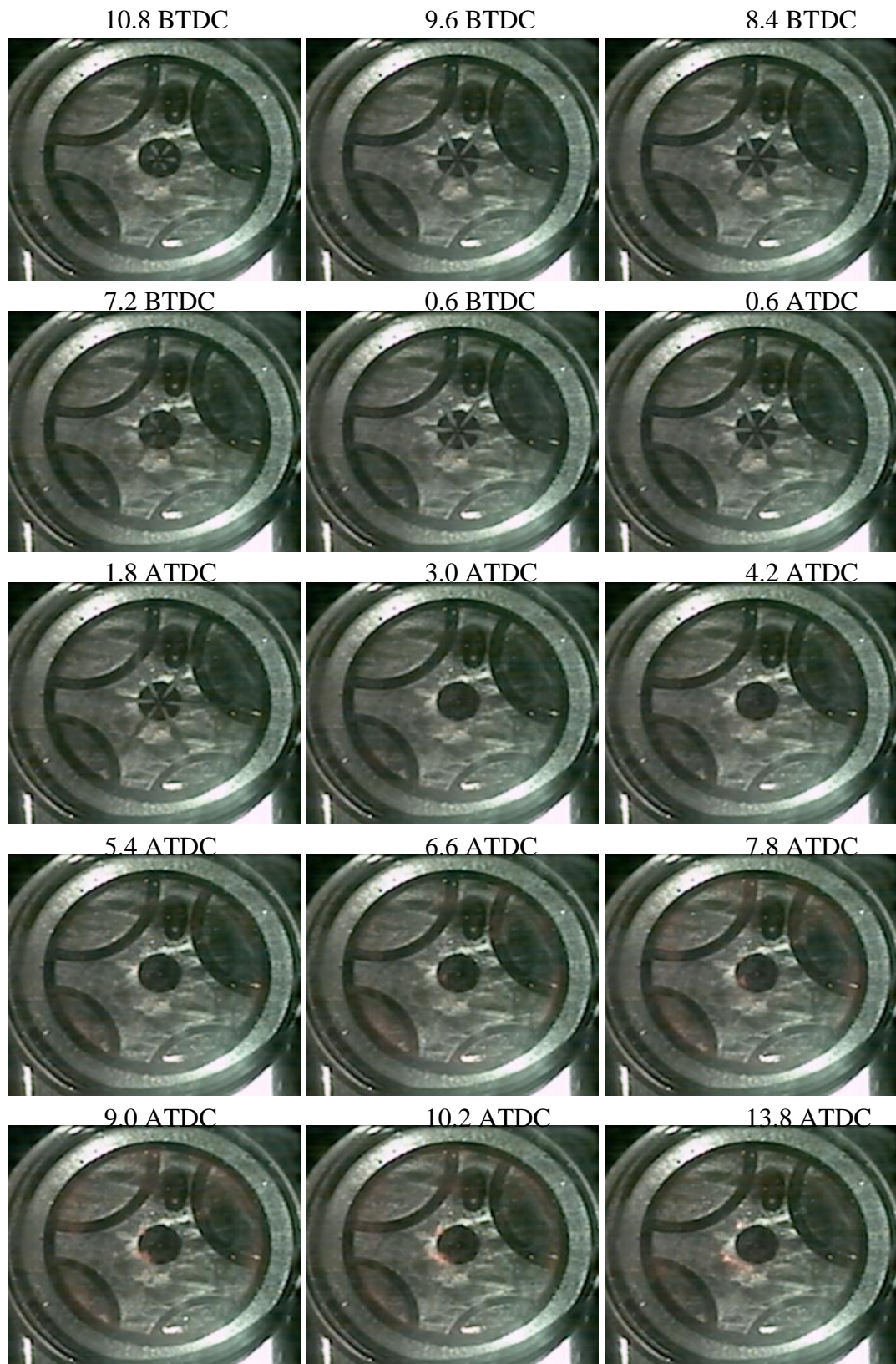


Figure 6.8 Combustion Image Sequence for BTL 50 B5 experiment at 1200 bar

6.5.2.3 Injection rate measurements for strategy B

Using the test rig as described in previous sections, the injection rate measurements for this strategy using base diesel and BTL 50 were performed. Figure 6.9 shows the results of the injection rate for strategy B. As in the case of strategy A, the injection duration for BTL is shorter than for base diesel, which has been observed as well in the high speed imaging of Figure 6.8.

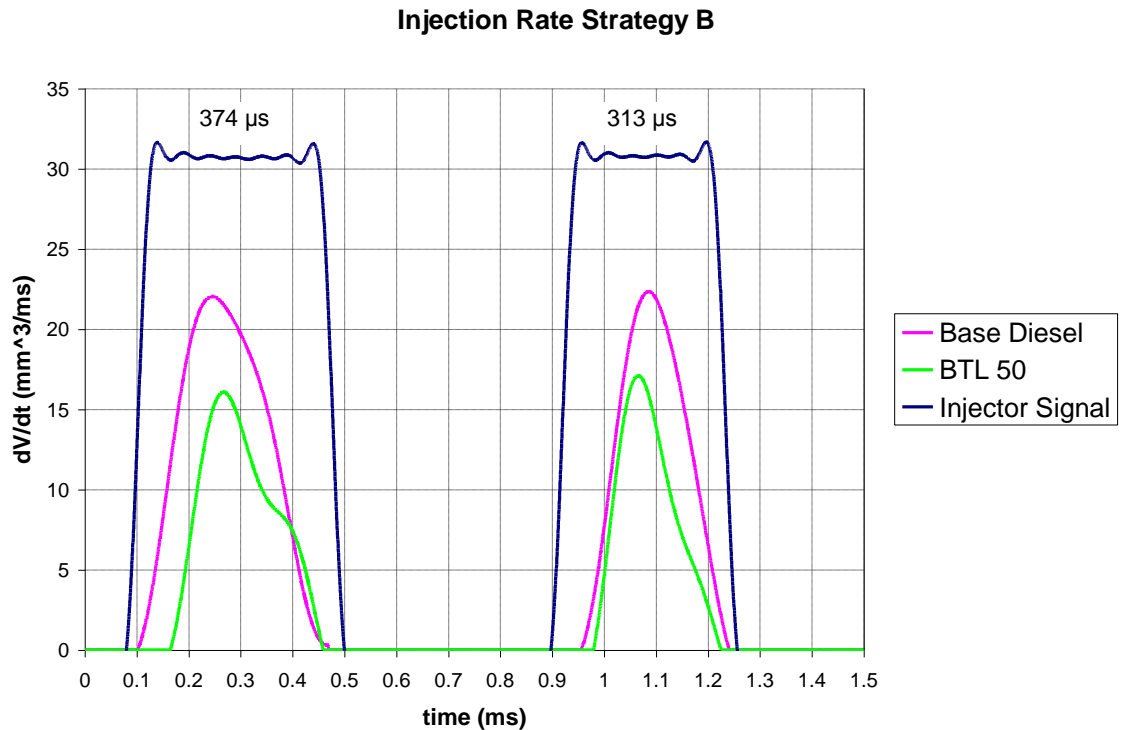


Figure 6.9 Injection Rate Measurements for Strategy B, Base Diesel and BTL 50

The injection rate calculated for base diesel shows 5.4 mm^3 for the first injection and 3.2 mm^3 for the second injection. These values are very similar to the values obtained for strategy A and very close to the theoretical values provided by the manufacturer.

The values estimated for BTL give 3.8 and 2.4 mm^3 for the first and second injection, respectively. This represents a reduction in the amount of fuel injected of 30% which can explain the low values obtained for the IMEP of these experiments.

6.5.3 Strategy E

6.5.3.1 Effect of Injection Timing on Performance and Emissions

The last strategy studied for BTL 50, was strategy E, with 16° CA of dwell angle. Table 6.5 shows the characteristics of the 5 injection timings investigated, the combustion characteristics as well as engine power and emissions.

Table 6.5 Injection, Combustion and Emissions Characteristics of Strategy E for BTL 50, 1200 bar

| Strategy E | | | | | | | | | | | |
|--------------------|--------------------|---|---|-------------------|-------------------|----------------------|-------------------------------|-------------------------------|------------------|------------------|-------------------|
| Dwell Angle | Test Number | SOI (1st injection) (CA BTDC) | SOI (2nd injection) (CA BTDC) | IMEP (bar) | Combustion | | | | EMISSIONS | | |
| | | | | | SOC | Duration (CA) | 1st ID (CA) | 2nd ID (CA) | HC (ppm) | NOx (ppm) | Soot (FSN) |
| 16 | E1 | 25 | 9 | 0.27 | 6.6 BTDC | 15.8 | 18.4 | 2.4 | 810 | 13 | 0 |
| | E2 | 23 | 7 | 0.34 | 5.8 BTDC | 16.0 | 17.2 | 1.2 | 745 | 13 | 0.01 |
| | E3 | 21 | 5 | 0.45 | 5.4 BTDC | 16.6 | 15.6 | - | 730 | 12 | 0.03 |
| | E4 | 19 | 3 | 0.45 | 4.6 BTDC | 16.4 | 14.4 | - | 718 | 12 | 0.01 |
| | E5 | 17 | 1 | 0.45 | 3.8 BTDC | 16.6 | 13.2 | - | 700 | 14 | 0.00 |

Figure 6.10 shows the cylinder pressure traces for the experiments with the 16° CA dwell angle for the BTL 50 fuel. The pressure lines for the five injection timings are very similar and they all follow the motoring pressure line until 2.8° CA BTDC. From this point onwards, the in-cylinder pressure of the first four cases departs from the motoring pressure to higher values but without showing a rapid increase. Experiment E5 follows the motoring pressure until 0.6° CA BTDC when it experiences a rapid increase in pressure indicating the start of premixed combustion. When reaching the maximum firing pressure, experiments E1 and E2 show a peak at 5.6 and 5.8° CA ATDC, respectively. However, the other cases are characterised with a plateau around the peak cylinder pressure at around 10° CA ATDC. The IMEP values obtained for this strategy vary from 0.3 to 0.45 bar depending on the injection timing.

Strategy E for diesel showed low IMEP values because during the second injection there was less fuel than expected injected inside the cylinder due to the negative effect of the pressure wave. This and the fact that the energy content in the injected fuel is reduced for BTL (see Table 6.1), explain the low IMEP values achieved for this strategy.

Figure 6.11 depicts the heat release rate curves of strategy E. In this case two patterns in the heat release rate are clearly shown. For experiments E1 and E2, after the first injection there is a slight decrease in the heat release rate due to the charge cooling effect; thereafter the first pre-combustion reactions provoke a slow increase in the heat release rate. This rise is momentarily interrupted by the second injection's cooling effect before the main increase in the heat release rate occurs. The slope of the heat release rate at this stage is not as steep as in the other strategies, and the rate is more relevant to diffusion combustion. The heat release rate for E1 and E2 reaches a peak at 2.2 and 4.2° CA ATDC, respectively. It starts decreasing initially rapidly and then from around 10° CA ATDC more gradually when diffusion combustion takes place. The E3, E4 and E5 cases show only the cooling effect due to the first injection. Then the heat release rate curves exhibit a slow increase due to the pre-combustion reactions followed by a few crank angles later the main combustion, before the second injection starts. For these injection timings the heat release rate at the start of combustion is very steep typical of premixed combustion. It reaches a peak around TDC and then it decreases before another increase in the heat release rate occurs. This second rise for experiment E3 achieves a higher value than in the premixed combustion phase and for E4 and E5 a bit lower but very close to the values achieved by the heat release rate in the premixed

combustion phase. Finally the heat release rate curves for these injection timings decrease quite rapidly until the end of combustion showing a total combustion duration of just over 16° CA for all of them.

The last three injection timings show the same IMEP value of 0.45 bar; therefore, E3 was chosen for further optical analysis and high speed combustion imaging was applied.

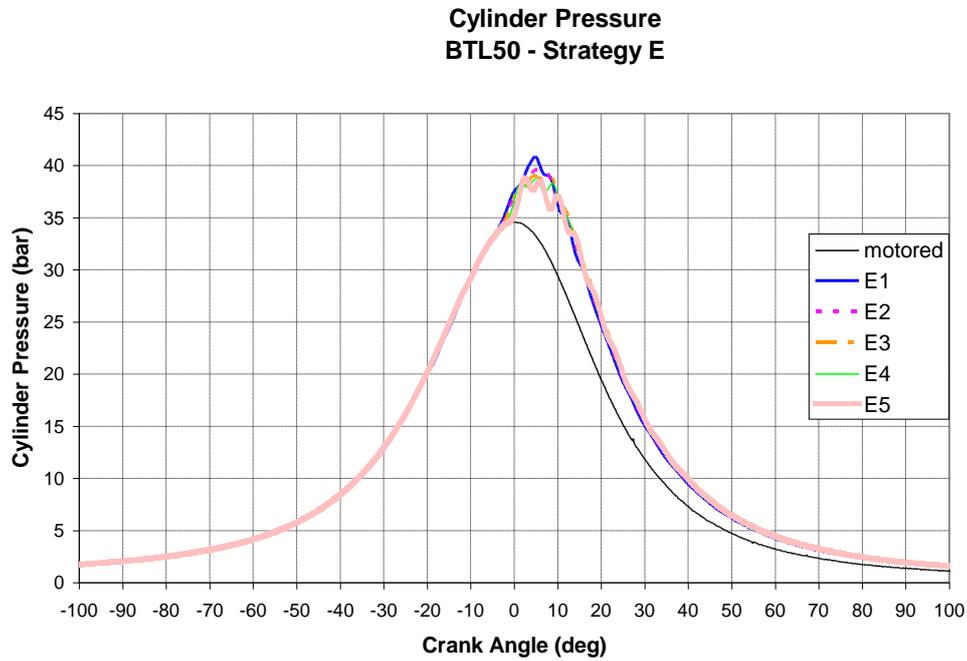


Figure 6.10 Cylinder pressure traces for BTL 50 experiments in Strategy E at 1200 bar

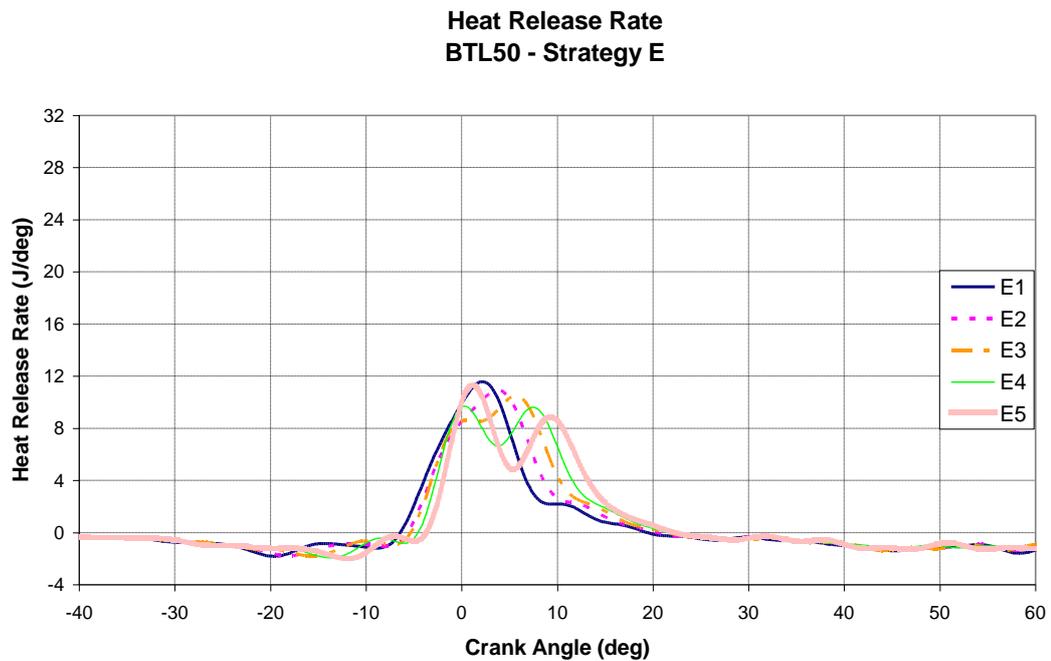


Figure 6.11 Heat release rate curves for BTL 50 experiments in Strategy E at 1200 bar

6.5.3.2 E3 Injection and Combustion Visualization

Figure 6.12 shows the combustion images sequence for experiment E3. Similarly to strategies A and B, the first injection duration is slightly shorter than expected. For strategy E with base fuel it was found that the second injection duration was adversely affected by the pressure wave created after the first injection and hence showed a shorter duration than expected. For this experiment the same phenomenon occurs again. According to the heat release rate curve the start of combustion takes place around 5° CA BTDC, but no apparent chemiluminescence flames are shown from frames 4.8 until 1.2 BTDC. As mentioned above during the combustion visualization of strategies A and B, the flame luminosity of the BTL 50 fuel with the split injection was very low. Strategy E's combustion reaches less than half the heat release rates of the previous strategies, this can explain why no flames appear visible during the premixed combustion of injection timing E3. However, the first visible flames appear around TDC and are nearer the centre of the combustion chamber than the previous cases. Although the heat release rate curve shows combustion has taken place at TDC, the proportion and intensity of luminous combustion region are fairly weak, with the exception of the diffusion flame seen near the injector tip after the second injection had finished due again to fuel dribbling from the nozzle

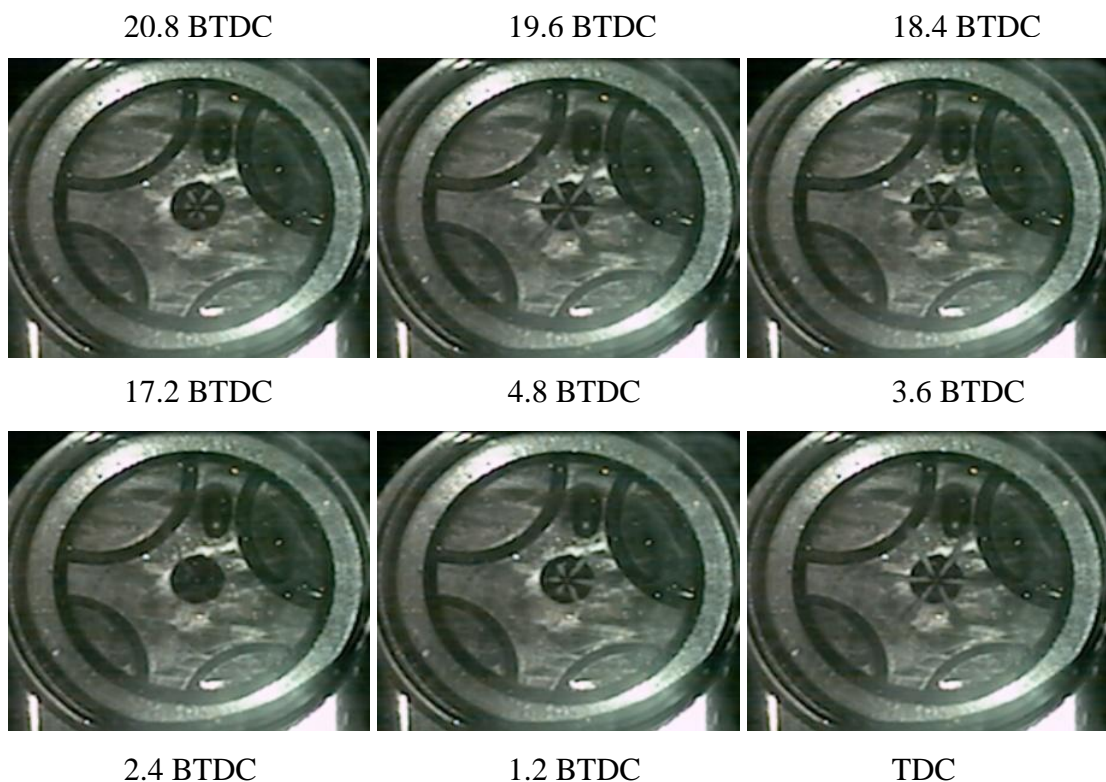


Figure 6.12 Combustion Images Sequence for BTL 50 E3 experiment at 1200 bar

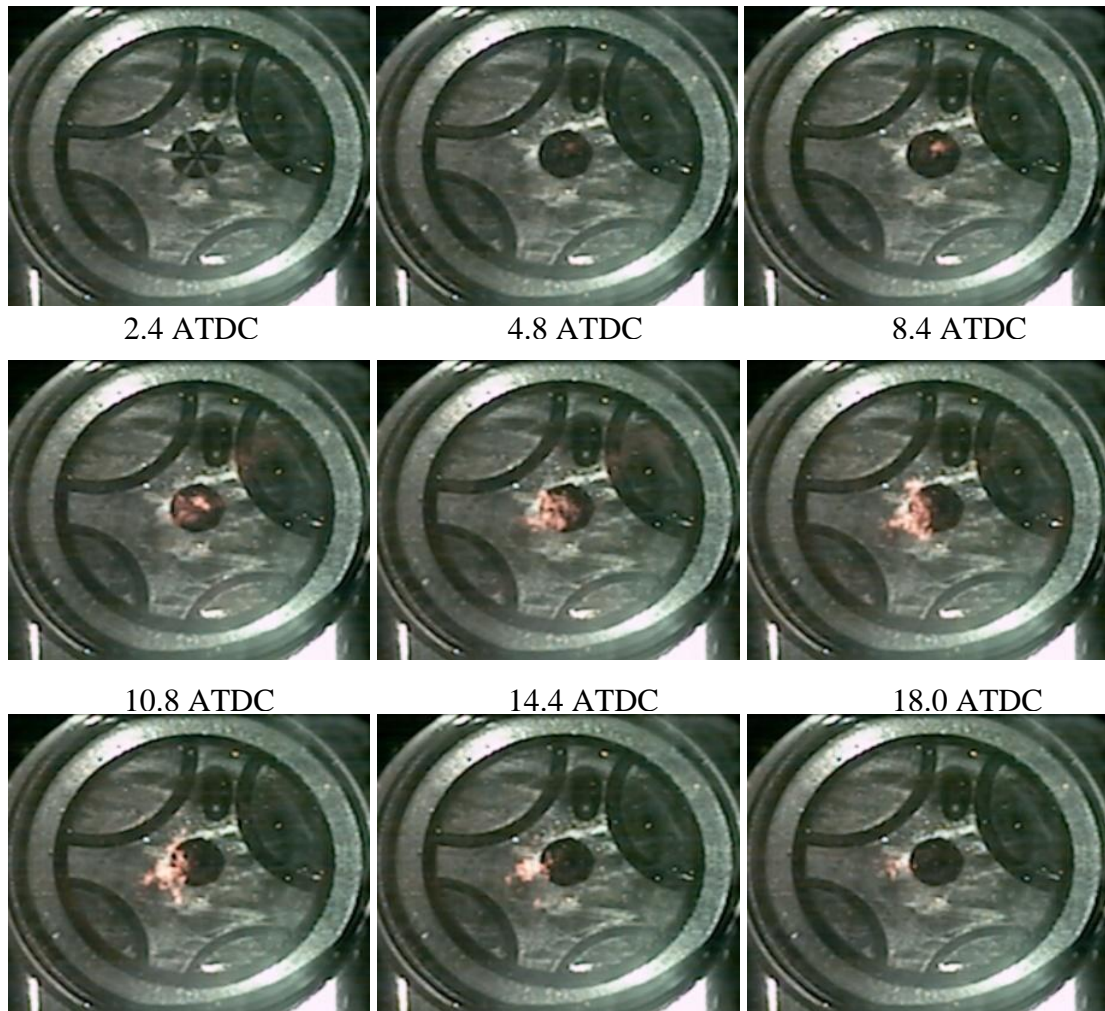


Figure 6.12 Combustion Images Sequence for BTL 50 E3 experiment at 1200 bar (cont'd)

6.5.3.3 Injection rate measurements for strategy E

The injection rate results for base diesel and BTL 50 are shown in Figure 6.13. The injection rate for diesel gives 5.5 and 2.2 mm³ for the first and second injection, respectively. It is important to note that there is a reduction of the fuel injected in the second injection. This phenomenon has been addressed in Chapter 5, Section 5.4.4.2. As for the BTL 50, the injection rate is calculated as 3.7 mm³ for the first injection and 1.6 mm³ for the second injection. The second injection quantity varies significantly from the values obtained in the experiments for strategy A and B due to the pressure wave effect.

The lower theoretical energy content supplied to the cylinder per injection with BTL 50 fuel (15% less than base diesel as shown in Table 6.1), combined with the reduction in the amount of BTL 50 fuel injected, explain the very low values of IMEP for strategy E. Such results imply that an increased injection duration will be required to produce the same power output if such a fuel is used to replace diesel.

Injection Rate Strategy E

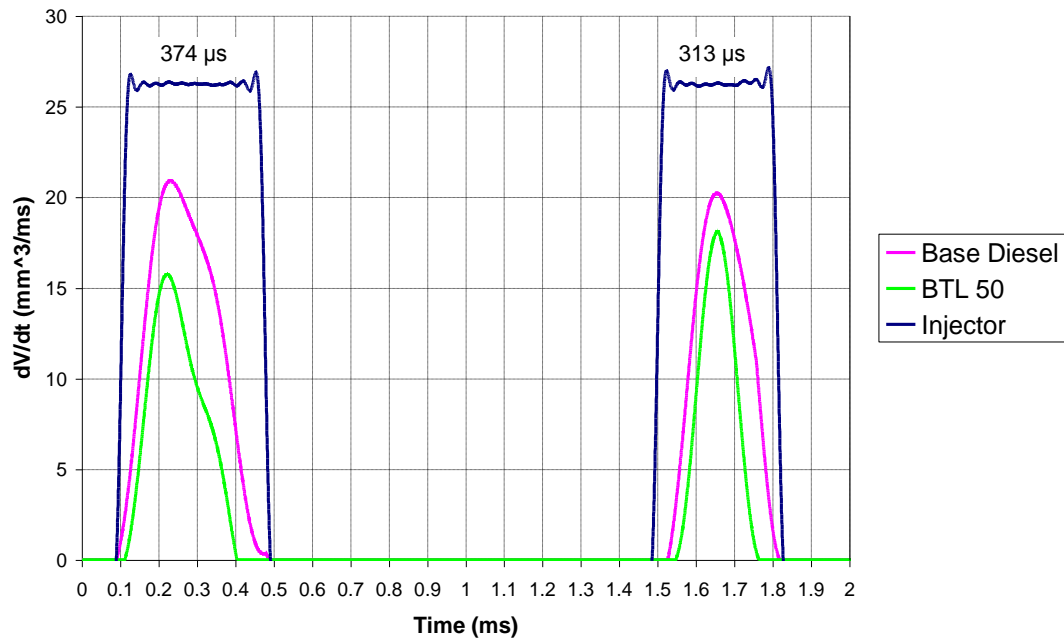


Figure 6.13 Injection Rate Measurements for Strategy E Base Diesel and BTL 50

6.6 Injection Strategies Studied for BTL 46

The same investigations of split injection are shown for the second of the BTL fuels, which has a lower Cetane Number and lower density than the BTL 50.

6.6.1 Strategy A

6.6.1.1 Effect of Injection Timing on Performance and Emissions

Table 6.6 shows the characteristics of strategy A with the biodiesel BTL 46. In order to understand the engine output values and compare them with the same strategy for base diesel and BTL 50, it is necessary to stress that the amount of energy being injected into the cylinder is reduced by 16% compared with base diesel.

Table 6.6 Injection, Combustion and Emissions Characteristics of Strategy A for BTL 46, 1200 bar

| Strategy A | | | | | | | | | | | |
|-------------|-------------|---|---|------------|------------|-------------------------|-------------------------|---------------|-----------|-----------|------------|
| Dwell Angle | Test Number | SOI (1 st injection) (CA BTDC) | SOI (2 nd injection) (CA BTDC) | IMEP (bar) | Combustion | | | | EMISSIONS | | |
| | | | | | SOC | 1 st ID (CA) | 2 nd ID (CA) | Duration (CA) | HC (ppm) | NOx (ppm) | Soot (FSN) |
| 8 | A1 | 19 | 11 | 0.63 | 1.4 BTDC | 17.6 | 9.6 | 11.6 | 740 | 20 | 0 |
| | A2 | 17 | 9 | 0.76 | 1.2 BTDC | 15.8 | 7.8 | 14.4 | 770 | 21 | 0 |
| | A3 | 15 | 7 | 0.75 | 1.0 BTDC | 14.0 | 6.0 | 14.8 | 850 | 18 | 0 |
| | A4 | 13 | 5 | 0.77 | 0.2 ATDC | 13.2 | 5.2 | 29.4 | 900 | 18 | 0 |
| | A5 | 11 | 3 | 0.72 | 1.2 ATDC | 12.2 | 4.2 | 30.8 | 1370 | 14 | 0 |

Figure 6.14 illustrates the cylinder pressure traces for the strategy A with BTL 46 fuel. For the first injection timing, the cylinder pressure line goes along the motoring pressure until 3° CA BTDC when it increases at a slightly faster rate. The rate of pressure rise stays constant until 2° CA ATDC where a more rapid rise occurs reaching a maximum value of 42.5 bar only 4° CA later. The cylinder pressure then rapidly decreases over the expansion stroke. As injection timing is retarded it can be seen in Figure 6.11 that the rapid rise of pressure occurs later. From experiment A3 onwards, the cylinder pressure shows a small increase compared to the motoring pressure (for A5 this is even lower than the maximum motoring pressure) as the pressure rise now occurs well after TDC. Results in this group of experiments all show a very rapid decrease of the cylinder pressure in the expansion stroke, which eventually gives a very low values of IMEP compared to strategy A with base and BTL 50 fuels.

As mentioned above, the energy content supplied to the cylinder is reduced by 16% compared to the diesel fuel. Due to the nature of this fuel, it was shown in Section 6.5.1.3 that the injection duration and therefore amount of fuel was reduced for the BTL fuels. Comparing with BTL 50, the BTL 46 has a lower density which is equivalent to have a higher bulk modulus. This implies that even less fuel is injected for BTL 46. These factors may explain why very low IMEP values are achieved for strategy A for the biodiesel BTL 46.

Figure 6.15 shows the heat release rate curves for BTL 46 fuel and the five injection timings with 8° CA dwell angle. As injection timing is retarded it can be seen that the peak heat release rate decreases considerably. This is because as combustion occurs more after TDC the in-cylinder temperatures reached during the combustion are lower. Another trend that is observed in Figure 6.12 is as injection timing is retarded the heat release rate occurs more gradually which indicates that more diffusion combustion occurs instead of the premixed combustion clearly identified in A1. The combustion appears to finish very early in the expansion stroke. The high uHC emissions values shown in Table 6.6 indicate very poor mixing leading to poor combustion as seen in the IMEP values.

As strategy A for BTL 46 showed a very low engine output, it was not further analysed with the optical techniques.

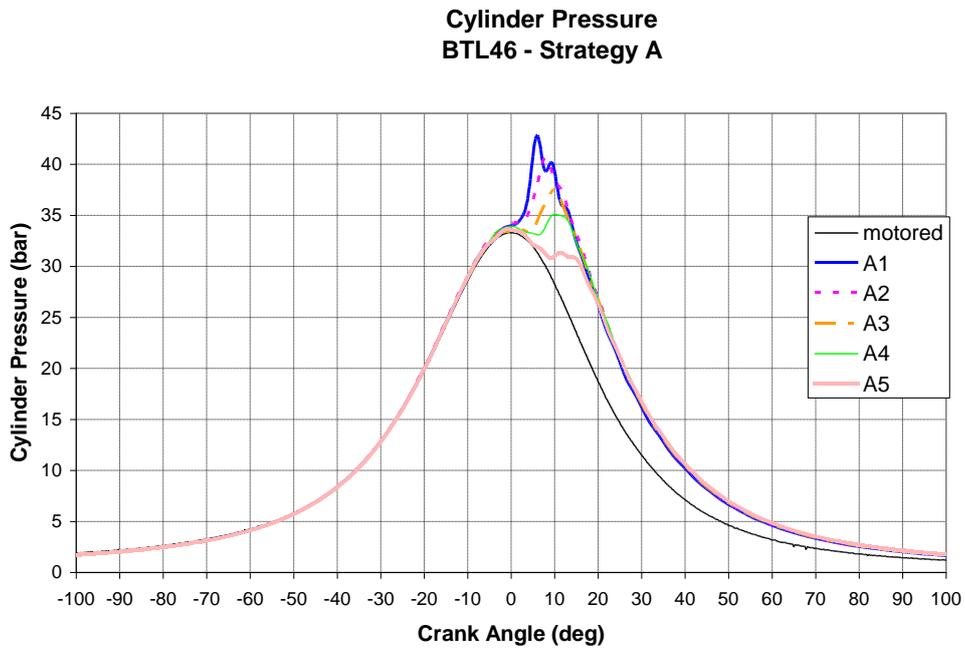


Figure 6.14 Cylinder pressure traces for BTL 46 experiments in Strategy A at 1200 bar

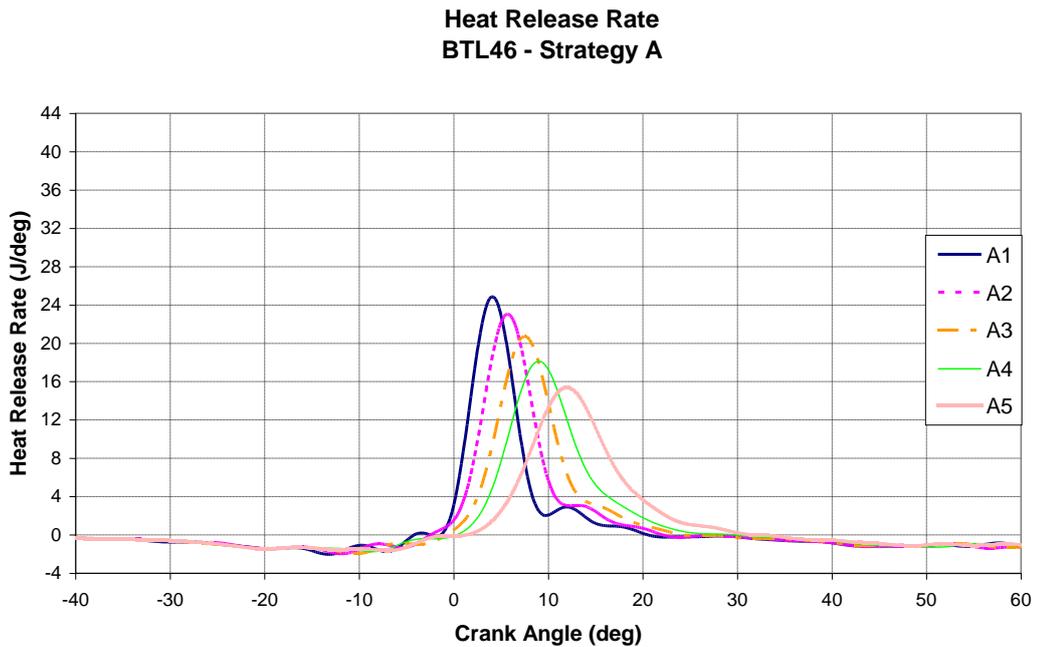


Figure 6.15 Heat release rate curves for BTL 46 experiments in Strategy A at 1200 bar

6.6.2 Strategy B

6.6.2.1 Effect of Injection Timing on Performance and Emissions

Table 6.7 shows the combustion characteristics, engine output as well as emissions values of the experiments carried out for strategy B (10° CA dwell angle) with BTL 46 as fuel.

Table 6.7 Injection, Combustion and Emissions Characteristics of Strategy B for BTL 46, 1200 bar

| Strategy B | | | | | | | | | | | |
|--------------------|--------------------|---|---|-------------------|-------------------|-------------------------------|-------------------------------|----------------------|------------------|------------------|-------------------|
| Dwell Angle | Test Number | SOI (1st injection) (CA BTDC) | SOI (2nd injection) (CA BTDC) | IMEP (bar) | Combustion | | | | EMISSIONS | | |
| | | | | | SOC | 1st ID (CA) | 2nd ID (CA) | Duration (CA) | HC (ppm) | NOx (ppm) | Soot (FSN) |
| 10 | B1 | 19 | 9 | 0.44 | 2.6 BTDC | 16.4 | 6.4 | 14.4 | 870 | 16 | 0 |
| | B2 | 17 | 7 | 0.55 | 1.8 BTDC | 15.2 | 5.2 | 14.2 | 880 | 15 | 0 |
| | B3 | 15 | 5 | 0.50 | 0.4 BTDC | 14.6 | 4.6 | 15.0 | 920 | 14 | 0 |
| | B4 | 13 | 3 | 0.52 | 0.6 ATDC | 13.6 | 3.6 | 15.6 | 1020 | 15 | 0 |
| | B5 | 11 | 1 | 0.64 | 1.8 ATDC | 12.8 | 2.8 | 16.4 | 1320 | 13 | 0 |

Figure 6.16 illustrates the cylinder pressure traces of the five different injection timings experimented for the strategy B. The cylinder pressure lines follow the same pattern: they go along with the motoring pressure line until approximately 2° CA BTDC for B1, TDC for B2 and later respectively for B3 to B5. From that moment the pressure increases more rapidly than the motoring pressure but it is not until a few crank angles later (4° CA for B1) when a more steep pressure rise occurs. This increase lasts only a few crank angles before starts decreasing rapidly over the expansion stroke. Similar to strategy A for BTL 46, as injection timing is retarded the peak cylinder pressure is retarded achieving a lower value. All the experiments show a very rapid decrease of pressure over the expansion stroke and exhibit a short combustion duration as seen in Table 6.7. Due to the small pressure increase around TDC and the rapid decrease over the expansion stroke the IMEP values for strategy B vary between 0.4 and 0.6 depending on the injection timing. Again these low IMEP values are probably due to the lower quantity injected due to the higher bulk modulus for this fuel and the lower energy content injected as the fuel has less density than diesel fuel.

Figure 6.14 depicts the heat release rates curves for strategy B. As mentioned above, all injection timings show a similar trend. For the first injection timing B1, the start of combustion occurs at 2.6° CA BTDC, it then experiences a rapid increase typical of premixed combustion. After reaching a maximum heat release rate at 5.8° CA ATDC it drops rapidly until about 10° CA ATDC where the decrease becomes more gradual while some diffusion combustion occurs. It quickly finishes at around 12° CA ATDC. For the experiments in strategy B, as injection timing is retarded the SOC is delayed. Figure 6.14 shows that the combustion duration increases slightly as the rapid premixed phase decreases and the diffusion phase of the combustion increases.

In the same way as strategy A for BTL 46, this strategy was not further study applying optical techniques due to the poor combustion that this fuel shows for the split injection investigation.

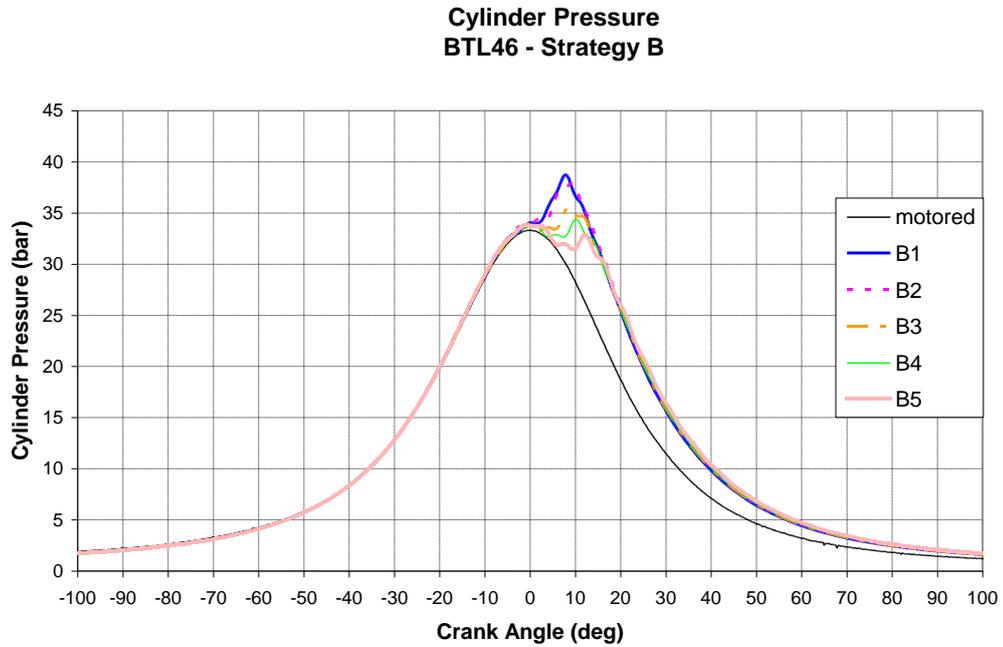


Figure 6.16 Cylinder pressure traces for BTL 46 experiments in Strategy B at 1200 bar

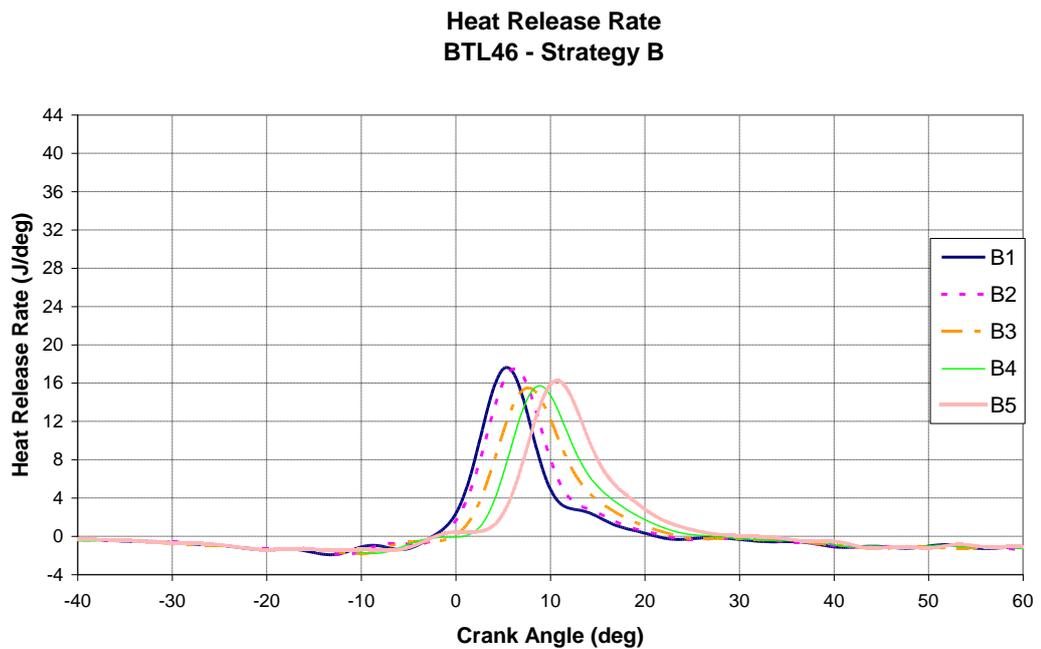


Figure 6.17 Heat release rate curves for BTL 46 experiments in Strategy B at 1200 bar

6.6.3 Strategy E

6.6.3.1 Performance and Emissions

Table 6.8 summarises the combustion properties and engine performance of the experiments investigated for strategy E with BTL 46 as fuel. The emissions values are also included for the five different injection timings.

Table 6.8 Injection, Combustion and Emissions Characteristics for BTL 46 Strategy E, 1200 bar

| Strategy E | | | | | | | | | | | |
|--------------------|--------------------|---|---|-------------------|-------------------|----------------------|-------------------------------|-------------------------------|------------------|------------------|-------------------|
| Dwell Angle | Test Number | SOI (1st injection) (CA BTDC) | SOI (2nd injection) (CA BTDC) | IMEP (bar) | Combustion | | | | EMISSIONS | | |
| | | | | | SOC | Duration (CA) | 1st ID (CA) | 2nd ID (CA) | HC (ppm) | NOx (ppm) | Soot (FSN) |
| 16 | E1 | 25 | 9 | 0.05 | 3.6 BTDC | 16.0 | 21.4 | 5.4 | 1180 | 8 | 0 |
| | E2 | 23 | 7 | 0.13 | 4.0 BTDC | 17.0 | 19.0 | 3.0 | 1090 | 9 | 0 |
| | E3 | 21 | 5 | 0.22 | 4.2 BTDC | 17.8 | 16.8 | 0.8 | 970 | 10 | 0 |
| | E4 | 19 | 3 | 0.19 | 3.6 BTDC | 18.6 | 15.4 | - | 1070 | 8 | 0 |
| | E5 | 17 | 1 | 0.19 | 2.6 BTDC | 18.4 | 14.4 | - | 1090 | 8 | 0 |

Figure 6.18 illustrates the cylinder pressure traces for strategy E. All five injection timings show very similar pressure curves, between 20 and 10° CA BTDC, depending on the injection timing, the pressure starts increasing at slightly higher rate than the motoring pressure. In all experiments there is no rapid pressure rise characteristic from a premixed combustion however the rise continues at the same rate until it starts slowing down before reaching the maximum cylinder pressure at around 5° CA ATDC . After this point the pressure decrease is at higher rate than the motoring pressure over the expansion stroke. The final values of IMEP (between 0.1 and 0.2 bar) indicate poor combustion.

Similar to the strategy E for the base diesel and BTL 50, the second injection duration is shorter than expected due to the negative effect of the pressure wave created after the first injection. Moreover the higher bulk modulus for BTL 46 has the effect of reducing the quantity injected for the same injection duration, explaining the very low IMEP values obtained under the 16°CA dwell angle conditions.

Figure 6.19 shows the heat release rate for strategy E. E1 to E3 show very similar heat release rates, although there is a 2° CA difference in the injection timing; the SOC occurs approximately at the same time and it then experiments an increase which is steep for E1 and less steep as the injection timing is delayed (E2 and E3). After achieving a maximum heat release rate, the decrease occurs quite rapidly at first and from 12° CA ATDC more slowly as the combustion is diffusion dominated. For E4 and E5 the heat release rate curves show one peak soon after the SOC due to the premixed combustion and then later one another and higher peak which indicates that most of the combustion occurs in the diffusion phase; this is controlled by the fuel/air mixing from the second injection since it occurs after the start of combustion. For strategy E, all injection timings show short combustion duration. As mentioned before, this indicates incomplete combustion which agrees with the very high values of uHC shown in Table 6.8.

The last strategy studied for BTL 46 confirms the unsuitability of this fuel for the split injection strategies investigated as part of this research and, as a result, no further optical analysis was carried out for strategy E.

**Cylinder Pressure
BTL46 - Strategy E**

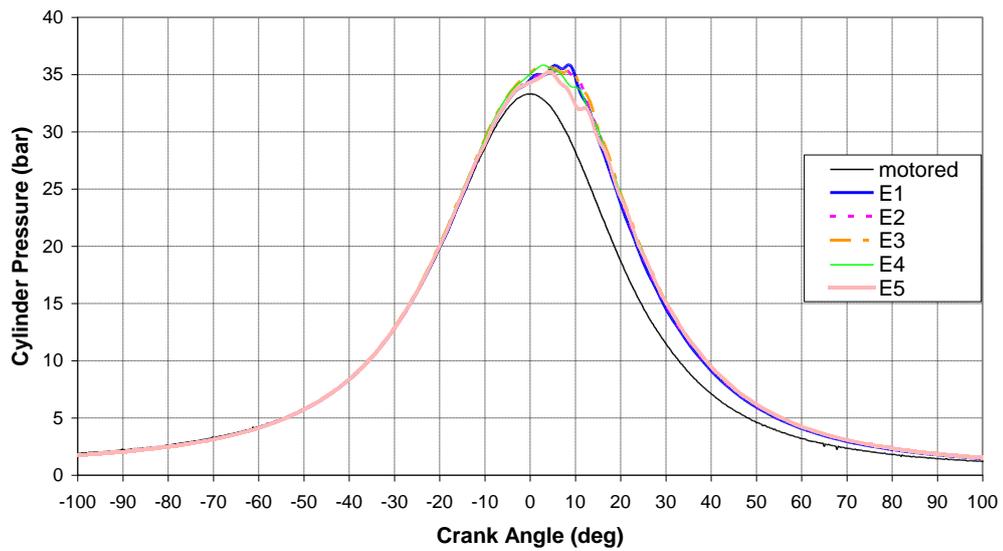


Figure 6.18 Cylinder pressure traces for BTL 46 experiments in Strategy E at 1200 bar

**Heat Release Rate
BTL46 - Strategy E**

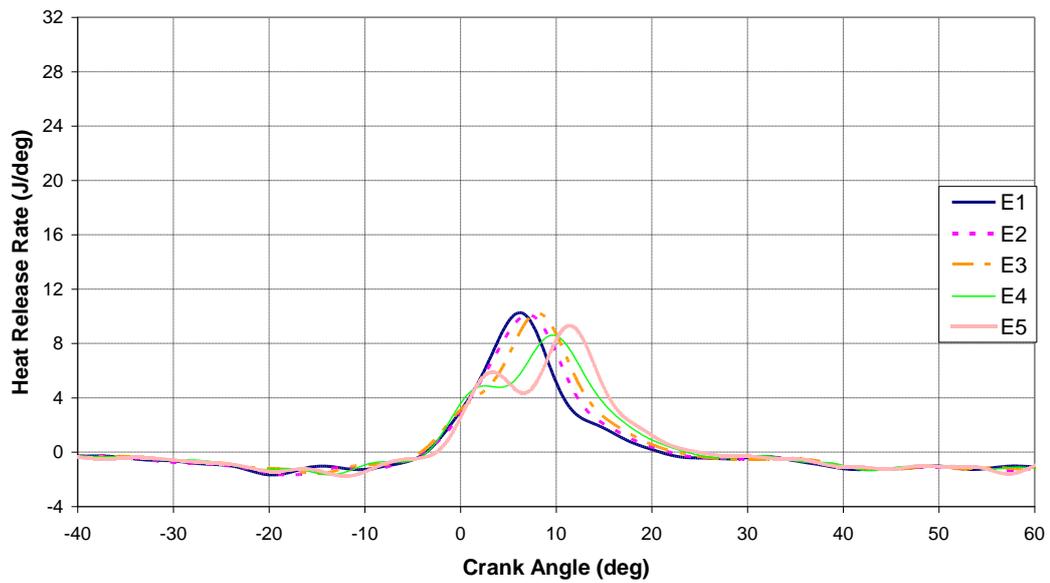


Figure 6.19 Heat release rate curves for BTL 46 experiments in Strategy E at 1200 bar

6.7 Conclusions of BTL 50 and BTL 46 split injection experiment

From the experiments performed with BTL 50 for split injection strategies, the following conclusions can be obtained:

- Strategy A has the highest IMEP values among the strategies studied with BTL 50. Taking into account that the theoretical amount of energy supplied to the cylinder was reduced by 15%, and that the actual amount of fuel injected was 70% of the base diesel due to the physical properties of the fuel itself such as lubricity and bulk modulus, these IMEP values are comparable to the ones obtained with base diesel. The low boiling temperatures of the BTL fuels lead to fast evaporation enhancing the fuel/air mixing process and hence a more homogeneous mixture as seen in the high speed combustion images where combustion takes place in the full circumference of the cylinder. Its pollutant emissions are lower than those of base diesel: the NO_x emissions are around 15% less and uHC are decreased by 50%. As expected by the absence of aromatic compounds, little soot emission is detected in the exhaust.
- Strategy B shows a decrease of the engine output with respect to strategy A obtaining an average of 30% less IMEP. as dwell angle increases and combustion is further delayed into the expansion stroke.
- Strategy E results in very low IMEP values as the dwell angle is increased. The IMEP values are between 0.3 and 0.5 bar while the uHC are increased by 100% with respect to strategy A. The second injection is adversely affected by the pressure wave, producing shorter duration than expected.

Experiments with BTL 46 for split injection strategies produce very low engine output. For the three strategies studied, the IMEP values were much lower than BTL50 and base diesel fuel, combustion duration was very short and consequently very high values of uHC emissions due to over dilution were obtained. The reduction in the IMEP values were principally caused by the reduced amount of energy supplied due to the lower density of BTL 46 fuel and smaller quantities injected. In addition, the longer ignition delay resulted in late combustion.

In general, it has been observed both through high speed images and fuel injection rig tests, less BTL fuels were injected into the cylinder for the same injector setting due to

the difference in their physical properties to the base diesel. In addition, the difference between the ignition delays of BTL 50 and base diesel fuel was found to be more significant than that indicated by the cetane numbers (50 vs 49.1). This difference could be attributed to not only the difference in the chemical properties but also their evaporation characteristics. Under the operating conditions investigated the reduction of fuel quantity has proven to very influential on engine performance. In addition, as seen in Figure 6.4 and Figure 6.8, the high volatility of the fuel improves mixing, achieving a homogeneous mixture which could lead to high performance and low emissions combustion.

Chapter 7 Conclusions and Recommendations for Future Work

7.1 Introduction

Diesel engines have shown a significant increase in the car market shares in Europe. However the main drawback of conventional diesel engines, the NO_x and soot emissions trade-off, remains to be a major challenge. In order to be able to reduce both NO_x and soot emissions simultaneously, combined approaches will need to be applied. This investigation has focused on in-cylinder studies of mixture formation, combustion and exhaust emissions in a single cylinder diesel engine operating with high level EGR and split injection strategy. The experiments have been carried out by means of in-cylinder pressure and high speed optical techniques, like high speed imaging and high speed two-colour method, to obtain cycle-resolved in-cylinder soot and combustion temperature measurements in the single cylinder optical engine.

7.2 The Two-Colour Method

One of the most common techniques to obtain diesel combustion temperature and soot concentration measurements is the two-colour method. This method has normally been implemented with single shot ICCD cameras. However, in diesel combustion large cycle-to-cycle variations in the soot radiation occur due to the soot motion inside the cylinder. Therefore images of different cycles have to be ensemble-averaged to obtain the temperature and soot concentration. As part of this study, the two-colour method has been further developed and successfully implemented in a high speed imaging system capable of obtaining cycle-resolved in-cylinder soot and combustion temperature measurements for up to 16 consecutive cycles at a framing speed of 10,000fps. As a result, soot formation and oxidation processes could be investigated throughout each combustion cycle.

7.3 Split Injection Investigation

Fuel injection, mixture formation, autoignition, combustion and emission characteristics of split investigation with EGR using base diesel have been reported and analysed in Chapter 5. Different injection timings and dwell angles at two injection pressures were examined. All the experiments were carried out in a single cylinder optical engine of

“Bowditch” design, featuring a flat glass window in the piston bowl to have optical access of the combustion chamber. This directly affects the mixing process and differs from conventional diesel engines where the piston bowl is shaped in order to enhance the in-cylinder flow and fuel/air mixing.

High speed spray and combustion imaging have been applied as well as the two colour method in order to obtain in-cylinder flame temperature and soot concentration measurements. These techniques in combination with in-cylinder pressure measurement, heat release analysis and exhaust pollutants emissions have been used to gain a better understanding of the fuel injection, vaporization, and mixing as well as the combustion characteristics related to diesel combustion operating with high level EGR and split injection strategy. The differences in the injection and combustion processes among the strategies studied have been observed by the application of these optical techniques. .

As expected, the injection pressure has a major effect in both emissions and performance. The mixing process at 800 bar injection pressure was poor, leading to incomplete combustion and therefore low IMEP values. Emissions of uHC were higher due to the incomplete combustion and the soot exhaust emissions were higher due to the local fuel-rich mixture during combustion as a consequence of the poor mixing.

The dwell angle between split injections was varied from 8° to 16° CA. Among the experiments studied with 1200 bar injection pressure, strategy A has the shortest dwell angle among the strategies studied. It showed higher IMEP values than the rest of strategies and low NO_x emissions. However due to the short time between injections fuel/air mixing was poor, leading to high uHC and soot emissions. Strategy B with a slightly longer dwell angle showed a big improvement compared to Strategy A. The IMEP values were similar and in some cases even higher, but the emissions were much lower. As dwell angle was increased, the mixing process improved leading to emissions' reduction. NO_x emissions were also reduced by a small percentage as combustion temperature decreased. The difference in the combustion characteristics between strategy A and strategy B was clearly shown in the optical measurements. Combustion imaging showed that by increasing the dwell angle, air/fuel mixing was improved and consequently a more complete combustion was observed. As for the difference in exhaust soot emissions, the two colour method was proven successful in showing lower soot formation during the combustion process. Strategy C and D showed

a single injection due to the pressure wave, and no combustion was produced. And finally, Strategy E gave the lowest IMEP values among the strategies studied. This was caused primarily by the reduced amount of fuel in the second injection due to negative effect of the pressure wave generated from the first injection.

This investigation has tried to investigate the effects of combined strategies namely high EGR and split injection to reduced both NO_x and soot emissions. This investigation has been carried out with an optical single cylinder engine, which is different than those used in automobiles. From a point of view of conventional diesel engines, this investigation could lead to higher engine output values and reduced exhaust emissions (soot and uHC), as the piston bowl is shaped, it would be expected to obtain a better fuel/air mixing which could lead to a more complete combustion, reducing the uHC exhaust emissions and a local learner fuel/air mixture which could lead to a reduction in the soot formation.

7.4 Split Injection with Biodiesel

As the final part of this investigation, two bio-diesel fuels namely BTL 46 and BTL 50 were tested at 1200bar fuel injection pressure. . These fuels are very different from base diesel. There is no sulphur content in the BTL fuels, which may influence on the lubricity of the fuel and affect the fuel injection system, and there is no aromatics which can reduce the soot formation by decreasing the PAH formation. The low boiling temperatures of these BTL fuels will lead to fast evaporation and enhance the mixing process leading to more homogeneous mixture than base diesel. However, the lower energy density of the BTL fuels results in reduced energy being supplied to the cylinder for the same quantity of fuel injected.

In the present study, it has also been observed by high speed spray images and verified by fuel injection rig tests that the fuel injection duration of BTL fuels was noticeably shorter than that of the base diesel for the same injector drive signal due to the different physical properties of BTL fuels. In addition, the difference between the ignition delays of BTL 50 and base diesel fuel was found to be more significant than that indicated by the cetane numbers, and it could be attributed to not only the difference in the chemical properties but also their evaporation characteristics.

In the case of BTL 50, the highest engine output was obtained with the shortest dwell angle. Due to the fast evaporation characteristics of BTL 50 fuel, its pollutant

emissions were lower than those of base diesel. The NO_x emission was 15% less and uHC were decreased by 50%. In addition, the better mixing and absence of aromatic compounds led to little soot emission in the exhaust.. As the dwell angle was increased from 8 CA to 10 CA, engine output was reduced by about 30%. As the dwell angle was set to 12 CA and 14 CA, the second injection failed to take place due to the pressure wave effect in the high pressure fuel line. Although the second injection did occur as the dwell angle was increased to 16 CA, its quantity was significantly reduced, resulting in much lower IMEP.

Experiments with BTL 46 for split injection strategies produced the lowest engine output. For the three strategies studied, the IMEP values were much lower than both for BTL50 and base diesel fuel when smaller quantity of fuel was injected for the same injector setting due to its physical properties. Combustion duration was very short and very high values of uHC emissions were obtained because of the over-dilution effect. Furthermore, the longer ignition delay of BTL 46 fuel shifted the combustion further into the expansion stroke, resulting less work output.

7.5 Recommendation for future work

During this investigation, the use of high levels of EGR in combination with split injection has shown potential in reducing both NO_x and soot emissions in diesel engines. Due to the time consuming nature of optical engine experiments, the current study was limited to certain fuel injection timings and quantities of split injections. It would be desirable to extend the current study to include further variations in the injection timing, dwell angel, and quantity of each injection with the help of the design of experiment technique. With the recent development in the Laser Induced Exciplex Fluorescence (LIEF) technique at Brunel University, it would also be very useful to investigate the interaction of fuel vapours between the two injections and its effect on the autoignition and combustion process. .

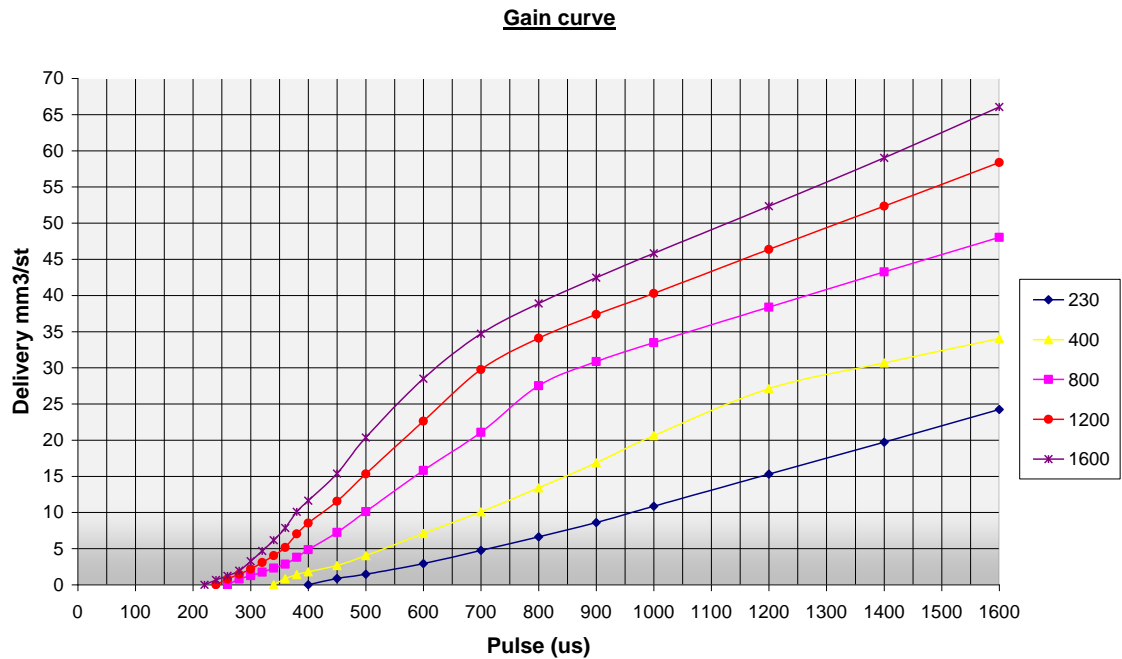
In the current study of BTL fuels, the quantity of fuel injected was kept the same as the base diesel fuel. It would be useful to conduct similar experiments on BTL fuels by increasing the fuel injection pulse width so that the same amount of energy will be supplied to the cylinder.

This study has shown that the two colour method was not adequate for studying the combustion and soot formation from these bio-diesels due to low combustion luminosity. In order to investigate the soot formation and oxidation with these bio-diesel

fuels the time-resolved LII could be applied to obtain soot particle size at different stages of combustion.

Appendix A

Injector Flow Rate Gain Curve



EC-Lab screenshot

Control

Engine Speed: 2018 RPM
Rail Pressure: 1131 bar

System errors

- ✓ No CAM signal
- ✓ Intermittent CAM signal
- ✓ Overspeed fuel cut-off

Pulses look-up window

| # | Name | Stat | Angle | Dura | Quantity |
|---|--------------|------|-------|------|----------|
| 1 | Pulse Nbr. 1 | X | 19.0 | 374 | |
| 2 | Pulse Nbr. 2 | X | 9.0 | 313 | |
| 3 | Pulse Nbr. 3 | | -12.0 | 0 | |
| 4 | Pulse Nbr. 4 | | -18.0 | 0 | |

Pump pressure control

Control mode:
 PWM duty cycle (%)
 Pressure (bar)

Pressure command: 1200
 Pressure feedback: 0
 Applied duty cycle: 0

Pump enabled

Pulse Nbr. 1
 Length (us): 374
 Angle (deg.): 19.0
 Pulse enabled

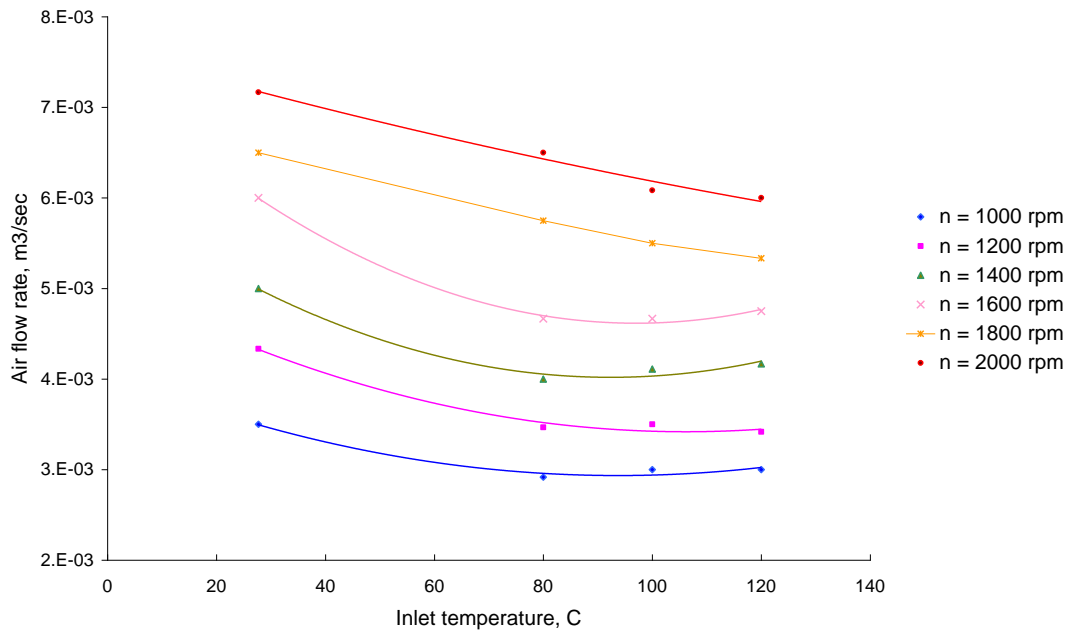
Pulse Nbr. 2
 Length (us): 313
 Angle (deg.): 9.0
 Pulse enabled

Pulse Nbr. 3
 Length (us): 0
 Angle (deg.): -12.0
 Pulse enabled

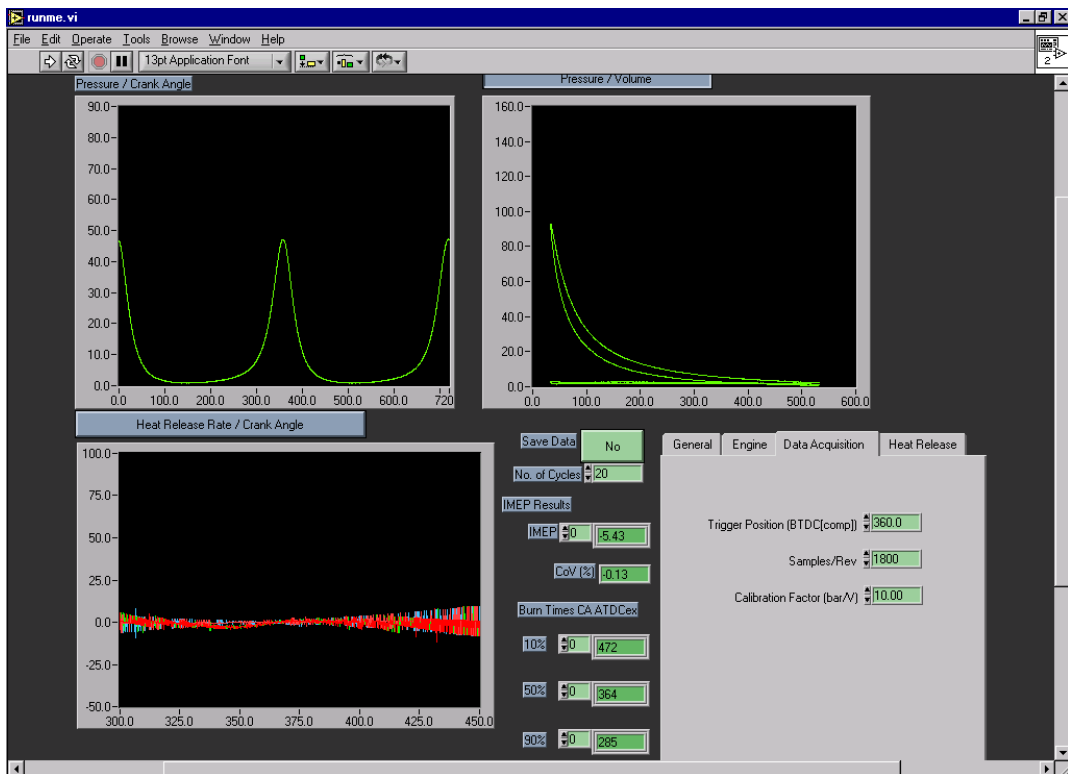
Pulse Nbr. 4
 Length (us): 0
 Angle (deg.): -18.0
 Pulse enabled

Appendix B

Hydra airflow rate graph



Hydra DAQ LabVIEW Program Screenshot



Appendix C

Tungsten Lamp Calibration Table

| Temp [K] | Current [A] | Temp [K] | Current [A] | Temp [K] | Current [A] |
|----------|-------------|----------|-------------|----------|-------------|
| 973 | 6.52 | 1313 | 10.83 | 1653 | 17.71 |
| 983 | 6.60 | 1323 | 11.01 | 1663 | 17.94 |
| 993 | 6.68 | 1333 | 11.18 | 1673 | 18.17 |
| 1003 | 6.77 | 1343 | 11.36 | 1683 | 18.40 |
| 1013 | 6.86 | 1353 | 11.54 | 1693 | 18.63 |
| 1023 | 6.95 | 1363 | 11.72 | 1703 | 18.86 |
| 1033 | 7.04 | 1373 | 11.91 | 1713 | 19.09 |
| 1043 | 7.14 | 1383 | 12.09 | 1723 | 19.33 |
| 1053 | 7.24 | 1393 | 12.28 | 1733 | 19.56 |
| 1063 | 7.34 | 1403 | 12.47 | 1743 | 19.80 |
| 1073 | 7.45 | 1413 | 12.66 | 1753 | 20.03 |
| 1083 | 7.56 | 1423 | 12.86 | 1763 | 20.27 |
| 1093 | 7.67 | 1433 | 13.05 | 1773 | 20.51 |
| 1103 | 7.78 | 1443 | 13.25 | 1783 | 20.75 |
| 1113 | 7.90 | 1453 | 13.45 | 1793 | 21.00 |
| 1123 | 8.02 | 1463 | 13.65 | 1803 | 21.24 |
| 1133 | 8.14 | 1473 | 13.85 | 1813 | 21.48 |
| 1143 | 8.27 | 1483 | 14.05 | 1823 | 21.73 |
| 1153 | 8.40 | 1493 | 14.26 | 1833 | 21.98 |
| 1163 | 8.53 | 1503 | 14.46 | 1843 | 22.22 |
| 1173 | 8.66 | 1513 | 14.67 | 1853 | 22.47 |
| 1183 | 8.80 | 1523 | 14.88 | 1863 | 22.72 |
| 1193 | 8.94 | 1533 | 15.09 | 1873 | 22.97 |
| 1203 | 9.08 | 1543 | 15.30 | 1883 | 23.23 |
| 1213 | 9.23 | 1553 | 15.52 | 1893 | 23.48 |
| 1223 | 9.38 | 1563 | 15.73 | 1903 | 23.73 |
| 1233 | 9.53 | 1573 | 15.95 | 1913 | 23.99 |
| 1243 | 9.68 | 1583 | 16.16 | 1923 | 24.25 |
| 1253 | 9.84 | 1593 | 16.38 | 1933 | 24.50 |
| 1263 | 10.00 | 1603 | 16.60 | 1943 | 24.76 |
| 1273 | 10.16 | 1613 | 16.82 | 1953 | 25.02 |
| 1283 | 10.33 | 1623 | 17.04 | 1963 | 25.28 |
| 1293 | 10.49 | 1633 | 17.27 | 1973 | - |
| 1303 | 10.66 | 1643 | 17.49 | | |

Appendix D

Relation between the pixel values and the apparent temperatures

| Shutter Lens | Gain (%) | Apparent Equations | Temperature | Cut-off pixels values |
|--------------|----------|--|-------------|----------------------------|
| f 2.8 | 55 | Ta1 = 2E-05pv + 1884.5 Ta2 = 3E-05pv + 1788.5 | | < 1,800,000 < 2,800,000 |
| | 60 | Ta1 = 3E-05pv + 1785.7 Ta2 = 5E-05pv + 1677.5 | | < 1,800,000 < 2,000,000 |
| | 65 | Ta1 = 4E-05pv + 1701.7 Ta2 = 5E-05pv + 1588.3 | | < 1,300,000 < 1,300,000 |
| | 70 | Ta1 = 4E-05pv + 1677.6 Ta2 = 5E-05pv + 1568.0 | | < 1,700,000 < 1,700,000 |
| | 75 | Ta1 = 4E-05pv + 1599.9 Ta2 = 5E-05pv + 1478.9 | | < 3,350,000 < 3,350,000 |
| f 4 | 60 | Ta1 = 2E-05pv + 1891.2 Ta2 = 4E-05pv + 1785.6 | | < 1,560,000 < 2,400,000 |
| | 65 | Ta1 = 4E-05pv + 1794.5 Ta2 = 5E-05pv + 1677.1 | | < 1,400,000 < 1,600,000 |
| | 70 | Ta1 = 3E-05pv + 1771.8 Ta2 = 4E-05pv + 1668.3 | | < 1,850,000 < 2,300,000 |
| | 75 | Ta1 = 4E-05pv + 1691.1 Ta2 = 5E-05pv + 1570.8 | | < 1,600,000 < 1,600,000 |
| | 80 | Ta1 = 4E-05pv + 1658.3 Ta2 = 5E-05pv + 1547.5 | | < 2,200,000 < 2,300,000 |
| f 5.6 | 70 | Ta1 = 2E-05pv + 1880.5 Ta2 = 4E-05pv + 1778.3 | | < 1,800,000 < 2,900,000 |
| | 75 | Ta1 = 4E-05pv + 1783.2 Ta2 = 5E-05pv + 1671.6 | | < 1,500,000 < 1,900,000 |
| | 80 | Ta1 = 4E-05pv + 1698.3 Ta2 = 6E-05pv + 1584.0 | | < 1,350,000 < 1,350,000 |
| | 85 | Ta1 = 4E-05pv + 1678.3 Ta2 = 5E-05pv + 1562.3 | | < 1,700,000 < 1,900,000 |
| | 90 | Ta1 = 4E-05pv + 1627.7 Ta2 = 5E-05pv + 1514.9 | | < 1,650,000 < 1,650,000 |

References

1. European Automobile Manufacturers' Association, <http://www.acea.be>. [Accessed on October 2008].
2. Environmental Protection Agency, <http://www.epa.gov>. [Accessed on October 2008].
3. European Commission, <http://www.ec.europa.eu>. [Accessed on October 2008].
4. Heywood, J. B., "Internal Combustion Engines Fundamentals", McGraw-Hill Science Engineering, 1988.
5. Addy Majewsky, W and K. Khair, M, "Diesel Emissions and Their Control", SAE International, 2006.
6. Shundoh, S. et al., "The Effect of Injection Parameters and Swirl on Diesel Combustion with High Pressure Fuel Injection", SAE 910489, 1991.
7. Shundoh, S. et al., "NO_x Reduction from Diesel Combustion Using Pilot Injection with High Pressure Fuel Injection", SAE 920461, 1992.
8. Ropke, S. et al., "NO_x Formation in Diesel Engines for Various Fuels and Intake Gases", SAE 950213, 1995.
9. Regulation (EC) 715-2007, Official Journal of the European Union, OJL 171, 2007.
10. Kittelson DB., "Engines and nanoparticles: a review", J Aerosol Sci 29:575-588, 1998.
11. Kittelson, DB; Piphon, ML; Ambs, JL; et al., "Particle concentrations in a diesel cylinder: comparison of theory and experiment", SAE 861569, 1986.
12. Dec, John E., "Soot Distribution in a DI Diesel Engine Using 2-D Imaging of Laser Induced Incandescence, Elastic Scattering and Flame Luminosity", SAE 920115, 1992.
13. Dec, John E., "Diesel Engine Combustion Studied in a Newly Designed Optical-Access Engine Using High Speed Visualization and 2-D Laser Imaging", SAE 930971, 1993.
14. Dec, John E., "Ignition and Early Soot Formation in a DI Diesel Engine Using Multiple 2-D Imaging Diagnostics", SAE 950456, 1995.

15. Dec, John E., "A Conceptual Model of DI Diesel Combustion Based on Laser Sheet Imaging", SAE 970873, 1997.
16. Senda, Jiro et al., "Experimental Analysis on Soot Formation Process in DI Diesel Combustion Chamber by Use of Optical Diagnostics", SAE 2002-01-0893, 2002.
17. Inagaki, K et al., "Quantitative Analysis of Soot Formation and Oxidation Process using Laser-Induced Incandescence", SAE 2003-01-1795, 2003.
18. Lee Chia-fon F., "Investigation of Soot Formation in Diesel Combustion Using Forward Illumination Light Extinction (FILE) Technique", SAE 2004-01-1411, 2004.
19. Lee Chia-fon F., "Investigation of Fuel Effects on Soot Formation Using Forward Illumination Light Extinction (FILE) Technique", SAE 2005-01-0365, 2005.
20. Lee Chia-fon F., "Study of Soot Formation of Oxygenated Diesel Fuels Using Forward Illumination Light Extinction (FILE) Technique", SAE 2006-01-1415, 2006.
21. Reitz R.D. et al., "Modelling the Effects of EGR and Injection Pressure on Soot Formation in a High-Speed Direct-Injection (HSDI) Diesel Engine Using a Multi-Step Phenomenological Soot Model", SAE 2005-01-0121, 2005.
22. Reitz R.D. et al., "Soot Structure in a Conventional Non-Premixed Diesel Flame", SAE 2006-01-0196, 2006.
23. Reitz R.D. et al., "Fuel Injection and Mean Swirl Effects on Combustion and Soot Formation in Heavy Duty Diesel Engines", SAE 2007-01-0912, 2007.
24. Zhao H., "HCCI and CAI Engines for the Automotive Industry", Woodhead Publishing Ltd, 2007.
25. Kaiser EW., Yang J., Culp T., Xu N. and Maricq M.M., "Homogeneous charge compression ignition engine-out emissions- does flame propagation occur in homogeneous charge compression ignition?", Int J Engine Research Vol 3 No 4, 2002.
26. U.S. Environmental Protection Agency (EPA), "Health assessment document for diesel engine exhaust". Prepared by the National Center for Environmental Assessment, Washington, DC, for the Office of Transportation and Air Quality; EPA/600/8-90/057F, 2002.
27. Holgate, S.T, UK Departments of Health, "Quantification of the Effects of Air Pollution on Health in the United Kingdom", The Stationery Office, London, 1998.

28. Najt, P. M. and Foster, D. E. "Compression-Ignited Homogeneous Charge Combustion", SAE 830264, 1983.
29. Aceves, S. M., Flowers, D. L., Martinez-Frias, J., Smith, J. R., Dibble, R., Au, M. and Girard, J. "HCCI Combustion: Analysis and Experiments", SAE 2001-01-2077, 2001.
30. Docquier, N., "Influence of Fresh Charge Preparation and Composition on Auto-Ignition Delays and Combustion Development in an Optical HCCI Direct Injection Diesel Engine", SAE 2003-01-3174, 2003.
31. Kashdan J.T, Nicolas Docquier and Bruneaux G., "Mixture Preparation and Combustion via LIEF and LIF of Combustion Radicals in a Direct-Injection, HCCI Diesel Engine", SAE 2004-01-2945, 2004.
32. Strålin, P., Wåhlin F. and Ångström H., "Effects of Injection Timing on the Conditions at Top Dead Center for Direct Injected HCCI", SAE 2003-01-3219, 2003.
33. Ra Y. and Reitz R. D., "The Use of Variable Geometry Sprays With Low Pressure Injection for Optimization of Diesel HCCI Engine Combustion", SAE 2005-01-0148, 2005.
34. N. P. Komninos, D. T. Hountalas and D. A. Kouremenos, "Description of in-Cylinder Combustion Processes in HCCI Engines Using a Multi-Zone Model", SAE 2005-01-0171, 2005.
35. Matsuo Odaka, Yasuhiro Daisho et al., "Ignition and Combustion Control of Diesel HCCI", SAE 2005-01-2132, 2005.
36. Guillaume Bression, Dominique Soleri, Sylvain Savy, Stéphane Dehoux, David Azoulay and Hedi Ben-Hadj Hamouda, Laurent Doradoux and Noureddine Guerrassi and Nick Lawrence, "A Study of Methods to Lower HC and CO Emissions in Diesel HCCI", SAE 2008-01-0034, 2008.
37. Y. Takeda, N. Keiichi, "Emissions Characteristics of Premixed Lean Diesel Combustion with Extremely Early Staged Fuel Injection", SAE 961163, 1996
38. Stefan Simescu, Thomas W. Ryan III, Gary D. Neely, Andrew C. Matheaus and Bapiraju Surampudi, "Partial Pre-Mixed Combustion with Cooled and Uncooled EGR in a Heavy-Duty Diesel Engine", SAE 2002-01-0963, 2002.

39. Stefan Simescu, Scott B. Fiveland, Lee G. Dodge, "An Experimental Investigation of PCCI-DI Combustion and Emissions in a Heavy-Duty Diesel Engine", SAE 2003-01-0345, 2003.
40. Sanghoon Kook and Choongsik Bae, "Combustion Control Using Two-Stage Diesel Fuel Injection in a Single-Cylinder PCCI Engine", SAE 2004-01-0938, 2004.
41. Tomohiro Kanda, Takazo Hakozaki, Tatsuya Uchimoto, Jyunichi Hatano, Naoto Kitayama and Hiroshi Sono, "PCCI Operation with Early Injection of Conventional Diesel Fuel", SAE 2005-01-378, 2005.
42. Tomohiro Kanda, Takazo Hakozaki, Tatsuya Uchimoto, Jyunichi Hatano, Naoto Kitayama and Hiroshi Sono, "PCCI Operation with Fuel Injection Timing Set Close to TDC", SAE 2006-01-0920, 2006.
43. W. L. Hardy and R. D. Reitz, "A Study of the Effects of High EGR, High Equivalence Ratio, and Mixing Time on Emissions Levels in a Heavy-Duty Diesel Engine for PCCI Combustion", SAE 2006-01-0026, 2006.
44. W. L. Hardy and R. D. Reitz, "An Experimental Investigation of Partially Premixed Combustion Strategies Using Multiple Injections in a Heavy-Duty Diesel Engine", SAE 2006-01-0917, 2006.
45. Ryan M. Nevin, Yong Sun, Manuel A. Gonzalez D. and Rolf D. Reitz, "PCCI Investigation Using Variable Intake Valve Closing in a Heavy Duty Diesel Engine", SAE 2007-01-0903, 2007.
46. Sangsuk Lee and Rolf D. Reitz, "Spray Targeting to Minimize Soot and CO Formation in Premixed Charge Compression Ignition (PCCI) Combustion with a HSDI Diesel Engine", SAE 2006-01-0918, 2006.
47. Gary D. Neely, Shizuo Sasaki, Yiqun Huang, Jeffrey A. Leet and Daniel W. Stewart, "New Diesel Emission Control Strategy to Meet US Tier 2 Emissions Regulations", SAE 2005-01-1091, 2005.
48. Malin Alriksson and Ingemar Denbratt, "Low Temperature Combustion in a Heavy Duty Diesel Engine Using High Levels of EGR", SAE 2006-01-0075, 2006.
49. G. Avolio, C. Beatrice, N. Del Giacomo, C. Guido, M. Migliaccio and V. Fraioli, "Effects of Highly Cooled EGR on Modern Diesel Engine Performance at Low Temperature", SAE 2007-24-0014, 2007.

50. T. C. Tow, D. A. Pierpont, R. D. Reitz, "Reducing Particulate and NO_x Emissions by Using Multiple Injections in a Heavy; Duty D.I. Diesel Engine", SAE 940897, 1994.
51. D. A. Nehmer, R. D. Reitz, "Measurement of the Effect of Injection Rate and Split Injections on Diesel Engine Soot and NO_x Emissions", SAE 940668, 1994.
52. Toshitaka Minami, Kouichi Takeuchi, Naoki Shimazaki, "Reduction of Diesel Engine NO_x Using Pilot Injection", SAE 950611, 1995.
53. D. A. Pierpont, D. T. Montgomery, R. D. Reitz, "Reducing Particulate and NO_x Using Multiple Injections and EGR in a D.I. Diesel", SAE 950217, 1995.
54. Zhiyu Han, Ali Uludogan, Gregory J. Hampson, Rolf D. Reitz, "Mechanism of Soot and NO_x Emission Reduction Using Multiple-Injection in a Diesel Engine", SAE 960633, 1996.
55. P. V. Farrell, C. T. Chang, T. F. Su, "High Pressure Multiple Injection Spray Characteristics", SAE 960860, 1996.
56. D. T. Montgomery and R. D. Reitz, "Effects of Multiple Injections and Flexible Control of Boost and EGR on Emissions and Fuel Consumption of a Heavy-Duty Diesel Engine", SAE 2001-01-0195, 2001.
57. P. J. Shayler, T. D. Brooks, G. J. Pugh and R. Gambrill, "The Influence of Pilot and Split-Main Injection Parameters on Diesel Emissions and Fuel Consumption", SAE 2005-01-0375, 2005.
58. Yuyin Zhang, Tomoaki Ito and Keiya Nishida, "Characterization of Mixture Formation in Split-Injection Diesel Sprays via Laser Absorption-Scattering (LAS) Technique", SAE 2001-01-3498, 2001.
59. Yuyin Zhang and Keiya Nishida, "Vapor/Liquid Behavior in Split Injection D.I. Diesel Engine Sprays in a 2-D Model Combustion Chamber", SAE 2003-01-1837, 2003.
60. P. J. Shayler and H. K. Ng, "Simulation Studies of the Effect of Fuel Injection Pattern on NO and Soot Formation in Diesel Engines", SAE 2004-01-0116, 2004.
61. Marco Bakenhus, Rolf D. Reitz, "Two-Colour Combustion Visualization of Single and Split Injections in a Single-Cylinder, Heavy-Duty D.I. Diesel Engine Using an Endoscope-Based Imaging System", SAE 1999-01-1112, 1999.

62. S. Kevin Chen, "Simultaneous Reduction of NO_x and Particulate Emissions by Using Multiple Injections in a Small Diesel Engine", SAE 2000-01-3084, 2000.
63. C. Beatrice, P. Belardini, C. Bertoli, N. Del Giacomo, Ma. Migliaccio, "Downsizing of Common-Rail D.I. Engines: Influence of Different Injection Strategies on Combustion Evolution", SAE 2003-01-1784, 2003.
64. M. Badami, F. Mallamo, F. Millo and E. E. Rossi, "Influence of Multiple Injection Strategies on Emissions, Combustion Noise and BSFC of a DI Common Rail Diesel Engine", SAE 2002-01-0503, 2002.
65. F. Mallamo, M. Badami and F. Millo, "Analysis of Multiple Injection Strategies for the Reduction of Emissions, Noise and BSFC of a DI CR Small Displacement Non-Road Diesel Engine", SAE 2002-01-2672, 2002.
66. Rickard Ehleskog and Raúl L. Ochoterena, "Soot Evolution in Multiple Injection Diesel Flames", SAE 2008-01-2470, 2008.
67. Yi Liu and Rolf D. Reitz, "Optimizing HSDI Diesel Combustion and Emissions Using Multiple Injection Strategies", SAE 2005-01-0212, 2005.
68. K. Gill and H. Zhao, "In-cylinder Studies of Fuel Injection and Combustion from a Narrow Cone Fuel Injector in a High Speed Single Cylinder Optical Engine", SAE 2008-01-1789, 2008.
69. Tobias Husberg, Ingemar Denbratt and Anders Karlsson, "Analysis of Advanced Multiple Injection Strategies in a Heavy-Duty Diesel Engine using Optical Measurements and CFD-Simulations", SAE 2008-01-1328, 2008.
70. Sylvain Mendez and Benoist Thirouard, "Using Multiple Injection Strategies in Diesel Combustion: Potential to Improve Emissions, Noise and Fuel Economy Trade-Off in Low CR Engines", SAE 2008-01-1329, 2008.
71. Tsung-Cheng Wang, Joong-Sub Han, Xingbin Xie, Ming-Chia Lai and Naeim A. Henein, Ernest Schwarz and Walter Bryzik, "Direct Visualization of High Pressure Diesel Spray and Engine Combustion", SAE 1999-01-3496, 1999.
72. C. Beatrice, C. Bertoli, N. Del Giacomo, P. Massoli and M.na. Migliaccio, "Combustion Behavior Analysis in a Transparent Research Engine Equipped with a Common Rail Diesel Injection System", SAE 2001-01-1825, 2001.

73. C. Beatrice, C. Bertoli, N. Del Giacomo, P. Massoli and M.na. Migliaccio, "Combustion Behavior Analysis in a Transparent Research Engine Equipped with a Common Rail Diesel Injection System", SAE 2000-01-1825, 2000.
74. Cheolwoong Park, Sanghoon Kook and Choongsik Bae, "Effects of Multiple Injections in a HSDI Diesel Engine Equipped With Common Rail Injection System", SAE 2004-01-0127, 2004.
75. Tobias Husberg, Savo Gjirja and Ingemar Denbratt, Johan Engström, "Visualization of EGR Influence on Diesel Combustion With Long Ignition Delay in a Heavy-duty Engine", SAE 2001-01-2947, 2004.
76. Tiegang Fang, Robert E. Coverdill, Chia-fon F. Lee and Robert A. White, "Low Temperature Combustion within a Small Bore High Speed Direct Injection (HSDI) Diesel Engine", 2005-01-0919, 2005.
77. Tiegang Fang, Robert E. Coverdill, Chia-fon F. Lee and Robert A. White, "Combustion and Soot Visualization of Low Temperature Combustion within an HSDI Diesel Engine Using Multiple Injection Strategy", SAE 2006-01-0078, 2006.
78. Schmidt, K. and Van Gerpen, J., "The Effect of Biodiesel Fuel Composition on Diesel Combustion and Emissions", SAE Paper 961086, 1996.
79. Last, R.J., Krüger, M. and Dürnholtz, M., "Emissions and Performance Characteristics of a 4-Stroke, Direct Injected Diesel Engine Fueled with Blends of Biodiesel and Low Sulfur", SAE Paper 961166, 1996.
80. Graboski, M.S., Ross, J.D. and McCormick, R.L., "Transient Emissions from No. 2 Diesel and Biodiesel Blends in a DDC Series 60 Engine", SAE Paper 961166, 1996.
81. Grimaldi, C.N. and Postriotti, L., "Experimental Comparison between Conventional and Bio-derived Fuels Sprays from a Common Rail Injection System", SAE 2000-01-1252, 2000.
82. Grimaldi, C.N., Mariani, F. and Postriotti, L.: "Performance and Emissions of a Common Rail DI Diesel Engine Using Fossil and Different Bio- Derived Fuels", SAE 2001-01-2017, 2001.
83. Grimaldi, C. N., Postriotti, L., Battistoni M. and Millo F., "Common Rail HSDI Diesel Engine Combustion and Emissions with Fossil / Bio-Derived Fuel Blends", SAE 2002-01-0865, 2002.

84. Lucio Postrioti, Michele Battistoni and Carlo N. Grimaldi and Federico Millo, "Injection Strategies Tuning for the Use of Bio-Derived Fuels in a Common Rail HSDI Diesel Engine", SAE 2003-01-0768, 2003.
85. Daniel D. Corgard and Rolf D. Reitz , "Effects of Alternative Fuels and Intake Port Geometry on HSDI Diesel Engine Performance and Emissions", SAE2001-01-0647, 2001.
86. Jiro Senda, Nobunori Okui, Teppei Suzuki and Hajime Fujimoto, "Flame Structure and Combustion Characteristics in Diesel Combustion Fueled with Bio-diesel", SAE 2004-01-0084, 2004.
87. Henry Ng and Munidhar Biruduganti and Kevin Stork, "Comparing the Performance of SunDieselTM and Conventional Diesel in a Light-Duty Vehicle and Heavy-Duty Engine", SAE 2005-01-3776, 2005
88. Gill K., "Investigation of Multiple Injections and Fuel Properties on Diesel Combustion and Emission", Brunel University PhD Thesis, 2007
89. Gary S. Settles, "Schlieren and shadowgraph techniques: visualizing phenomena in transparent media", Springer, 2001.
90. L. Melton & J. Verdieck, "Vapor/Liquid Visualization in Fuel Sprays", Proc. of 20th Symposium (Int.) on Combustion, pp. 1283-1290, 1984.
91. L. Melton & J. Verdieck, "Vapor/Liquid Visualization for Fuel Sprays", Combustion Science and Technology, 1984.
92. L. A Melton, Final Report of Army Research Office contract DAAL 03-86-k-0082, January 1988.
93. Zhao H. and Ladommatos N., "Engine Combustion Instrumentation and Diagnostics", Society of Automotive Engineers, Inc., 2001.
94. J. Senda et al., "Quantitative Analysis of Fuel Vapor Concentration in Diesel Spray by Exciplex Fluorescence Method", SAE Paper 970796, 1997.
95. J. B. Ghandhi and T. Kim, "Quantitative 2-D Fuel Vapor Concentration Measurements in an Evaporating Diesel Spray using the Exciplex Fluorescence Method", SAE paper 2001-01-3495, 2001.
96. M. D. Fry and J. E. Nightingale, "Use of high-speed photography to study in-cylinder mixture preparation on a four-valve SI engine", SAE 944007, 1994.

97. Beeck Manfred-Andreas, Hentdchel Werner, "Laser metrology: a diagnostic tool in automotive development processes", *Optics and lasers in engineering*, vol. 34, no2, 2000.
98. Kiranjeev Gill, Hua Zhao, Kelly Sison Chris Marriner, "In-cylinder Studies of Multiple Diesel Fuel Injection in a Single Cylinder Optical Engine", SAE 2005-01-0915, 2005.
99. Colin E. Webb, Julian D. C. Jones, "Handbook of Laser Technology and Applications: Applications", Taylor & Francis, 2004, ISBN 0750309660.
100. L. A. Melton, "Soot diagnostics based on laser heating," *Appl. Opt.* **23**, 2201-2208, 1984.
101. Kock, B.F., T. Eckhardt, and P. Roth, In-cylinder sizing of diesel particles by time-resolved laser-induced incandescence (TR-LII). *Proceedings of the Combustion Institute*, 2002. 29(2): p. 2775-2782.
102. Kock, B.F., et al., Two-color time-resolved LII applied to soot particle sizing in the cylinder of a Diesel engine. *Combustion and Flame*, 2006. 147(1-2): p. 79-92.
103. Oh, K.C. and H.D. Shin, The effect of oxygen and carbon dioxide concentration on soot formation in non-premixed flames. *Fuel*, 2005. 85(5-6): p. 615-624.
104. Hottel, H.G., Broughton, F.P., "Determination of true temperature and total radiation from luminous gas flames", *Ind. and Engng Chem.*, 4-2, pp166, 1932.
105. Matsui, Y., Kamimoto, T. and Matsuoka, S., "A study of the time and space resolved measurement of flame temperature and soot concentration in a DI diesel engine by the two-colour method", SAE 790491, 1979.
106. Matsui, Y., Kamimoto, T. and Matsuoka, S., "A study on the application of the two-colour method to the measurement of flame temperature and soot concentration in diesel engines", SAE 800970, 1980.
107. Matsui, Y., Kamimoto, T. and Matsuoka, S., "Formation and oxidation processes of soot particulates in a DI diesel engine – an experimental study via the two-colour method", SAE 820464, 1982.
108. Zhao H. and Ladommatos N., "A Guide to Measurement of Flame Temperature and Soot Concentration in Diesel Engines Using the Two-Colour Method Part 1: Theory", SAE 941956, 1994.

109. Zhao H. and Ladommatos N., "A Guide to Measurement of Flame Temperature and Soot Concentration in Diesel Engines Using the Two-Colour Method Part 2: Implementation", SAE 941957, 1994.
110. C. Arcoumanis, C. Bae, A. Nagwaney, and J. H. Whitelaw, "Effect of EGR on Combustion Development in a 1.9L DI Diesel Optical Engine", SAE 950850, 1995.
111. Hoang Xuan Quoc, Jean-Marc Vignon, and Maurice Brun, "A New Approach of the Two-Colour Method for Determining Local Instantaneous Soot Concentration and Temperature in a D.I. Diesel Combustion Chamber", SAE 910736, 1991.
112. Joseph S. Shakal, Jay K. Martin, "Imaging and Spatially Resolved Two-Colour Temperature Measurements through a Coherent Fiber Optic: Observation of Auxiliary Fuel Injection Effects on Combustion in a Two-Stroke DI Diesel", SAE 940903, 1994.
113. M. Bakenhus and R. D. Reitz, "Two-Colour Combustion Visualization of Single And Split Injections in a Single-Cylinder Heavy-Duty DI Diesel Engine Using an Endoscope-Based Imaging System", SAE 1999-01-112, 1999.
114. Gregory J. Hampson & Rolf D. Reitz, "Two-Colour Imaging of In-Cylinder Soot Concentration and Temperature in a Heavy-Duty DI Diesel Engine with Comparison to Multidimensional Modeling for Single and Split Injections", SAE 980524, 1998.
115. Y. Tominaga, H. Tajima, A. Strom and K. Uno, "Flame Temperature Measurement in Diesel Engine on Two Colour Method utilizing CMOS Camera", Journal of the Visualization Society of Japan, VOL.25;NO.Suppl.2;PAGE.97-98, 2005.
116. <http://www.perkins.com> [accessed on October 2008].
117. E. R. K. Rajput, "A Textbook of Automobile Engineering", Laxmi Publications, 2007.
118. Paulo César de Ferreira Gomes and David A. Yates, "Analysis of the Influence of Injection Timing on Diesel Combustion by the Two-Colour Method", SAE 982890, 1998.
119. J. V. Pastor et al., "Analysis Methodology of Diesel Combustion by Using Flame Luminosity, Two-Colour Method and Laser-Induced Incandescence", SAE 2005-24-012, 2005.
120. J. V. Pastor et al., "Contribution to the application of two-colour imaging to diesel combustion", Measurement Science and Technology, 2007.

121. S. Pöttker, U. Wagner et al., "Investigations of HCCI Combustion Using Multi-Stage Direct-Injection with Synthetic Fuels", SAE 2004-01-2946, 2004.
122. S. Merkel et al., "Investigation of a New Injection Strategy for Simultaneous Soot and NO_x Reduction in a Diesel Engine with Direct Injection", SAE 2008-01-1790, 2008.
123. Sison K. "In-cylinder Studies of Diesel Combustion with Oxygenated Fuels and Multiple Injections", Brunel University PhD Thesis, 2006.
124. R. D. Larrabee, "Spectral emissivity of tungsten", J. Opt. Soc. Am. 49, 1959.
125. Yan, J. Borman, G, "Analysis and In-Cylinder Measurement of Particulate Radiant Emissions and Temperature in a Direct Injection Diesel Engine", SAE 881315, 1988.
126. Power Transmission and Motion Control (PTMC 2004), Professional Engineering Publishing Ltd, eds. Burrows CR, Johnston DN, and Edge KA, 2004, ISBN: 86058 466.
127. W. Zeuch, "Neue Verfahren zur Messung des Einspritzgesetzes und Einspritz-Regelmässigkeit von Diesel-Einspritzpumpen", MTZ, Jahr. 22 Heft 9 1961.